



Delft University of Technology

Leaching and efflorescence of alkali-activated slag materials

A multi-scale experimental and simulation study

Liu, C.

DOI

[10.4233/uuid:5dc64875-580c-4e3f-9c63-5aeef70d4b8c](https://doi.org/10.4233/uuid:5dc64875-580c-4e3f-9c63-5aeef70d4b8c)

Publication date

2025

Document Version

Final published version

Citation (APA)

Liu, C. (2025). *Leaching and efflorescence of alkali-activated slag materials: A multi-scale experimental and simulation study*. [Dissertation (TU Delft), Delft University of Technology].
<https://doi.org/10.4233/uuid:5dc64875-580c-4e3f-9c63-5aeef70d4b8c>

Important note

To cite this publication, please use the final published version (if applicable).
Please check the document version above.

Copyright

Other than for strictly personal use, it is not permitted to download, forward or distribute the text or part of it, without the consent of the author(s) and/or copyright holder(s), unless the work is under an open content license such as Creative Commons.

Takedown policy

Please contact us and provide details if you believe this document breaches copyrights.
We will remove access to the work immediately and investigate your claim.

LEACHING AND EFFLORESCENCE OF ALKALI-ACTIVATED SLAG MATERIALS

A MULTI-SCALE EXPERIMENTAL
AND SIMULATION STUDY

CHEN LIU

Leaching and Efflorescence of Alkali-activated Slag Materials

—A multi-scale experimental and simulation study

Dissertation

For the purpose of obtaining the degree of doctor
at Delft University of Technology

by the authority of the Rector Magnificus Prof. dr. ir. T.H.J.J. van der Hagen
chair of the Board for Doctorates
to be defended publicly on
Thursday 2 October 2025 at 10.00

By

Chen LIU

Master of Science in Materials Science and Engineering
Wuhan University of Technology, P.R. China
Born in Tianjin, P.R. China

This dissertation has been approved by the promoters

Promotor: Prof. dr. G. Ye

Promotor: Prof. dr. Ir. E. Schlangen

Composition of the doctoral committee:

Rector Magnificus

Chairperson

Prof. dr. G. Ye

Delft University of Technology, promotor

Prof. dr. ir. E. Schlangen

Delft University of Technology, promotor

Independent Members:

Prof.dr. A. Vollpracht

RWTH Aachen University

Prof.dr. M.J. Santofimia Navarro

Delft University of Technology

Prof.dr. Z. Liu

Wuhan University of Technology

Prof.dr. Z. Li

Harbin Institute of Technology

Dr.ir. B. Šavija

Delft University of Technology

Prof.dr. H.M. Jonkers (reserve member)

Delft University of Technology



Keywords: Alkali-activated slag; leaching; efflorescence; molecular dynamics simulation; C-(N-)A-S-H gels; solid-state NMR; degradation; cracking; reactive transport modelling; lightweight fine aggregate

Printed by: Ipkamp Printing, The Netherlands

Thesis format by: Chen Liu

Cover design: Junkai Lan & Chen Liu

Copyright © 2025 by Chen Liu

All rights reserved. This copy of the thesis has been supplied on the condition that anyone who consults it is understood to recognise that its copyright rests with its author and that no quotation from the thesis and no information derived from it may be published without the author's prior consent.

ISBN: 978-94-6518-100-4

An electronic version of this dissertation is available at <http://repository.tudelft.nl/>

长风破浪会有时，直挂云帆济沧海。

Contents

<i>List of Abbreviations</i>	<i>V</i>
<i>Summary</i>	<i>VII</i>
<i>Samenvatting</i>	<i>IX</i>
Chapter 1	
<i>Introduction</i>	<i>I</i>
1.1 Research background	1
1.2 Research aim and objectives	2
1.3 Research scope	3
1.4 Research strategy	3
1.5 Research outline	4
Chapter 2	
<i>Literature survey</i>	7
2.1 Introduction	7
2.2 General introduction of AAMs	7
2.3 Leaching	9
2.3.1 Leaching of PC-based materials	9
2.3.2 Leaching of AAS materials	9
2.4 Efflorescence	15
2.4.1 Efflorescence of PC-based materials	15
2.4.2 Efflorescence of AAS materials	15
2.5 Problem definition	19
2.6 Conclusions	20
Chapter 3	
<i>Leaching behaviour of synthetic C-(N-)A-S-H gels</i>	21
3.1 Introduction	21
3.2 Experiments	21
3.2.1 Gel synthesis.....	21
3.2.2 Leaching test.....	23
3.3 Atomistic simulation	23
3.3.1 Model construction	23
3.3.2 Dissolution free energy calculation	25
3.3.3 Diffusion calculation	27
3.4 Results and discussion	27
3.4.1 XRD pattern of synthetic gels	27
3.4.2 Leaching behaviour of synthetic gels.....	28
3.4.3 Dissolution free energy of Ca and Na in gels	31
3.4.4 Diffusion coefficient of Ca and Na in the nanopore of gels	33
3.5 Discussion	35
3.5.1 Impact of gel chemistry on the leaching potential of Ca and Na	35

3.5.2 Mechanisms behind the different leaching potential of Ca and Na	36
3.5.3 Perspective on the dissolution of cations in gels.....	37
3.6 Conclusions.....	37

Chapter 4

Structural evolution of synthetic C-(N-)A-S-H gels subjected to leaching..... 39

4.1 Introduction	39
4.2 Materials and methods.....	39
4.2.1 Materials.....	39
4.2.2 Methods	40
4.3 Results and discussion	41
4.3.1 Ion concentrations in the leachate	41
4.3.2 Gel composition.....	43
4.3.3 Gel structure.....	45
4.4 Summary and perspectives.....	53
4.5 Conclusions	54

Chapter 5

Leaching mechanisms of AAS pastes..... 55

5.1 Introduction	55
5.2 Materials and methods.....	55
5.2.1 Raw materials and mixture design	55
5.2.2 Experimental methods	57
5.3 Results and discussion	58
5.3.1 Ion concentrations.....	58
5.3.2 Reaction degree of slag	61
5.3.3 Phase assemblage.....	62
5.3.4 Paste chemistry	65
5.3.5 Pore structure.....	69
5.3.6 Compressive strength.....	70
5.4 Summary and perspective	71
5.5 Conclusions	72

Chapter 6

***Prediction of pore structure deterioration of AAS pastes due to long-term leaching* 73**

6.1 Introduction	73
6.2 Experiments	73
6.2.1 Materials and sample preparation	73
6.2.2 SEM characterisations	74
6.3 Modelling.....	74
6.3.1 Microstructure formation.....	76
6.3.2 Ion diffusion.....	78
6.3.3 Pore structure deterioration.....	80
6.4 Experimental results and discussion	82
6.4.1 Pore structure analyses of AAS pastes subjected to water immersion.....	82
6.4.2 Elemental composition of AAS pastes subjected to water immersion	86

6.5 Modelling results and discussion	91
6.5.1 Model validation.....	91
6.5.2 Pore solution	92
6.5.3 Phase assemblage.....	93
6.5.4 Pore structure.....	95
6.6 Conclusions.....	96

Chapter 7

<i>Cracking of AAS pastes induced by water immersion</i>	97
7.1 Introduction	97
7.2 Methodology	97
7.2.1 Outline of this chapter.....	97
7.2.2 Materials and mixtures.....	98
7.2.3 Experimental methods	99
7.2.4 Numerical simulation.....	101
7.3 Experimental results	103
7.3.1 Strength	103
7.3.2 Phase assemblage.....	105
7.3.3 Paste chemistry	106
7.3.4 Leaching behaviour.....	107
7.3.5 Gel stability.....	108
7.3.6 Pore structure.....	109
7.4 Simulation results	110
7.5 Discussion	111
7.5.1 Cracking mechanisms of AAS materials underwater	111
7.5.2 Potential mitigation strategies	113
7.6 Conclusions.....	114

Chapter 8

<i>Efflorescence mechanisms of AAS pastes.....</i>	115
8.1 Introduction	115
8.2 Methodology	116
8.2.1 Materials and mixtures.....	116
8.2.2 Efflorescence tests under different conditions.....	116
8.2.3 Leaching tests	117
8.2.4 Paste characterisations.....	119
8.3 Results	119
8.3.1 Visual observation of efflorescence.....	119
8.3.2 Leaching tests of AAS pastes	125
8.3.3 Characterizations of AAS pastes	129
8.4 Discussion	137
8.4.1 Efflorescence process of AAS pastes	137
8.4.2 Efflorescence mechanisms of AAS pastes.....	138
8.5 Conclusions.....	140

Chapter 9

<i>Mitigating the efflorescence of AAS mortars by aluminosilicate-based lightweight fine aggregates</i>	143
9.1 Introduction	143
9.2 Materials and methods	143
9.2.1 Raw materials	143
9.2.2 Mortar preparation	144
9.2.3 Efflorescence and leaching tests	145
9.2.4 Characterizations	145
9.3 Results	147
9.3.1 Efflorescence tests	147
9.3.2 Leaching tests	149
9.3.3 Impacts of LWFA on AAS mortars	152
9.4 Discussion	160
9.4.1 Mitigating mechanisms of LWFA on the efflorescence of AAS mortars	160
9.4.2 Advantages and limitations of LWFA in AAS materials	161
9.5 Conclusions	161

Chapter 10

<i>Retrospection, conclusions, and prospects</i>	163
10.1 Retrospection	163
10.2 Conclusions	164
10.3 Contributions	166
10.4 Prospect	167
<i>Appendix A</i>	169
<i>Appendix B</i>	173
<i>Appendix C</i>	175
<i>Reference</i>	177
<i>List of publications</i>	193
<i>Acknowledgments</i>	195
<i>Curriculum Vitae</i>	197

List of Abbreviations

AAMs	Alkali-activated materials
AAS	Alkali-activated slag
AASF	Alkali-activated slag and fly ash
ASTM	American Society for Testing and Materials
BFS	Blast furnace slag
BSE	Backscattered electron
C-S-H	Calcium-silicate-hydrate
C-(A-)S-H	Calcium-(aluminium-)silicate hydrates
C-(N-)A-S-H	Calcium-(sodium-)aluminium-silicate hydrates
CVs	Collective variables
DFT	Density functional theory
DTG	Derivative thermogravimetry
EDX	Energy-dispersive X-ray spectroscopy
EN	European Standards
FEM	Finite element method
FTIR	Fourier transform infrared spectroscopy
GCMC	Grand Canonical Monte Carlo
GEMS	Gibbs Energy Minimisation Software
GGBFS	Ground granulated blast furnace slag
Ht	Hydrotalcite-like phases
ICP-OES	Inductively coupled plasma optical emission spectroscopy
ITZ	Interfacial transition zone
LBM	Lattice Boltzmann method
LOI	Loss on ignition
LWFA	Lightweight fine aggregate
MAS NMR	Magic-angle spinning nuclear magnetic resonance spectroscopy
MCL	Mean chain length
MD	Molecular dynamics
MIP	Mercury Intrusion Porosimetry
Ms	Silicate modulus, $\text{SiO}_2/\text{Na}_2\text{O}$ ratio
N-A-S-H	Sodium-aluminum-silicate hydrates

N-(C-)A-S-H	Sodium-(calcium-)aluminum-silicate hydrates
NA	Nitrogen absorption
NEN	Nederlands Normalisatie-instituut
NH	Sodium hydroxide
NPT	Isothermal-isobaric ensemble
NS	Sodium silicate
NVT	Canonical ensemble
PC	Portland cement
PDF	Powder diffraction file
RH	Relative humidity
SAM	Salicylic acid-methanol
SEM	Scanning electron microscope
TGA	Thermogravimetric analysis
w/b	Water-to-binder ratio
WDS	Wavelength-dispersive spectrometer
XRF	X-ray fluorescence
XRD	X-ray diffraction

Summary

Alkali-activated slag (AAS) materials, composed of blast furnace slag as precursor and alkali solutions as activators, are emerging as sustainable alternatives in construction due to their significantly lower CO₂ emissions compared to traditional Portland cement (PC) -based materials. These cement-free binders often demonstrate comparable or even superior mechanical properties and chemical resistance. However, long-term durability remains a concern, particularly in humid environments where AAS materials are more susceptible to degradation than PC materials.

Leaching has been identified as the primary deterioration phenomenon in AAS materials under humid environments, yet the underlying mechanisms remain poorly understood. Additionally, efflorescence, characterised by white deposits on the material surface, is believed to be a consequence of leaching. However, the relationship between leaching and efflorescence in AAS materials remains unclear, necessitating further investigation. This thesis aims to bridge these knowledge gaps by investigating the leaching behaviour of AAS materials at multiple scales and developing effective strategies to mitigate efflorescence.

To systematically explore leaching mechanisms, three C-(N)-A-S-H gels, with varying Ca/Si and Al/Si ratios, were synthesised using the sol-gel method. Their leaching behaviours in water were studied experimentally, while further insights into ion dissolution discrepancies were provided by molecular dynamics (MD) simulation. The results revealed that Na showed a significantly higher leaching rate than other ions, with gels containing a higher Ca/Si ratio and a lower Al/Si ratio showing a higher Na leaching potential. Solid-state NMR analysis indicated structural changes in gels after immersion, with longer mean chain lengths attributed to the charge compensator redistribution within the gel interlayer.

The degradation of AAS pastes subjected to leaching was investigated in both sodium hydroxide (NH) and sodium silicate (NS) activation systems. The impacts of leaching on the pore solution chemistry, slag reaction, phase assemblage, and pore structure were studied. Initially, leaching lowered the pH of the pore solution, inhibiting further slag reaction and reaction product formation. Over time, leaching resulted in gel decomposition, leading to a coarser pore structure and a reduction in compressive strength. Comparatively, NS pastes exhibited greater resistance to leaching, attributed to their denser pore structure. To predict the long-term pore structure degradation, a diffusion-dissolution model was developed. Simulated results indicated that after 10 years of water immersion, significant pore structure deterioration was confined to a depth of 1.5 mm, while gel reorganisation due to the leaching of Na extended up to 100 mm.

Despite their superior resistance to leaching, NS pastes developed significant cracks after water immersion, with crack severity increasing alongside higher silicate moduli. Chemical changes in AAS pastes with varying silicate moduli (m=0, 0.5, 1, and 1.5) were analysed pre- and post-immersion. Additionally, the simulation result indicated that the paste with high silicate moduli (m=1 and 1.5) showed a larger gradient of water content. The wetted part relaxed pore pressure locally, inducing compressive stress at the surface and tensile stress at the centre. If the tensile stress exceeds the material's tensile strength, cracking initiated at the centre and can even further propagate to the surface.

Efflorescence in AAS paste cylinders was examined under semi-contact water conditions. Higher alkali dosages, coarser pore structures, and lower relative humidities were found to accelerate efflorescence formation. NS pastes were more susceptible to cracking under these conditions, further promoting efflorescence product formation along cracks. A quantitative evaluation method was developed to assess efflorescence severity by measuring Na content in efflorescence deposits. The study confirmed a positive correlation between Na leaching and efflorescence intensity and clarified efflorescence mechanisms in both NH and NS systems.

An aluminosilicate-based lightweight fine aggregate (LWFA), specifically expanded shale, was employed to mitigate efflorescence in NH mortars. Substituting sand with LWFA at 20% and 50% by volume reduced the efflorescence by 14.6% and 43%, respectively. The mitigation mechanisms of LWFA were unveiled in terms of gel chemistry, pore solution and pore structure. The pozzolanic reaction of LWFA contributed additional Si and Al to the system, enhancing Na ion binding within gels and reducing its availability for efflorescence formation. Additionally, the internal curing effect of LWFA densified the surrounding pastes, hindering ion and water transport, thereby further restricting efflorescence development. Notably, LWFA incorporation improved the flexural strength of mortars without significantly compromising compressive strength.

This study advances the understanding of leaching behaviours and the resulting structural changes in C-(N-)A-S-H gels. The developed diffusion-dissolution and water transport models offer valuable insights into microstructural degradation and crack formation in AAS materials exposed to humid conditions. Furthermore, the proposed quantitative method provides new insights into efflorescence assessment, and the introduction of LWFA offers an efficient strategy to mitigate the efflorescence of AAS concretes. The findings contribute to both academia and industry by enhancing fundamental knowledge of AAS durability and guiding the development of more sustainable and durable AAS materials for construction applications.

Samenvatting

Alkali-geactiveerde slakmaterialen (AAS), samengesteld uit hoogovenslak als precursor en alkalische oplossingen als activatoren, verschijnen als duurzame alternatieven in de bouw vanwege hun aanzienlijk lagere CO₂-uitstoot vergeleken met traditionele materialen op basis van Portlandcement (PC). Deze cementvrije bindmiddelen vertonen vaak vergelijkbare of zelfs betere mechanische eigenschappen en chemische bestendigheid. De duurzaamheid op lange termijn blijft echter een punt van zorg, met name in vochtige omgevingen waar AAS-materialen gevoeliger zijn voor degradatie dan PC-materialen.

Uitlogging is geïdentificeerd als het belangrijkste degradatieverschijnsel van AAS in vochtige omstandigheden, maar de onderliggende mechanismen zijn nog onvoldoende begrepen. Daarnaast wordt uitbloeiing — gekarakteriseerd door witte afzettingen op het materiaaloppervlak — beschouwd als een gevolg van uitlogging. De relatie tussen uitlogging en uitbloeiing bij AAS is echter onduidelijk en vereist verder onderzoek. Dit proefschrift heeft tot doel deze kennishanden te dichten door het uitlooggedrag van AAS op meerdere schalen te onderzoeken en effectieve strategieën voor het beperken van uitbloeiing te ontwikkelen.

Om de uitloogmechanismen systematisch te bestuderen, werden drie C-(N-)A-S-H-gels met verschillende Ca/Si- en Al/Si-verhoudingen gesynthetiseerd via de sol-gelmethode. Hun uitlooggedrag in water werd experimenteel onderzocht terwijl verdere inzichten in de verschillen van het oplossen van ionen werden verkregen met moleculaire dynamica (MD)-simulaties. De resultaten onthullen dat Na een duidelijk hogere uitloogsnelheid vertoonde dan andere ionen; gels met een hogere Ca/Si-verhouding en een lagere Al/Si-verhouding hadden een grotere mogelijkheid voor Na-uitlogging. Vaste-stof NMR-analyse wees op structurele veranderingen in de gels na onderdompeling, waarbij de toegenomen gemiddelde ketenlengte werd toegeschreven aan herverdeling van ladingscompenserende ionen in de tussenlaag van de gel.

De degradatie van AAS-pasta's onder uitlogging werd onderzocht in zowel natriumhydroxide-(NH) als natriumsilicaat- (NS) geactiveerde systemen. De effecten van uitlogging op de chemie van de porie-oplossing, de slakreactie, fase-samenstelling en poriestructuur werden bestudeerd. In de beginfase werd de pH van de porie-oplossing verlaagd door uitlogging, waardoor verdere slakreactie en de vorming van reactieproducten werden geremd. Na verloop van tijd leidde uitlogging tot afbraak van gel, wat resulteerde in een grovere poriestructuur en een afname van de druksterkte. Vergelijkenderwijs vertoonden NS-pasta's een relatief grotere weerstand tegen uitlogging, wat werd toegeschreven aan hun dichtere poriestructuur. Om de lange termijn degradatie van de poriestructuur te voorspellen, werd een diffusie-oplossingsmodel ontwikkeld. Gesimuleerde resultaten wezen uit dat na 10 jaar dompeling in water significante aantasting van de poriestructuur beperkt bleef tot een diepte van ongeveer 1,5 mm, terwijl herstructureren van de gel door Na-uitlogging zich kon uitstrekken tot circa 100 mm.

Ondanks de grotere weerstand tegen uitlogging ontwikkelden NS-pasta's na onderdompeling in water aanzienlijke scheurvorming, waarbij de hevigheid van de scheur toenam bij hogere siliciummoduli. Chemische veranderingen in AAS-pasta's met verschillende siliciummoduli ($m = 0, 0,5, 1$ en $1,5$) werden zowel voor als na onderdompeling geanalyseerd. Simulatiegegevens gaven bovendien aan dat pasta's met hoge siliciummoduli ($m = 1$ en $1,5$) een grotere gradiënt

in waterinhoud vertoonden. Het bevochtigde deel liet lokaal de poriedruk ontspannen, wat compressiespanningen bij het oppervlak en trekspanningen in het centrum veroorzaakte. Als die trekspanningen de treksterkte van het materiaal overschrijden, ontstaan er vanuit het centrum scheuren die zich naar het oppervlak kunnen uitbreiden.

Uitbloeiing in cilinders van AAS-pasta werd bestudeerd onder half-contact watercondities. Hogere alkalihoeveelheden, grovere poriestructuren en lagere relatieve vochtigheid versnellen de vorming van uitbloeiing. NS-pasta's waren onder deze omstandigheden gevoeliger voor scheurvorming, wat de afzetting van uitbloeiingsproducten langs de scheuren verder bevorderde. Er werd een kwantitatieve evaluatiemethode ontwikkeld om de ernst van uitbloeiing te beoordelen door het Na gehalte in de uitbloeifafzettingen te meten. De studie bevestigde een positieve correlatie tussen Na-uitlogging en de intensiteit van uitbloeiing en verduidelijkten de uitbloeimechanismen in zowel NH- als NS-systemen.

Een op aluminosilicaat gebaseerd lichtgewicht fijn toeslagmateriaal (LWFA), te weten geëxpandeerde schalie, werd ingezet om uitbloei in NH-mortels te beperken. Vervanging van zand door LWFA met 20% en 50% in volume verminderde de uitbloeiing respectievelijk met 14,6% en 43%. De mitigatiemechanismen van LWFA werden verklaard vanuit de gelchemie, de porie-oplossing en poriestructuur. De puzzolaanreactie van LWFA leverde extra Si en Al aan het systeem, wat de binding van Na-ionen in de gels versterkte en hun beschikbaarheid voor uitbloeiing verminderde. Daarnaast zorgde het interne uithardings-effect van LWFA voor verdichting van de omliggende pasta's, waardoor ionen- en watertransport werd belemmerd en de ontwikkeling van uitbloeiing verder werd geremd. Opmerkelijk was dat toevoeging van LWFA de buigsterkte van mortels verbeterde zonder de druksterkte significant nadelig te beïnvloeden.

Dit onderzoek vergroot het begrip van uitlooggedrag en de daaruit voortvloeiende structurele veranderingen in C-(N)-A-S-H-gels. De ontwikkelde diffusie-oplossings- en watertransportmodellen bieden waardevolle inzichten in microstructurele degradatie en scheurvorming van AAS-materialen die aan vochtige omstandigheden worden blootgesteld. Bovendien levert de voorgestelde kwantitatieve methode nieuwe mogelijkheden voor de beoordeling van uitbloeiing, en biedt de toepassing van LWFA een effectieve strategie ter beperking van uitbloeiing in AAS-beton. De bevindingen dragen bij aan zowel de wetenschap als de industrie door het fundamentele begrip van AAS-duurzaamheid te verdiepen en de ontwikkeling van duurzamere en betrouwbaardere AAS-materialen voor bouwtoepassingen te ondersteunen.

Chapter 1

Introduction

1.1 Research background

In light of the growing international concern regarding global warming and CO₂ emissions, numerous nations and industries are actively engaging in initiatives aimed at achieving a “carbon neutral” status in the coming decades. Considering that at least 8% of global emissions emanate from the cement industry [1], conventional construction manufacturing bears a significant responsibility to mitigate such a colossal carbon footprint. Despite continuous efforts by researchers and engineers in this domain to devise innovative techniques for cleaner production, cement manufacturing remains an energy-intensive industry, primarily due to its inherent reliance on fossil fuels. So far, global conventional concrete production is estimated to reach approximately 6 billion tons each year [2], which is still a fundamental material for the development of human society. Therefore, to address this challenge without compromising the increasing demand for building materials, the exploration and development of alternative cementitious materials emerges as a pivotal pathway to curtail the carbon contributions stemming from the building sector.

Alkali-activated materials (AAMs) have emerged as crucial components in the current and future toolkit of sustainable building materials, attracting widespread attention in both academic and industrial areas [3]. Since these cement-free materials are normally synthesised by industrial by-products and solid wastes, they can deliver a huge reduction of CO₂ emission in comparison with conventional concrete products. More importantly, AAMs can exhibit comparable or even superior properties to traditional cementitious materials in some aspects, such as early strength development, chemical resistance, and thermal endurance [4–6]. Hence, AAMs are regarded as promising building materials for engineering practice.

However, despite the advantages offered by this sustainable binder, it is essential to acknowledge and address its considerable issues. Among these challenges, leaching stands out as a frequently encountered issue under curing and serving conditions, which deserves heightened attention and concern. In essence, leaching is the process through which constituents of solid materials are released into a liquid phase. Although both cementitious materials and AAM systems share the problem of leaching when exposed to humid conditions, the resulting impacts on the properties of materials are quite different. The fundamental distinction arises from the unique chemical reactions and reaction products involved in these two materials. More specifically, AAMs gain strength through alkaline activation while cement materials are hardened via hydration. In cement systems, extra water supply can facilitate the continued hydration of unhydrated clinkers, which contributes to an improved microstructure development of the matrix [7,8]. Conversely, external water supplies appear to reduce the pore solution alkalinity. This may not only hinder the reaction of precursors but also disrupt the stability of reaction products in AAMs thermodynamically, leading to the coarsening of pore structure or compromising the structural integrity [9–11].

Despite previous studies reporting unsatisfying properties of AAMs after leaching [9–15], there remains limited knowledge to elucidate the underlying mechanisms. The impacts of

leaching on the dissolution behaviours and structural evolution of gels, precursor reaction, pore solution, pore structure and overall structural integrity remain unclear. Clarifying the mechanisms of leaching in AAMs is essential not only for a better understanding of their reduced performances subjected to water exposure but also for developing optimal mix designs and reliable predictive models for AAMs.

Moreover, efflorescence, as a derivative issue of leaching, refers to the occurrence of whitish deposits that occasionally manifest on or in proximity to the surface of porous construction and building materials [16]. The formation of efflorescence products contains a succession of physicochemical reactions, primarily characterised by the interaction between leached alkali (earth) metal ions with carbonate ions. As a consequence of the limited availability of alkali metal ions, efflorescence products predominantly consist of calcium carbonate in cementitious materials [17]. These products typically exhibit a loose and fluffy texture [18], which is merely considered an aesthetic problem [19]. However, efflorescence in AAMs is much more pronounced than in PC materials, attributed to the unique chemistry involved. The activation process of precursors introduces a large amount of alkali metal ions. Na, as the most prevalently used alkali metal ion, usually shows weaker bonding within the gel structure and higher mobility in the pore solution than Ca [20]. These characteristics facilitate the migration of Na to the surface of materials under moist conditions, where Na can react with (bi)carbonate ions to the formation of sodium (bi)carbonate [21–25]. The excessive formation of efflorescence products has the potential to induce considerable expansion, which can be detrimental to the stability of the matrix [26]. Hence, efflorescence in AAMs is not only a cosmetic concern but could potentially evolve into a structural issue.

However, the efflorescence mechanisms of AAMs have not yet been fully clarified in the existing literature. For instance, the effects of efflorescence on the phase assemblage, pore structure, and mechanical properties of AAMs remain largely unknown. The relationship between leaching and efflorescence also needs to be established. A universally accepted method for the quantification of efflorescence is still lacking, making precise assessment challenging. Furthermore, previous mitigation methods have mainly focused on the binder level, but many of the strategies have proved ineffective in industrial applications. Therefore, an effective strategy for mitigating efflorescence in AAMs is expected to be developed.

1.2 Research aim and objectives

This thesis aims to understand the mechanisms of leaching and efflorescence of AAS materials and to develop an effective method to mitigate efflorescence. To fulfil the research aim, the following objectives are defined:

- ◆ to clarify the leaching behaviours of ions in synthetic C-(N-)A-S-H gels
- ◆ to investigate the structural change of synthetic C-(N-)A-S-H gels due to leaching
- ◆ to reveal the leaching mechanisms of AAS pastes
- ◆ to predict the microstructural deterioration of AAS pastes induced by leaching
- ◆ to unveil the cracking mechanisms of AAS materials under water immersion
- ◆ to understand the efflorescence mechanisms of AAS pastes
- ◆ to mitigate the efflorescence of AAS mortars by lightweight fine aggregate (LWFA)

1.3 Research scope

C-(N-)A-S-H gels were synthesised using the sol-gel method (chemical solutions). Due to the lack of fly ash and metakaolin, ground granulated blast furnace slag (GGBFS) is the predominant precursor used in AAM production in the Netherlands. Hence, slag served as the sole precursor, activated by sodium hydroxide (NH) solutions and sodium silicate (NS) solutions to prepare AAS materials. No admixture was used. Efflorescence of AAS materials was obtained by the bottom of the sample being in contact with water.

1.4 Research strategy

The research covers studies of leaching and efflorescence of AAS materials at gel, paste, and mortar scales, as schematically illustrated in *Figure 1.1*.

As the starting point of this thesis, I initiated an exploration into the C-(N-)A-S-H gel, which is the main reaction product in AAS materials. Three stoichiometrically tailored gels with representative ranges of Ca/Si and Al/Si ratios in AAS materials were synthesised using the sol-gel method. The leaching behaviours of ions in gels were experimentally monitored, and the discrepancy in the leaching of Ca and Na ions in different gels was fundamentally revealed by molecular dynamics (MD) simulation. Additionally, the structural evolution of gels induced by the leaching of Na ions was comprehensively explored by NMR.

Subsequently, I employed AAS pieces to investigate the impact of water immersion on the pore solution, slag reaction, phase assemblage, and pore structure of AAS pastes, and to reveal the leaching mechanisms. Then, I used bulk cylindrical samples to specifically identify the microstructural deterioration of pastes resulting from leaching. A thermodynamics-based diffusion-dissolution model was developed to predict the deteriorated depth of AAS materials subjected to leaching in the long term. In addition, the structural integrity of prismatic AAS pastes with different silicate moduli was compared underwater. A water transport model was established to understand the cracking mechanisms of pastes with high silicate moduli.

The efflorescence of AAS pastes was observed when exposed to different atmospheres. A novel method to quantitatively determine efflorescence was proposed by calculating the Na amount in efflorescence products. The relationship between leaching and efflorescence was established, and the efflorescence process of AAS pastes was elucidated. LWFA was employed to mitigate the efflorescence of AAS mortars. The underlying mechanisms were revealed in terms of paste chemistry, pore solution and pore structure.

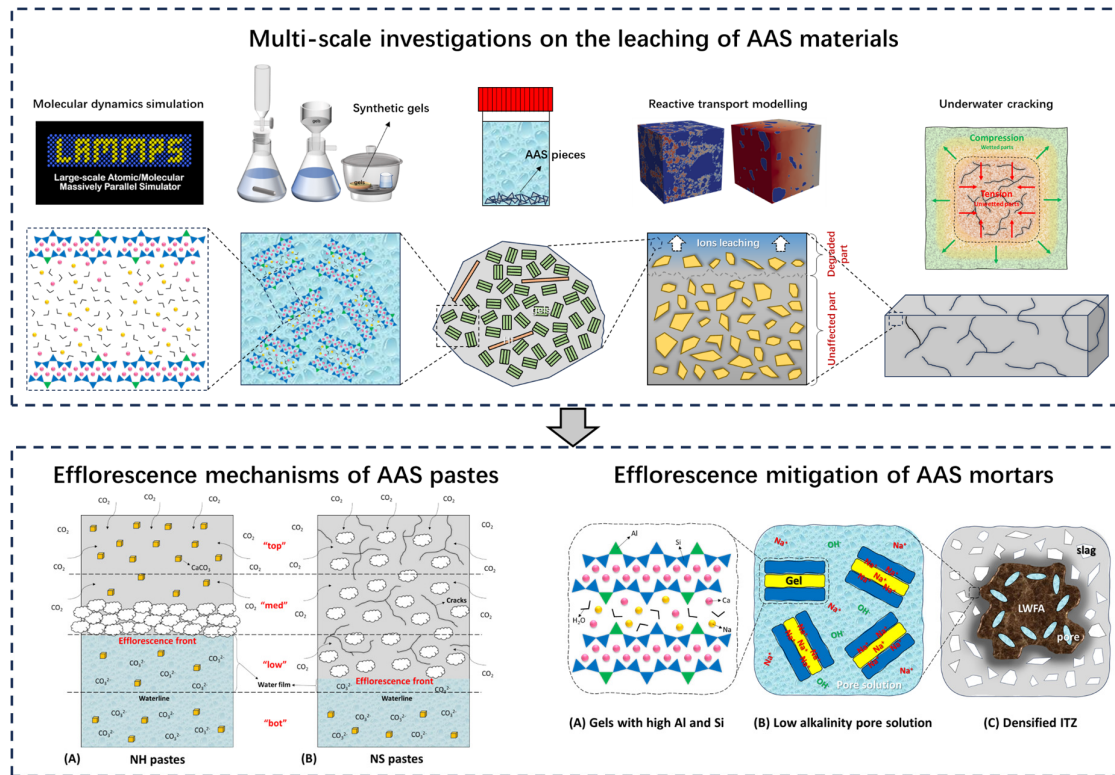


Figure 1.1. Schematic diagram of multi-scale investigations on leaching and efflorescence of AAS materials.

1.5 Research outline

The outline of this thesis is shown in *Figure 1.2*, which can be subdivided into five parts. *Part I* includes a general introduction and a literature survey related to this research. *Part II* covers the leaching of synthetic C-(N)-A-S-H gels, which are the main reaction products in AAS materials. *Part III* presents the leaching mechanisms of AAS materials at paste scales. *Part IV* focuses on the efflorescence mechanisms and mitigation strategy of AAS materials. Finally, *Part V* highlights the conclusions, contributions and perspectives of this thesis.

Chapter 1 introduces the research background, aim, objectives, scope, and strategy of this thesis.

Chapter 2 provides a literature survey regarding the leaching and efflorescence of AAS materials.

Chapter 3 shows the leaching behaviours of synthetic C-(N)-A-S-H gels and investigates the leaching potential of Ca and Na ions using MD simulations.

Chapter 4 concentrates on the structural evolution of synthetic C-(N)-A-S-H gels due to the leaching of Na.

Chapter 5 examines the leaching mechanisms of AAS pastes in terms of pore solution, slag reaction, phase assemblage, paste chemistry, pore structure and compressive strength.

Chapter 6 studies the microstructural deterioration of AAS pastes subjected to water immersion with depth. A diffusion-dissolution model is developed to predict the degradation of pore structure over a prolonged period.

Chapter 7 focuses on the cracking mechanisms of AAS pastes with high silicate moduli underwater. A water transport model is established to elucidate the underlying mechanisms.

Chapter 8 presents the efflorescence of AAS pastes under different conditions. An effective quantitative method is introduced. The relation between leaching and efflorescence is established. The efflorescence process and the critical impacting factors are discussed.

Chapter 9 explores the effectiveness of LWFA on efflorescence mitigation in AAS mortars. The impacts of LWFA on paste chemistry, pore solution, and pore structure of AAS mortars are investigated to reveal the mechanisms behind.

Chapter 10 summarises the general conclusions and scientific contributions of this thesis. Recommendations for AAS materials concerning leaching and efflorescence in engineering practice and perspectives for further research are provided.

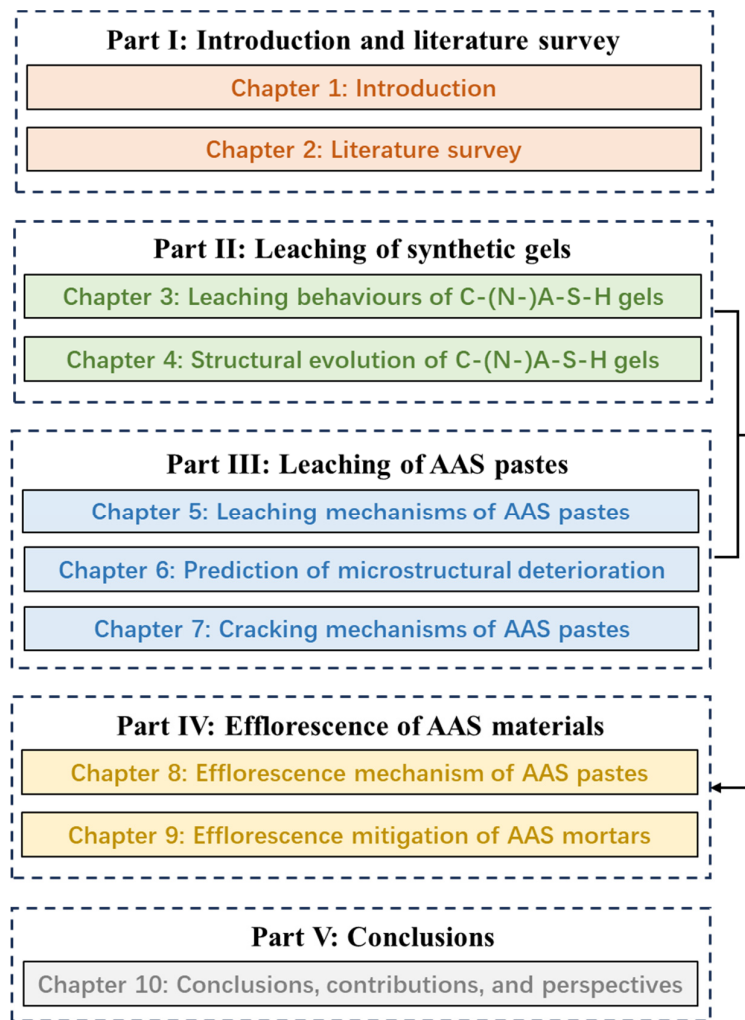


Figure 1.2. Research outline of this thesis

Chapter 2

Literature survey

2.1 Introduction

This chapter gives a state-of-the-art literature review on the leaching and efflorescence of alkali-activated slag (AAS) materials. It begins with a concise overview of the reaction products and microstructure formation of AAS materials. The discussion then shifts to a comparative analysis of the properties of Portland cement (PC) and AAS materials subjected to leaching. Studies exploring the leaching mechanisms of AAS pastes and synthetic C-(N-)A-S-H gels are summarised. Efflorescence, as a derivative issue of leaching, is subsequently introduced, with a focus on its occurrence in both PC and AAS materials. The mechanisms underlying efflorescence and potential strategies for its mitigation in AAS systems are reviewed. The chapter concludes by identifying critical knowledge gaps in the understanding of leaching and efflorescence phenomena in AAS materials.

2.2 General introduction of AAMs

Alkali activation refers to the chemical reaction between a solid calcium silicate or aluminosilicate material (referred to as the “precursor”) and an alkaline solid or liquid. This concept was first explored in 1908 [27]. Since then, numerous researchers have dedicated their efforts to advancing this field, with a primary goal of developing sustainable alternative binders to PC [3].

Alkaline activators typically include caustic alkalis (MOH), silicates ($M_2O \cdot nSiO_2$), and weak base salts (M_2CO_3 , M_2SiO_4 , etc.), where “M” represents alkali metal cations such as sodium (Na) or potassium (K). Na-based activators are more commonly used due to their lower cost compared to K-based alternatives. Among these, NaOH and $Na_2O \cdot nSiO_2$ are the most widely employed, as their high pH levels promote early strength development.

The precursors of AAMs are derived from a diverse range of sources, including natural pozzolans, industrial by-products, mineral residues, and agricultural wastes [3,6,28,29]. Commonly used precursors, such as blast furnace slag, fly ash, and metakaolin, are favoured for their hydraulic and pozzolanic reactivity, as these properties also make them suitable for PC systems. These precursors react under alkaline conditions to release ions that contribute to the formation of hardened reaction products. The reaction of the precursor depends not only on its chemical composition and structure but also on the nature of the alkaline activator used. *Figure 2.1* illustrates the reaction process and products during the alkali activation of precursors. Based on the chemical composition, the precursors can be roughly categorised into two types.

High-Ca precursors: Blast furnace slag, a representative high-Ca material, typically shows an amorphous structure and high reactivity at ambient temperatures. The main reaction product is calcium (sodium) aluminosilicate hydrates (C-(N-)A-S-H gels). This gel resembles the C-(A-)S-H gel found in PC systems but features a lower Ca/Si ratio, a higher Al/Si ratio, and higher alkali metal contents. Compared to C-(A-)S-H gels, C-(N-)A-S-H gels exhibit a more cross-linked

structure (see Section 2.3.2.3 for detailed information). In slag-based systems with moderate to high magnesium contents, hydrotalcite-like phases may also form as secondary products.

Low-Ca precursors: Materials like fly ash and metakaolin exhibit higher levels of crystallisation and polymerisation, resulting in lower reactivity compared to high-Ca precursors. Elevated curing temperatures are often necessary to achieve satisfactory early strength unless high alkali and silicate moduli are used. In these systems, the primary reaction product is N-(C-)A-S-H gels or N-A-S-H gels. Overall, the Ca content in gels is positively related to that in precursors. With decreasing Ca content, gels evolve from C-(N)-A-S-H gels, to N-(C)-A-S-H gels and eventually to N-A-S-H gels. As this study focuses on AAS materials, the subsequent sections of this literature review will mainly summarise the leaching and efflorescence behaviours of slag blended systems.

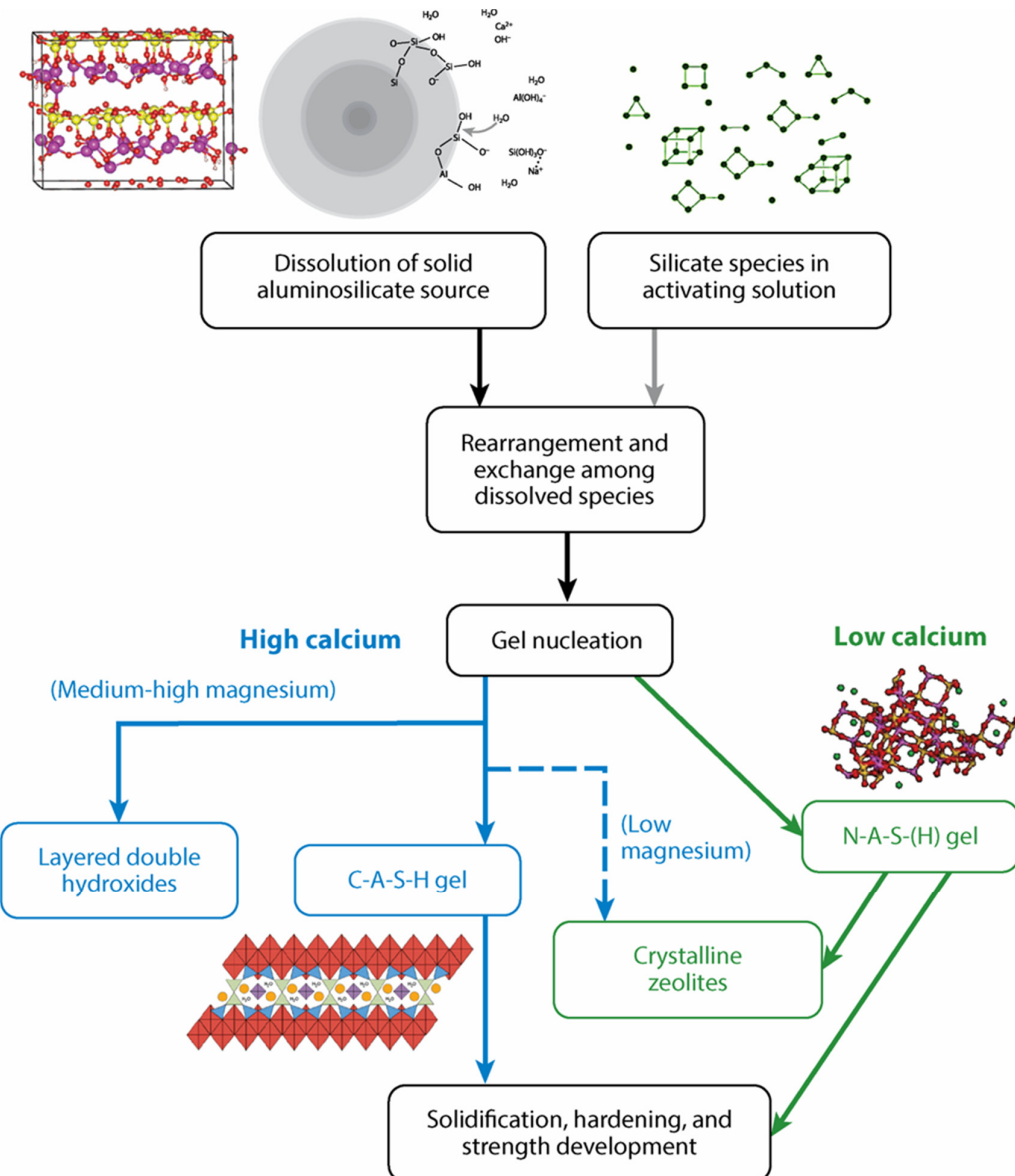


Figure 2.1. Reaction process and products of alkali activation of solid aluminosilicate precursors with high or low calcium contents [29].

2.3 Leaching

Leaching is the process by which constituents of solid materials are released into a liquid phase. This phenomenon is observed in both PC-based materials and AAS materials, whether during curing or in service. This section begins with an overview of leaching research in PC-based materials. Then, studies focusing specifically on AAS materials are discussed, examining the impact of leaching on the mechanical properties and long-term durability. Finally, the discussion concludes with the leaching mechanisms of AAS materials, drawing insights from studies on pastes and synthetic gels. It should be noted that the mitigation strategies for leaching are excluded in this section due to limited research on this topic.

2.3.1 Leaching of PC-based materials

The pore solution in PC-based materials typically maintains a high pH, ranging from 12.5 to 13.9 [30,31], depending on factors such as cement type, water-to-binder ratio, and initial alkali content. While PC-based materials are generally stable in alkaline environments, prolonged exposure to water can induce a form of “chemical corrosion” [32]. Researchers have conducted experiments and simulations on the impact of leaching on cement pastes [33–36]. The primary degradation processes include the dissolution of calcium hydroxide and the decalcification of C-S-H gels [32,34,36]. Additionally, the leaching resistance of cement pastes is influenced by the porosity of the matrix [36], the addition of supplementary cementitious materials [34], external chemical environments [33,35] and the pore solution alkalinity [34].

Interestingly, while leaching can have adverse effects, external water exposure can also benefit PC-based materials. Bentz et al. [37] found that water-immersed cement exhibited higher hydration degrees than sealed samples. Similar findings have been reported in another study [38], which demonstrated that cement can hydrate under external water exposure. Continuous hydration is beneficial for the reduction of large capillary pores and the densification of microstructure.

Water curing also enhances the mechanical properties and durability of PC-based materials. For instance, Shafiq et al. [39] observed that moist curing decreased oxygen diffusion and water permeability in concrete compared to dry conditions. Bhalodia et al. [40] reported higher compressive strength in water-cured concrete than in samples cured under sealed conditions. Similarly, Han et al. [41] noted that shrinkage in ultra-high-performance concretes was greater under sealed conditions than under water immersion. This shrinkage reduction under high-humidity conditions occurs because water immersion mitigates self-desiccation effects [42].

Accordingly, while leaching can cause some degradation in PC-based materials, it is not generally considered a significant problem due to the beneficial effects of hydration promoted by external water. However, leaching in AAS materials presents unique challenges compared to PC-based materials.

2.3.2 Leaching of AAS materials

2.3.2.1 Impacts of leaching on AAS materials

Leaching has been shown to negatively impact the mechanical properties and durability of AAS materials. Yao et al. [11] reported a negative development of compressive strength of

AAS pastes during 90 d of water immersion. This decline was attributed to an increase in mesopores and macropores in water-immersed samples compared to those under ambient conditions. Similarly, Abdollahnejad et al. [43] found that water-immersed AAS samples exhibited lower compressive strengths than their sealed counterparts, as a result of higher porosity in the immersed samples. Additional studies by Nedeljković et al. [44], Zhang et al. [45] and Sevinç [46] corroborated these findings, consistently showing lower compressive strength under immersed conditions than sealed conditions. In addition to compressive strength, Liu et al. [47] investigated the flexural strength and elastic modulus of AAS mortars under water immersion, as shown in *Figure 2.2*. They found that sodium silicate-based (NS) mortars were more susceptible to water immersion than those activated by NaOH (NH). Specifically, the flexural strength of NS mortars decreased during the immersion of 90 d. However, water curing was found to support the development of the elastic modulus of AAS mortars more effectively than ambient conditions.

Nedeljković et al. [48] investigated the effect of curing conditions on the carbonation resistance of AAS pastes. The samples were cured for 56 d and then exposed to accelerated carbonation conditions (1 vol.%) for 500 d. They found that the moist-cured samples showed a higher depth of CO₂ penetration than sealed samples. Wei et al. [49] investigated the acid resistance of one-part AAS pastes. The samples were cured for 28 d and then exposed to sulphuric acid ponding. They found that water-cured samples had poorer resistance to acid attack than sealed samples. This was attributed to significant leaching during water curing, resulting in a coarser microstructure. Liu et al [47] studied the effects of curing conditions on the sorptivity, carbonation and freeze-thaw resistances of AAS mortars. The samples were first cured for 28 d and then exposed to different testing conditions. As shown in *Figure 2.2*, water curing increased the water sorptivity of AAS mortars compared to sealed curing. While the carbonation depth of AAS mortars under sealed and water curing was comparable, water-immersed samples were found to be more susceptible to freeze-thaw cycles. This was likely due to the degradation of pore structure, which became unable to withstand the crystalline pressure induced by ice formation.

Moreover, unexpected cracks have been observed in AAS pastes under moist and water conditions, raising concerns about their durability [14,15,50]. Hubler et al. [14] found cracks on AAS pastes subjected to underwater conditions, attributing the issue to stress gradients within the samples. Maghsoodloorad et al. [50] identified cracks in alkali-activated phosphorus slag pastes exposed to hydrothermal curing after 1 d of pre-curing in moist conditions (*Figure 2.3A*). These cracks were hypothesised to result from the instability of reaction products in the matrix. Similarly, Hwang et al. [15] investigated the effect of MgO content on AAS pastes under sealed and water curing conditions. As shown in *Figures 2.3B* and *C*, visible cracks were observed in both elongated strips and small cubes of AAS samples after water immersion. The severity of cracking was more pronounced in samples with slag containing higher MgO contents and finer particle size distributions. They assumed this phenomenon to be the elevated formation of hydrotalcite-like phases, which may induce internal stresses leading to cracking. Despite these observations, the mechanisms underlying cracking in AAS materials under water immersion remain unclear, and no consensus has been reached within the research community.

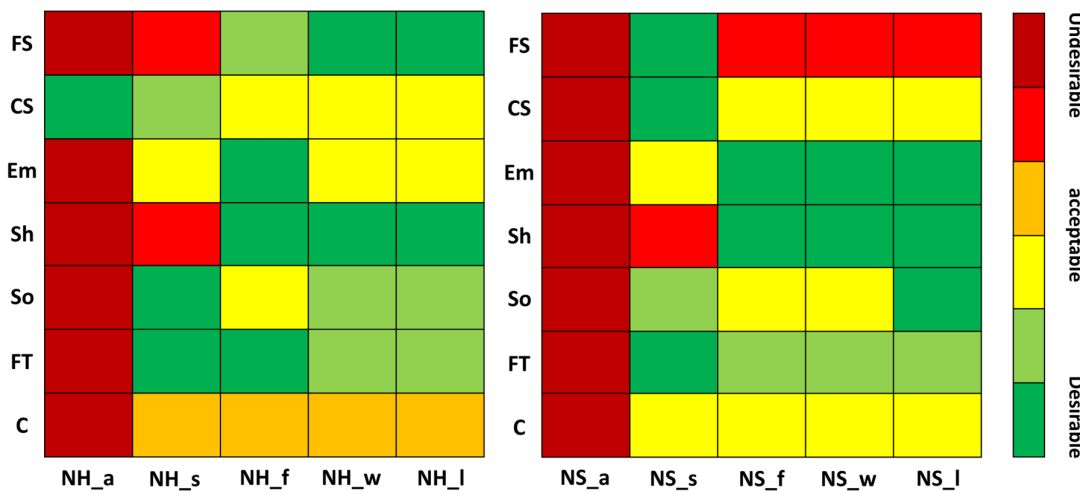


Figure 2.2. A comparative analysis of mechanical properties, volume stability, and durability of AAS mortars under various conditions [47]. "FS", "CS", "Em", "Sh", "So", "FT" and "C" refer to flexural strength, compressive strength, elastic modulus, shrinkage, sorptivity, and freeze-thaw and carbonation depth, respectively. "a", "s", "f", "w" and "I" indicate the ambient, sealed, fog, water and limewater curings, respectively. The NaOH (NH) and Na₂SiO₃-based (NS) mortars were evaluated individually.

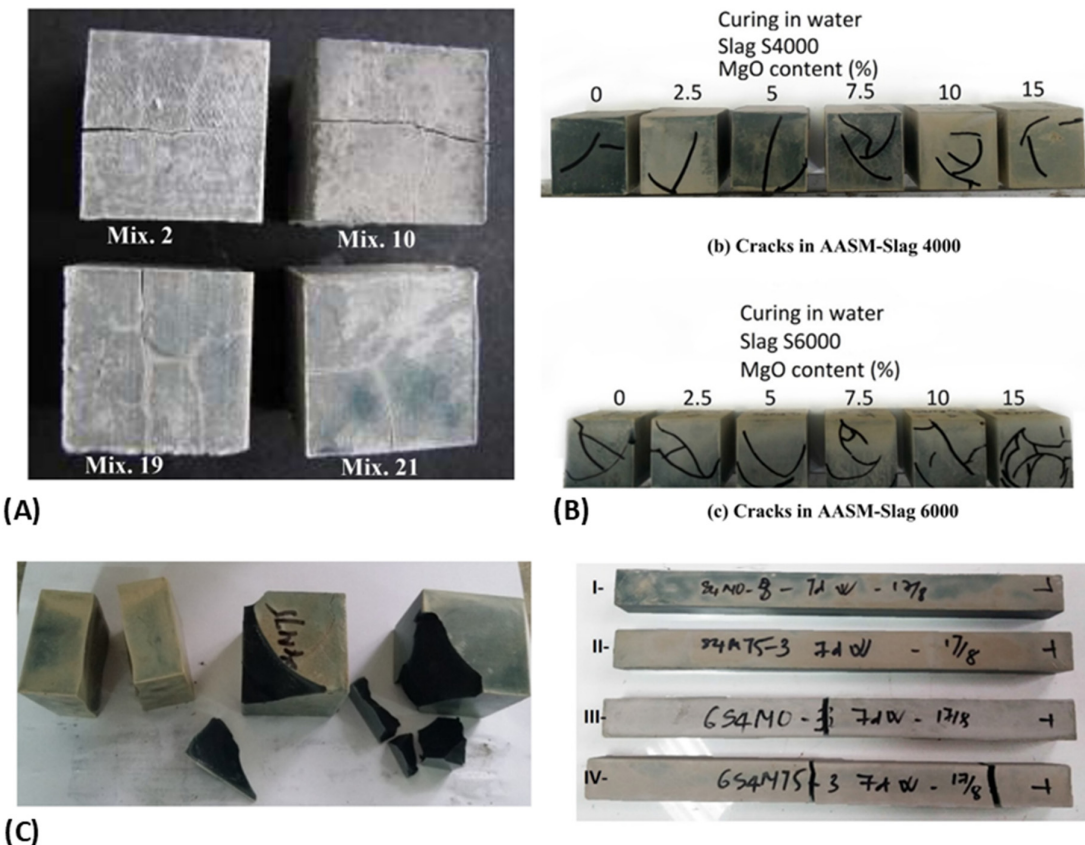


Figure 2.3. Cracking of AAMs under high-humidity conditions. (A) alkali-activated phosphorus slag after hydrothermal curing [50]; (B–C) strips and cubes of AAS pastes after water immersion [15].

2.3.2.2 Leaching mechanisms of AAS pastes

As discussed in *Section 2.3.2.1*, reduced mechanical properties and durability of AAS materials subjected to moist or water conditions are generally attributed to leaching. Historically, the leaching mechanisms of AAS materials have been studied. Pawar et al. [51] investigated the influence of sealed and fog curings on the pore solution of AAS pastes. A substantially lower concentration of Na ions was detected in the pore solution of samples under moist conditions compared to sealed conditions. Nedeljković et al. [48] also reported a lower pH of pore solution in the samples under moist curing. They further found that the samples under moist conditions exhibited a coarser microstructure, resulting in poorer resistance to carbonation. Srinivasamurthy et al. [52] studied the impact of fly ash-to-slag ratio and alkali dosages on the leaching behaviour of AAS pastes. The inclusion of slag reduced porosity, hindering the leaching potential of Na and Si. However, the degradation of gels due to leaching was identified, resulting in lower flexural and compressive strengths of AAS materials.

Accordingly, the leaching of alkali metal ions is a well-documented phenomenon in AAS pastes exposed to water immersion. However, there remains no consensus on the impact of leaching on AAS pastes. A deeper understanding of the leaching mechanisms is necessary.

2.3.2.3 Leaching mechanisms of C-(N)-A-S-H gels

C-(N)-A-S-H gel is the predominant reaction product in Ca-rich AAMs (*Section 2.2*). In contrast to the C-(A)-S-H gel in the PC system, C-(N)-A-S-H gel shows a lower Ca/(Si+Al) ratio (0.6-1.2) and a higher Al/Si ratio (0.1-0.3) [53–61]. This distinct chemical composition results in a more cross-linked structure, predominantly composed of Q², with some Q¹ and Q³ configurations [56,62]. In pure AAS systems, the gels are generally non-cross-linked, as depicted in *Figure 2.4*. The employment of alkali activators introduces Na⁺ ions, which become chemically incorporated into the interlayers of C-(N)-A-S-H gels to balance the negative charges arising from silicon-aluminium substitution [57]. The uptake of alkali metal ions is associated with the elemental composition of gels, with a higher content observed in the gel with a higher Al/Si ratio and a lower Ca/(Si+Al) ratio. Besides, a high degree of Si substitution by Al effectively enhances the mean chain length and the degree of polymerisation of the aluminosilicate tetrahedra within C-(N)-A-S-H gels.

Understanding the leaching behaviour of C-(N)-A-S-H gels is essential to unveil the leaching mechanisms of AAS materials. To eliminate the interference of other phases, synthetic C-(N)-A-S-H gels were often employed, with elemental ratios comparable to those found in real AAS systems. Myers et al. [56] studied the leaching behaviour of C-(N)-A-S-H gels equilibrated at 50 °C. With the increase of the Ca/Si ratio of gels, the ion concentration of Si decreased, whereas the ion concentration of Ca increased in the leachate. Additionally, the concentration of Al in the leachate decreased with the increase of Ca/Si ratios but increased with the increase of alkali contents. These ion concentrations were used to calculate the solubility products of C-(N)-A-S-H gels, contributing to the database for thermodynamic modelling. However, the property change of gels before and after leaching was not discussed.

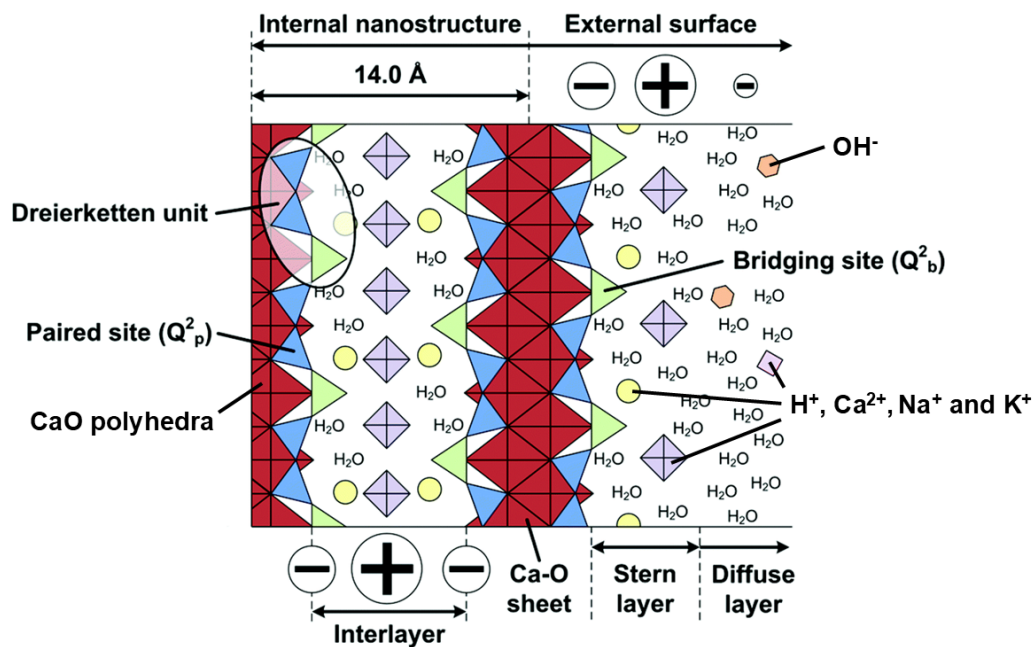


Figure 2.4. Schematic representation of non-cross-linked C-(N,K)-A-S-H gels [57]. Positive and negative symbols indicate the local charge distribution within the structure. The representation of symbol size, number, and placement is schematic, not crystallographically precise, and does not distinguish between different types of hydrated alkali complexes.

Research specifically focusing on the leaching of C-(N)-A-S-H gels subjected to water immersion was limited. Nonetheless, studies examining the behaviour of these gels under acidic conditions provide valuable insights. Wang et al [59] investigated the degradation of C-(N)-A-S-H and N-A-S-H gels exposed to sulfuric acid solutions. Both gels showed increased polymerisation in acidic environments. Dealumination and decalcification were observed in the C-(N)-A-S-H gels, along with considerable and rapid losses of Na and minor losses of Si. The presence of gypsum in the exposed samples led to severe expansion cracking. Jin et al. [63] provided insights into the decalcification process of C-(A)-S-H gels in NH₄Cl solutions. Decalcification enhanced the length of silicate chains and increased the polymerisation degree within the gel network. This process resulted in a phase transition from C-(A)-S-H gels to amorphous Al-Si gels and a nanomorphological change from a foil-like structure to a flocculent one. Additionally, mild decalcification coarsened the gel pore, while severe decalcification led to significant volume contraction and densification of gel pores. The gel with a moderate Al content showed increased structural stability during the decalcification.

In addition to experimental characterisations, computational methods including density functional theory (DFT), MD simulation and Grand Canonical Monte Carlo (GCMC) simulation are powerful computational strategies that can also provide valuable insight into the leaching behaviour of gels [64,65]. A common methodology to simulate the ionic diffusion in the nanopore of gel is the so-called “slit pore models”, as shown in Figure 2.5. The diffusion coefficients obtained from these simulations can mirror the leaching behaviour of ions. Pioneering work by Kalinichev et al. [64] applied this method to simulate the dynamics of Na and Cs ions in nanoconfined water within C-S-H gels. The inner-sphere, outer-sphere, and non-absorbed cations were distinguished, and their diffusion behaviours were characterised through atomic density and diffusivity profile. Their results verified that cations could integrate into the gel surface. Pan et al. [66] found that the diffusion coefficient of Na ions

proximate to gel substrates was lower than that situated at a great distance from the substrates. Jiang et al. [67] stated that the absorption capacity of monovalent cations on the surface of C-S-H increased as the ionic radius decreased, following the order $\text{Na}^+ > \text{K}^+ > \text{Cs}^+$.

Despite extensive experimental and computational research on the leaching of gels, significant gaps remain in understanding the leaching mechanisms of C-(N-)A-S-H gels. Key aspects, such as the specific leaching behaviour, associated elemental changes, and the structural evolution of these gels before and after leaching, are not yet fully elucidated.

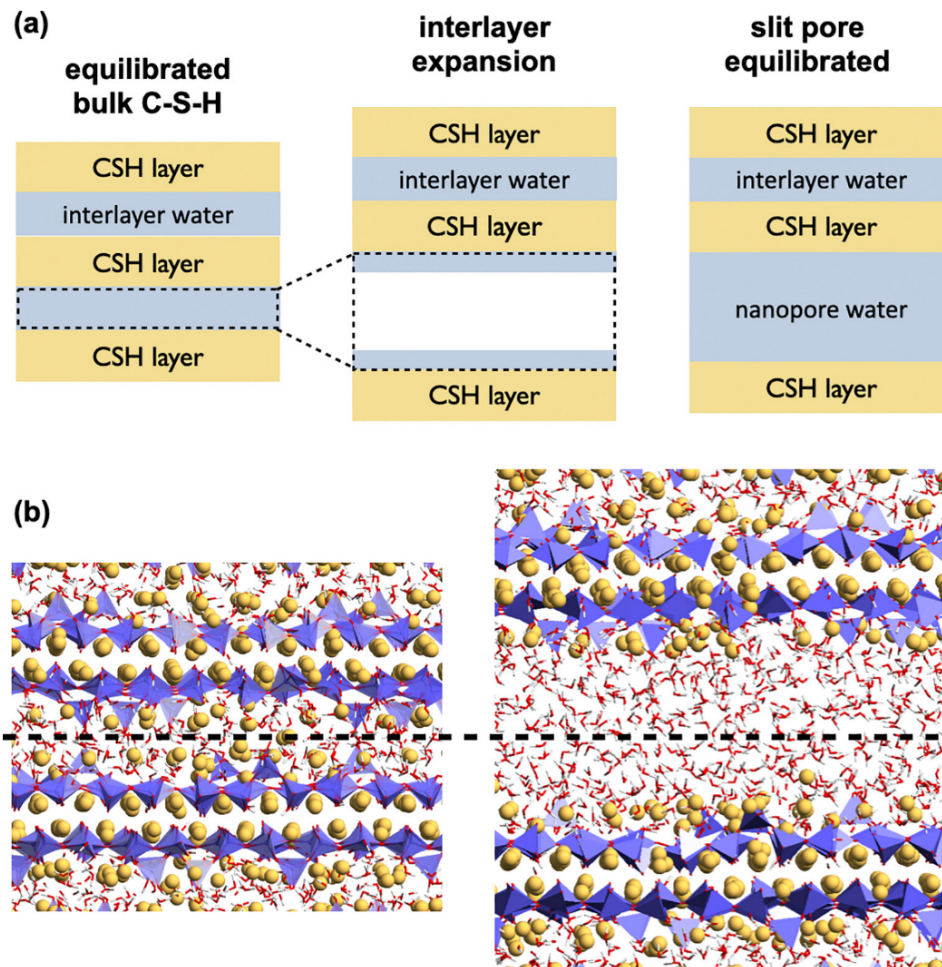


Figure 2.5. (a) A schematic representation of the construction process of “slit pore models”. (b) An equilibrated bulk C-S-H gel model is shown (left), and an equilibrated bulk C-S-H gel with a slit nanopore created by the expansion of the interlayer (right) [65].

2.4 Efflorescence

2.4.1 Efflorescence of PC-based materials

Efflorescence refers to the whitish deposits that appear on or near the surface of materials [68], often observed on new or recently constructed cementitious materials. These deposits mainly consist of calcium carbonate [17] and typically feature a loose and fluffy texture [18]. Dow et al. [18] investigated the formation mechanisms of efflorescence on PC-based building materials. The involved physicochemical reactions are depicted in *Figure 2.6*. Six primary processes govern the formation of efflorescence. Under moist conditions, a thin water film forms on the surface of the materials, which facilitates the dissolution of atmospheric CO_2 and its conversion into aqueous species. Simultaneously, the concentration gradient between the water film and pore solution drives the migration of free cations, such as Ca ions, from the pore solution and reaction products to the surface. Once sufficient ions accumulate in the water film, calcium carbonate precipitates due to its low solubility, leading to the formation of visible efflorescence.

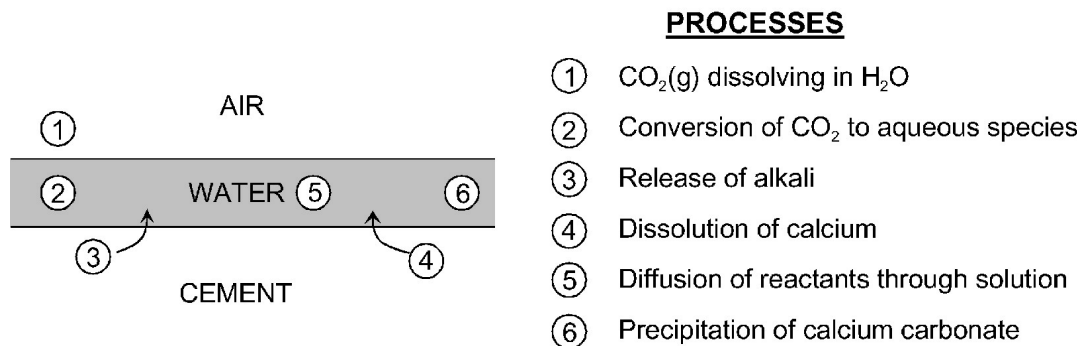


Figure 2.6. Schematic diagram of the formation of efflorescence on PC-based materials [18].

2.4.2 Efflorescence of AAS materials

In PC-based materials, efflorescence presents an aesthetic concern and poses minimal structural risk. However, in AAMs, efflorescence can have more severe implications due to their significantly higher alkali metal ion content compared to PC materials [69]. These alkali ions form weak bonds with the gel structure and are highly mobile in the pore solution. Additionally, subflorescence [18], the efflorescence beneath the surface of materials, can induce significant expansion, leading to structural damage if the resulting expansive stress exceeds the tensile strength of AAS materials. *Figure 2.7* shows the efflorescence of alkali-activated fly ash pastes at 7 and 90 d. Over time, portions of the cylindrical samples spalled, indicating material deterioration due to the formation and expansion of efflorescence products within the matrix. Hence, efflorescence in AAMs is considered not only a cosmetic concern but also a potential structural problem [26]. In this section, the formation mechanism of efflorescence in AAS materials is first introduced. Then, research on the influential factors governing efflorescence is summarised. Finally, mitigation strategies for efflorescence are discussed.

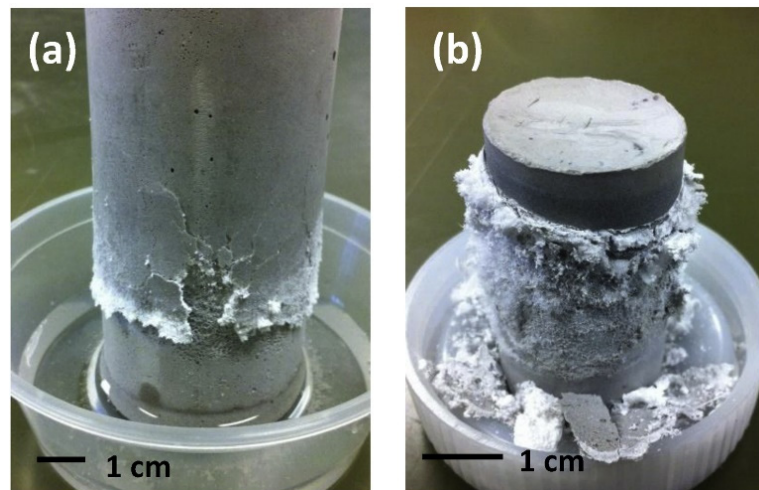
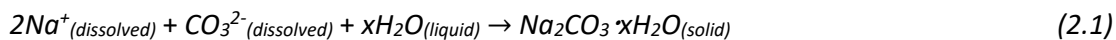


Figure 2.7. Efflorescence of alkali-activated fly ash pastes in contact with water at the bottom after (a) 7 d and (b) 90 d [23].

2.4.2.1 Formation mechanisms of efflorescence

The formation mechanisms of efflorescence in AAS materials share similarities with those in PC systems (Figure 2.6). However, the distinct phase assemblage of efflorescence products in AAS systems arises from differences in chemical reactions within these materials. In AAS systems, alkali components play dual roles: the OH^- disrupts the structure of slag, while the Na^+ ion contributes to counterbalancing the charge within the gel structure. Normally, excess alkali is typically added during the preparation of AAS materials, resulting in a high concentration of free alkali ions in the pore solution. Compared to Ca in PC systems, Na in AAS materials exhibits significantly higher mobility and concentration in the pore solution [69]. Na can readily migrate to the surface of materials under moist conditions. Unlike calcium carbonate, sodium carbonate does not form immediately upon migration due to its high solubility. Instead, as water evaporates from the surface, the concentration of ions increases, leading to the gradual appearance of white deposits. The deposits are typically composed of hydrated sodium carbonate ($\text{Na}_2\text{CO}_3 \cdot x\text{H}_2\text{O}$) [11,22,23,26], which forms according to the following chemical reaction (Equation 2.1) [18].



2.4.2.2 Influential factors of efflorescence

As discussed in Section 2.4.2.1, efflorescence formation in AAS materials is primarily driven by the leaching of alkali metal ions. Based on previous work, three main factors governing leaching and efflorescence can be classified: alkali dosages, gel chemistry and microstructure.

Alkali dosages

Allahverdi et al. [70] investigated the correlation between the alkali activators, compressive strength and efflorescence in AAS pastes. The paste with a lower alkali content showed a lower compressive strength but less intensive efflorescence. Conversely, higher alkali dosages resulted in denser microstructures and increased compressive strength but also exacerbated efflorescence. Similar findings were also reported by Srinivasamurthy et al. [71], Jia et al. [72] and Liu et al. [73], who reported that an increased alkali dosage enhanced the leaching of Na, intensifying efflorescence potential.

Gel chemistry

Xiao et al. [11,74] investigated the effect of slag contents (0%, 25%, 50%, 75% and 100%) on the efflorescence of alkali-activated slag and fly ash (AASF) pastes. Their findings revealed that higher slag contents (>50%) resulted in faster and more intense efflorescence. As mentioned at the end of *Section 2.2*, Ca-rich systems (more slag) favour the formation of C-(N-)A-S-H gels while calcium-poor systems (more fly ash) favour the formation of N-A-S-H gels. As Na is more strongly bound in N-A-S-H gels than in C-(N-)A-S-H gels, the paste with more slag was more susceptible to efflorescence [75]. In contrast, Srinivasamurthy et al. [76] reported that the inclusion of slag (ranging from 10% to 30%) reduced the efflorescence of AASF pastes by promoting the formation of N-(C-)A-S-H gels, which lowered the open porosity of the matrix. Jia et al. [72] further stated that the paste with gels with lower Na/Si ratios and higher degrees of polymerisation showed reduced efflorescence. Additionally, Ali et al. [77] reported that the substitution of slag with waste glass powder minimised the efflorescence of the AAS paste. The introduction of waste glass contributed to generating gels with lower Ca/Si and higher Al/Si ratios, which hindered the visual efflorescence [77].

Microstructure

Zhang et al. [22,26] found that the incorporation of sodium silicate and slag effectively reduced initial efflorescence in fly ash-based geopolymers. Similar results were reported in [23,71,73,76,78,79], highlighting that slag and soluble Si contributed to microstructure densification, which hindered the mobility of Na ions within the matrix and lowered the efflorescence severity. Moreover, a prolonged curing period also contributes to the densification of the microstructure. Yao et al. [11] noted that AAS pastes pre-cured for 60 d exhibited a slower efflorescence rate than those cured for only 7 d. Similarly, Zhang et al [80] reported that pre-curing for 3 and 7 d improved both the compressive strength and efflorescence resistance of AAS materials compared to that pre-cured for only 1 d. Additionally, elevated curing temperatures are also effective in mitigating efflorescence [22,81,82], as an increased curing temperature can accelerate the reaction of precursors during early ages, promoting the development of a denser microstructure that reduces efflorescence.

2.4.2.3 Mitigation strategies for efflorescence of AAS materials

Numerous studies have been dedicated to developing mitigation strategies for the efflorescence of AAS materials. The most commonly employed and effective approach involves the addition of admixtures, which can be classified into Al-rich admixtures, cation exchange admixtures, nanoparticles, hydrophobic agents and other chemical admixtures. It should be noted that certain potential mitigation methods, such as decreasing alkali dosage, incorporating slag and soluble Si, and elevating curing temperatures, have been introduced in *Section 2.4.2.2*.

Al-rich materials

Kani et al. [81] found that the incorporation of calcium aluminate cement was effective in reducing both alkali leaching and efflorescence. The additional Al raised the Al/Si ratio in gels, resulting in a more cross-linked gel structure. This improved structure decreased the mobility of Na ions, limiting their potential for efflorescence. Similarly, Maghsoudloorad et al. [50] reduced the efflorescence in alkali-activated phosphorus slag binder through the incorporation of Al-rich cements. Zhang et al. [83] addressed the efflorescence in alkali-

activated steel slag by adding high Al-based solid waste. This contributed to the formation of N-A-S-H gels, which presented enhanced absorption of alkali metal ions.

Cation exchange agents

Wang et al. [84] found that 5A zeolite effectively inhibited the efflorescence of AAS binder. The pH of the pore solution decreased with the increase in dosage of 5A zeolite. This was attributed to the exchange of Na ions in the pore solution with Ca ions from the zeolite. This cation exchange decreased Na concentration while increasing Ca concentration, leading to a lower alkalinity in the pore solution and inhibited efflorescence. Furthermore, 5A zeolite acted as a filler, which densified the pore structure and improved the compressive and bending strengths of AAS binders with moderate dosages. Huang et al. [85] compared the efficiency of cation exchange between 5A zeolite and vermiculite. They claimed that both materials effectively decreased the concentration of Na in the pore solution. However, 5A zeolite exhibited a faster and stronger exchange effect but a lower overall exchange capacity than vermiculite.

Nanoparticles

Wang et al. [86] found that the addition of nano-silica reduced the porosity and pore size of the matrix, effectively alleviating efflorescence. Smaller nano-silica particles demonstrated a more pronounced effect [87]. Silica fume is a frequently used nanoparticle in AAMs, as it has shown promising effects in microstructural refinement, permeability reduction and strength improvement [88–90]. A denser microstructure resulting from silica fume has been confirmed to impede efflorescence [90,91]. However, Saludung et al. [91] attributed this reduction to a decreased Na/Si ratio of gels [91]. This study revealed that the sample with silica fume had a lower leaching rate of Na ions despite having comparable porosity to samples without silica fume. This indicated that silica fume is conducive to the binding of sodium ions, further mitigating efflorescence.

Hydrophobic agents

Xue et al. [24] found that the silane surface modification substantially enhances the hydrophobicity of the surface of AAMs. As illustrated in *Figures 2.8 (a–c)*, silane-treated samples display increased water contact angles, indicating improved water repellence. This treatment reduced water absorption and moisture evaporation, effectively lowering the leaching of alkali metal ions and visual efflorescence (*Figures 2.8 d and e*). Moreover, surface modification with polydimethylsiloxane and mica also inhibits the efflorescence of AAS materials by filling large capillary pores, reducing overall porosity and creating a waterproof surface [92]. This would suppress both alkali leaching and efflorescence.

Other than surface treatment, the introduction of organic chemicals through direct addition to the mixtures [93] and aggregate treatment [94] has been explored. Wu et al. [93] added a calctite solution to AASF mortars. The filter membrane of alkaline stearate was generated during the reaction between calctite and alkaline activators, which contributed to minimising the leaching of Na ions and reducing the surface efflorescence fraction from 92.2% to 2.8%. Pasupathy et al. [94] employed two hydrophobic agents, fumed silica and silane crème, for coating the sand in AASF concretes. Both agents reduced the efflorescence of AASF concretes, with fumed silica performing better than silane crème. In addition, fumed silica improved the compressive strength of concretes, while the silane crème showed a detrimental effect, likely due to retardation during the polymerisation process.

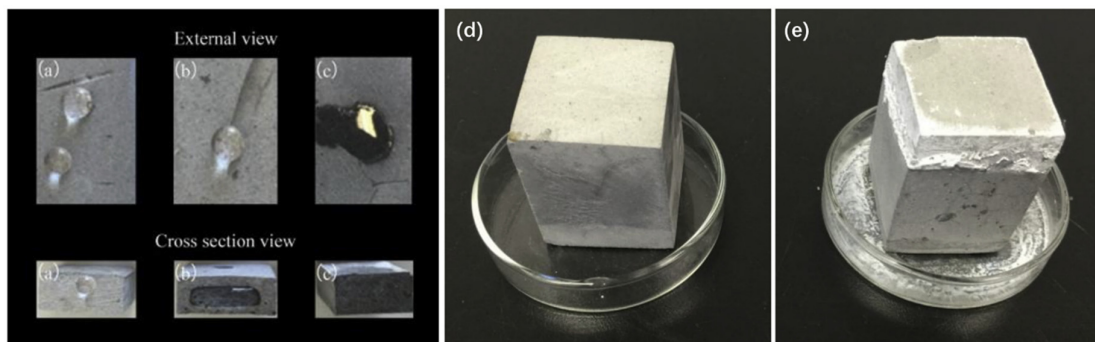


Figure 2.8. Appearance of water drops on the surface of AAMs (a) with 120 s immersion of silane treatment, (b) with 60 s immersion of silane treatment, and (c) without treatment. Visual observation of efflorescence of AAMs (d) with and (e) without silane treatment [24].

Other admixtures

Tang et al. [95] found that the addition of calcium hydroxide mitigated the efflorescence of AAS mortars. The inclusion of calcium hydroxide promoted the formation of C-(N-)A-S-H gels. On one hand, these additional gels enhanced the total binding capacity of Na ions, as indicated by the leaching of both powder and bulk samples. On the other hand, an elevated content of calcium hydroxide densified the microstructure, reducing water absorption and hindering the migration pathway for Na ions. Zhao et al. [96] investigated the effect of rice husk ash on the efflorescence of AAS pastes. They found that the addition of rice husk ash increased the pore connectivity and water absorption rate. In contrast, the formation of cavities in the matrix with rice husk ash lowered the water evaporation rate, with a higher dosage exhibiting lighter efflorescence.

2.5 Problem definition

Due to their different chemical reactions compared to PC-based materials, AAS materials are more vulnerable to leaching. The adverse effects of leaching on the mechanical properties and durability of AAS materials were reported, and the underlying mechanisms were studied at the paste and gel levels. Additionally, as a derivative problem of leaching, efflorescence poses not only aesthetic concerns but also structural challenges for AAS materials. The formation mechanisms, influential factors and mitigation strategies of efflorescence for AAS materials were summarised according to previous work. However, knowledge gaps on leaching and efflorescence of AAS materials still exist based on the following aspects:

1. The main reaction product in AAS systems, the C-(N-)A-S-H gels, lacks a comprehensive understanding of its leaching mechanisms. The leaching behaviour, chemical composition changes and structural evolution of C-(N-)A-S-H gels subjected to water immersion have been scarcely reported. A deeper understanding of the role and mobility of alkali metal ions within the gel structure is essential.
2. Although leaching-induced degradation in AAS materials has been confirmed, the specific mechanisms behind reduced mechanical properties and durability remain unclear. Additionally, cracking problems of AAS materials subjected to leaching have been observed, whereas the underlying mechanisms are controversial and not well-defined.
3. The efflorescence mechanisms of AAS materials have not been fully clarified, particularly the impact of relative humidity on efflorescence remains unclear. The relationship

between leaching and efflorescence is not well-established. The cracking during the efflorescence of AAS materials also needs to be further understood.

4. Current mitigation strategies for efflorescence primarily focus on the binder and paste levels. However, in mortars and concretes, aggregates constitute a considerable portion of the mass and volume, yet their role in efflorescence mitigation remains unclear. Research on upscaling efflorescence mitigation strategies for AAS mortars and concretes is needed.

2.6 Conclusions

Based on the literature survey on the leaching and efflorescence of AAS materials, the following conclusions are summarised:

1. Under high-humidity conditions, PC-based materials exhibited better strength and microstructural development than under ambient or sealed conditions. Conversely, AAS materials were more vulnerable to high-humidity conditions, exhibiting inferior mechanical properties and durability compared to those maintained under sealed conditions.
2. A lower pore solution alkalinity and deteriorated microstructure of AAS pastes were identified after water leaching, leading to reduced properties of AAS materials. Additionally, cracks have been observed in AAS pastes subjected to high-humidity conditions, while the underlying mechanisms have not yet reached a consensus.
3. Due to their high alkali content, AAS materials were prone to showing more severe efflorescence than PC-based materials. Efflorescence posed both aesthetic and structural concerns for AAS materials. Alkali dosages, gel chemistry and microstructure were three critical influential factors for efflorescence.
4. Mitigation strategies for the efflorescence of AAS materials have been developed through the addition of various admixtures, including Al-rich materials, cation exchange agents, nanoparticles, hydrophobic chemicals and other additives. Typically, the mitigation mechanism was attributed to reducing the leaching of Na in AAS materials. Upscaling efflorescence mitigation strategies for AAS mortars and concretes was required.

Chapter 3

Leaching behaviour of synthetic C-(N-)A-S-H gels

3.1 Introduction

The C-(N-)A-S-H gel serves as the primary reaction product in AAS systems, exhibiting a lower Ca/(Si+Al) ratio (0.6 – 1.2) and a higher Al/Si ratio (0.1 – 0.3) compared to the C-(A-)S-H gel in PC systems [60,61]. Additionally, Na ions can be absorbed by the interlayer of C-(N-)A-S-H gels, effectively compensating for the negative charges induced by Si-Al substitution [57]. While there has been some research on the properties of synthetic C-(N-)A-S-H gels using both experimental methods [57–59] and atomic simulations [65,97–101], as discussed in *Chapter 2*, most studies have focused on C-(A-)S-H gels in PC systems. Due to the weak binding and high mobility of Na ions, C-(N-)A-S-H gels have leaching problems. However, the leaching behaviours of ions in C-(N-)A-S-H gels, particularly Na ions, which are absent in normal PC systems, are rarely investigated.

Given that the leaching of ions is the fundamental process when AAS materials are exposed to water, a better understanding of this issue is of great significance. In this chapter, I first synthesised three types of C-(N-)A-S-H gels with varying Ca/Si (0.8 and 1.2) and Al/Si (0.1 and 0.3) ratios, which represent typical elemental ratios in AAS systems. Then, I measured the ion concentration in the leachate of gels and quantified the leaching ratio of different ions. Finally, I calculated the dissolution free energy of Ca and Na in the gel with different Ca/Si and Al/Si ratios employing MD simulations with the metadynamics method. The diffusion coefficient of Ca and Na ions in the nanopore between the gel substrates with different compositions was simulated to investigate the mobility of alkali metal ions in the pore solution.

3.2 Experiments

3.2.1 Gel synthesis

The gel in this work was synthesised through the sol-gel method [102]. The gel synthesis was carried out using solutions of 0.6 M $\text{Na}_2\text{SiO}_3 \cdot 5\text{H}_2\text{O}$, 0.24 M $\text{Ca}(\text{NO}_3)_2 \cdot 4\text{H}_2\text{O}$, 0.12 M $\text{Al}(\text{NO}_3)_3 \cdot 9\text{H}_2\text{O}$, and 10 M NaOH, the latter utilised for pH adjustment. All solutions were prepared using deionised water as the solvent. The proportions of the solutions were tailored to the targeted elemental ratios presented in *Table 3.1*. The gels were named following the format “target Ca/Si_target Al/Si” in the gels. The Ca/Si (0.8 and 1.2) and Al/Si (0.1 and 0.3) ratios of the gels were tailored to cover the common range of elemental ratios in AAS materials [103,104]. It should be noted that the high solubility of Si and Al and low solubility of Ca under high alkaline conditions [105] implies that the molar Ca/Si ratios calculated from the reactants are lower than the target Ca/Si ratio in gels (*Table 3.1*).

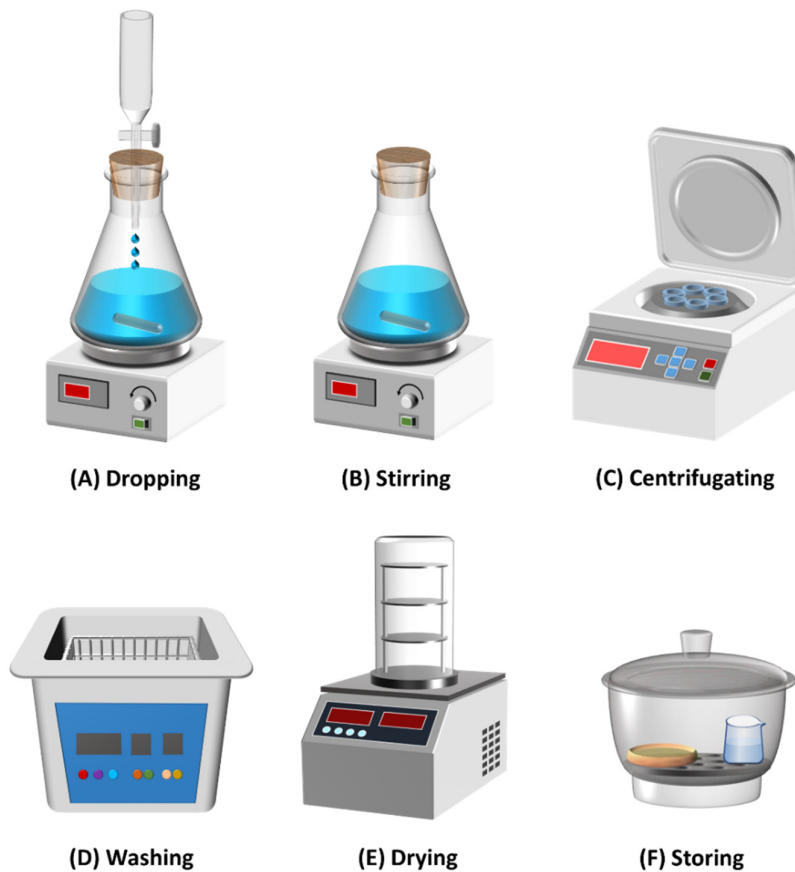


Figure 3.1. Procedures of gel synthesis and storage.

During the synthesis process, high-purity N₂ from a gas cylinder was progressively released into the glove box containing all experimental setups for at least 20 min, with the valve opened to the external environment. This process aimed to exhaust any residual air present in the glove box. Then, the valve was closed and the recirculation mode was initiated, which allowed the whole gel synthesis process to be carried out under a pure N₂ atmosphere with standard atmospheric pressure. Figure 3.1 shows the procedures of gel synthesis and storage. The solutions were carefully added drop-by-drop into a conical flask following the order of NaOH, Na₂SiO₃, Al(NO₃)₃, Ca(NO₃)₂, and deionised water (Figure 3.1A), and constant stirring was applied for 7 d in the sealed conical flasks to maintain a constant environment (Figure 3.1B). Following the experiments, the valve was reopened and all the samples and reactor were removed. Both the supernatant and the newly formed gels were collected following centrifugation (Figure 3.1C). The pH values of the supernatant from the 0.8_0.1, 0.8_0.3, and 1.2_0.3 gels were 14.2, 14.1, and 14.1, respectively, as measured by titration. These pH values align with the pH of pore solutions in real AAS pastes [69]. To further purify the freshly formed gels, a thorough washing procedure was applied. This involved three successive treatments with deionised water (500 ml each time) and a single wash with absolute alcohol (500 ml). Each washing cycle took place in an ultrasonic bath for two minutes (Figure 3.1D). Subsequent to the washing, the gel samples were freeze-dried for 3 days (Figure 3.1E). Afterwards, the gels were finely ground into powders and stored in a desiccator prior to the measurements [55,106,107], where the desiccator contained a saturated CaCl₂ solution (relative humidity (RH) ≈ 30%) and solid NaOH serving as a CO₂ trap.

Table 3.1. Component of chemical solutions for C-(N)-A-S-H gels synthesis. (unit: ml)

Target gels (Ca/Si_Al/Si)	0.6M Na ₂ SiO ₃	0.24M Ca(NO ₃) ₂	0.12M Al(NO ₃) ₃	10M NaOH	H ₂ O
0.8_0.1	80	100	40	50	80
0.8_0.3	80	100	120	50	—
1.2_0.3	50	150	75	50	25

Table 3.2. Chemical compositions and elemental ratios of the synthetic gels.

Target gels (Ca/Si_Al/Si)	CaO	SiO ₂	Al ₂ O ₃	Na ₂ O	Ca/Si	Ca/(Si+Al)	Al/Si	Na/Si
0.8_0.1	40.7	50.9	3.7	4.7	0.85	0.78	0.09	0.18
0.8_0.3	38.3	46.1	8.5	7.1	0.89	0.74	0.21	0.29
1.2_0.3	49.1	41.5	7.5	1.9	1.27	1.05	0.21	0.09

The chemical composition of gels measured by X-ray fluorescence (XRF), along with the calculated atomic ratios of synthetic gels, is shown in Table 3.2. It can be seen that the obtained atomic ratios of gels closely align with the targeted ones. The phase assemblage of the synthetic gels was identified by X-ray diffraction (XRD) using a Bruker D8 Advance diffractometer with CuK α radiation (1.54 Å), with a step size of 0.02° and a dwell time of 5 s per step.

3.2.2 Leaching test

In order to monitor the leaching behaviour of the gels, around 0.500 g (\pm 0.005 g) of gel was immersed in 100 g of deionised water within a polyethene bottle at 20 °C. The bottle was shaken every 10 min for the first hour and then every 30 min from 1 h to 6h. After 5 min, 10 min, 30 min, 1 h, 3 h, and 6 h of water immersion, the leachate was extracted using a 0.22 µm syringe-driven filter by Millex®, respectively. The ion concentration of Si, Al, Ca, and Na in the obtained leachate was measured using a PerkinElmer Optima 5300DV inductively coupled plasma optical emission spectroscopy (ICP-OES). Then, the leaching amount of ions can be determined. Finally, the leaching ratio of a certain ion (leaching amount/total amount) can be calculated if the total amount of that ion in gels is available. To this end, around 0.100 g (\pm 0.005 g) of solid was dissolved in 100 ml of 0.1 M HCl solution. Upon the complete dissolution of the solid phase, the leachate was collected, and the ion concentration was measured by ICP-OES. The leaching ratio of ions is a parameter that can reflect the leaching stability of ions.

3.3 Atomistic simulation

3.3.1 Model construction

In C-(N)-A-S-H gels, Na ions typically exhibit similar behaviour to Ca ions, while Al ions and Si ions serve as anionic groups (*i.e.*, [AlO₄₋₆] and [SiO₄]) for charge balance [108]. In this regard, the equivalent Ca/Si ratio of C-(N)-A-S-H is estimated by the (Ca+Na)/(Al+Si) ratio. The value of the (Ca+Na)/(Al+Si) ratio for synthetic gels is similar to (slightly higher than) the Ca/Si ratio of the 14 Å tobermorite, thereby making the 14 Å tobermorite a suitable prototype for constructing the amorphous molecular models of C-(N)-A-S-H gels. The model construction procedure is demonstrated in Figure 3.2. First, the orthorhombic unit cell (Figure 3.2B) was

constructed by redefining the lattice vectors of an original monoclinic unit cell of 14 Å tobermorite (*Figure 3.2A*) obtained from the literature [109]. Then, the orthorhombic unit cell was duplicated into a 2×4×1 supercell of C-S-H (*Figure 3.2C*). The bridging [SiO₄] groups were partly removed or replaced by [AlO₄] groups to align with the Ca/Si and Al/Si ratios of the C-(N-)A-S-H gels in *Table 3.2*. Na ions were inserted into the interlayers to achieve the desired Na/Si ratios and to neutralise the net negative charges engendered by the substitution of Al ions for Si ions (*Figure 3.2D*). However, the stoichiometric addition of Na ions did not lead to complete charge compensation. Hence, additional H⁺ or OH⁻ were introduced into the structures for final charge balancing.

All the developed C-(N-)A-S-H models went through a comprehensive annealing process utilising a reactive force field [110] to ensure structural stability before their use in constructing the surface models for cation dissolution (*Section 3.3.2*) and diffusion (*Section 3.3.3*) calculations. During the annealing process (*Figure 3.2E*), the system was heated from 300 K to 500 K in 500 ps and equilibrated at 500 K for 1000 ps. Then, it was cooled to 300 K in 500 ps and equilibrated at 300 K for 1000 ps. The whole process was conducted under the isothermal-isobaric ensemble (NPT) with a time step of 0.2 fs. Note that N: number of particles is constant; P: pressure is constant; T: temperature is constant. The annealing scheme for accelerating the protonation of cement minerals has been widely adopted in previous studies [110,111].

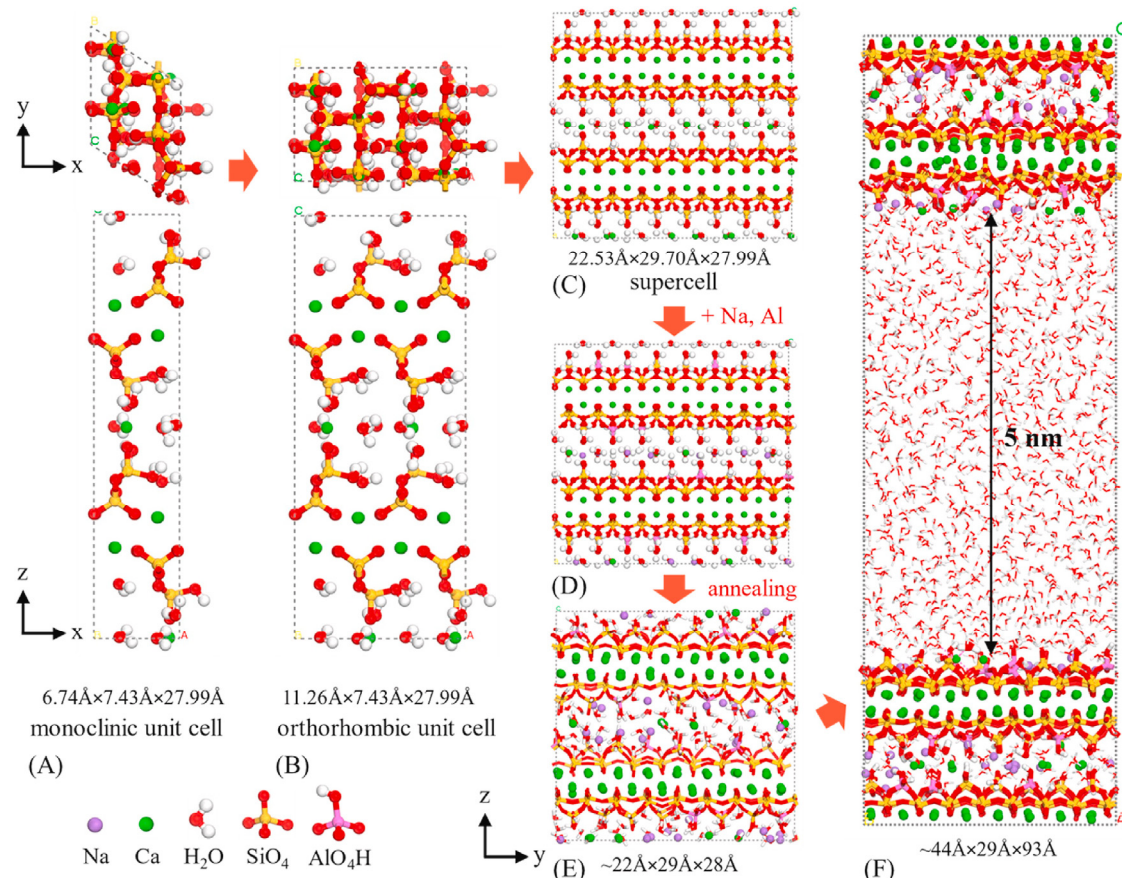


Figure 3.2. Schematic demonstration of the model construction procedure, taking the “0.8_0.1” gel model as an example.

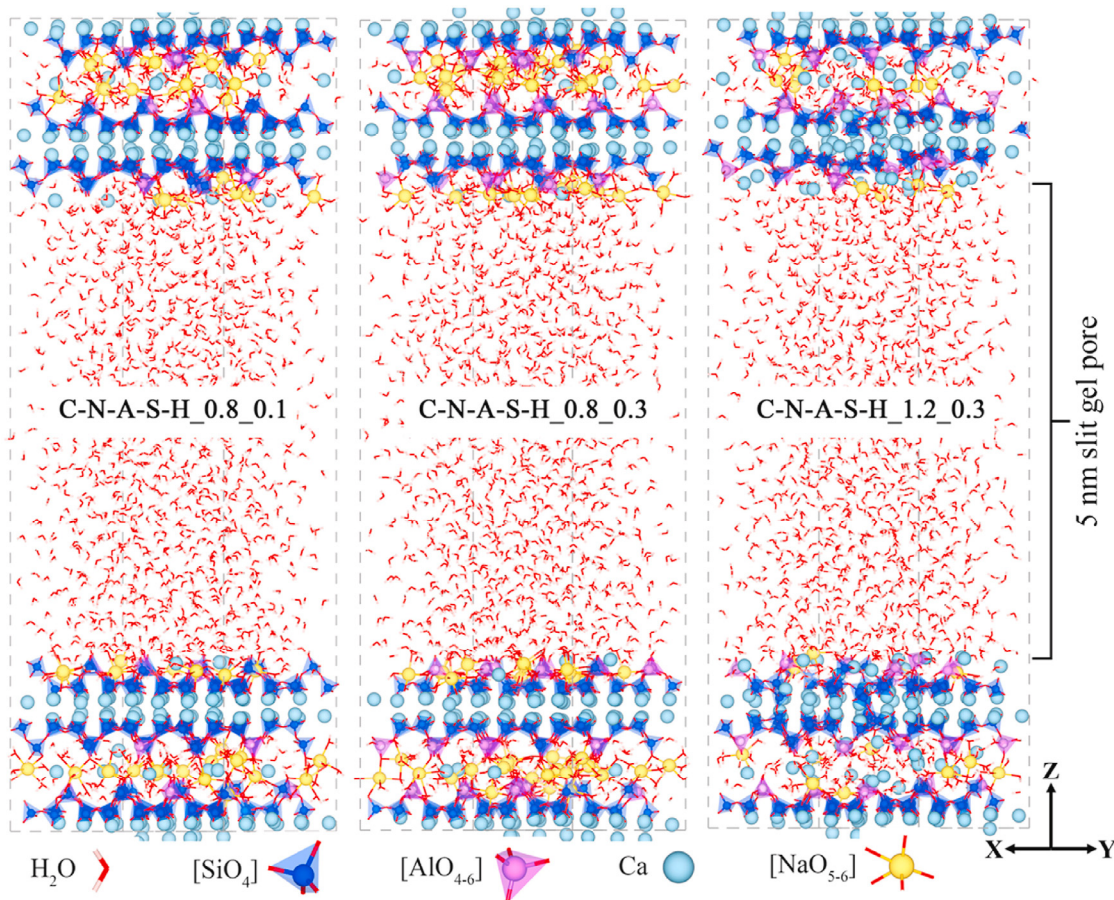


Figure 3.3. Schematic representation of nanopore models of three C-(N)-A-S-H gels. “0.8” and “1.2” refer to Ca/Si ratios, while “0.1” and “0.3” denote the Al/Si ratios. To clearly illustrate the entire gel structure, the gel model is rotated 45° along the z-axis. A more detailed view of the gel structure at the ab plane is shown in Figure 3.4.

The “nanopore model” is widely used to investigate the dissolution and diffusion of ions in gels [65,112] (as mentioned in Section 2.3.2.3), which is constructed by cleaving the gel structure at the interlayer (Figure 3.2F). According to the nanoscale C-S-H model [113], the gel pore of C-S-H is about 2 – 5 nm. Since our study focuses on ion transport, a larger gel pore is necessary to increase the transport space and sample ions, ensuring the accuracy of the modelling. Therefore, I produced a 5 nm slit pore between the gel substrates and saturated it with water (Figure 3.2F). According to the model construction procedure (Figure 3.2), three C-(N)-A-S-H surface models are built, which are presented in Figure 3.3. All C-(N)-A-S-H gel models have similar dimensions, approximately 45 Å × 30 Å × 95 Å, with a total atom count of around 11,600. All MD simulations were carried out using the LAMMPS software [114].

3.3.2 Dissolution free energy calculation

Dissolution free energy measures the energy change when a solute dissolves in a solvent, essential for predicting solubility and designing materials. Dissolution free energy is the most important quantity that bridges dissolution thermodynamics and kinetics [115]. However, the calculation of free energy from standard MD simulations is infeasible because the ion dissolution process usually takes more than microseconds to be observed, while MD typically has a simulation time limit of a few nanoseconds. Therefore, advanced sampling methods

such as metadynamics [116], umbrella sampling [117], steered MD [118], etc., have been developed to enhance the sampling of configuration space within an affordable computational cost. Metadynamics has the advantage of no requirement for predefined reaction pathways, making it a desirable candidate for simulating complicated processes like dissolution, where the exact dissolution pathway was unknown before.

To understand the intrinsic leaching potential of Na and Ca ions in the C-(N)-A-S-H gel, the dissolution free energy of C-(N)-A-S-H gels was calculated. The calculation was implemented by a well-tempered metadynamics method [119,120] with the external library Plumed [121] patched in LAMMPS. The dissolution free energy barrier is typically determined by the breaking and formation of chemical bonds within 5 Å of the surface. Using a larger dissolution distance cutoff does not significantly affect the accuracy of the free energy calculations but would substantially increase the computational load. Therefore, the free energy landscape of cations was calculated within 12 Å above the surface, which was a very safe cutoff. Based on previous experience in the Ca ion dissolution simulation of belite [122] and C-S-H gels [112], three collective variables (CVs) of displacement components of target Na and Ca ions in x, y, and z directions were used as the biasing CVs while an additional CV of the coordination number of target ions with surface oxygen (*i.e.* number of surface restraints) was calculated as an observation CV during the metadynamics simulation. To eliminate the influence of the initial configuration on the ion dissolution, four representative sites for each type of Ca and Na were selected to calculate the dissolution free energy, as presented in *Figure 3.4*. All selected sites of cations shared a close number of surface restraints around 3 with gels [123,124]. The well-tempered metadynamics used the biasing potential of Gaussians with a width of 0.1 Å and added frequency of every 200 timesteps. The initial height of the Gaussian potentials was 1.5 kJ/mol and changed by a bias factor of 10 during the metadynamics sampling to obtain better convergence. The free energy calculations were performed under the canonical ensemble (NVT) using a reactive force field with a time step of 0.2 fs. Note that N: number of particles is constant; V: volume is constant; T: temperature is constant.

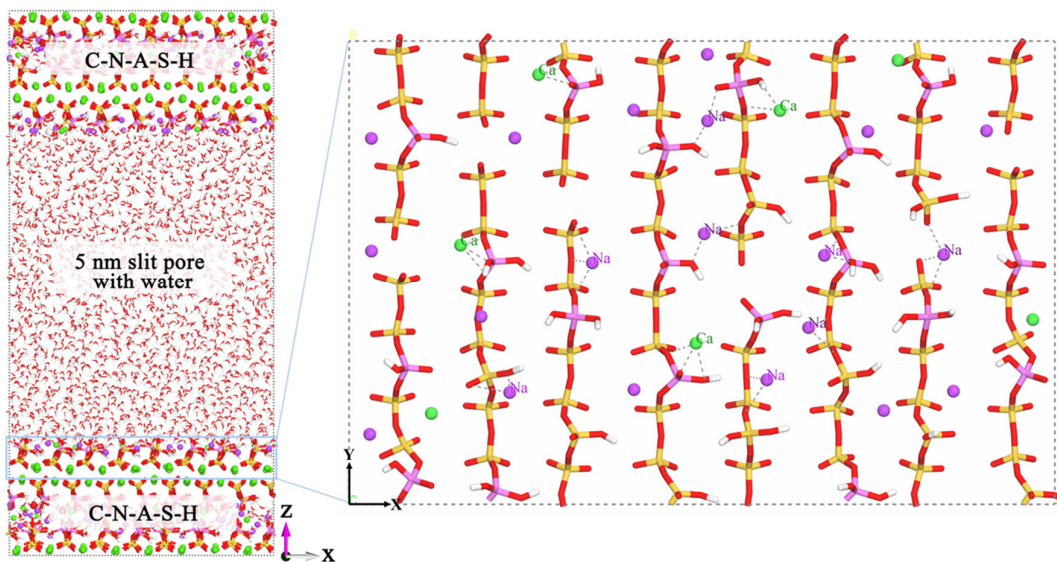


Figure 3.4. Atom arrangement of the disordered surface with four selected representative sites for Ca and Na. All selected sites of cations share a close number of surface restraints around 3 with gel substrates. The gel structure of “0.8_0.3” serves as an example, as shown. The figure on the right is the zoomed-in view of the gel structure on the xy plane.

3.3.3 Diffusion calculation

The variation in the composition of C-(N-)A-S-H alters the surface charges and textures of the gel, which influences the diffusion and transport of the ions in the nanopores as recognised by previous studies [100,101]. To gain insights into the experimental leaching outcomes of gels, the diffusion properties of cations in the nanopore of C-(N-)A-S-H gels with different compositions were investigated. The diffusion models were constructed by randomly scattering sixteen NaOH or Ca(OH)₂ molecules in the solution of the nanopore models (Figure 3.3), which aimed to mimic the mobility of cations at different distances from the gel substrates. Considering that the diffusion process was nonreactive and that the timespan was considerably long, the diffusion properties were calculated using the classical Clay force field (ClayFF) [125] with a time step of 1 fs. In ClayFF, free hydroxyl groups (OH⁻) and hydroxyl of silicate (Si-OH) shared the same parameters of Lenard-Jones and quadratic bonding potentials. The oxygen charge in free hydroxyl groups was -0.95 e, consistent with the original ClayFF parameters. All other atom types also retained their original ClayFF charges, except for non-bridging oxygens in the aluminosilicate chains. The charge of these oxygens was adjusted to maintain overall charge neutrality within the various C-(N-)A-S-H gels. I took into account the difference of Ca ions in the C-(N-)A-S-H and pore solution as how they were defined in ClayFF. The Na ions however took the same set of parameters in ClayFF.

The whole system was first equilibrated under a canonical (NVT) ensemble for 1 ns with cations in the solution being fixed. Then I released the cations and ran MD simulations for 10 ns under a microcanonical (NVE) ensemble to calculate the mean square displacement as a function of time, *i.e.*, MSD(t). The diffusion coefficients of Ca and Na ions were calculated from MSD(t) based on the Einstein equation (Equation 3.1). A bin size of 7 Å was used, and snapshots were recorded every 1 ps, resulting in a total of 10000 snapshots over the 10 ns simulation for the calculation of MSD and diffusion coefficients. While the pore solution of C-(N-)A-S-H gels was well-known to be alkaline, containing Na and Ca ions [126], accurately determining the exact ion concentration remains challenging. In practice, the solubility of cations within a 5 nm pore solution box was constrained. Therefore, to ensure sufficient ion statistics for analysis while minimising the number of introduced ions, 16 Na (or Ca) ions were selected for diffusion coefficient calculations.

$$D = \frac{1}{2N} \lim_{t \rightarrow \infty} \frac{MSD(t)}{t} \quad (3.1)$$

where N=3 is the dimensionality for the bulk diffusion.

3.4 Results and discussion

3.4.1 XRD pattern of synthetic gels

As observed in Figure 3.5, representative reflections corresponding to 14 Å tobermorite [PDF# 00-029-0331] [107] are identified in the synthetic solids, which indicates the presence of the high-purity C-(N-)A-S-H gel. The intensity of these characteristic peaks changes with the variation of Ca/Si and Al/Si ratios. For instance, the peak referring to d₀₀₂, located between 5-10°, correlates with the property of the interlayer. It is reported in [107] that the signal in the gel with a higher Ca/Si ratio is more pronounced than that with a low Ca/Si ratio. This is in agreement with our results, in which an evident reflection regarding d₀₀₂ is discernible exclusively in the gel with a Ca/Si ratio of 1.2.

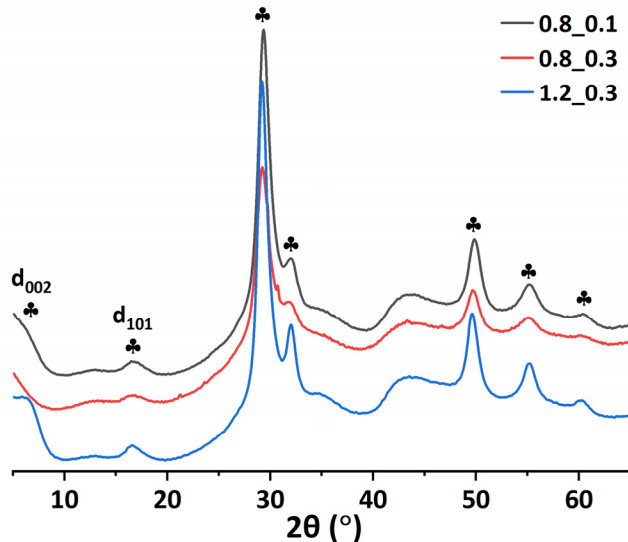


Figure 3.5. XRD pattern of the synthetic gels with different elemental ratios. ♦: C-(N-)A-S-H gels.

This phenomenon likely arises for two main reasons. First, the gel with lower Ca and higher Al contents possesses a larger interlayer distance [106], potentially resulting in a lower peak value of d_{002} below 5°. Second, the gel with lower Ca and higher Al contents tends to exhibit a less ordered and more crosslinked structure [62], leading to a faint reflection of the characteristic 14 Å tobermorite. This hypothesis is supported by the observation that the intensity of characteristic peaks is generally higher in the 1.2_0.3 gel than in the other two gels. Additionally, the presence of d_{101} peak is also detected across all three gels, which is considered the Si in bridging sites in gel chains [127].

3.4.2 Leaching behaviour of synthetic gels

The leaching behaviour of the gels was systematically monitored. As mentioned in Section 3.2.2, both the leaching amount and leaching ratio were calculated. The leaching amount of ions is prominently dependent on the inherent elemental compositions of gels, whereas the leaching ratio can mirror the leaching potential of a certain element.

Figure 3.6 shows the ion concentration and leaching rate of Si and Al in the three C-(N-)A-S-H gels with time. Generally, a discernible upward trend is observed in ion concentration as a function of leaching time, with most ions attaining a steady state after 360 min of water immersion. This observation indicates that the leaching of gel is a rapid process at the solid/liquid ratio of 1/200. In paste or concrete, where the gels are part of a dense matrix, the leaching of ions naturally would be much slower. As shown in Figures 3.6A and B, the curves of ion concentration and leaching ratio of Si have a similar shape. The gel with a lower Ca/Si ratio manifests a higher extent of Si leaching, which suggests that the presence of Ca is beneficial for the stability of Si. Additionally, the leaching ratio of Si in the 0.8_0.3 gel is slightly higher than that of the 0.8_0.1 gel. This is probably attributed to the Ca/(Si+Al) ratio of the 0.8_0.1 gel (0.77) is marginally higher than that of the 0.8_0.3 gel (0.74), as presented in Table 3.2. The gel with a higher Ca/(Si+Al) ratio shows a lower leaching amount of Si.

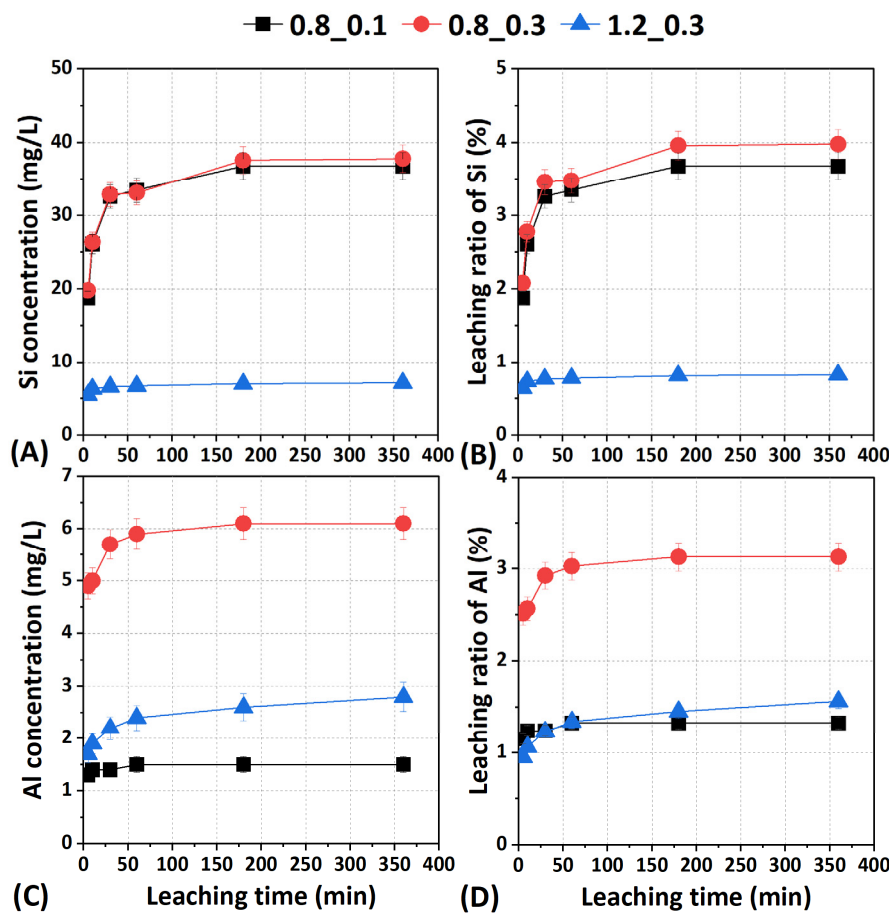


Figure 3.6. Leaching behaviour of Si and Al ions in C-(N)-A-S-H gels within 360 min. (A) and (C): Si and Al concentrations in the leachate of gels with time. (B) and (D): leaching ratios of Si and Al in gels with time.

The ion concentration of Al in the leachate with time is depicted in Figure 3.6C. It is observed that the 0.8_0.3 gel exhibits the highest concentration, followed by the group of 1.2_0.3 and 0.8_0.1. Given that the initial content of Al in the 0.8_0.3 gel is higher than that of the other two gels, it logically results in the highest leaching amount. As shown in Figure 3.6D, at a lower Ca/Si ratio of 0.8, an increased content of Al leads to enhancements in both the leaching amount and the leaching ratio of Al. This indicates that the extra Al in the 0.8_0.3 gel shows higher leaching potential, which is probably due to the presence of $[\text{AlO}_5]$ and $[\text{AlO}_6]$ in the interlayer [97]. Furthermore, comparing the 0.8_0.3 and 1.2_0.3 gel reveals that the gel with a higher content of Ca shows a lower leaching ratio of Al. This indicates that the presence of Ca is conducive to the immobility of Al, which is consistent with the results of Si (Figure 3.6B). This agrees well with the solubility results in [57] and confirms that Ca is essential to the stability of structural ions of Si and Al.

Figures 3.7A and B show the leaching behaviour of Ca in C-(N)-A-S-H gels. The leached amount and ratio of Ca present a coherent trend across the three gels. The gel with a higher Ca/(Si+Al) ratio shows a higher Ca leaching potential. This considerable difference is primarily due to the varying initial locations of Ca in a gel. Typically, interlayer Ca and intralayer Ca are the two fundamental forms present in a 14 Å tobermorite structure [109]. The intralayer Ca is situated within the CaO sheet and is usually resistant to dissolving, barring being subjected to severe

structural failure [128]. Therefore, the majority of leached Ca ions stems from the interlayer Ca, which serves to maintain charge balance in the interlayer. Due to the low content of Ca in the 0.8_0.1 and 0.8_0.3 gels, the responsibility of compensating the charge is extensively taken over by Na ions. This results in a deficiency of interlayer Ca ions in the basal spacing, and thus a low leaching amount of Ca.

Figure 3.7C shows the ion concentration of Na in the leachate of C-(N-)A-S-H gels. Generally, the concentration of Na is notably higher than that of Si, Al, and Ca, indicating a relatively weak interaction between Na and gels. Additionally, the gel of 0.8_0.3 shows the highest concentration of Na, followed by the 0.8_0.1 and 1.2_0.3 groups. This is primarily due to a higher Na content (Table 3.2) in the starting gels. Interestingly, the trend of the leaching ratio of Na is contrary to the leaching amount. As observed in Figure 3.7D, Na in the gel of 1.2_0.3 shows the highest leaching ratio, whereas the gel of 0.8_0.3 shows the lowest. This implies that the gel with an increased Ca/Si ratio and a decreased Al/Si ratio has a higher leaching potential of Na. To further understand the underlying mechanisms, MD simulations were carried out.

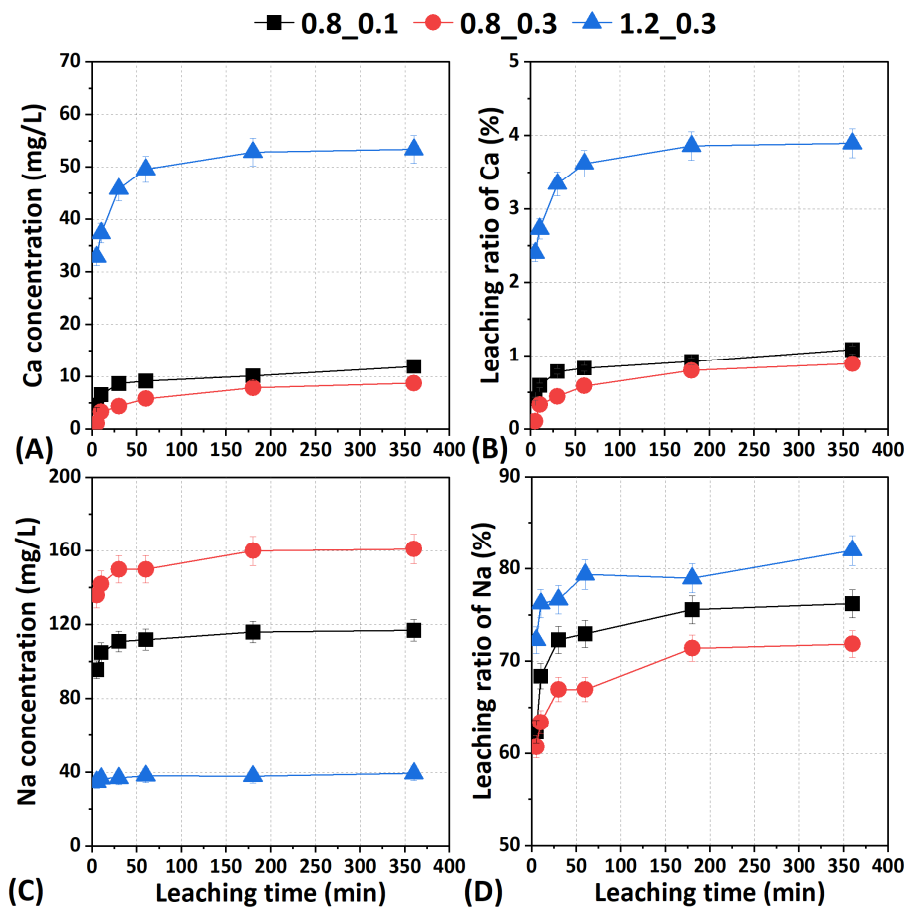


Figure 3.7. Leaching behaviour of Ca and Na ions in C-(N-)A-S-H gels within 360 min. (A) and (C): Ca and Na concentrations in the leachate of gels with time. (B) and (D): leaching ratios of Ca and Na in gels with time.

3.4.3 Dissolution free energy of Ca and Na in gels

Figure 3.8 illustrates a 2D map depicting the dissolution free energy of Ca and Na from C-(N-)A-S-H gels as a function of the dissolution distance and the coordination number of cations with gels. The term “cation-Os” denotes the coordination number of surface cations with the oxygen of silicate/aluminate chains, which accounts for the number of restraints on the surface cations [112]. Only the dissolution distance of cations along the Z-axis is considered, since the movement of cations along the x- and y-axes is confined by other ions on the gel surface. It is observed that each system undergoes multiple free energy minima (intermediate states) and saddle points (transition states) until the cations are fully dissolved. The difference in free energy between the minimum points and saddle points represents the dissolution free energy barrier, which inversely indicates the inherent ease of cation dissolution. In general, the barrier of free energy increases with the coordination number, as the dissolution of cations becomes more difficult with the increase of restraints. Additionally, the initial dissolution position on the x-axis is lower than zero, as an indicator of the initial absorption of cation by gels. This is probably due to vacancies and defects on the surface of amorphous C-(N-)A-S-H gels [112,129].

Figures 3.8A–C show the dissolution free energy of surface Ca ions from three C-(N-)A-S-H gels. Initially, Ca shows a coordination number of 2 – 5 with the surface oxygen of gels. As the dissolution progresses, Ca gradually detaches from the surface, resulting in a decrease in cation-Os (indicating that more surface restraints are broken) until it reaches zero. The general profile of the free energy landscape of Ca is similar across the three gels, whereas the gel of 0.8_0.3 shows a larger barrier than that of the other two, as indicated by the red regions (deep free energy basin) in *Figure 3.8B*. *Figures 3.8D–F* show the dissolution free energy of Na in three C-(N-)A-S-H gels. The initial coordination number of surface Na ions is comparable to Ca before dissolution. However, the gradient of free energy of Na is much lower, indicating a lower energy barrier for dissolution and thus a higher leaching potential of Na. Interestingly, the initial coordination number of surface Na in the gel of 1.2_0.3 (*Figure 3.8F*) is lower than that of the remaining two. This reduction in the coordination with gels is probably due to the higher Ca/Si ratio of gels. The gel with a higher Ca/Si ratio shows a shorter mean chain length [20], making it more surrounded by water molecules, which partially lessens the contact of surface ions with the gel matrix.

Based on the free energy landscape, the overall dissolution free energy barrier can be calculated by searching the transition states using the nudged elastic band method [130]. Considering the surface complexity, the average dissolution free energies of four representative sites for each type of cation were calculated (*Figure 3.4*). The average dissolution free energy barriers for Ca and Na are compared in *Figure 3.9*. It can be seen that the dissolution free energy of Ca is generally higher than that of Na, consistent with the leaching result, where Ca shows a lower leaching ratio than Na. Additionally, both Ca and Na in the gel of 0.8_0.3 have higher dissolution free energy than the other two gels, which indicates that cations in the gel with a lower Ca/Si ratio and a higher Al/Si ratio show lower leaching potential. The lower dissolution free energies of 1.2_0.3 compared to 0.8_0.1 suggest that the positive effect of the elevated Ca/Si ratio in promoting the dissolution of cations is larger than the negative effect of the reduced Al/Si ratio. These findings align well with the experimental results in *Figure 3.7*, likely due to the difference in the surface charge of different gels. To further investigate the impact of surface charge on the dissolution and diffusion of cations, the diffusion coefficient of Ca and Na ions was calculated in the nanopore.

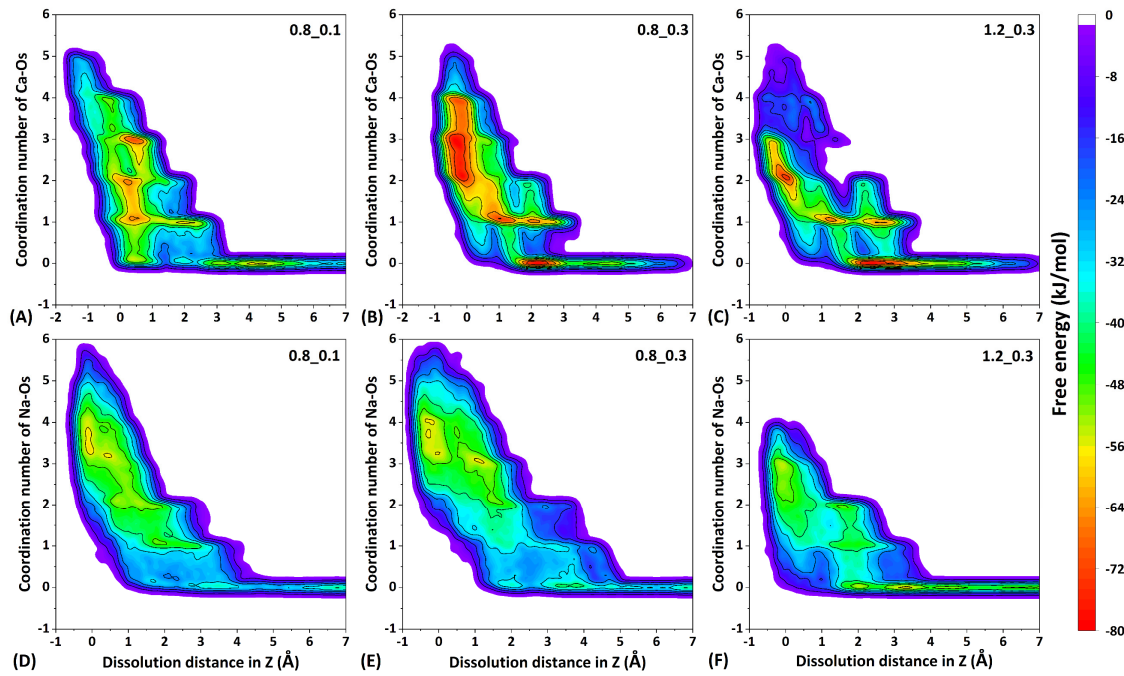


Figure 3.8. 2D dissolution free energy landscape for Ca and Na from three gels as a function of dissolution distance and of “cation-Os” coordination number (i.e., number of surface restraints). “Os” refers to the surface oxygen of the solid (gels). The maximum free energy in each system is normalised to zero.

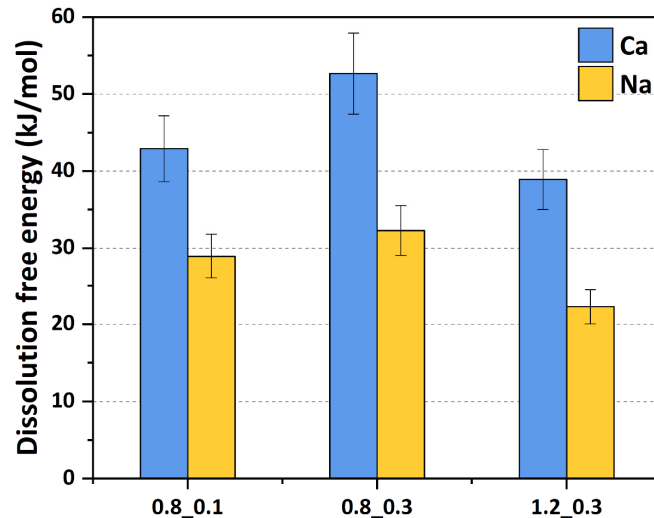


Figure 3.9. The average dissolution free energy barrier (between the transition state and initial state) of Ca and Na located at four representative sites. The average dissolution free energy of Ca in the three gels is ~43, ~53 and ~39 kJ/mol, respectively. The average dissolution free energy of Na in the three gels is ~29, ~32 and ~22 kJ/mol, respectively.

3.4.4 Diffusion coefficient of Ca and Na in the nanopore of gels

In this section, the diffusion behaviour of Ca ions and Na ions at different distances from the gel substrate is investigated. Atomic density distribution refers to the spatial distribution of atoms within a system. It involves analysing the quantity or concentration of atoms in different regions of the simulated space. *Figure 3.10* shows the atomic density distribution of Ca and Na ions in the nanopore ($Z = 42 - 92 \text{ \AA}$) along the Z direction with time. At the very beginning ($t = 0$), Ca and Na ions exhibit generally uniform distributions in the nanopores. As the simulation proceeds, the atomic density of both cations becomes higher near the gel substrates, which indicates the cations in the nanopore are to some extent adsorbed to the upper and lower substrates of C-(N-)A-S-H gels. This is due to the negative surface charges of gels, as well-documented in experiments [131,132]. This adsorption capacity reflects the ability of C-(N-)A-S-H gels in bearing cations and serves as an indicator to inversely compare the ease of cation leaching from the gel.

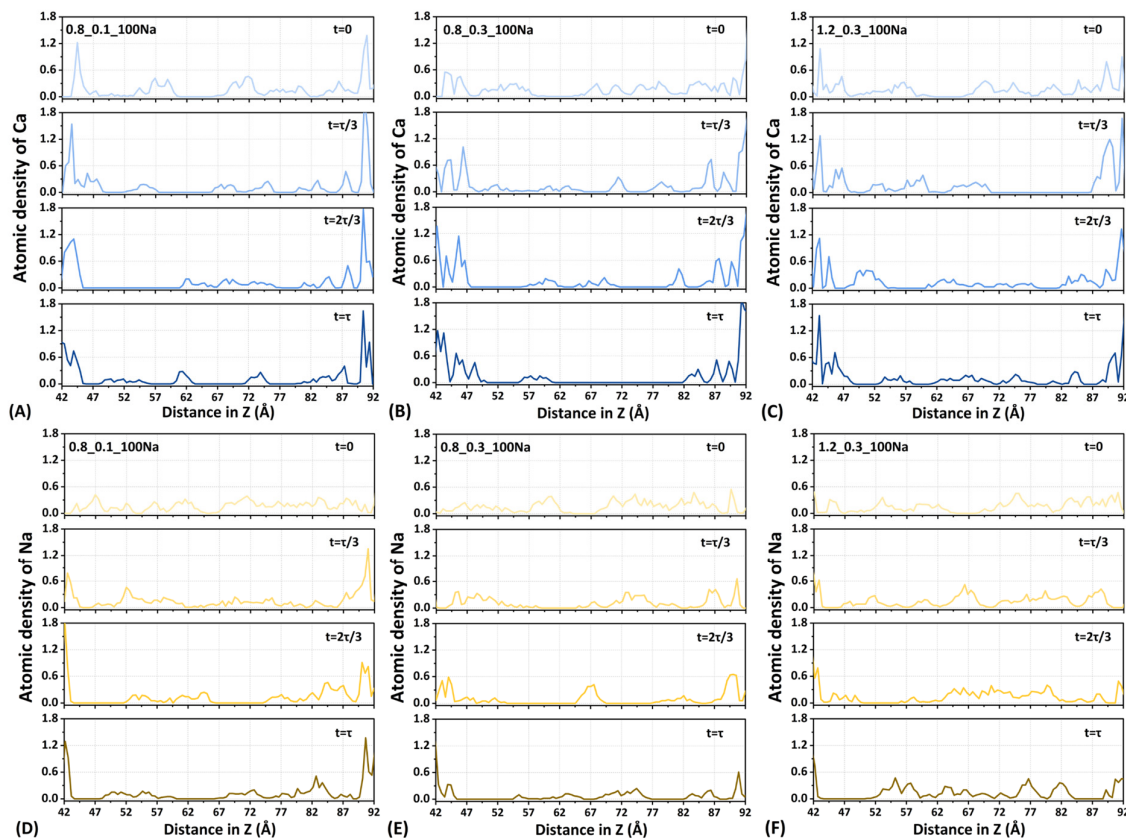


Figure 3.10. Atomic density profiles of Ca and Na ions along the Z-axis of a 5 nm nanopore (from 42 to 92 \AA) perpendicular to the surface of gel slabs. τ is the total simulation time. In each inset, the locations near 42 \AA and 92 \AA at the “distance in Z” correspond to the gel substrates, while that at around 67 \AA is considered the centre of the nanopore of gels.

To quantitatively describe the mobility of cations impacted by the absorption of gel surfaces in confined nanopore water, the diffusion coefficients of Ca and Na ions are calculated using the trajectory of cations at various distances from the gel substrates, as shown in *Figure 3.11*. In general, the diffusion coefficient of Na ions is higher than that of Ca ions at equivalent locations of the nanopore. This is mainly due to a higher intrinsic diffusion coefficient of Na than Ca [133,134]. In addition, the diffusion coefficient of both cations in proximity to the gel substrate is notably lower than that of ions positioned in the middle of the nanopore. This once again indicates the adhesive behaviour of the gel substrates.

Figure 3.12. illustrates the average diffusion coefficients of Ca and Na ions in the nanopore between the C-(N-)A-S-H gel substrates. It is observed that the average diffusion coefficient of Ca ions is consistently lower than that of Na ions in all three gels. This is due to a higher intrinsic diffusivity of Na ions than Ca ions under aqueous conditions [135]. Besides, the diffusion coefficient of both Ca and Na ions in the gel of 1.2_0.3 is higher than that in the gels of 0.8_0.1 and 0.8_0.3. This indicates that the gel with a high Ca/Si ratio shows less effective absorption of cations. On the other hand, the comparison of the diffusion coefficient of Na in the gels of 0.8_0.1 and 0.8_0.3 implies that a higher Al incorporation promotes the absorption of Na.

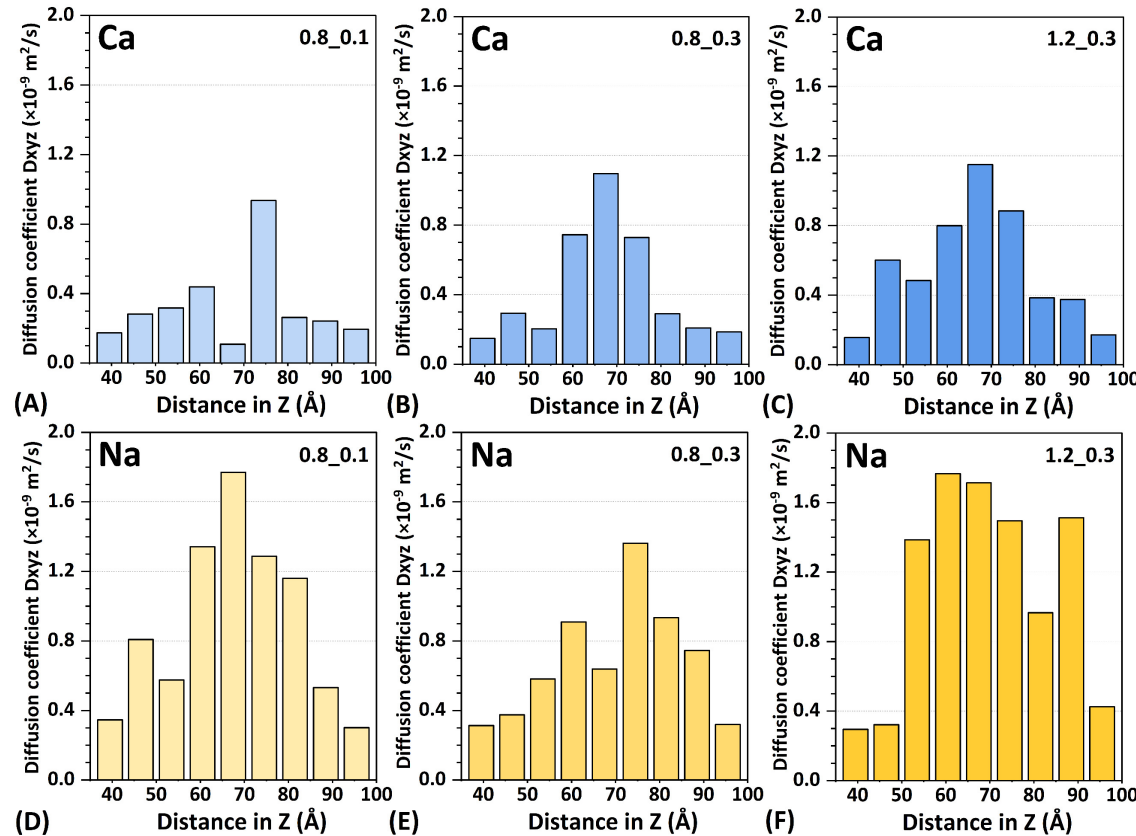


Figure 3.11. Diffusion coefficient distributions of Ca and Na ions along the Z-axis of the nanopore solution perpendicular to the surface of three gels. In each inset, the locations near 40 Å and 95 Å at the “distance in Z” correspond to the gel substrates, while that at 67 Å is near the centre of the nanopore of the gels.

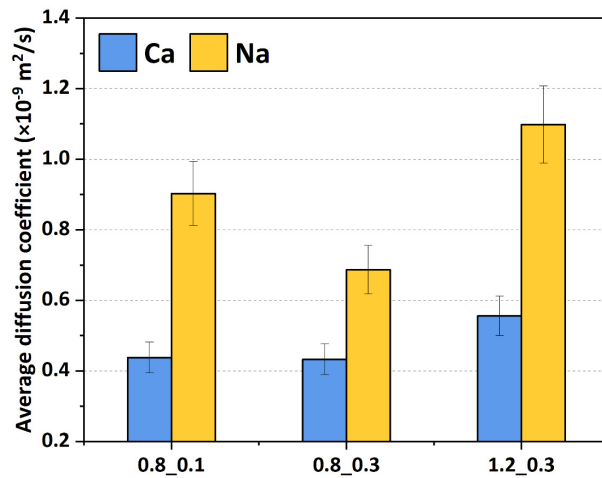


Figure 3.12. Average diffusion coefficients of Ca and Na ions in the nanopore of three gels. The average diffusion coefficients of Ca ions in the three gels are 0.44 , 0.43 and $0.56 \times 10^{-9} \text{ m}^2/\text{s}$, respectively. The average diffusion coefficients of Na ions in the three gels are 0.9 , 0.69 and $1.1 \times 10^{-9} \text{ m}^2/\text{s}$, respectively.

3.5 Discussion

3.5.1 Impact of gel chemistry on the leaching potential of Ca and Na

Figure 3.13 shows the relationship between the dissolution free energy and diffusion coefficient of Ca and Na in the three C-(N-)A-S-H gels. It is observed that the dissolution free energy of both Ca and Na is negatively correlated with their respective diffusion coefficients. As for the same cation, the diffusion coefficient is closely related to the charge on the gel surface. Therefore, this indicates that the binding energy between gels and cations is also related to the surface properties of gels. More specifically, the gel with a lower Ca/Si ratio and a higher Al/Si ratio shows increased charge negativity on the surface, strengthening the binding between cations and gels, and thereby hindering the dissolution potential of cations.

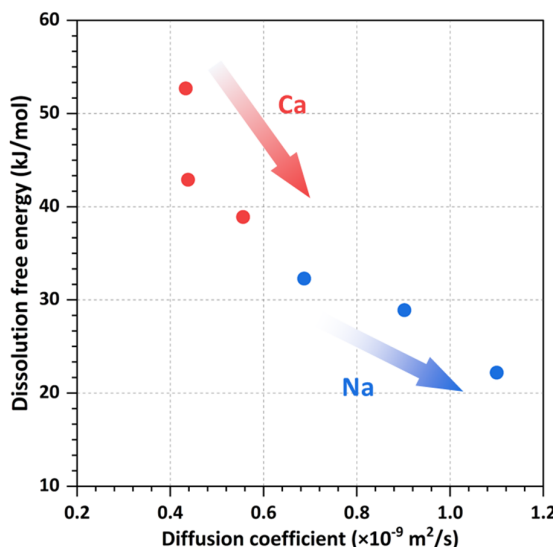


Figure 3.13. Relationship between the dissolution free energy and diffusion coefficient of Ca and Na in three gels.

3.5.2 Mechanisms behind the different leaching potential of Ca and Na

Typically, the discrepancy in the dissolution of cations is dependent on the interaction between cations and silicic (or aluminium) acid anions, a concept explained by the electric double-layer theory and the charge screening effect of cations [136–138]. *Figure 3.14A* shows the schematic representation of the electric double layer surrounding a silicic acid anion, and *Figure 3.14B* shows the potential energy distributed in these layers. When these anions (e.g. $\text{SiO}(\text{OH})_3^-$ or $\text{SiO}_2(\text{OH})_2^{2-}$) are present in an electrolytic solution, a double layer forms around their charged surface. Positively charged species from the solution are attracted to this surface, resulting in a higher concentration of ions in the absorbed layer (double layer) compared to the adjoining bulk solution. The inner part of this absorbed layer is known as the “Helmholtz layer” or “Stern layer” [139], which is tightly bound to the surface. The outer part of this absorbed layer is designated as the “diffusion layer”, where the force from the anion gradually diminishes, eventually reaching an equilibrium with that of the bulk solution, as the distance from the Stern layer increases.

The formation of silicate chains involves the condensation of Si or Al tetrahedra, and the strength of binding between two anions is closely associated with the property of a double layer. As the two anions approach each other in a solution, there exists a certain distance at which they begin to experience a repulsive force. This force, represented by the total potential energy, is determined by the competition between repulsive potential energy and attractive potential energy (Van der Waals), as shown in *Figure 3.14C*. It can be seen that the gel condensation process can only occur if the two anions collide with sufficient velocity to overcome this potential barrier.

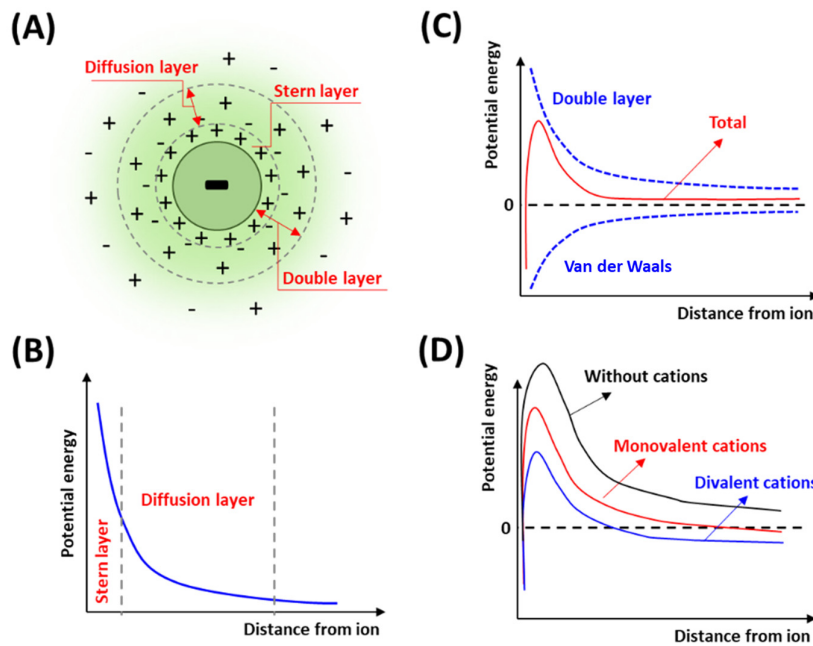


Figure 3.14. Schematic representation of (A) electric double layer distribution surrounding an anion [140]; (B) potential energy distribution surrounding a sole anion [140]; (C) potential energy distribution between two approaching anions [138]; (D) potential energy distribution in the presence of cations with different valences [138].

However, this barrier can be substantially lowered through the addition of cations, which can form a shielding double layer. This shielding effect of cations is particularly effective at a higher valence [141,142], as shown in *Figure 3.14D*. The previous results have shown that the required ion concentration of monovalent alkali ions (Li, Na, K) for gel condensation is nearly 100 times higher than that of divalent alkali ions (Mg, Ca, Ba) [141]. This indicates that Ca is more effective than Na in promoting gel formation, thereby the binding between Ca ions and Si/Al anions is more robust. As a result, the leaching potential of Ca ions is lower than that of Na ions.

3.5.3 Perspective on the dissolution of cations in gels

During the MD simulation process, I observed that some OH^- can leach away from gel substrates along with cations. This might indicate an increase in the pH of the host solution. However, the variation of pH due to the dissolution of cations is not considered in this study, since our focus is primarily on the dissolution behaviour of limited cations at very early ages, which may not significantly impact the pH of the host solution on their own. In reality, the leaching of C-(N-)A-S-H gels results in elevated pH in the solution [9]. The increase in pH can influence the solubility of various species, including cations, and can alter the kinetics and thermodynamics of dissolution processes. Understanding these complex interactions between pH changes, cation dissolution, and the stability of C-(N-)A-S-H gels is crucial for accurately modelling and predicting the behaviour of these materials in practical applications. Further investigation into these reactions is warranted to comprehensively grasp their implications and optimise the performance of C-(N-)A-S-H gels in various environmental and engineering contexts.

3.6 Conclusions

In this chapter, the leaching behaviour of ions in C-(N-)A-S-H gels was investigated, with a focus on Ca and Na. The leaching mechanisms behind the experimental results were revealed by MD simulations. The conclusion can be drawn as follows.

1. A higher Ca/Si ratio and a lower Al/Si ratio contributed to an elevated crystallisation of gel structure. The presence of Ca was conducive to the immobilisation of Si and Al.
2. An elevated Ca/Si ratio and a reduced Al/Si ratio of gels promoted the dissolution of cations. This was because a higher Ca/Si ratio and a lower Al/Si ratio can reduce the charge negativity of gel surfaces, resulting in weak binding and absorption of cations to the gel matrix. On the other hand, the gel with a higher Ca/Si ratio featured shorter and more defective aluminosilicate chains, which resulted in fewer surface restraints to surface cations, lessening the prohibition of ion leaching.
3. The leaching affinity of Ca and Na ions within an identical gel was dependent on their different inherent dissolution free energies. As indicated by MD simulations, Ca generally showed a higher average dissolution free energy than Na, which led to a lower leaching potential of Ca than Na in C-(N-)A-S-H gels.
4. This chapter confirmed the significant leaching of Na from C-(N-)A-S-H gels. The impact of this severe leaching of Na on the gel structure was investigated in *Chapter 4*.

Chapter 4

Structural evolution of synthetic C-(N-)A-S-H gels subjected to leaching

4.1 Introduction

As discussed in *Chapter 2*, the majority of leaching studies regarding gels have focused on C-(A-)S-H gels, which are representative of the gels in PC-based materials. Additionally, the exposure condition for these studies typically involves weak acidic (ammonium salts) to expedite the leaching of gels for understanding the impact of decalcification on C-(A-)S-H gels [63,128]. However, Na is the specific cation existing in AAS materials. A significant amount of Na ions leaching from the gels has been identified in *Chapter 3*. The subsequent structural change of gels induced by the leaching of Na ions remains unclear.

In this chapter, three synthetic C-(N-)A-S-H gels used in *Chapter 3* were employed to fill this gap. These gels were immersed in deionised water for up to 28 d. Subsequently, the change in chemical composition and structure of gels was investigated. Eventually, a schematic representation was depicted to unveil the mechanisms behind the structural evolution of gels induced by leaching.

4.2 Materials and methods

4.2.1 Materials

Three distinct stoichiometrically tailored gels were synthesised, denoted as 0.8_0.1, 0.8_0.3, and 1.2_0.3, which follow the same procedure outlined in *Chapter 3*. The former refers to the Ca/Si ratio, and the latter denotes the Al/Si ratio. However, since the gels used in *Chapters 3* and *4* were synthesised in two separate batches, their chemical composition showed slight differences. The chemical composition and elemental molar ratios of C-(N-)A-S-H gels are shown in *Table 4.1*.

For the leaching experiments, 1.500 g (± 0.005 g) of gel was mixed with 150.0 g (± 0.1 g) of deionised water in a sealed polyethene bottle. The samples were allowed to equilibrate at room temperature ($20 \pm 2^\circ\text{C}$) and shaken twice a week [57]. Considering the possibility of structural change of gels occurring over an extended period, the water immersion times were prolonged compared to those in *Chapter 3*. After immersion for 8 h, 1 d, 7 d and 28 d, the gels were filtered and washed with water and absolute ethanol four times. Subsequently, the leached gels were subjected to the same drying and storage procedures as described in *Chapter 3*. The leachates of the gels were centrifuged, and the resulting supernatants were collected for further ion concentration analysis.

Table 4.1. Chemical composition (wt.%) and elemental molar ratios for the synthetic gels.

Ca/Si_Al/Si	CaO	SiO ₂	Al ₂ O ₃	Na ₂ O	Ca/Si	Al/Si	Na/Si
0.8_0.1	41.8	49.4	4.1	4.7	0.90	0.10	0.18
0.8_0.3	37.2	45.9	9.4	7.5	0.87	0.24	0.32
1.2_0.3	48.9	42.3	7.4	1.4	1.24	0.21	0.07

4.2.2 Methods

4.2.2.1 Aqueous phase characterisations

The ion concentrations of Na, Ca, Si, and Al in the leachates were quantified using the ICP-OES instrument as mentioned in *Chapter 3*. The pH of the leachate was measured by a pH meter from Metrohm, Switzerland.

4.2.2.2 Solid phase characterisations

Characterisation of the powdered C-(N-)A-S-H gels, both before and after leaching, was carried out using several analytical techniques: XRF, XRD, Fourier-transform infrared spectroscopy (FTIR) and solid-state magic-angle spinning (MAS) nuclear magnetic resonance (NMR) spectroscopy.

For quantitative determination of the elemental composition of the C-(N-)A-S-H gel after leaching, XRF measurements were conducted using a Panalytical Axios Max WD-XRF spectrometer. Powder XRD measurements were carried out with a Bruker D8 Advance diffractometer, utilising CuK α radiation (1.54 Å), with a step size of 0.02° and a dwell time of 5 s per step. FTIR measurements were performed on a Nicolet™ iS50 FTIR Spectrometer, covering a wavenumber range of 600 to 4000 cm⁻¹, with a resolution of 4 cm⁻¹ and 20 scans were collected per sample.

The single-pulse ²⁹Si MAS NMR spectra were acquired at 79.4 MHz on a Bruker Avance 400 NMR (9.4 T) spectrometer, using a 4 mm Bruker CP/MAS probe with a spinning frequency of ν_R = 10.0 kHz, a 45° excitation pulse ($\gamma B_1/2\pi$ = 71 kHz), a relaxation delay of 30 s, and 5600 scans. ²⁹Si chemical shifts were referenced to tetramethylsilane (TMS), with β -Ca₂SiO₄ (δ (²⁹Si)) = -71.33 ppm [143] as a secondary reference. Deconvolution of the ²⁹Si MAS NMR spectra was carried out by least-squares fitting using a combination of Gaussian and Lorentzian peak shapes, and MATLAB® codes from a recent study [144].

The ²³Na and ²⁷Al MAS NMR spectra were recorded on a narrow-bore Bruker Avance 950/54 μ s² NMR spectrometer (22.3 T), employing a triple-resonance ¹H-X-Y 2.5 mm Bruker CP/MAS probe with a spinning frequency of ν_R = 25.0 kHz, a pulse width of 0.5 μ s for rf field strengths of $\gamma B_1/2\pi$ = 81 kHz and 100 kHz for ²³Na and ²⁷Al, respectively. The measurements included a relaxation delay of 2 s, ¹H decoupling ($\gamma B_2/2\pi$ = 70 kHz) during acquisition, and typically 4096 scans. ²³Na and ²⁷Al isotropic chemical shifts were referenced to external samples of 1.0 M aqueous NaCl and AlCl₃·6H₂O solutions, respectively.

4.3 Results and discussion

4.3.1 Ion concentrations in the leachate

The evolution of ion concentrations for Na, Ca, Al and Si in the leachate from C-(N-)A-S-H gels exposed to water is shown in *Figure 4.1* as a function of the leaching time. Among these ions, Na is the predominant species, followed by Si, Ca, and Al. The concentration of Na stabilises after 1 d (*Figure 4.1A*), indicating that a significant portion of Na rapidly leaches from the gels. Since the fresh gels underwent centrifugation and ultrasonic washing four times, this loss of Na is primarily attributed to the release of charge-balancing Na from the interlayer, rather than from physically absorbed Na on the gel surface. This finding is consistent with [12,58] and also supported by the observation in *Chapter 3*, suggesting that Na is weakly bonded within the basal spacing of C-(N-)A-S-H gels. Additionally, the Na concentration in the leachate exhibits a positive correlation with the initial Na content in the unexposed C-(N-)A-S-H gels (*Table 4.1*). It is noteworthy that this initial Na content decreases with an increasing Ca/Si ratio, while the Al/Si ratio remains fixed, consistent with the results in *Chapter 3*.

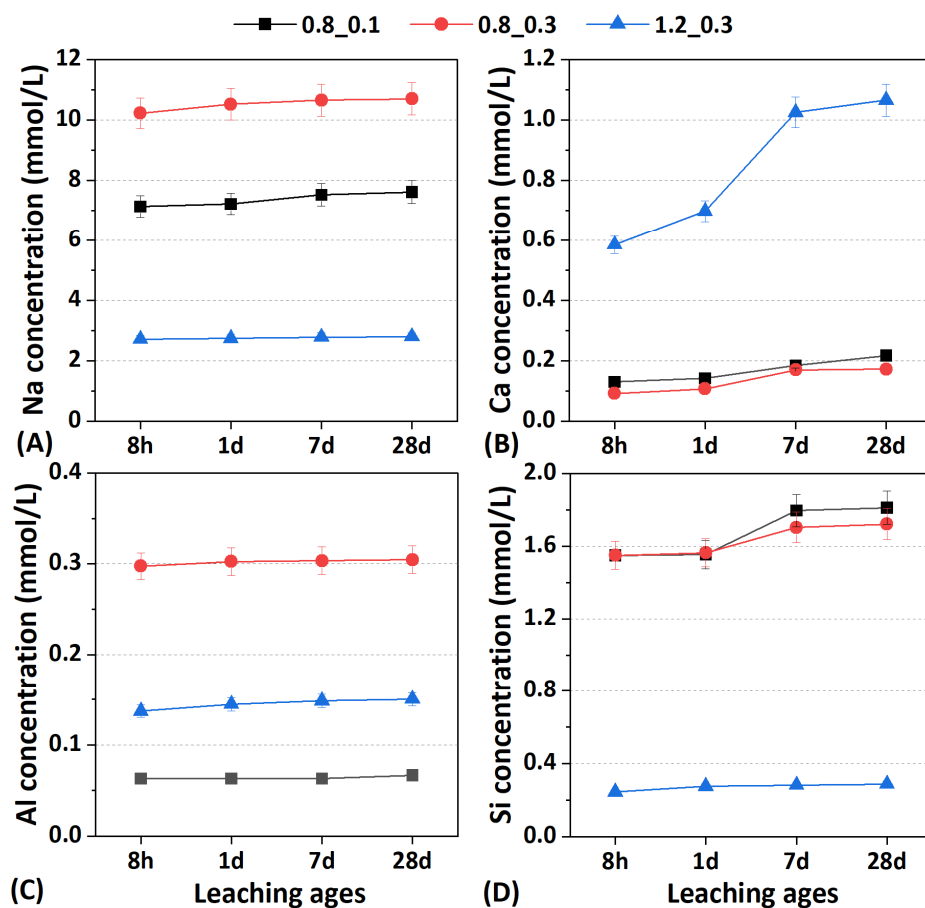


Figure 4.1. Ion concentrations of Na, Ca, Al and Si in the leachates of the three C-(N-)A-S-H gels exposed to water and synthesized with Ca/Si = 0.8 and Al/Si = 0.1 (black squares), Ca/Si = 0.8 and Al/Si = 0.3 (red circles), and Ca/Si = 1.2 and Al/Si = 0.3 (blue triangles). The error bars, showing the standard deviations, are for some of the measurements below the size of the symbols for the measured values.

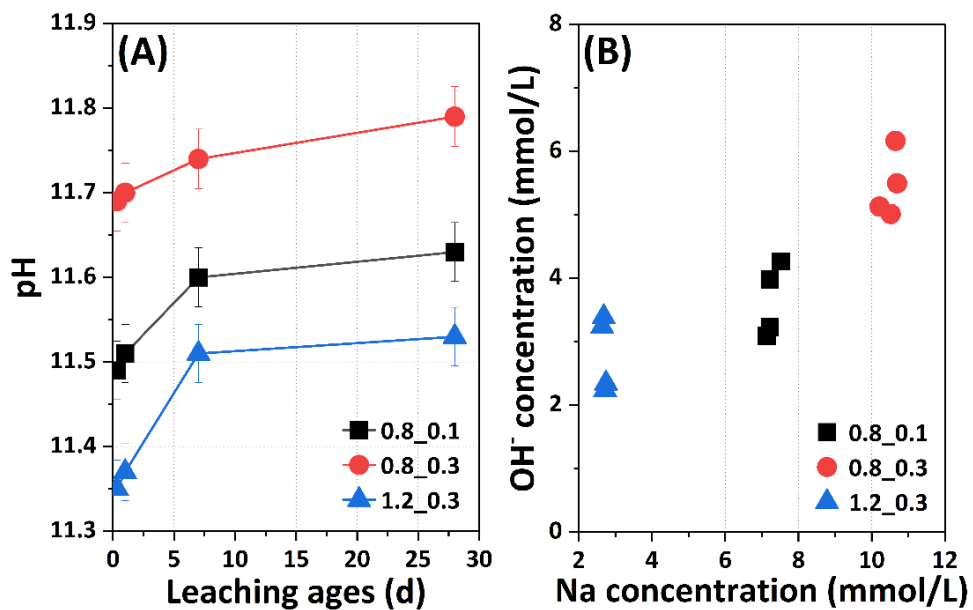


Figure 4.2. (A) pH evolution of the leachates for the three C-(N)-A-S-H gels with exposure time. (B) Correlation between the concentrations of Na⁺ and OH⁻ ions in the leachates for the C-(N)-A-S-H gels at the three different exposure times.

In contrast to Na, Ca ions leach at a slower rate (Figure 4.1B). The concentration of Ca reveals a gradual increase over time for all three samples, with the highest leaching observed in the 1.2_0.3 gel, which has the highest initial Ca content. Dissolution of Al is also detected, with the amount of dissolved Al being proportional to its initial content in the solid phase (Figure 4.1C). The leaching behaviour for Si resembles that of Ca, however, the equilibrium concentration of Si after 28 d is higher than that of Ca in gels with a low Ca/Si ratio (e.g., Ca/Si < 1; Figure 4.1D). The molar ratios of dissolved Ca to Si in the leachates are 3.7 for the 1.2_0.3 gel after 28 d of immersion and 0.1 for gels with a Ca/Si ratio of 0.8. This suggests an incongruent leaching pattern for Ca and Si, where the gel with a higher Ca content experiences a greater loss of Ca alongside a comparatively lower loss of Si. While the initial Na content in the 1.2_0.3 gel is lower than that in the 0.8_0.3 gel, a larger portion of Ca acts as a charge compensator, balancing the negative charges resulting from the substitution of Si by Al in the silicate chains. This is compounded by more disrupted alumino-silicate chains present at higher Ca/Si ratios [145]. Given that interlayer Ca is more susceptible to leaching than Ca within the principal layers, the 1.2_0.3 gel shows a greater loss of Ca.

The pH evolution of the leachates is depicted in Figure 4.2A as a function of exposure time, showing that the pH increases with the dissolution of the C-(N)-A-S-H gels, exceeding 11.5 after 28 d of water immersion. The formation of C-(N)-A-S-H gels involves a series of alkali-consuming reactions, yielding aqueous ions such as Ca²⁺, Na⁺, [Al(OH)₄]⁻, [SiO(OH)₃]⁻ and [SiO₂(OH)₂]²⁻. Conversely, the disintegration of these gels in water is supposed to be an alkali-releasing process. Given that the concentration of Na is much higher than that of Ca, Si, and Al in the leachate, the pH is mainly influenced by the initial Na content in the solids. As a result, gels with higher alkali ion content, such as the 0.8_0.1 and 0.8_0.3 gels, exhibit increased leaching of OH⁻ ions. This is further supported by the data in Figure 4.2B, which confirms a positive correlation between the concentration of OH⁻ in the leachates and the aqueous Na concentration.

4.3.2 Gel composition

The XRD patterns for the three C-(N-)A-S-H gels, prior to water exposure, are shown in *Figure 4.3A*. These patterns exhibit four distinct characteristic peaks of C-(N-)A-S-H gels, which are comparable with the reflections observed for poorly ordered analogues of orthorhombic 14-Å tobermorite (PDF# 00-029-0331) [107]. These peaks are approximately positioned at 2θ values of $5 - 7^\circ$, 17° , 29° , and 32° , resembling the XRD reflections of gels in *Chapter 3*. A detailed description of the three gels can be found in *Section 3.4.1*. After 28 d of water immersion, the XRD result indicates no significant structural changes in the three C-(N-)A-S-H gels, as shown in *Figures 4.3B–D*. However, minor peaks corresponding to calcite are detected in the 1.2_0.3 gel, while such peaks are absent in the 0.8_0.1 and 0.8_0.3 gels. This indicates that the gel with a higher Ca/Si ratio is more susceptible to carbonation. Overall, the XRD results imply that water leaching leads to changes that have a minimal impact on the overall structure of the gels.

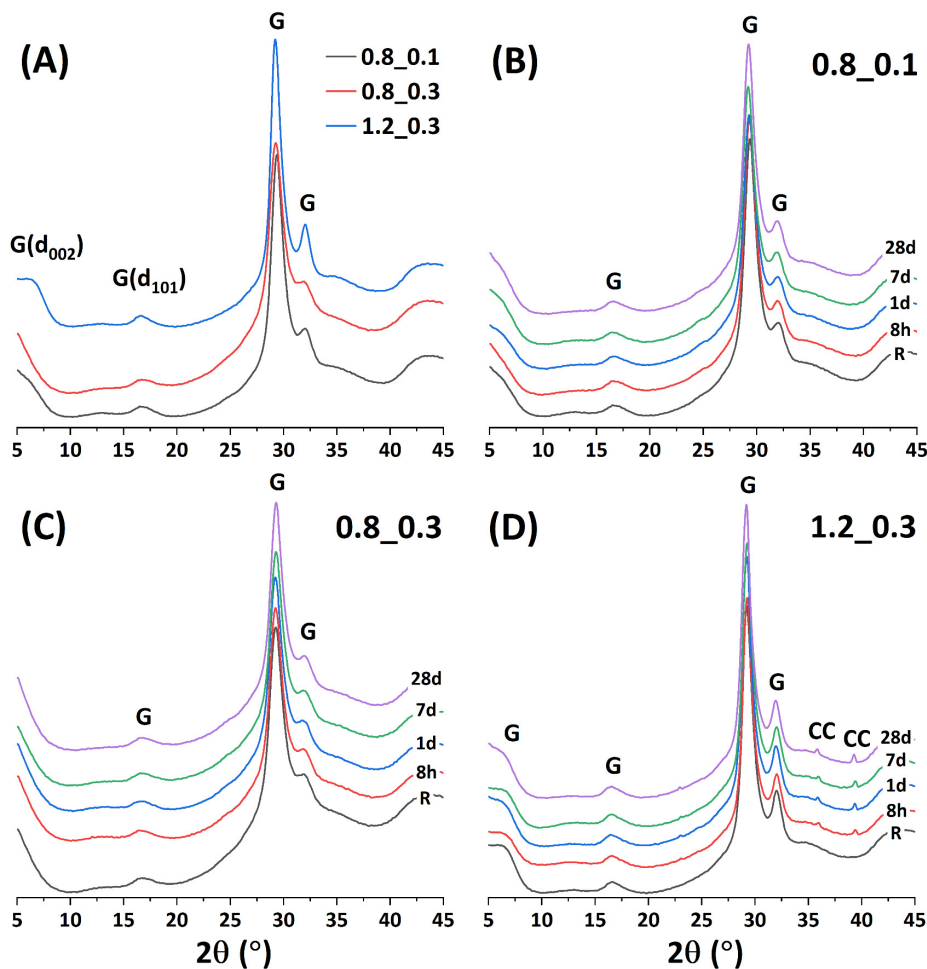


Figure 4.3. (A) Powder XRD pattern of the three unexposed C-(N-)A-S-H gels. (B–D) XRD patterns for the three C-(N-)A-S-H gels at different leaching times. G: C-(N-)A-S-H gel; CC: calcite.

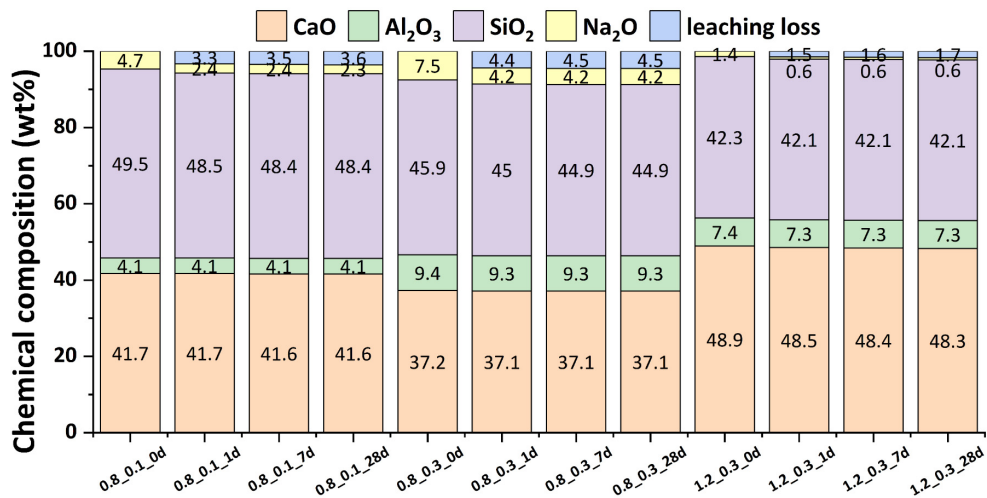


Figure 4.4. Chemical compositions of the C-(N)-A-S-H gels before and after water immersion for 1, 7, and 28 d. The leaching loss is calculated using the ICP results of the leachates for gels.

Changes in the chemical composition of the C-(N)-A-S-H gels over the leaching period are shown in Figure 4.4. It is observed that the two gels with a low Ca/Si ratio experience higher weight loss than the 1.2_0.3 gel, primarily due to higher leaching of Na and Si. The rapid and significant leaching of Na ions is attributed to the higher mobility of Na compared to the other ions, with the highest loss observed for the 0.8_0.3 sample, which has the highest initial Na content. The highest loss in Si content is noted in the gels with the lowest Ca/Si ratio (although small) and may reflect the presence of longer aluminosilicate chains rather than a preference for dimers, as seen in gels with high Ca/Si ratios. Considering that the Ca/Si ratio of C-(A)-S-H phases in cement systems is higher than that of C-(N)-A-S-H gels in AAS systems [53], it is plausible that the leaching stability of C-(N)-A-S-H gels is less robust. Therefore, this result can well explain the phenomenon of gel decomposition in AAS pastes after long-term water immersion [126].

The Ca/Si, Al/Si, and Na/Si ratios for the C-(N)-A-S-H gels, before and after water exposure, calculated from the data in Figure 4.4, are shown in Figure 4.5. No variations in the Ca/Si and Al/Si ratios are observed with exposure time, within the uncertainty limits of the data. For the Al/Si ratios, this indicates a congruent dissolution of Si and Al during water leaching. In terms of the Na/Si ratios, all three C-(N)-A-S-H gels show Na loss within the first day of leaching, after which the values stabilise and remain invariant for the remaining exposure time. As shown in Figure 4.5C, compared with the gels of 0.8_0.1 and 0.8_0.3, the gel with a higher Al/Si ratio appears to have a higher Na/Si ratio before and after leaching. This indicates that the gel with a higher Al incorporation is more effective in immobilising Na, which is consistent with the findings in Chapter 3.

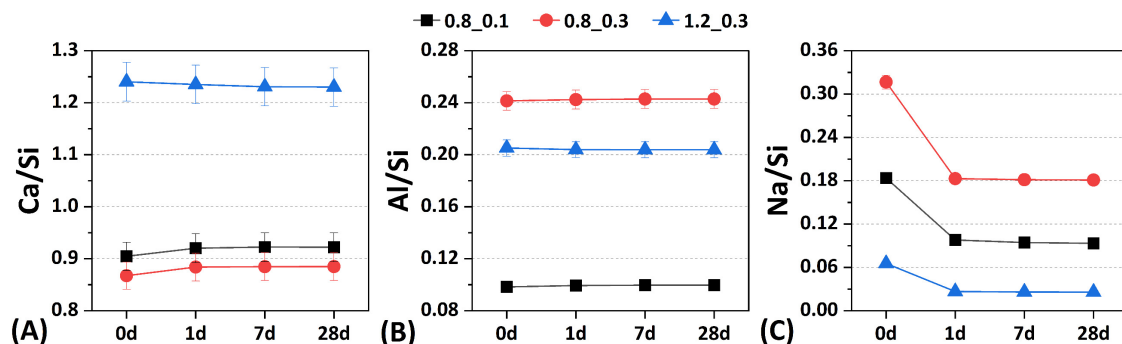


Figure 4.5. Molar Ca/Si, Al/Si and Na/Si ratios for the C-(N)-A-S-H gels at different leaching ages. The error bars, showing the standard deviations, are for some of the measurements below the size of the symbols for the measured values.

4.3.3 Gel structure

4.3.3.1 FTIR

FTIR spectra of the C-(N)-A-S-H gels, both before and after leaching, are shown in Figure 4.6A. The spectra display five distinct regions associated with Si-O bondings. The wavenumbers ranging from 600 to 800 cm⁻¹ correspond to the bending vibrations of Si-O-Si(Al) groups within gels, as well as the vibration of water molecules [146]. The bands in the range from 800 to 1200 cm⁻¹ are attributed to the vibrations of Si-O groups [147,148]. Specifically, the band around 830 cm⁻¹ is linked to the symmetric stretching vibrations of Si-O bonds [149] associated with the Q¹ site within the dreierketten chains [150]. However, no significant differences in these stretching vibrations for the Q¹ sites are observed across the different gels in the FTIR spectra. A minor shoulder, indicated by the asterisk in Figure 4.6A, is positioned at a lower frequency than the Q¹ peak for the 1.2_0.3 gel. This signal was also observed for C-S-H phases by Yan et al. [107], though no assignment has been proposed for it. The band at 883 cm⁻¹ corresponds to the bending vibration of Si-O bonds [151], and the 1.2_0.3 gel exhibits a more pronounced intensity at this wavenumber compared to the other two gels. This difference may be attributed to a more ordered structure in the 1.2_0.3 gel due to its higher Ca content. The most prominent peak around 960 cm⁻¹ represents the asymmetric stretching vibration of Si-O bonds within the “fingerprint region” for Q² sites [107]. It is noteworthy that the shift towards lower wavenumbers for the Q² peak suggests a decrease in the polymerisation degree of the C-(N)-A-S-H gel [148], in agreement with that the 1.2_0.3 gel, which has a high Ca/Si ratio, exhibits a less polymerised structure. The asymmetric Si-O stretching vibration located at 1050 cm⁻¹ is ascribed to the Si-O bond in Q³ sites, with both the 1.2_0.3 and 0.8_0.3 gels displaying higher intensity at this wavenumber compared to the 0.8_0.1 gel. This suggests that gels with higher Al/Si ratios tend to have more crosslinked structures, aligning with earlier findings on AAS materials [62].

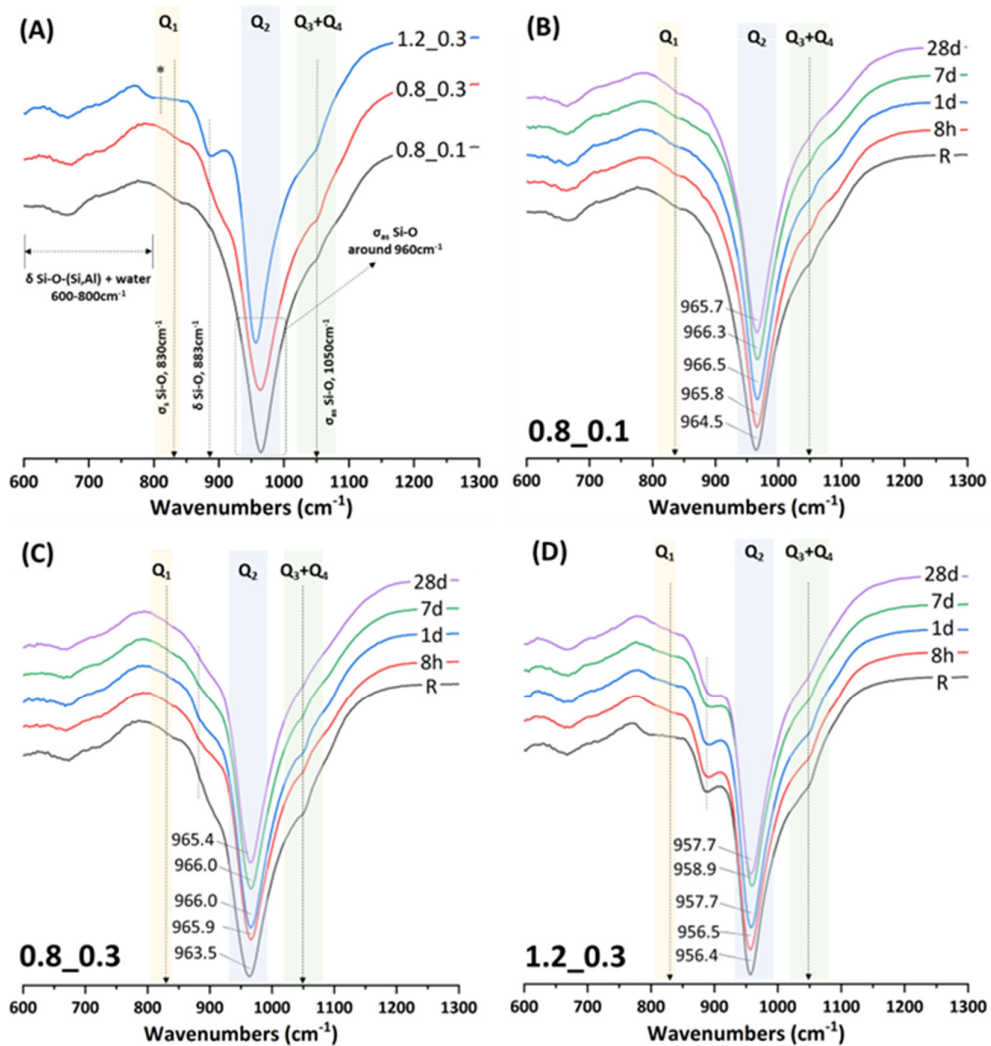


Figure 4.6. (A) FTIR spectra of the C-(N-)A-S-H gels before leaching. (B–D) FTIR spectra of the three C-(N-)A-S-H gels following the time evolution of leaching. δ indicates bending vibrations, σ_{as} asymmetric stretching vibrations, and σ_s symmetric stretching vibrations. R indicates the reference samples before leaching, whereas the other spectra are denoted by their leaching times (8 h, 1 d, 7 d, and 28 d).

The time evolution of leaching is illustrated by the FTIR spectra in Figures 4.6B–D for the three C-(N-)A-S-H gels. These spectra show no additional signals compared to those before leaching, indicating that no new phases are formed. Instead, variations in intensity reflect minor structural rearrangements, predominantly involving Qⁿ species, within the C-(N-)A-S-H gels. The signals from the Q¹ sites remain very similar across all leaching times, while progressive changes are evident for the Q² sites, particularly around the peak at 960 cm⁻¹, as shown in Figure 4.7. All three C-(N-)A-S-H gels display similar changes in frequencies with leaching time, characterised by an initial increase (from 1 to 7 d), followed by a gradual decrease until 28 d. This pattern suggests that the polymerisation degree of the C-(N-)A-S-H gels initially increases and then decreases during 28 d of water immersion, likely due to the loss and redistribution of cations during leaching. However, the decrease in wavenumbers upon prolonged leaching is smaller than the initial increase observed during the first days, indicating that the gels after 28 d of leaching are more cross-linked as compared to the structures before leaching.

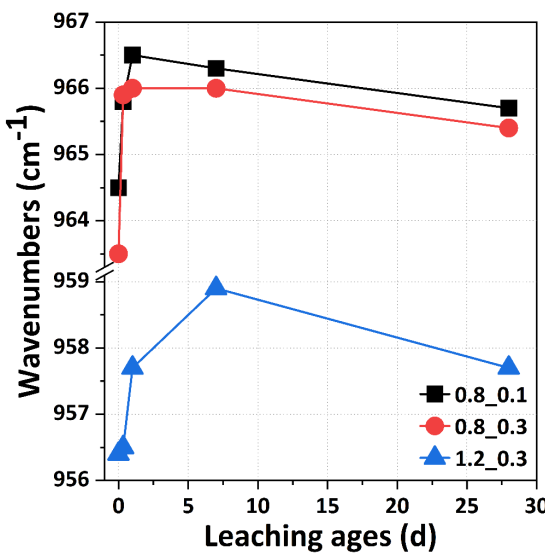


Figure 4.7. Changes of the FTIR wavenumbers for the asymmetric stretching vibration of Si-O bonds in Q^2 sites of the C-(N-)A-S-H gels as a function of the leaching time.

4.3.3.2 NMR

The low crystallinity of the C-(N-)A-S-H gels poses challenges for quantitative structural analysis using conventional powder XRD and FTIR techniques. For such phases that lack long-range order, solid-state NMR can often provide more detailed insights into the local structure. Through the use of ^{29}Si , ^{27}Al , and ^{23}Na MAS NMR, it is possible to quantitatively analyse the basic dreierketten chains of silicate units, as well as the presence of tetrahedrally, fivefold and octahedrally coordinated Al species, and Na ions associated with the structures [56,145,150]. This approach may lead to models that consider the nearest coordination environments, as schematically illustrated in Figure 4.8 for a C-(N-)A-S-H gel.

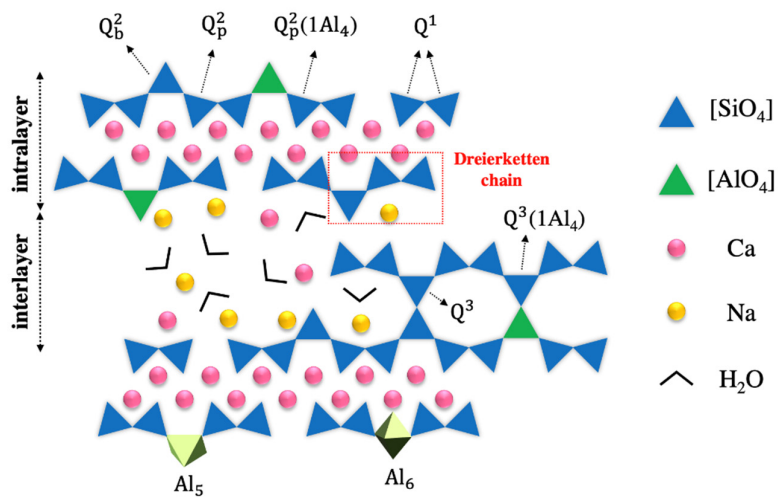


Figure 4.8. Schematic model for the structure of a C-(N-)A-S-H gel based on the defect tobermorite model and emphasising the local environment of various silicate and aluminate species. It should be noted that five- (Al_5) and six-fold (Al_6) coordinated Al are only present in gels with high Ca/Si ratios (i.e., $\text{Ca/Si} \geq 1.2$ [152]).

²⁹Si MAS NMR

The ²⁹Si MAS NMR spectra of the C-(N-)A-S-H gels before and after 28 d of water immersion are shown in *Figure 4.9*. The spectra are dominated by three resonances at approximately -79.5 ppm, -82 ppm, and -85 ppm, which correspond to the Q¹, Q²(1Al₄), and Q_p² sites, respectively, of the basic structure (*Figure 4.8*). Additionally, less resolved peaks and shoulders are observed at lower frequencies, likely originating from Q³(1Al) (~ -90 ppm) and Q³ sites (-93 ppm) [12]. The two Q³ sites have also been reported in ²⁹Si NMR spectra of Al-substituted natural tobermorite [153,154] and synthetic C-(N-)A-S-H phases with a low Ca/Si ratio [57,59,155]. It should be noted that a second paired site (Q_{pb}²; -86.7 ppm), originating from paired sites within the middle of octameric or longer silicate units, has been observed in synthetic C-(A-)S-H phases [145]. However, no indications of this site are seen in the current ²⁹Si NMR spectra (*Figure 4.9*), so it has not been included in the analysis. Following the defect tobermorite model for C-(N-)A-S-H gels and C-(A-)S-H gels [145], a resonance from the bridging sites (Q_b²) sites is also present at roughly -83 ppm and should exhibit half the intensity of the Q_p² sites.

The individual ²⁹Si NMR spectra were simulated using resonances from the Q¹, Q_p², Q_b², Q²(1Al₄), Q³ and Q³(1Al₄) sites, following the optimised simulation approach previously described for synthetic C-(A-)S-H phases [145]. This includes maintaining the intensity relation I(Q_p²)/I(Q_b²) = 2. The simulations provide relative intensities for the six distinct SiO₄ sites, enabling the estimation of the mean chain length (MCL) of alumino-silicate tetrahedra in the synthetic gels before and after leaching. For the MCL calculation, both Al₄ and Si in Q³ sites were included, but only on the side of the chain to which they belong. The MCL is given by the following expression:

$$MCL = \frac{2 \left[Q^1 + Q^2 + \frac{3}{2} Q^2(1Al_4) + Q^3 + Q^3(1Al_4) \right]}{Q^1} \quad (4.1)$$

where Q² = Q_p² + Q_b². *Figure 4.10* shows the intensity fractions of the different silicate environments, based on the optimised simulations illustrated in *Figure 4.9*, resulting in the MCL values listed in *Table 4.2*.

The Q_p² resonance dominates the spectra of the C-(N-)A-S-H gel with a Ca/Si ratio of 0.8, reflecting the presence of longer silicate chains at this low Ca/Si ratio. Moreover, the higher Al/Si ratio of 0.3 in two of the gels is clearly reflected in the increased relative intensity for the Q²(1Al₄) peak, which increases before leaching for the 0.8_0.1, 0.8_0.3, and 1.2_0.3 gels, corresponding to the Al/Si ratios of the gels. Comparing the ²⁹Si MAS NMR spectra of the C-(N-)A-S-H gels before and after leaching reveals minimal changes (*Figure 4.9*), indicating that 28 d of water immersion does not significantly alter the main structure of C-(N-)A-S-H gels. The intensity of the Q² peaks (*Figure 4.10*) shows a slight increase in all synthetic gels after water immersion, with a corresponding decrease in Q¹ sites. These changes are also reflected by an increase in MCL after leaching (*Table 4.2*), attributed to a decalcification of the C-(N-)A-S-H gels, since an increase in MCL corresponds to a decrease in the Ca/Si ratio. The decalcification is further supported by a shift in the Q_p² sites from about -85.0 ppm to -85.4 ppm after leaching, consistent with previous ²⁹Si NMR studies on C-S-H phases synthesised at different Ca/Si ratios [156]. Interestingly, the increase in MCL after leaching is notably higher for the C-(N-)A-S-H gel with Al/Si = 0.1 compared to those with Al/Si = 0.3. This suggests that

the presence of Al_4 in the chain structure of C-(N)-A-S-H gels partly hinders decalcification during leaching, possibly due to the substitution of Si by Al in the chains, which reduces the overall charge and allows for the binding of Ca ions.

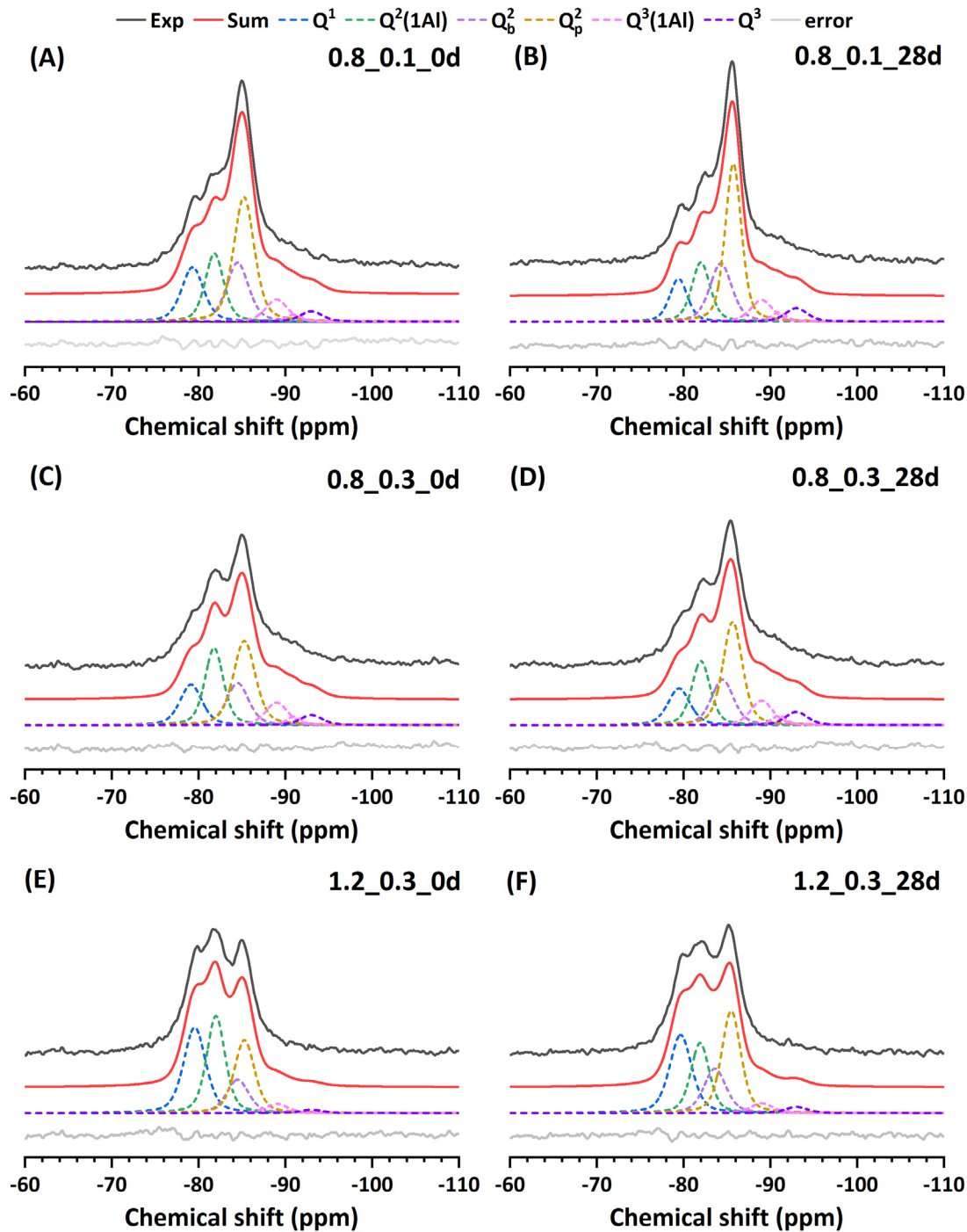


Figure 4.9. ^{29}Si MAS NMR spectra (9.4 T, $\nu_R = 10.0$ kHz) of the three C-(N)-A-S-H gels before leaching (0 d) and after water immersion for 28 d. The experimental spectra are shown in black, optimised simulated spectra in red, and difference spectra in grey.

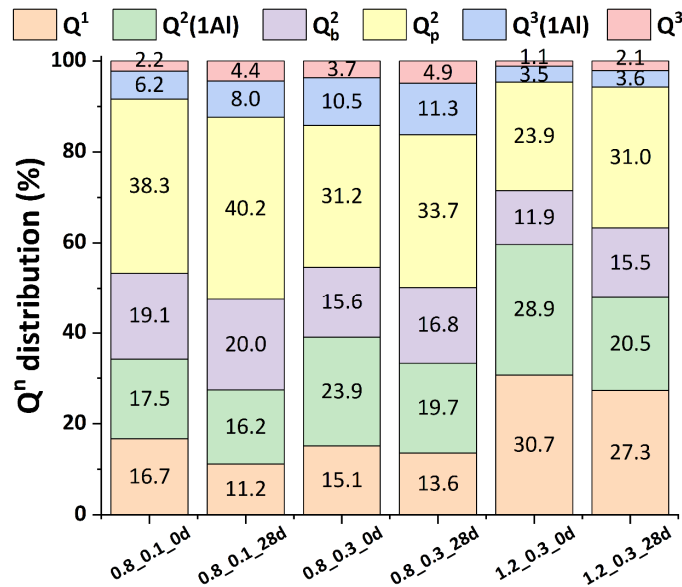


Figure 4.10. Distribution of intensities for the distinct SiO_4 environments for the C-(N-)A-S-H gels before and after 28 d of leaching, as determined from simulations of the ^{29}Si NMR spectra in Figure 4.9.

Table 4.2. Mean chain length (MCL) of aluminosilicate tetrahedra for the C-(N-)A-S-H gels before and after 28 d of leaching as determined from Equation 4.1 using the simulated intensities of the ^{29}Si MAS NMR spectra

	0.8_0.1_0d	0.8_0.1_28d	0.8_0.3_0d	0.8_0.3_28d	1.2_0.3_0d	1.2_0.3_28d
MCL	13.0	19.2	14.8	16.1	7.5	8.1

The presence of Q^3 and $Q^3(1Al)$ sites is consistently observed for all three gels before leaching (Figures 4.10), in agreement with earlier findings from ^{29}Si NMR studies of C-(N-)A-S-H gels in AAS pastes [62]. Notably, the gel with a Ca/Si ratio of 0.8 exhibits higher content of Q^3 and $Q^3(1Al)$ sites, indicating that a lower Ca/Si ratio promotes the formation of more cross-linked C-(N-)A-S-H gel structures. Furthermore, a slight increase in Q^3 and $Q^3(1Al)$ intensities is observed after 28 d of exposure, reflecting increased cross-linking as a result of decalcification during the leaching period.

^{27}Al MAS NMR

The ^{27}Al MAS NMR spectra for the synthetic C-(N-)A-S-H gels, both before and after 28 d of leaching, are shown in Figure 4.11. These spectra reveal distinct centerband resonances for Al in tetrahedral (50 – 80 ppm), five-fold (30 – 50 ppm) and octahedral (0 – 20 ppm) coordination. No indications of secondary phases, as confirmed by powder XRD results (Figure 4.3). The spectra are dominated by tetrahedrally coordinated Al, evidenced by a narrow peak at 74.5 ppm for the 1.2_0.3 gel, and a broader resonance at roughly 65 ppm for all samples. Very low-intensity resonances corresponding to five-fold and octahedrally coordinated aluminium (Al_5 and Al_6) are observed in the Ca/Si = 0.8 gel, which aligns with expectations based on recent studies of C-(A-)S-H phases [145,152]. In contrast, these resonances are slightly higher in intensity in the Ca/Si = 1.2 gel. This observation supports the approach used

for simulating the ^{29}Si NMR spectra (Figures 4.9 and 4.10), which does not account for specific peaks for Si neighbouring Al_5 or Al_6 sites within the alumino-silicate chains.

The ^{27}Al NMR spectra after 28 d of water exposure exhibit very similar intensities to those observed before leaching, supporting the findings in Figure 4.4 that Al does not leach out from the C-(N)-A-S-H gel structure. The Al_5 and Al_6 resonances are unaffected by leaching, while small shifts to lower frequencies are observed for the broad Al_4 resonances. Previous studies have reported the presence of multiple tetrahedrally coordinated Al sites in C-(A)-S-H phases with Ca/Si ratios ranging from 0.6 to 1.4 and Al/Si ratios up to 0.3 [145,155]. In a recent study [145], three different Al_4 sites were identified using ^{27}Al MAS and multiple-quantum (MQ) MAS experiments at 14.1 and 22.3 T, all located in bridging site but charge-balanced by different ions: $\text{Al}_4(\text{a})$ (centre of gravity $\delta_{\text{cg}} = 75.4$ ppm at 22.3 T) – charge-balanced by a nearby Na ion, $\text{Al}_4(\text{c})$ ($\delta_{\text{cg}} = 66.1$ ppm) – an Al site charge-balanced by $\frac{1}{2}$ Ca ion and H_3O^+ , and $\text{Al}_4(\text{d})$ ($\delta_{\text{cg}} = 61.3$ ppm) – charged-balanced by interlayer Ca ions, either alone or in conjunction with Na ions. In an earlier study [155], it was suggested that the Al resonance at ~ 74 ppm represents Al in a bridging site charge-balanced by Al_5 and Al_6 species in the interlayer or on the surface of the C-(A)-S-H gels, while the resonances at ~ 66 ppm and ~ 58 ppm originate from AlO_4Q^2 (*i.e.*, a bridging site) and AlO_4Q^3 (*i.e.*, a cross-linked site) units, respectively. The narrow resonance at 74.5 ppm, seen in all spectra before leaching and most clearly for the 1.2_0.3 gel, is assigned to the $\text{Al}_4(\text{a})$ site. In contrast, the broader Al4 peak may be a combination of resonances from $\text{Al}_4(\text{c})$, $\text{Al}_4(\text{d})$, and cross-linked Q^3 Al sites. Upon leaching, the intensity of the $\text{Al}_4(\text{a})$ site clearly reduces in the two gels with Ca/Si = 0.8.

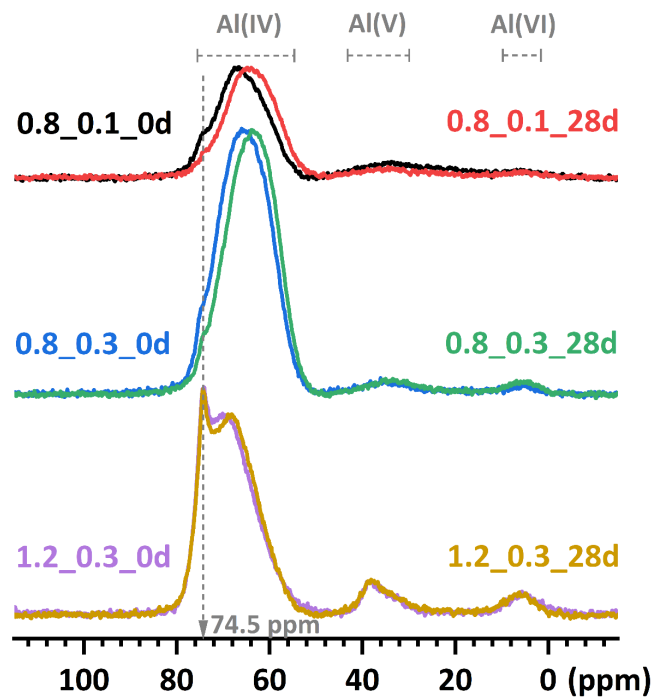


Figure 4.11. ^{27}Al NMR spectra (22.3 T, $\nu_R = 25.0$ kHz) of the C-(N)-A-S-H gels before (0 d) and after 28 d of water immersion (28 d).

Moreover, the shift of the main resonance to a lower frequency (from 65.4 ppm to 64.3 ppm) for the $\text{Ca/Si} = 0.8$ gels suggests a larger interaction with Ca ions in the interlayer, supporting the assignment of the $\text{Al}_4(\text{c})$ and $\text{Al}_4(\text{d})$ sites. Similarly, for the C-(N-)A-S-H gel with Ca/Si of 1.2, a shift from 70.1 ppm to 68.6 ppm is observed for the dominant broad resonance after leaching. This shift may reflect an increased role of Ca ions in charge balancing the Q^2 and Q^3 AlO_4 sites as Na ions are removed from the interlayers. It is noted that there are no discernible changes in the relative intensities for the Al_5 and Al_6 resonances before and after leaching, indicating that these Al species remain unaffected by water immersion, particularly at relatively low Ca/Si ratios.

^{23}Na MAS NMR

The ^{23}Na NMR spectra of the gels before and after 28 d of water immersion (Figure 4.12) show a featureless resonance for the central transition around -2 ppm, with no apparent second-order quadrupolar broadening effects. This might reflect that the spectra are acquired at a very high magnetic field (22.3 T), eventually in combination with mobility or dynamic processes for the Na ions present in the C-(N-)A-S-H gels, which average out the second-order quadrupolar interaction. The ^{23}Na NMR spectra are closely aligned with those reported in a recent study on synthetic C-(A-)S-H phases [145]. The observed resonance can be assigned to outer-sphere hydrated sodium ions ($[\text{Na}(\text{H}_2\text{O})_{6-x}]^+$, $x \leq 6$), which are either adsorbed onto the surface of the C-(A-)S-H particles or present in the interlayer of the structure. A small shift to lower frequency is observed after leaching in the two $\text{Ca/Si} = 0.8$ samples, which may reflect a reduction in the average number of water molecules surrounding the Na ion. This could be due to stronger binding to silanol groups in the C-(A-)S-H structure.

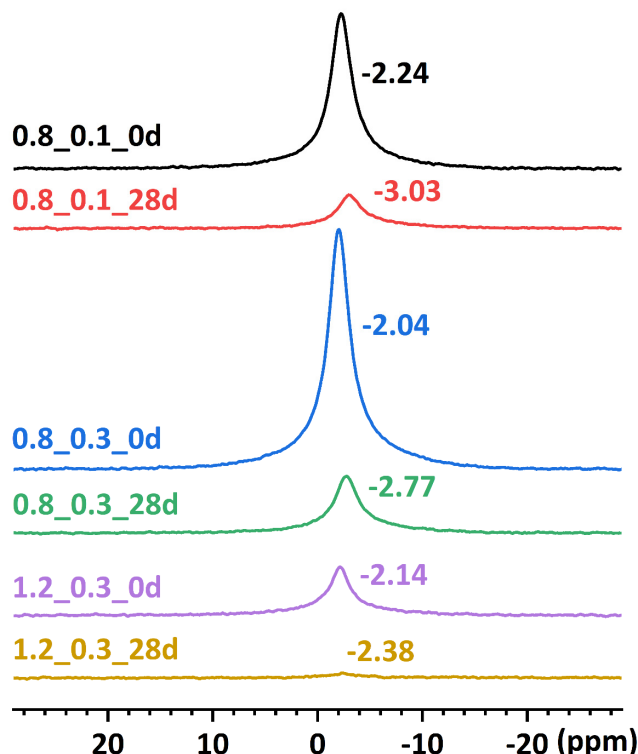


Figure 4.12. ^{23}Na NMR spectra (22.3 T, $\nu_R = 25.0$ kHz) of the C-(N-)A-S-H gels before (0 d) and after 28 d of water immersion (28 d).

The ^{23}Na NMR spectra of the gels after leaching show a significant decrease in intensities, clearly indicating that a large portion of sodium is removed from the C-(N-)A-S-H structure upon water immersion, which is consistent with the bulk XRF measurements (*Figure 4.4*). The ^{23}Na NMR intensities reveal that approximately 70% of Na ions (quantified from ^{23}Na NMR spectra) leached out from the C-(N-)A-S-H gels with $\text{Ca/Si} = 0.8$, and nearly all Na was removed for the $\text{Ca/Si} = 1.2$ gel.

4.4 Summary and perspectives

The leaching of ions during water immersion and consequent chemical changes in the gels are accomplished by structural changes of the C-(N-)A-S-H gels, as clearly reflected in the FTIR and solid-state NMR results. The polymerisation degree of the gels, indicated by the MCL values (*Table 4.2*), increases after water immersion as a result of Na leaching. While the leaching process for conventional C-(A-)S-H gels has been investigated in recent studies [128], the specific impact of Na leaching on structural changes of C-(N-)A-S-H gels in AAS systems has not been thoroughly examined. Based on the results of this study, a mechanism is proposed, schematically presented in the model in *Figure 4.13*.

In Na-free C-(A-)S-H systems, Ca serves as the primary charge compensator in the interlayer. The introduction of Na can partially take over the charge-compensating role of Ca, resulting in a gel structure where Na is present in the interlayers [56,106,155,157] (*Figure 4.13A*). The Ca ions that are substituted by Na as charge compensators can take part in the formation of the Ca-O sheets, resulting in a reduced fraction of Q^2 sites and, consequently, shorter average alumino-silicate chains [158]. Upon exposure to water, Na ions are rapidly released from the interlayer, which triggers a structural reorganisation where some Ca ions from the Ca-O sheets migrate to the interlayer to balance the charges (*Figure 4.13B*). This mechanism is supported by the ^{27}Al NMR spectra (*Figure 4.11*), where a small shift of the Al(4) resonance to a lower frequency is observed upon leaching, which can be assigned to increasing coordination to Ca ions in the second-nearest coordination sphere. The reduction of intralayer Ca ions may explain the increase in Q^2 sites [16] and the increased MCL values (*Table 4.2*) observed after leaching, as also evidenced by the increase in wavenumbers for the Q^2 sites in the FTIR spectra at the early stages (*Figure 4.6*).

The results from the work provide novel perspectives for understanding the process of Na leaching during water immersion. It is widely recognised that the MCL or polymerisation degree of gels is dependent on the Ca content in the intralayer. Previous studies [63,159] have reported that a reduction in intralayer Ca results in notable volume deformation and a decline in mechanical properties, commonly occurring after the leaching of interlayer Ca. The results of this study suggest that the leaching of interlayer Na can trigger a simultaneous restructuring of intralayer Ca, which affects its properties, following earlier reported results [52,54].

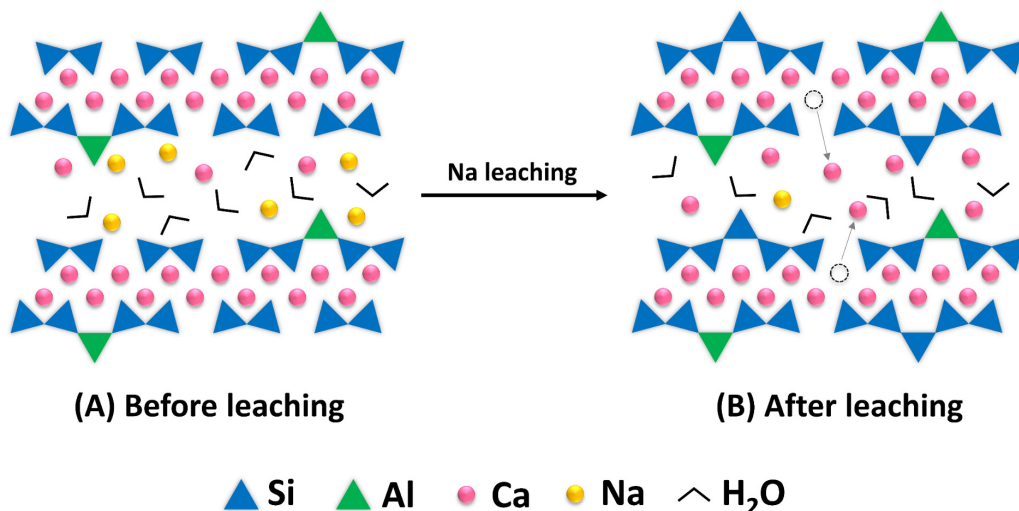


Figure 4.13. A schematic model for the impact of Na leaching on the structure of C-(N-)A-S-H gels as a result of water immersion. The oxygens in the Ca-O sheets are not shown. The SiO₄ and AlO₄ tetrahedra are shown as triangles.

4.5 Conclusions

In this chapter, the chemical composition and structural transformations of C-(N-)A-S-H gels subjected to water immersion were investigated. The results indicated that leaching in these synthetic C-(N-)A-S-H gels was a rapid process, stabilising within seven days and with minimal formation of secondary phases, except for a minor presence of calcium carbonate in the leached gel with a high Ca/Si ratio of 1.2. Na leached occur rapidly within a few hours, with approximately 70% of Na removed from gels with a Ca/Si ratio of 0.8 after 28 d of immersion. In contrast, the leaching of other elements was negligible, with the most notable being Ca, particularly in the gel with a higher Ca/Si ratio.

Interestingly, while the gel with the Ca/Si ratio of 1.2 experienced only limited decalcification during water immersion, significant Na loss was observed for all gels. Both processes contributed to an increased polymerisation of aluminosilicate tetrahedra within the gel structure. I proposed that the mechanism underlying the impact of Na leaching on the gel structure was related to the change in charge compensation within the interlayer of the C-(N-)A-S-H gels. As Na leached out from the interlayer, calcium progressively took the role of charge compensator, resulting in structural modifications. This mechanism was supported by the findings from ²³Na, ²⁷Al, and ²⁹Si NMR, as well as from FTIR measurements.

Chapter 5

Leaching mechanisms of AAS pastes

5.1 Introduction

In *Chapter 2*, it is highlighted that the mechanical properties and durability of AAS materials diminish when exposed to humid environments, with leaching identified as a primary contributing factor. However, the specific mechanisms by which leaching affects the performance of AAS materials remain inadequately understood. In particular, theoretical explanations are lacking on how leaching influences the reaction kinetics of slag, the evolution of phase assemblage, paste chemistry and microstructural changes in AAS pastes over prolonged immersion periods.

Building on the findings from *Chapters 3* and *4*, where the leaching behaviour of synthetic C-(N-)A-S-H gels was examined, this chapter investigates the leaching behaviour of AAS pastes as a composite system. Samples were prepared using sodium hydroxide (NH) and sodium silicate (NS) solutions, cured for 1 d, and then immersed in tap water for up to 90 d. The ion concentration of leachate and pore solution, the degree of slag reaction, phase assemblages, paste chemistry, pore structure, and compressive strength of AAS pastes under sealed and immersed conditions were compared. The chapter concludes with a discussion on the degradation mechanisms of AAS paste due to water immersion, providing insights into their long-term durability in practical applications.

5.2 Materials and methods

5.2.1 Raw materials and mixture design

The slag used in this chapter was supplied by ORCEM in the Netherlands. The chemical composition of slag, determined through X-ray fluorescence (XRF) using a Panalytical Axios Max WD-XRF spectrometer, is presented in *Table 5.1*. A laser diffraction analyser was employed to assess the particle size distribution of the slag, which ranged from 0.1 to 50 μm with a median particle size (d_{50}) of 17.88 μm .

For activator preparation, NaOH solution (solid content of 50 wt.%) and Na_2SiO_3 solution (100 g containing 8.25 g Na_2O , 27.5 g SiO_2 , and 64.25 g water) were used. The NH activator was prepared by diluting the NaOH solution with demineralised water. The NS activator was prepared by combining Na_2SiO_3 solution, NaOH solution, and demineralised water. The specific mixture proportions are listed in *Table 5.2*. NH- and NS-based pastes, both with a consistent Na_2O (in the activator) -to-slag mass ratio of 5%. The mixing process was conducted using a Hobart mixer, with activators added to the slag during 1 min of low-speed mixing, followed by 1 min at high speed to ensure homogeneous blending.

Table 5.1. Chemical composition of slag determined by XRF (%).

	CaO	Al ₂ O ₃	SiO ₂	MgO	Fe ₂ O ₃	SO ₃	K ₂ O	TiO ₂	other	LOI
Slag	38.28	13.9	32.19	9.52	0.31	1.52	0.51	1.27	1.17	1.33

LOI: loss on ignition at 1000 °C

Table 5.2. Mixture proportions of AAS pastes.

	Slag (g)	SiO ₂ (mol)	Na ₂ O (mol)	Water (g)	w/b	Ms
NH	1000	0	0.8	430	0.43	0
NS	1000	0.8	0.8	430	0.43	1

Notes: w/b = water-to-binder ratio; Ms = SiO₂/Na₂O molar ratio (silicate modulus)

An outline of the experimental procedure is provided in *Figure 5.1*. The experiments in this chapter were designed to simulate severe environmental conditions to which AAS pastes may be exposed. To achieve this, samples intended for micro-characterisation were initially sealed in plastic tubes for 1 d, and then crushed into smaller pieces (2 – 4 mm) before immersion. For compressive strength testing, AAS specimens were sealed at room temperature (20 °C) for 24 h. After this initial curing period, half of the hardened specimens were demoulded and immersed in water, while the other half continued curing under sealed conditions. Both sealed and water-immersed samples were cured for up to 90 d. For the ion concentration measurements in leachate and pore solution, distilled water was used to avoid any interference from ions present in tap water. For all other experiments, tap water was used as the immersion medium, which was refreshed weekly.

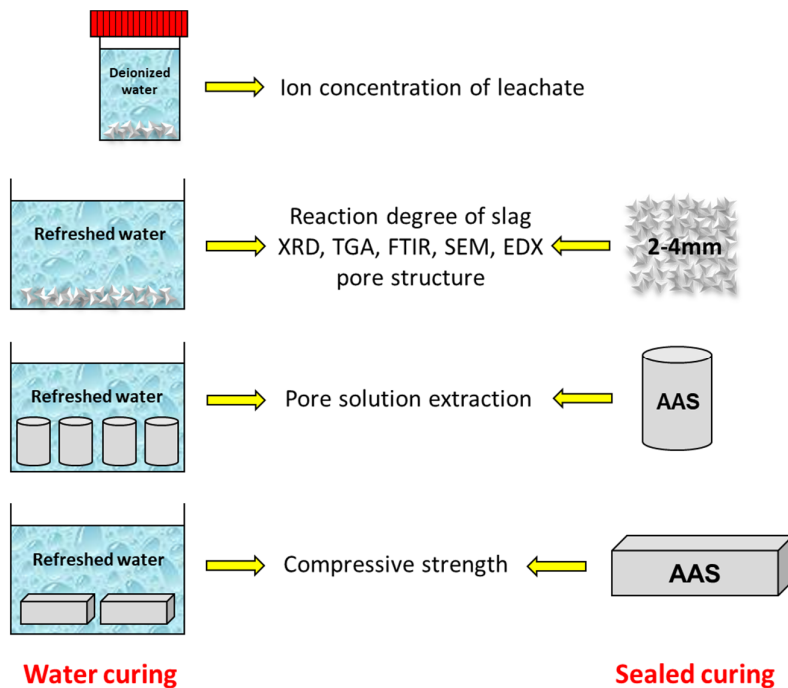


Figure 5.1. Experimental workflow for this chapter. The characterisation methods include ICP-OES, XRD, thermogravimetric analysis (TGA), FTIR, and scanning electron microscope (SEM) with energy-dispersive X-ray spectroscopy (EDX).

5.2.2 Experimental methods

5.2.2.1 Ion concentration measurements

The ion concentration in the pore solution of hardened AAS samples was extracted using the steel-die method [160]. A pressure of up to 350 MPa was applied to compress the samples (about ϕ 25 mm \times 40 mm, as shown in *Figure 5.1*) cured under both sealed and water-immersed conditions. The extracted pore solution was then filtered through the Whatman 41 filter paper (20 μm) to remove any particulates. For ICP-OES analysis, the filtered solution was diluted with 0.2 vol% nitric acid, allowing for accurate measurement of Na, K, Ca, Al and Si ions using a PerkinElmer Optima 5300DV ICP-OES spectrometer. The concentration of OH⁻ was determined by titration with 0.1 mol/L hydrochloric acid, using phenolphthalein as an indicator. For the leaching tests, 10 g of small piece samples (2 – 4 mm) were placed in 100 g of distilled water in sealed plastic bottles at a constant temperature of 20 °C. The bottles were shaken twice a week. Leachate samples were collected after immersion periods of 7, 28, 60 and 90 d. Ion concentrations in the supernatant were measured using the ICP-OES instrument, and the pH was measured by titration.

5.2.2.2 Selective dissolution

The degree of slag reaction in AAS pastes was determined using the selective dissolution [161], as SEM image analysis is unsuitable for these samples after water immersion. Leaching in AAS pastes is depth-dependent, causing variability that prevents obtaining a homogeneous sample for SEM analysis. Thus, a selective dissolution approach was adopted to measure the overall reaction degree of slag in AAS pastes. The selective dissolution method, established in previous studies [162–164], allows for the chemical extraction of reaction products and unhydrated cement pastes, leaving behind only unreacted slag. In this chapter, a modified version of this method, known as the “salicylic acid-methanol” (SAM) extraction, was employed [165]. In this method, well-ground and reaction-arrested powdered samples (0.3 g) were mixed with 30 ml of methanol and 2 g of salicylic acid. The mixture was stirred for 1 h and then filtered. The insoluble residue was washed several times with deionised water and methanol until a neutral pH was achieved. Finally, the residue was dried at 105 °C until it reached a constant mass. The reaction degree of slag was calculated based on the mass loss after SAM extraction. Note that certain components in AAS pastes, such as calcium carbonate and hydrotalcite, are resistant to dissolution by the SAM method. Therefore, TGA was used for a more accurate determination of the reaction of slag. Each mixture was tested in quadruplicate to ensure reproducibility.

5.2.2.3 XRD, TGA and FTIR

XRD and TGA were employed to identify the phase assemblages of AAS pastes under both sealed and water-immersed conditions, while FTIR was utilised to examine changes in the gel structure in AAS pastes with and without leaching. Fine powdered samples were used for all three analyses, and the reaction of slag was stopped using the solvent exchange method [166]. The samples were ground in a mortar with isopropanol for 0.5 h, and then the powder was allowed to stand for 15 min to ensure complete solvent exchange. The samples were then filtered using filter paper and a vacuum pump, with absolute alcohol used to wash the samples multiple times during filtration. Diethyl ether was used during a final wash, leaving the powder in an almost dry state. The powder was then transferred into a glassy dish and stored in a drying oven at 40 °C for 10 min, followed by being placed in a vacuum or desiccator.

These pretreatments remove all free water from the sample, leaving only the chemically bound water. XRD was conducted using a Bruker D8 Advance diffractometer with CuK α (1.54 Å) radiation. The reaction-arrested powdered samples were scanned between 5° and 70°, with a step size of 0.02° and a dwell time of 5 s per step. TGA was carried out with a NETZCH TG-449-F3-Jupiter. The powdered samples were heated from 40 °C to 1000 °C at a rate of 10 °C /min in an argon atmosphere. FTIR was conducted using a Spectrum TM 100 Optical ATR-FTIR spectrometer with the wavelength of the spectrum ranging between 600 and 4000 cm⁻¹ with a resolution of 4 cm⁻¹.

5.2.2.4 SEM and EDX

SEM and EDX were performed to characterise the morphology and chemical composition of AAS pastes. A FEI Quanta FEG 650 electron microscope equipped with a Thermoscientific MagnaRay wavelength-dispersive spectrometer (WDS) was used for these analyses. The vacuum-dried samples were impregnated using a low-viscosity epoxy resin. After 1 d of drying, the sample was polished first with sandpaper with a grit size from 30 µm to 10 µm and then with a polishing cloth and diamond pastes (6 µm to 1 µm) to achieve a smooth surface. To improve the surface conductivity and imaging quality, a carbon coating was applied before SEM analyses. SEM imaging was performed in backscattered electron (BSE) mode with an acceleration voltage of 15 kV under low vacuum conditions. Point analysis of pastes was applied, with 60 points selected to ensure comprehensive and representative data.

5.2.2.5 Pore structure characterisation

Due to the limitation of mercury intrusion porosimetry (MIP) in detecting ultra-fine nanopores present in NS pastes, nitrogen absorption (NA) testing was used to characterise the pore structure within the range of 0.3 to 300 nm. The analysis was conducted on 2–4 mm reaction-arrested piece samples using a Micrometrics Gemini VII 2390 instrument, with relative pressures ranging from 0.05 to 0.998.

5.2.2.6 Compressive strength

The compressive strength of AAS pastes was measured according to NEN-196-1 [167], with a loading speed of 2.4 kN/s. Six replicate samples were tested for each mixture to calculate an average value.

5.3 Results and discussion

5.3.1 Ion concentrations

5.3.1.1 Leachate

Figure 5.2 shows the elemental concentrations in the leachate of 1 d cured AAS pastes with time. Generally, the concentration of all detected ions increases with time, with most ions stabilising by around 60 d. Notably, the pH of the leachate from NH pastes is higher than that of NS pastes, and trends in Na, K and Al concentrations are consistent with changes in pH as well. This difference may be attributed to the denser microstructure of NS pastes. In NS systems, considerable soluble silicon ions like [SiO(OH)₃]⁻ and [SiO₂(OH)₂]²⁻ are initially present in the activator (*i.e.*, initial pore solution). The C-(N-)A-S-H gels can form immediately when Ca and/or Al species are released from slag [168]. In contrast, NH systems lack soluble Si in the activator, meaning that Si in C-(N-)A-S-H gels must be derived entirely from slag dissolution. This difference results in a higher gel formation rate in NS pastes compared to NH

pastes, as reported in [169,170]. The formation of additional gels in NS pastes has two main effects: (1) it increases the requirement of Na ions to balance the charge within the gel interlayer [104] and (2) it contributes to a denser microstructure (*Figure 5.14*), which restricts the migration of ions. Additionally, due to the same dosage of Na₂O in both activators, the initial pH of the NH activator is higher than that of the NS activator. This is because sodium hydroxide is a strong base, while sodium silicate is a relatively weak base. Consequently, the leachate from NH paste has a higher pH.

The concentration of Si in the leachate of the NS paste is higher than that of the NH paste, mainly attributed to the soluble silicate initially introduced by the NS activator. However, unlike other ions, the concentrations of Si and Ca ions fluctuate within 90 d, with both showing similar trends. This phenomenon is consistent with the “dissolution-reprecipitation mechanism” proposed by Katrina et al. [171]. The increase in Si and Ca concentrations is likely driven by the concentration gradient between the leachate and the pore solution. Conversely, the decreases in Si and Ca concentrations probably result from the reincorporation of Ca or Si onto dissolving surfaces or the potential formation of reaction products on the paste surfaces under alkaline conditions. The dynamic equilibrium process of dissolution and reprecipitation in the leachate accounts for the observed fluctuations in Ca and Si concentrations. It is also important to note that ion concentrations in real environmental conditions would likely differ due to the influence of liquid flow and the frequency of water replacement.

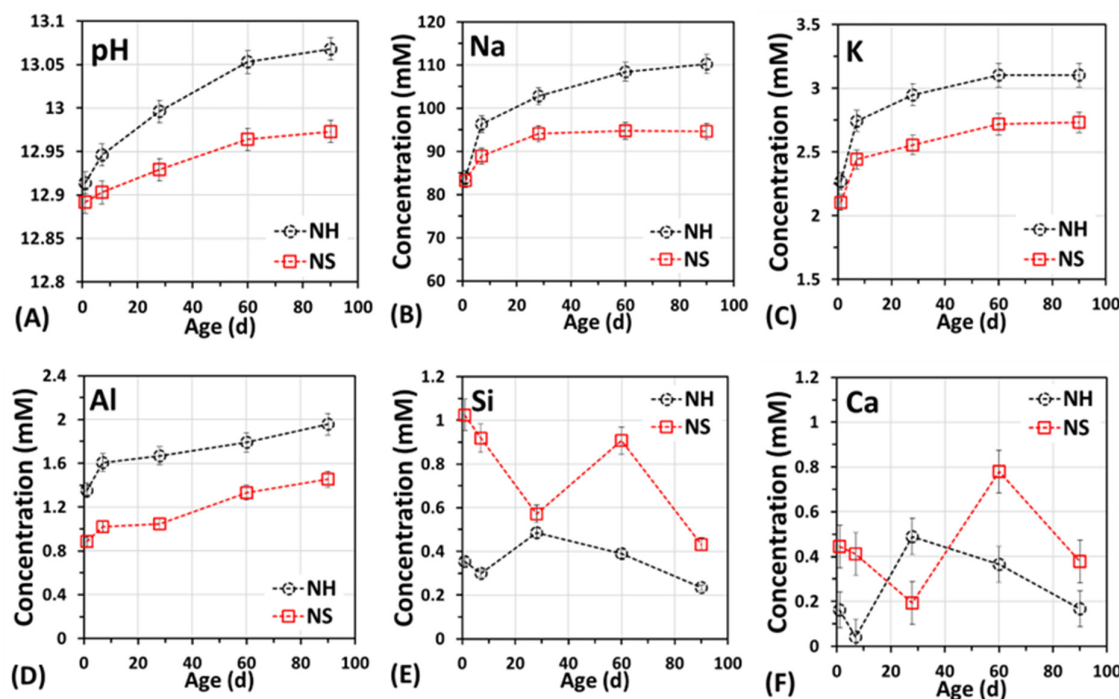


Figure 5.2. pH and elemental concentrations of the leachate of piece AAS pastes with time.

5.3.1.2 Pore solution

Figure 5.3 presents the elemental concentrations in the pore solution of AAS cylinders cured under sealed and water-immersed conditions. Across both curing conditions, Na dominates the pore solution composition, while much lower concentrations of K, Si, Al and Ca are observed. Despite the low content of K in the slag (Table 5.1), K readily leaches out, with its concentration increasing with time. This behaviour is probably due to the weak bonding of K within the gels and its high mobility [172]. Moreover, the concentrations of Na and K in water-immersed pastes are approximately half those in sealed pastes, which suggests significant leaching in immersed pastes. In particular, the looser pore structure of NH pastes provides more pathways for ion transport, facilitating the leaching of alkali metal ions.

The content of Al is higher in the NS than NH system, which agrees with the results found by Zuo et al. [69]. The concentration of Si in the pore solution of the sealed NS paste is higher than that in the sealed NH paste with the same dosage of Na_2O . This difference is due to the inclusion of soluble Si in the NS activator. However, in water-immersed samples, Si concentrations are significantly lower than in sealed samples, indicating that a substantial amount of Si is readily available in the pore solution and leaches out at an early stage. In addition, fluctuations in Ca and Si concentrations are also observed in both types of pastes, likely due to a dynamic equilibrium between slag dissolution and gel precipitation [171,173]. Notably, the concentrations of all detected elements and the pH in the pore solution of water-cured paste are considerably lower than sealed pastes. This reduction in ion concentration due to leaching alters the reaction environment of the slag, potentially affecting its reaction degree.

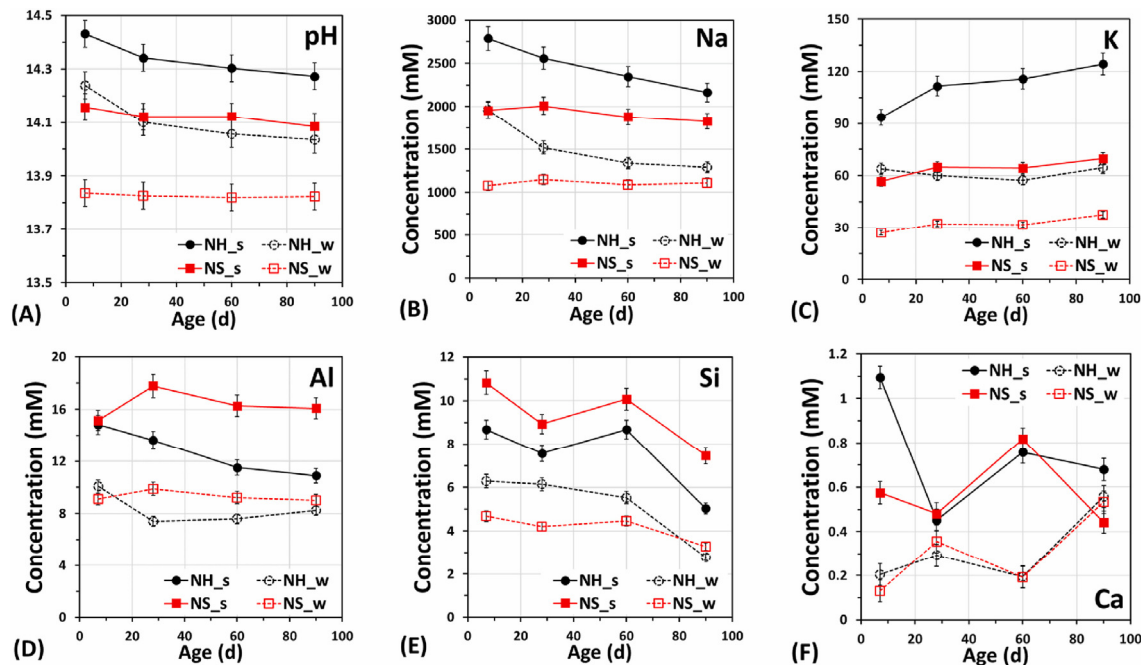


Figure 5.3. Elemental concentrations and pH of the pore solution of AAS cylinders under sealed (s) and water-immersed (w) conditions.

5.3.2 Reaction degree of slag

Figure 5.4 shows the reaction degree of slag in AAS pastes cured under sealed and water-immersed conditions, respectively. Under sealed conditions, the reaction degrees of slag in both pastes gradually increase over time, reaching over 50% by 90 d. Initially, at 7 d, the reaction degree of slag in the NH paste is slightly higher than in the NS pastes, likely due to the higher pH, which promotes early slag reactions. However, after 7 d, the reaction degree of slag in the NH paste becomes lower than that in the NS paste, consistent with [104]. This is because the initial fast reaction in the NH system leads to the formation of a dense layer of reaction products that covers the unreacted slag, potentially hindering further slag reaction. Under water-immersed conditions, the reaction degrees of slag in both pastes are significantly lower than those under sealed conditions. As the leaching of ions and intrusion of water, the pH of the pore solution gradually decreases over time (Figure 5.3A). Since a higher pH is beneficial for the disintegration of the glassy phases in slag, the dilution of the pore solution leads to a reduction in the reaction degree of slag. Additionally, the difference in reaction degree between sealed and water-immersed samples is more pronounced in the NH group than in the NS group. This is likely because the more porous microstructure of NH pastes is more vulnerable to water ingress. Fortunately, although AAS pieces were immersed in water after only 1 d of sealed curing, the chemical reaction of slag continues, albeit at a slower rate.

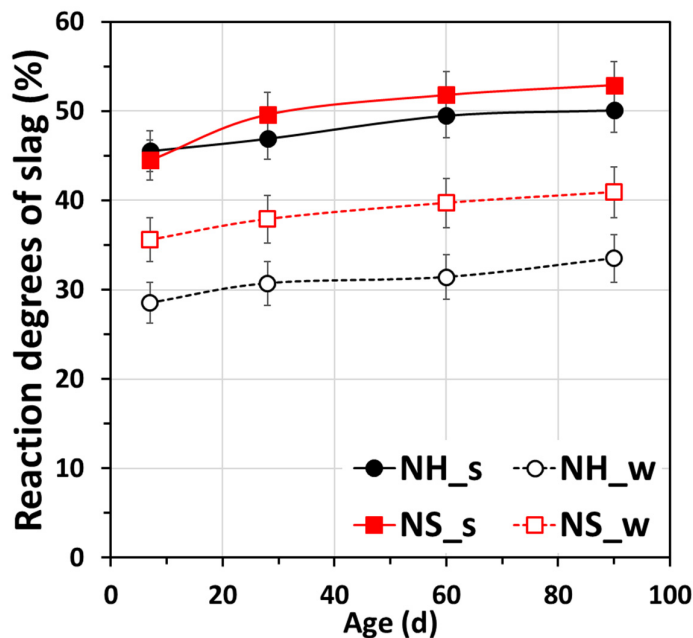


Figure 5.4. Reaction degrees of slag in AAS pastes under sealed and water-immersed conditions.

5.3.3 Phase assemblage

5.3.3.1 XRD analysis

In the early hours of water immersion, flocculent solids were observed accumulating at the bottom of the container holding the AAS samples. *Figure 5.5* shows the morphology and XRD pattern of these solids, which were identified as calcite. Due to the leaching of alkali ions, the pH of the leachate of AAS pastes increases gradually, and the leachate can be considered as an alkaline solution. Given the employment of tap water in this leaching test, CO_2 (either originally dissolved in the water or absorbed from the environment) in the leachate will spontaneously hydrolyse to bicarbonate ions (HCO_3^-) and carbonate ions (CO_3^{2-}) via a multi-step reaction sequence ($\text{CO}_2 + 2\text{OH}^- \rightarrow \text{HCO}_3^- + \text{OH}^- \rightarrow \text{CO}_3^{2-} + \text{H}_2\text{O}$) [174,175]. These carbonate ions subsequently react with leached Ca ions from the AAS pastes, or Ca ions in the tap water, precipitating CaCO_3 in the leachate. Furthermore, CaCO_3 precipitation was also identified on AAS pastes.

Figure 5.6 shows the XRD pattern of AAS pastes under sealed and water-immersed conditions. Over time, both sealed NH and NS pastes exhibit increased intensity in the characteristic peaks of gels and hydrotalcite, with the NH system showing clearer peaks due to the formation of more crystalline reaction products [61,104]. In contrast, water-immersed pastes display significantly weaker signals for these components. This may stem from two factors: the lower reaction degree of slag in water-immersed conditions produces fewer reaction products, and the substantial leaching of ions disrupts the equilibrium between the pore solution and reaction products. This leaching likely destabilises the existing products, leading to their gradual decomposition over prolonged immersion. The next section provides further evidence supporting this decomposition.

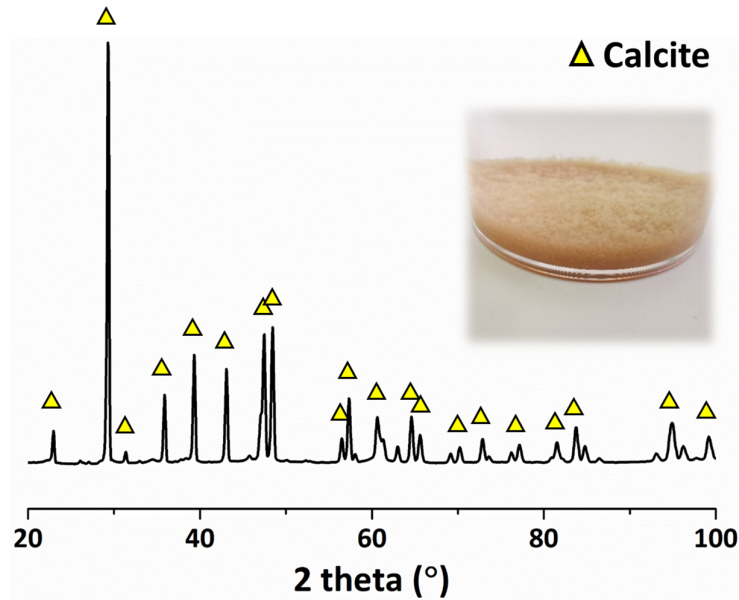


Figure 5.5. Morphology and XRD pattern of flocculent solid in the leachate of AAS pastes

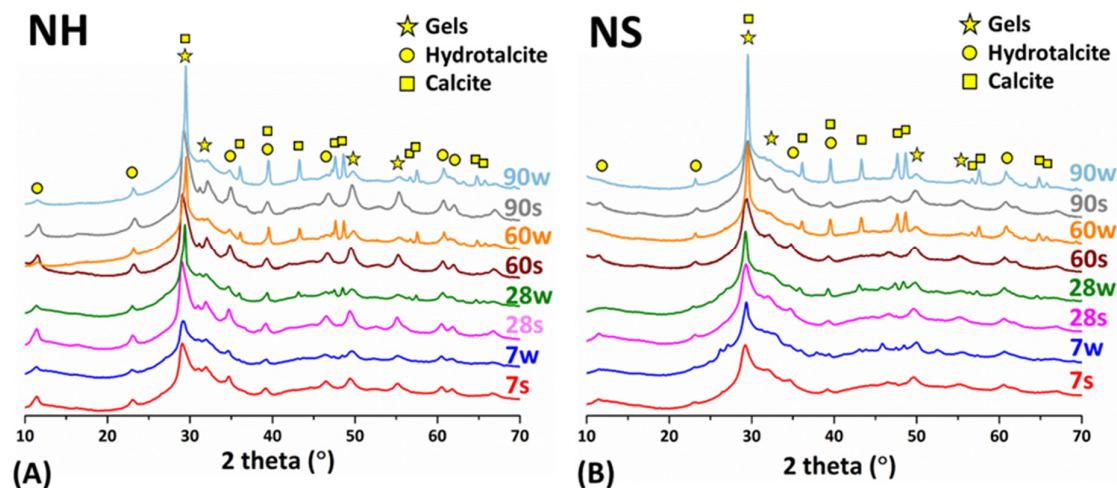


Figure 5.6. XRD patterns of AAS pastes under sealed and water-immersed conditions.

Carbonation appears only in the water-immersed pastes, with peak intensity increasing over time. This increase is likely due to the rough surface texture of the paste samples, which offers ample nucleation sites for calcium carbonation [176]. According to [177], approximately 100 g of paste can bind around 40 – 50 g of CO₂ in a Portland cement system. In these systems, Ca(OH)₂ often serves as a key hydrate, stabilising the matrix by converting to calcium carbonate when exposed to CO₂ [178]. Nevertheless, in AAS systems that lack Ca(OH)₂, CO₂ reacts directly with Ca ions in the pore solution and subsequently with gels [179], leading to gel decalcification and even potential decomposition [180]. This process of underwater carbonation in AAS materials warrants close attention due to its implications for durability.

5.3.3.2 TGA

Figure 5.7 shows the TG and DTG curves of AAS pastes under sealed and water-immersed conditions. According to [104,181–183], different AAS reaction products decompose within distinct temperature ranges: C-(N)-A-S-H gels between 40 – 200 °C, hydrotalcite-like phases between 200 – 400 °C and calcium carbonate between 600 – 800 °C. In addition, the total bound water content, measured as weight loss up to 650 °C, serves as an indicator of the quality of reaction products [184]. Figure 5.8 shows the weight loss of AAS pastes across different temperature ranges.

Generally, the contents of gels, hydrotalcite and total bound water are significantly higher in sealed AAS pastes than in water-immersed ones, which indicates a greater volume of reaction products in the sealed samples. Notably, in sealed pastes, the quantities of gels, hydrotalcite, and total bound water increase steadily from 7 to 90 d. In contrast, water-immersed pastes show an initial increase from 7 to 60 d, followed by a decline at 90 d (Figures 5.8A–C), which suggests the decomposition of reaction products. This decrease in reaction products in water-immersed samples is likely due to ion leaching, which alters the pore solution composition (Figure 5.3). The concentration gradients created by ion leaching can induce osmotic pressure, causing ions originally integrated within the gel structure to migrate out, resulting in gel decomposition [185]. Furthermore, consistent ion leaching reduces the reaction degree of slag (Figure 5.4), leading to lower gel formation. Combined, these effects contribute to the observed reduction in reaction products at 90 d in water-immersed samples. Moreover, as shown in Figure 5.8D, the amount of calcium carbonate in water-immersed pastes increases with immersion time. This trend is likely linked to the ongoing leaching of calcium ions from

the paste, which promotes calcium carbonate formation in an open water-immersed environment.

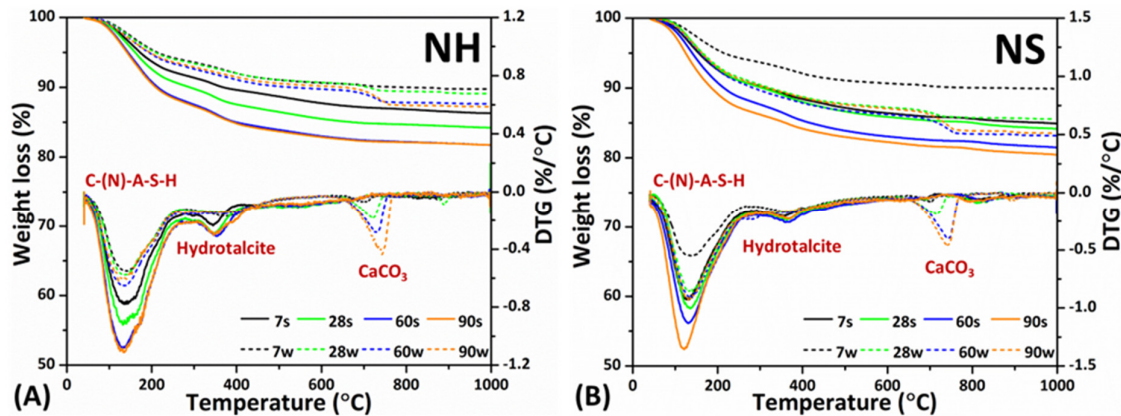


Figure 5.7. TG and DTG of AAS pastes under sealed and water-immersed conditions.

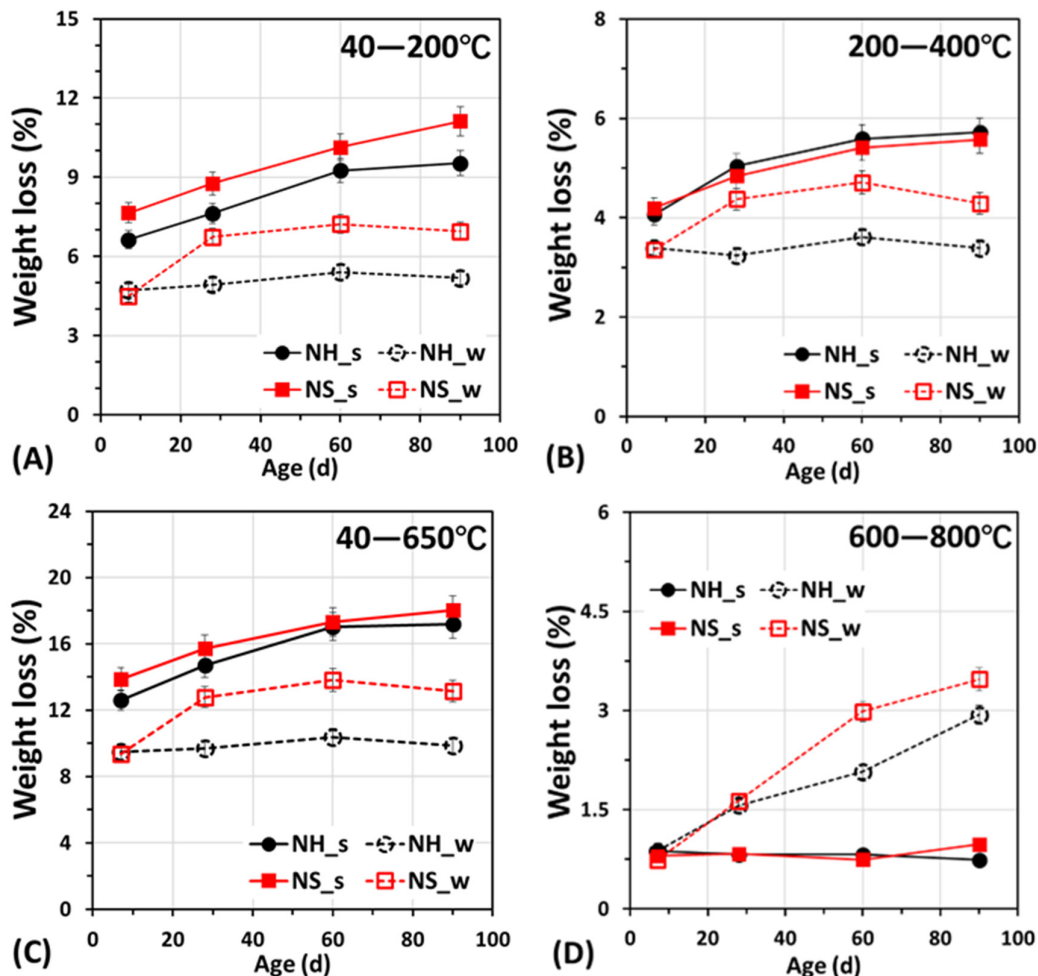


Figure 5.8. Weight loss of AAS pastes at different temperature ranges, normalised by mass.

5.3.4 Paste chemistry

5.3.4.1 FTIR

The FTIR spectra of AAS pastes are presented in *Figure 5.9*. According to [58,186], the main bands around $940 - 970\text{ cm}^{-1}$ represent the asymmetrical stretching vibration of Si-O-T (T=Si, Al) and/or Si-O-M (M=alkali metal elements), which is the characteristic structure of Q^2 units. A minor shoulder around 1050 cm^{-1} is also assigned to Si-O-T and/or Si-O-M bonds, albeit with a lower substitution of Al [187]. Another band, at around 900 cm^{-1} , represents the deformation vibration of Si-O-Al or Si-O-Si. Finally, the bands at $800 - 825\text{ cm}^{-1}$ correspond to the Si-O stretching vibrations of the Q^1 unit [107,188].

Figures 5.9A and B show that both NH and NS pastes in sealed conditions exhibit visible signals for Q^1 and Q^2 units, with no significant changes in intensity or position over time. The Q^2 peak in sealed NS pastes (945 cm^{-1}) is higher than in NH pastes (941 cm^{-1}), suggesting that gels in NS pastes are more polymerised than in NH pastes. This interpretation is further supported by the less pronounced Q^1 peak in NS pastes. The soluble Si in the NS activator increases Si participation in gel formation, resulting in lower Ca/Si ratios in C-(N-)A-S-H gels (*Figure 5.12*). A lower Ca/Si ratio favours the formation of longer silicate chains, reflected in a higher Q^2 and lower Q^1 content [189].

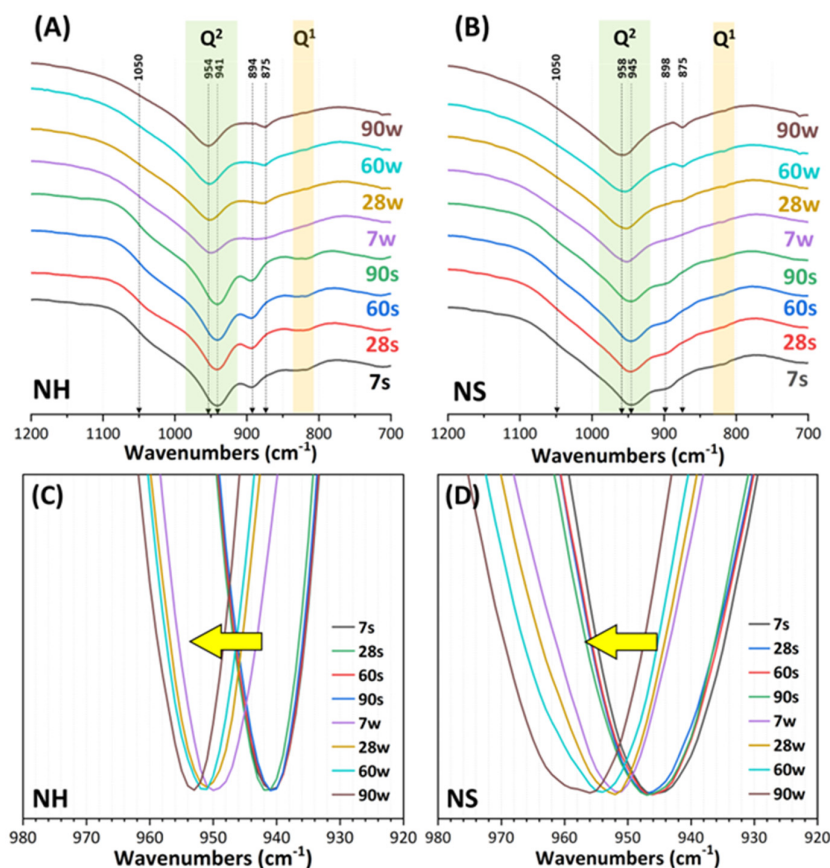


Figure 5.9. FTIR spectra of (A) NH and (B) NS pastes under sealed and water-immersed conditions. (C) and (D) are the insets of FTIR spectra of NH and NS pastes in the range between 920 and 980 cm^{-1} . The yellow arrows indicate the increasing shift of peaks in pastes after water immersion.

Furthermore, the intensity of Q^1 and Q^2 units is lower in water-immersed pastes than in sealed pastes. To better illustrate this, *Figures 5.9C and D* zoom in on the Q^2 band ($930 - 970 \text{ cm}^{-1}$). Generally, NS pastes display a broader Q^2 peak than NH pastes. As reported in [62,190], the width of the peak is often dependent on the degree of crystallisation of gels. A sharper peak indicates a more crystalline structure, which correlates with the XRD results (*Figure 5.6*). While sealed AAS pastes show minimal changes over time, water-immersed samples exhibit significantly higher wavenumbers for the Q^2 peak across all curing ages, indicating increased polymerisation of C-(N)-A-S-H gels following leaching. This is in agreement with the leaching results in *Chapter 4*, where the synthetic C-(N)-A-S-H gels show a higher polymerisation degree after water immersion. This increase in polymerisation likely results from the leaching of Na from the gels, which affects charge balance within the interlayer structure. Concurrently, the leaching of Ca ions, which leads to the formation of calcium carbonate over time, also impacts the Ca/Si ratio in gels. Lower Ca/Si ratios are associated with lower polymerisation. Additionally, a peak around 875 cm^{-1} , corresponding to the bending (v_2) mode of CO_3^{2-} [191], appears in water-immersed samples, confirming the presence of calcium carbonate and supporting the XRD and TGA results.

5.3.4.2 SEM and EDX

Figure 5.10 shows the surface morphology of NS pastes under sealed and water-immersed conditions at 28 d. In sealed conditions (*Figure 5.10A*), the surface of pastes is smooth, with unreacted slag particles closely encapsulated by the surrounding reaction products. In contrast, in water-immersed samples (*Figure 5.10B*), the surface appears rougher and is covered with solid particles. To identify the chemical composition of these particles, the cross-section of the exposure front of the NS pastes was observed, and EDX point analysis was conducted on the surface layer, as shown in *Figure 5.11*. The result reveals an outer calcium carbonate layer that covers the internal matrix. This outer layer, however, has a weak bond with the underlying matrix, resulting in large cracks near the interface.

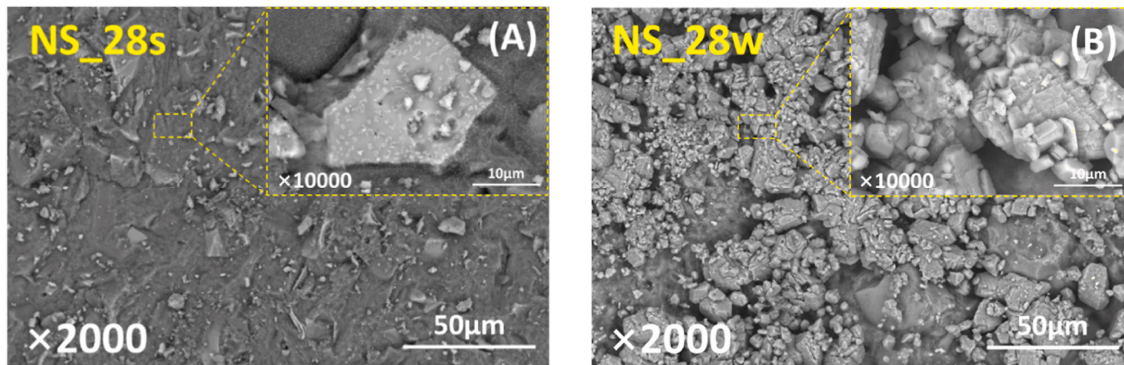


Figure 5.10. Morphology of the surface of NS pastes under (A) sealed and (B) water-immersed conditions.

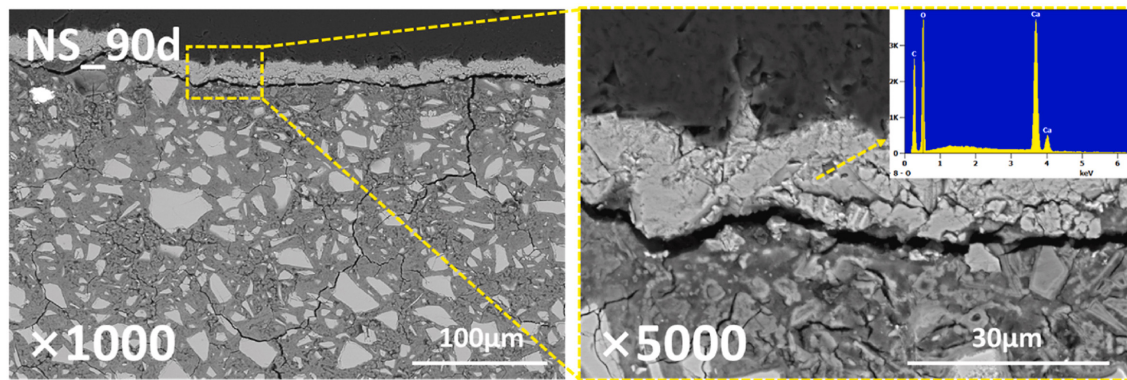


Figure 5.11. Cross-section of the exposure front of the NS pastes after 90 d of water immersion.

Figure 5.12 shows the atomic Na/Si ratio versus the Ca/Si ratio of the reaction product of AAS pastes. Due to the high soluble Si content in the initial NS activator, NS pastes generally exhibit a lower Ca/Si ratio and a higher Na/Si ratio compared to NH pastes. This indicates a competitive role of Ca and Na in charge balancing within the gel structure. The Na/Si ratio in sealed NS pastes significantly decreases from 7 d to 90 d, while sealed NH pastes show minimal change over the same period. In NS pastes, the abundance of soluble Si ions promotes early gel formation. However, with the limited reaction of slag, Ca remains insufficient, resulting in a greater reliance on Na for charge balance within the C-(N-)A-S-H gels at early ages. With the extension of time, as more Ca ions dissolve from the slag, they gradually replace Na [192]. In contrast, the NH system, with no additional Si beyond that in the slag, maintains a more stable Ca/Si ratio close to that of the slag composition from 7 d to 90 d. After 90 d of water immersion, both NH and NS pastes show nearly zero Na/Si ratios, indicating that Na is weakly bound in the gel and can significantly leach out over time. This observation is consistent with the leaching of Na in synthetic gels in *Chapters 3 and 4*, though the leaching process in pastes is slower. The Ca/Si ratio in sealed and immersed pastes is comparable.

Figure 5.13 shows the atomic Na/Si ratio versus the atomic Ca/Si ratio of the reaction product of AAS pastes under sealed and water-immersed conditions. A linear correlation between the Mg/Si and Al/Si ratios in AAS pastes, which implies the presence of hydrotalcite-like phases, as previously reported [103,104,193,194]. The positive X-axis intercept reflects the level of Al incorporation within gels. The average Al/Si ratio in both NH and NS pastes is comparable, with no evident differences between sealed and water-immersed pastes. This indicates a proportional dissolution between Si and Al from gels. The slopes of the trendlines, referring to the Mg/Al ratio, range from 1.92 to 4.35, which is consistent with hydrotalcite formed in AAS pastes [195,196]. The Mg/Al ratio in both pastes slightly increases with time, with NH pastes showing a marginally higher Mg/Al ratio than NS pastes. The overlapping trendlines for sealed and water-immersed pastes suggest that hydrotalcite is stable under immersed conditions.

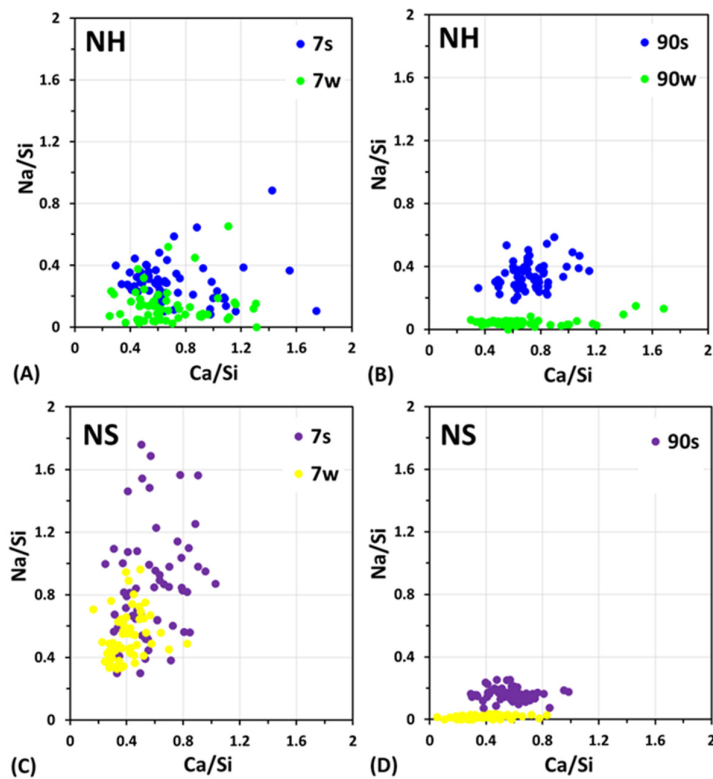


Figure 5.12. Atomic Na/Si ratio versus atomic Ca/Si ratio of the reaction product of AAS pastes under sealed and water-immersed conditions.

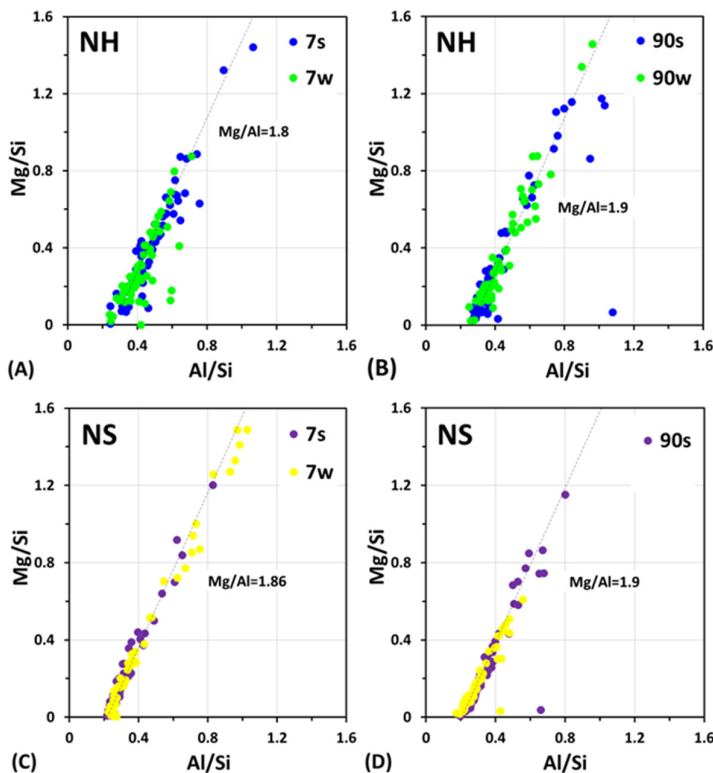


Figure 5.13. Atomic Mg/Si ratio versus atomic Al/Si ratio of the reaction product of AAS pastes under sealed and water-immersed conditions.

5.3.5 Pore structure

Figures 5.14A and B show the pore volume and pore size distribution of NH pastes, determined by NA, respectively. As reported in [197], pores in AAS pastes can be classified as gel pores (0 – 10 nm) and capillary pores (10 – 100 nm). In sealed NH pastes, the pore volume decreases with time, while in water-immersed pastes, the pore volume increases, indicating a coarsening of the pore structure. Due to the limitation of the NA test (1 – 300 nm), pores larger than 300 nm are excluded in these experiments. Notably, the pore volume in the water-immersed paste at 90 d appears lower than at 60 d, likely because larger capillary pores, exceeding 300 nm, dominate in the 90 d sample and thus fall outside the measurement range. As shown in the pore distribution (Figure 5.14B), both gel pores and capillary pores in water-immersed NH pastes increase with time, confirming that immersion significantly coarsens the pore structure in these samples.

Figure 5.14C shows the pore volume of NS pastes. Under sealed conditions, the pore volume between 1 – 300 nm is minimal at 60 and 90 d, while the paste under immersed conditions is much higher than that of the sealed one. This suggests a pronounced effect of water exposure on porosity. Despite this, NS pastes appear less affected by leaching than NH pastes, as the microstructure of water-immersed NS pastes remains relatively dense up to 60 d, likely due to the inherently denser structure of NS pastes. After 90 d, the pore volume in water-immersed NS pastes surpasses that at 7 d, reflecting microstructural degradation due to prolonged immersion. Figure 5.14D shows the pore size distribution of NS pastes, with water-immersed samples displaying a higher content of gel pores compared to sealed samples, consistent with findings in other studies [10,11]. Since gel formation is lower in water-immersed pastes, the gel structure is looser, resulting in more nano-sized pores.

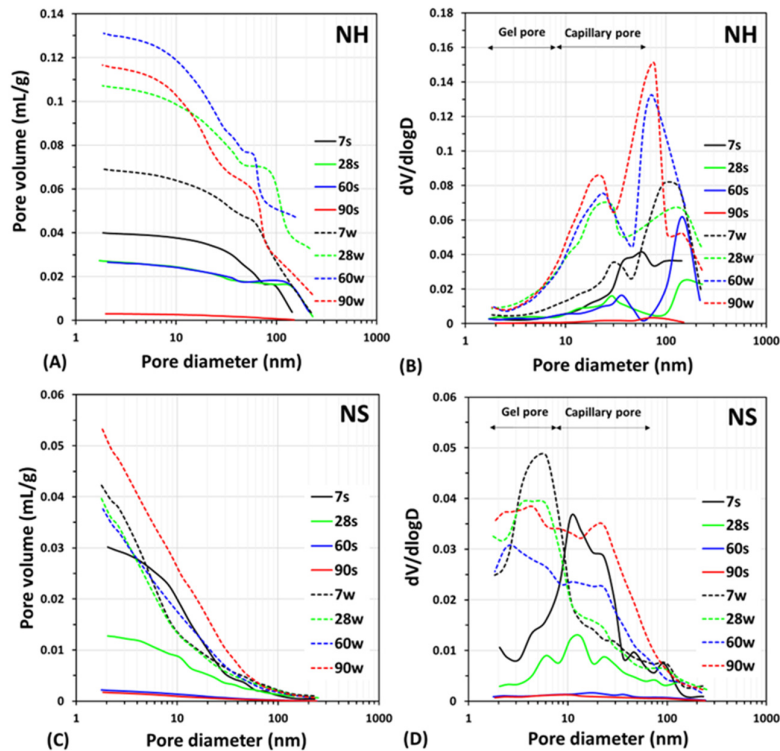


Figure 5.14. Pore volume and pore size distribution of AAS pastes under sealed and water-immersed conditions, determined by nitrogen absorption.

Gel decomposition over time is evident in the increased gel pores at 90 d, aligning with the trends observed for gel content in *Figure 5.8*. In addition, gel decomposition contributes to an increase in capillary pores. As shown in *Figure 5.14D*, capillary pores within the 10 – 100 nm range increase considerably with time, especially at 60 d and 90 d, further indicating that water immersion significantly degrades the microstructure by enlarging the pore network in NS pastes.

5.3.6 Compressive strength

Figure 5.15 shows the compressive strength of AAS pastes over time. NS pastes consistently exhibit higher compressive strength than NH pastes under both sealed and water-immersed samples, due to a lower porosity of NS pastes. However, water immersion reduces the compressive strength of NH and NS pastes by approximately 15% and 12% at 90 d, respectively, indicating that water exposure has a detrimental effect on strength.

It is notable that water-immersed samples, particularly NS pastes, show larger deviations in compressive strength compared to sealed samples, a trend also observed in previous studies [11]. This variability is likely caused by stress gradients within the samples [14]. NS pastes are prone to shrinkage and cracking due to the emptying of small capillary pores [198–201]. To relieve these stresses, water must migrate from the surface to the interior at a specific rate to counteract the autogenous shrinkage that results from ongoing chemical reactions. This migration rate is highly dependent on the permeability and dimensions of the sample. The dense microstructure of NS pastes limits the rate at which water can diffuse inward, leading to an uneven stress distribution. This stress gradient increases the likelihood of cracking compared to the more uniform stress in sealed samples. Further analysis of the cracking of AAS pastes subjected to water immersion is covered in *Chapter 7*.

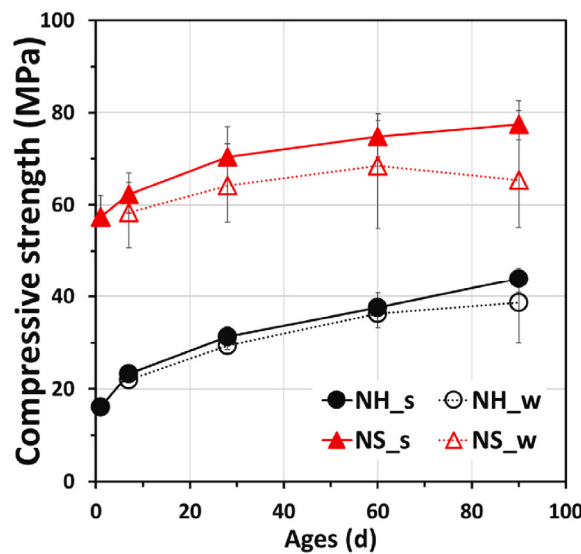


Figure 5.15. Compressive strength of AAS pastes under sealed and water-immersed conditions.

5.4 Summary and perspective

The degradation of AAS pastes under water-immersed conditions is revealed and the underlying mechanisms can be summarised in *Figure 5.16*, including low reaction rate, gel decomposition and carbonation.

Low reaction rate

When an immature hardened AAS paste is immersed in water, large amounts of alkali (metal) ions are liable to leach out. The ion concentrations in the leachate generally increase while the ion concentrations and pH of the pore solution decrease over time. The reduced pore solution alkalinity limits the reaction of slag, resulting in a decreased formation rate of reaction products. As a result, water-immersed AAS pastes have a higher content of both gel and capillary pores compared to sealed pastes.

Gel decomposition

The dilution of the pore solution disrupts the equilibrium between liquid and solid phases, leading to gradual changes in gel chemistry over time. Under water-immersed conditions, the gels in AAS pastes show a higher degree of polymerisation than under sealed conditions, along with lower Na/Si ratios. These changes indicate a transformation in the C-(N-)A-S-H gels during prolonged water exposure, ultimately contributing to gel decomposition. This degradation is evident in the decrease in gel content from 60 d to 90 d, which correlates with increased porosity, particularly in NS pastes immersed for extended periods.

Carbonation

As alkali metal and hydroxide ions leach out from AAS pastes, the pH of the leachate rises above 13, making it easier for atmospheric CO_2 to dissolve into an alkaline solution. The dissolved CO_2 hydrolyses into CO_3^{2-} , which can then react with Ca^{2+} , forming calcium carbonate in the leachate. Additionally, a calcium carbonate layer develops on the surface of AAS pastes and continues to accumulate over time. While Ca in this carbonate layer can stem from environmental water, it can also originate from the paste itself. This internal decalcification should be monitored closely, as it can lead to further gel decomposition, compromising the structural integrity of the material.

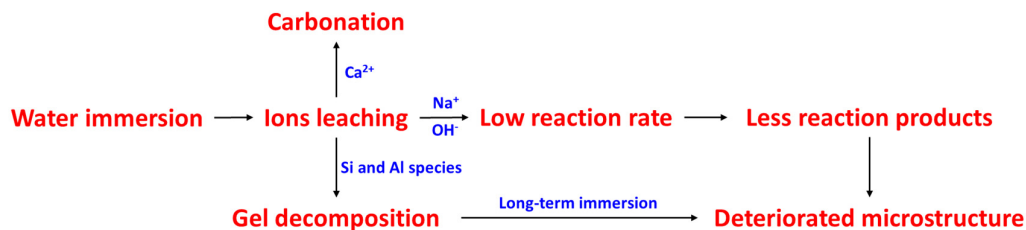


Figure 5.16. Flowchart of degradation mechanisms of AAS pastes subject to water immersion.

5.5 Conclusions

In this chapter, the properties of AAS pastes immersed in tap water are investigated. The degradation of pastes was found, and the underlying mechanisms were unveiled. Based on the results and discussion, the findings are summarised as follows:

1. Under water-immersed conditions, considerable leaching of Na and hydroxide ions from AAS pastes occurred, leading to a gradual drop in the pH of the pore solution. This reduction in pH inhibited the slag reaction, resulting in a lower formation rate of reaction products and impeding microstructure development.
2. C-(N-)A-S-H gels in water-immersed conditions showed a higher degree of polymerisation than in sealed conditions. Both Ca/Si and Na/Si ratios in the gels decreased with time, with nearly complete leaching of Na after 90 d of immersion. Prolonged leaching led to gel decomposition, as evidenced by the decline in gel content from 60 d to 90 d in water-immersed samples.
3. Hydroxide ions released from AAS pastes increased the pH of the leachate, which promoted the absorption of external CO₂. The dissolved CO₂ reacted with Ca ions, forming calcium carbonate both in the leachate and on the paste surface.
4. The combination of reduced slag reactivity, gel decomposition and carbonation deteriorated the pore structure of water-immersed AAS pastes. Consequently, compressive strengths of NH and NS pastes were 15% and 12% lower under water-immersed conditions compared to sealed conditions.

Chapter 6

Prediction of pore structure deterioration of AAS pastes due to long-term leaching

6.1 Introduction

Leaching, a process significantly influenced by the structural scale, necessitates consideration of transport processes within bulk structures. While extensive research has addressed chloride penetration [202–205], sulfate attack [206–208] and acid corrosion [209–211] in AAS materials, the effects of leaching under water immersion remain underexplored. Although water is less aggressive than salts or acids, the degradation of AAS pastes has been confirmed in *Chapter 5*. Therefore, leaching in water is a fundamental issue that warrants prioritised investigations.

In this chapter, NH and NS pastes were prepared in the same manner as described in *Chapter 5*, but cast into cylindrical shapes to investigate the deterioration of AAS pastes with depth. The samples were sealed for 28 d, followed by 90 d of immersion in deionised water. SEM combined with EDX was employed as the main experimental method to characterise the pore structure and elemental composition of pastes at different depths from the exposure front. Additionally, a diffusion-dissolution model was developed to provide deeper insights beyond the experimental observations and to predict the depth of microstructural degradation induced by long-term leaching.

6.2 Experiments

6.2.1 Materials and sample preparation

The materials and mixture proportions, detailed in *Chapter 5*, were used without alteration (*Table 5.2*). AAS pastes were cast into small polyethene moulds (ϕ 25 mm \times 40 mm) and sealed for 28 d to ensure phase and microstructure maturity. After demolding, the sides and bottoms of the cylindrical samples were sealed with aluminium tape and immersed in deionised water (2 L), refreshed weekly, for up to 90 d (*Figure 6.1A*). Unlike the tap water used in *Chapter 5*, deionised water was chosen to eliminate interference from ionic contaminants.

Four sample types were prepared: “NH_28d,” “NH_90d,” “NS_28d,” and “NS_90d,” where “NH” and “NS” denote the type of alkali activator, and the suffix indicates immersion duration. For example, “NH_28d” refers to NH paste immersed for 28 d. After water immersion, the aluminium tape was removed, and the cylinders were halved along their height (*Figure 6.1B*). The halves were immersed in isopropanol for 7 d to halt slag reactions, dried, and impregnated with low-viscosity epoxy resin. Once the resin hardened (24 h), the cross-section of the samples perpendicular to the top and bottom surfaces (*Figure 6.1C*) was polished using sandpaper and diamond paste.

Part of this chapter is published on:

C. Liu, Z. Xu, S. He, G. Ye. (2025) A reactive transport model to predict microstructural deterioration of alkali-activated slag induced by leaching. *Cement and Concrete Research*. (under review)

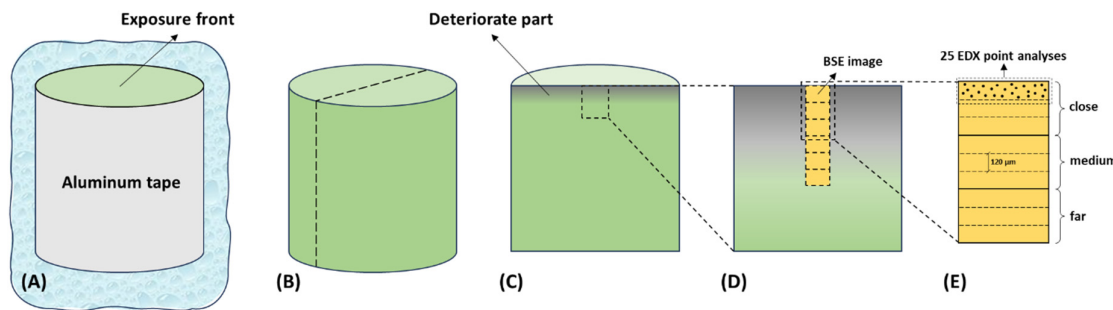


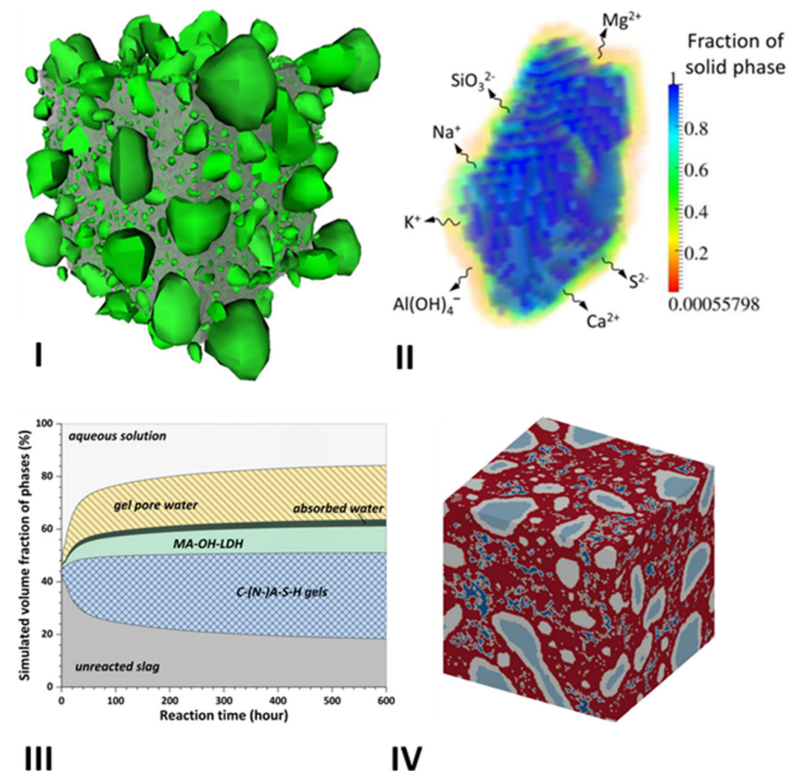
Figure 6.1. Schematic diagram of the preparation of samples and the positioning of BSE images and EDX point analyses. The dark grey part in (C) and (D) represents the deteriorated microstructure near the exposure front of the paste.

6.2.2 SEM characterisations

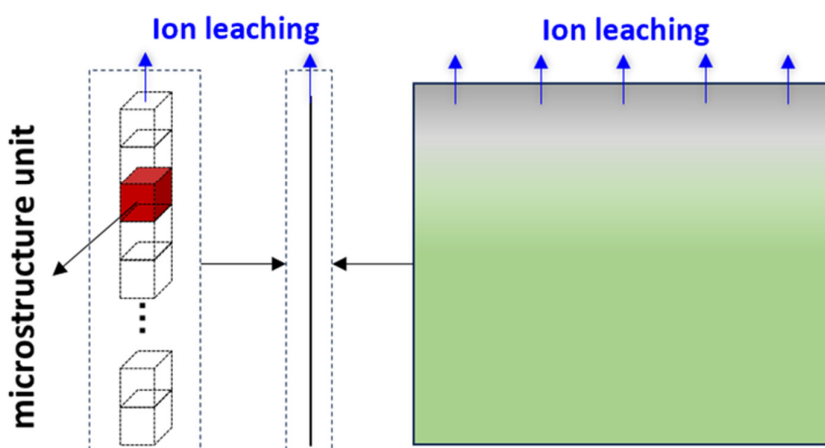
Prior to SEM tests, the polished surface was carbon-coated to enhance the conductivity and imaging quality. SEM analysis operates in backscattered electron (BSE) mode at 15 kV and a 10 mm working distance under a high vacuum. BSE images were captured frame by frame from the exposure surface inward, using a magnification of 1000. ImageJ software was used to stitch images [212]. For porosity quantification, BSE images were converted to 8-bit grayscale, with standardised brightness and contrast adjustments. Threshold values of 70 and 120 were selected to identify different pores from the exposure surface. The rationale for selecting these thresholds is detailed in *Section 6.4*. The segmented images classified regions into pores and solid materials, with porosity calculated as the proportion of pixels below the threshold to the total pixels at each depth. This analysis was conducted on 10 stitched images to determine porosity at various depths. EDX point analyses were conducted near the exposure front to assess elemental distribution. Three BSE images—representing “close,” “medium,” and “far” distances from the exposure front—were obtained at 1000 \times magnification. Each image was divided into three sections (approximately 120 μ m in height), and 25 EDX point analyses were performed in each section (*Figure 6.1E*).

6.3 Modelling

When AAS pastes are immersed in water, the gradient of ion concentrations between exterior water and interior pore solution triggers the leaching of ions through ion diffusion. This leaching process can destroy the thermodynamic equilibrium between the pore solution and reaction products, resulting in the decomposition of reaction products and subsequent microstructural deterioration. To better understand these processes and predict degradation due to leaching, a thermodynamics-based diffusion-dissolution model was developed. The modelling approach was divided into three key modules: (1) microstructure formation of the initial AAS pastes, (2) ion diffusion during water immersion, and (3) pore structure deterioration caused by leaching.



(A) Microstructure construction (Geomicro3D)



(B) Reactive transport (LBM + Gems)

Figure 6.2. Schematic diagram of the modelling procedure of AAS pastes subjected to water immersion.

Figure 6.2 shows the modelling procedure of AAS pastes under water immersion. The initial microstructure of AAS pastes was constructed by the Geomicro3D model [213]. This model replicates the spatial distribution of real-shape slag particles within the alkaline activator (Figure 6.2A I), simulates slag dissolution in the alkaline solution (Figure 6.2A II), models the formation of reaction products (Figure 6.2A III), and generates the final microstructure of AAS pastes (Figure 6.2A IV). GeoMicro3D also provides detailed data on ion concentrations in the pore solution and solid reaction products, which is crucial for simulating ion diffusion and

microstructure degradation. Experimental results (*Section 6.4*) indicate that NH pastes exhibit higher porosity and greater vulnerability to leaching compared to NS pastes. Consequently, the simulations primarily focus on NH pastes.

To balance computational efficiency and cost, the modelling of ion diffusion and microstructure degradation was conducted on a one-dimensional continuum scale (*Figure 6.2B*). This approach divided the model into numerous microstructural units, which represented the microstructure of AAS pastes. This one-dimensional approach aligned with the experimental setup (*Figure 6.1C*), where AAS cylinders can be approximated as fitting within a one-dimensional percolation model. At this continuum scale, porosity and diffusion coefficients, obtained from the GeoMicro3D model, were utilised to simulate the transport and degradation processes [213].

6.3.1 Microstructure formation

The input of simulated NH pastes was identical to the mixture design in the experiments (*Table 5.2*). Using the GeoMicro3D model, the initial microstructure of the NH paste was generated. This included simulating the spatial distribution of slag particles within the alkaline activators, slag dissolution, nucleation and growth of reaction products, and the spatial arrangement of these products. Each microstructural unit was defined as $95\text{ }\mu\text{m} \times 95\text{ }\mu\text{m} \times 95\text{ }\mu\text{m}$, with a voxel size of $1\text{ }\mu\text{m} \times 1\text{ }\mu\text{m} \times 1\text{ }\mu\text{m}$. The effectiveness of this model for AAS materials has been validated in prior studies [213]. Since constructing the initial microstructure is not the primary focus of this chapter, further details are available in [213].

Figure 6.3A presents the simulated microstructure of NH pastes at 28 d, showcasing the coexistence of liquid and solid phases, including unreacted slag and reaction products. The evolution of the volume fractions of these phases over time is shown in *Figure 6.3B*. The primary phases in the NH paste include unreacted slag, C-(N-)A-S-H gels, hydrotalcite (MA-OH-LDH), absorbed water, gel pore water, and aqueous solution. The C-(N-)A-S-H gels are regarded as ideal solid solutions comprising eight tobermorite-like end-members (CNASH_ss) [214], while hydrotalcite is treated as a solid solution with Mg/Al ratios of 2, 3, and 4 (MA-OH-LDH_ss) [215]. *Table 6.1* outlines the thermodynamic properties of these solid solutions.

In this model, absorbed water refers to the water surrounding C-(N-)A-S-H gels, with 0.3 moles of water assigned to every mole of gel [213]. For gel pore water, Thomas et al. [216] proposed an $\text{H}_2\text{O}/\text{SiO}_2$ molar ratio of 4 for water retained within the gel pores of C-S-H gels during cement hydration. In the CNASH_ss model, the $\text{H}_2\text{O}/\text{SiO}_2$ ratio varies between 0.797 and 2.5, necessitating the addition of water to maintain a ratio of 4 moles of water per mole of C-(N-)A-S-H gel [213].

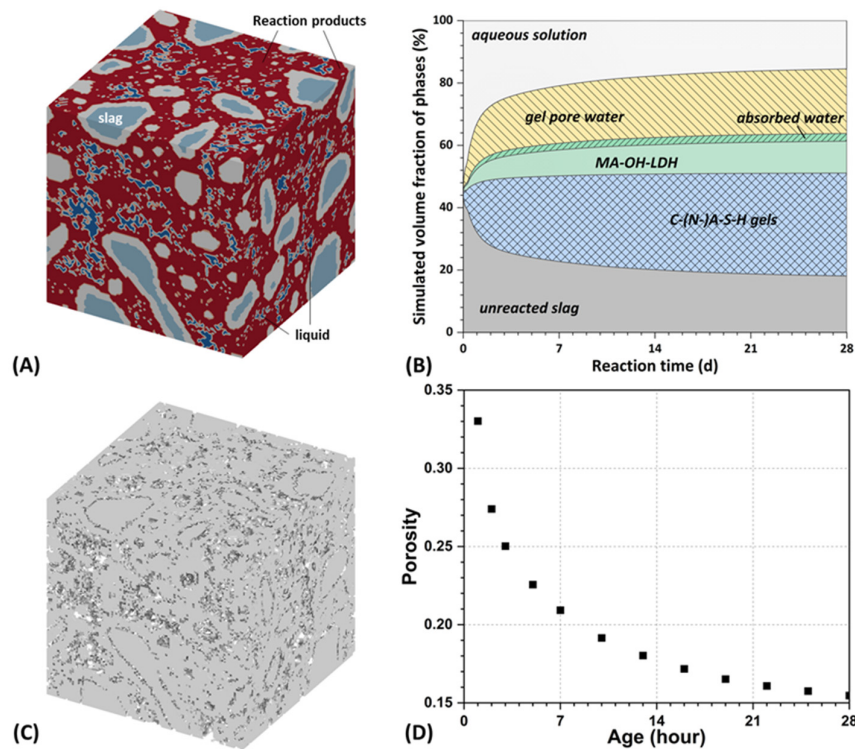


Figure 6.3. (A) Simulated 3D microstructure ($95 \mu\text{m} \times 95 \mu\text{m} \times 95 \mu\text{m}$) of the NH paste at 28 d. (B) Simulated volume fraction of liquid and solid phases of the NH paste with time. (C) Simulated pore structure of the NH paste at 28 d. (D) Simulated porosity of the NH paste during 28 d of reaction.

The microstructure generated by GeoMicro3D is represented as voxel-based three-dimensional data. Each voxel simultaneously contains pore solution, unreacted slag, and reaction products. Numerical testing [213] has shown that a voxel was considered impermeable and classified as solid when its solid volume fraction exceeded 0.688. In the simulation, if the solid content of a voxel was below 0.688, its porosity was calculated as its actual value. Conversely, if the solid content was 0.688 or higher, the voxel was considered impermeable, and the porosity of this voxel was set to zero. The total porosity of the microstructural unit was then determined by averaging the porosity values of all voxels. Using this criterion, the solid structure of NH paste at 28 d is shown in Figure 6.3C, while the evolution of porosity over time is depicted in Figure 6.3D. With this assumption, the calculated porosity of the generated microstructure would be lower than the actual porosity. However, the underestimation of the porosity was limited. For example, the calculated porosity of NH paste at 28 d was 15.7% (shown in Figure 6.3D), while the actual porosity of the generated NH paste was 16.1%. The subsequent leaching and transport simulations were based on the microstructure simulated at 28 d, under the assumption that no further slag reactions occur during leaching. This assumption is reasonable, as slag reactions stabilise after 28 d, as mentioned in Chapter 5 (Figure 5.4).

Although the voxel resolution of the generated microstructure was $1 \mu\text{m} \times 1 \mu\text{m} \times 1 \mu\text{m}$, it should be noted that the voxel porosity above 0.312 ($1 - 0.688$) was taken into account. Therefore, the resolution of the generated microstructure can be equivalent to about 300 nm. This resolution was generally consistent with that of BSE images (400 nm), making the comparison between experimental and simulated porosity reasonable.

Table 6.1. Thermodynamic properties of CNASH_ss and MA-OH-LDH_ss at 289.15 K and 1 bar.

	$V^\circ(\text{cm}^3 \text{ mol}^{-1})$	$\Delta H_f^\circ(\text{kJ mol}^{-1})$	$\Delta G_f^\circ(\text{kJ mol}^{-1})$	$S^\circ(\text{J mol}^{-1} \text{ K}^{-1})$	$C_p^\circ(\text{J mol}^{-1} \text{ K}^{-1})$
CNASH_ss model [214]					
5CA	57.3	-2491	-2293	163	177
INFCA	59.3	-2551	-2343	154	181
5CNA	64.5	-2569	-2382	195	176
INFCNA	69.3	-2667	-2474	198	180
INFCN	71.1	-2642	-2452	186	184
T2C	80.6	-2721	-2465	167	237
T5C	79.3	-2780	-2517	160	234
TobH	85	-2831	-2560	153	231
MA-OH_LDH_ss model [215]					
M_4AH_{10}	219	-7160	-6358	549	648
M_6AH_{12}	305	-9007	-8023	675	803
M_8AH_{14}	392	-10853	-9687	801	958

6.3.2 Ion diffusion

The intrinsic diffusion coefficient (D^k), also referred to as the effective diffusion coefficient [217], describes the diffusion rate of ions in a free solution. In porous materials such as AAS pastes, ion diffusion is significantly slower than in free solution. This reduction is due to the tortuous pathways and the limited cross-sectional area available for transport. The relationship between the diffusion coefficient of an ion k in the pore solution (D_p^k) of AAS pastes and D^k is given by *Equation 6.1*.

$$D^k = \frac{1}{F_0} D_p^k \quad (6.1)$$

where F_0 is the formation factor, which depends on the pore structure geometry of AAS pastes. F_0 can be calculated from the diffusive flux across the AAS paste (J_p) and the diffusive flux across a free zone (J_f), expressed by *Equation 6.2*.

$$F_0 = \frac{J_f}{J_p} \quad (6.2)$$

Due to the complex geometry of AAS pastes, J_p cannot be directly calculated using Fick's law. It can only be calculated by numerical simulation of ion diffusion in AAS paste. A lattice Boltzmann method (LBM) was adopted to simulate ion diffusion in the AAS paste microstructure [213]. Then, the formation factor can be obtained by *Equation 6.2*. Normally, the formation factor is highly dependent on the porosity of the samples. According to [218], the relationship between the formation factor and the porosity (ϕ) can be described by *Equation 6.3*.

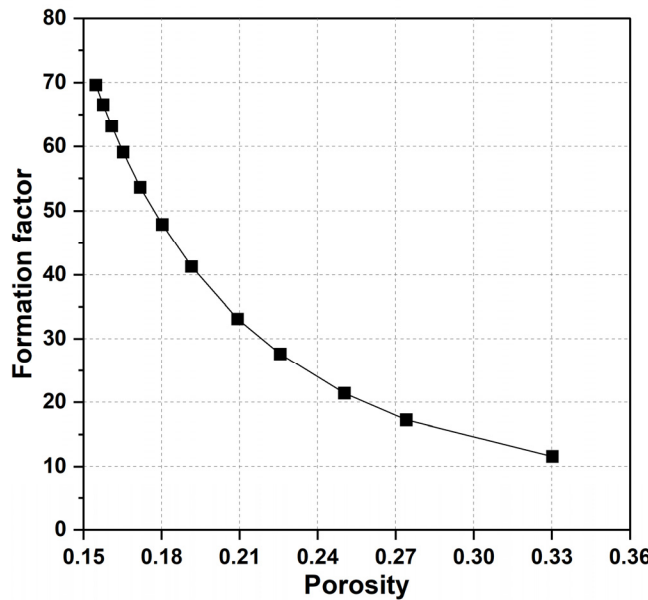


Figure 6.4. Correlation between the simulated formation factor and simulated porosity of NH pastes.

$$F_0 = a\phi^b \quad (6.3)$$

where a and b are fitting constants. Figure 6.4 shows the relationship between the formation factor and porosity for NH pastes over the first 28 d. It can be seen that the formation factor and porosity can be well correlated by Equation 6.3.

Since the quantity of ions is conservative, the diffusion of ions in AAS paste can be described by the continuity equation, which is written as:

$$\frac{\partial \Psi}{\partial t} + \nabla \cdot \mathbf{J} = S \quad (6.4)$$

where Ψ is the quantity of ions per unit volume, \mathbf{J} is the ionic flux and S is the source term. S represents the generation of ions per unit volume per unit time. In a simple diffusion, S is equal to 0. However, the transport of ions breaks the thermodynamic equilibrium between liquid and solid phases, which results in the dissolution of ions from the decomposition of reaction products. Thus, the source term should be considered. In this case, Ψ can be calculated according to Equation 6.5.

$$\Psi = \phi \cdot C^k \quad (6.5)$$

where ϕ is the porosity of the AAS paste and C^k is the concentration of ion k .

\mathbf{J} is a vector representing both orientation and quantity of ionic flux. As mentioned in Section 6.2.1, the cylindrical AAS paste sample has been sealed with aluminium tape except for the top surface. It is rational to assume that the ion diffusion is one-dimensional. Therefore, the ionic flux J can be treated as a scalar variable and expressed as:

$$J = -D^k \frac{\partial C^k}{\partial x} \quad (6.6)$$

Substituting *Equations 6.5* and *6.6* into *Equation 6.4*, it gives the governing equation of ion diffusion for AAS pastes immersed in deionised water, as shown in *Equation 6.7*.

$$\frac{\partial(\phi C^k)}{\partial t} = \frac{\partial}{\partial x} \left(D^k \frac{\partial C^k}{\partial x} \right) + S \quad (6.7)$$

Since the AAS paste is exposed to deionised water, the boundary condition at the exposed surface is described by:

$$C^k|_{x=0} = 0 \quad (6.8)$$

Equation 6.7 is then solved by the finite volume method to obtain the distribution of ion concentrations.

6.3.3 Pore structure deterioration

The formation of AAS paste involves two key thermodynamic interactions: the dissolution of slag and the precipitation of solid reaction products. As slag dissolves, the concentration of ions in the pore solution increases. Once the pore solution becomes saturated or supersaturated, the ions begin to precipitate, forming solid reaction products, which decreases the ion concentration in the solution. These interactions establish a dynamic equilibrium between the pore solution and the solid reaction products. However, when AAS paste is exposed to water, ion leaching occurs, reducing ion concentrations in the pore solution and disrupting the established equilibrium. This imbalance creates an unstable thermodynamic environment, leading to the decomposition of the solid reaction products and initiating the degradation of AAS pastes. As the decomposition progresses, the solid reaction products gradually dissolve, increasing the concentration of dissolved ions in the pore solution.

Figure 6.5 shows the overall flowchart of the modelling process for pore structure deterioration induced by leaching. To simulate this process, accurate thermodynamic properties of the reaction products were required. In addition to the CNASH_ss and MA-OH-LDH_ss models, the CEMDATA18 database [219] was used as the basic thermodynamic database. The dissolution of reaction products was simulated using GEM-Selektor [220,221], a Gibbs Energy Minimisation program package for thermodynamic modelling. The simulation was conducted under standard conditions (20 °C and 1 bar). After completing the thermodynamic modelling, the reaction products were updated to calculate the porosity and ion concentrations in the pore solution. Using the updated porosity values, the diffusion coefficients of ions were recalculated. The iterative process continued until the target simulation time was reached.

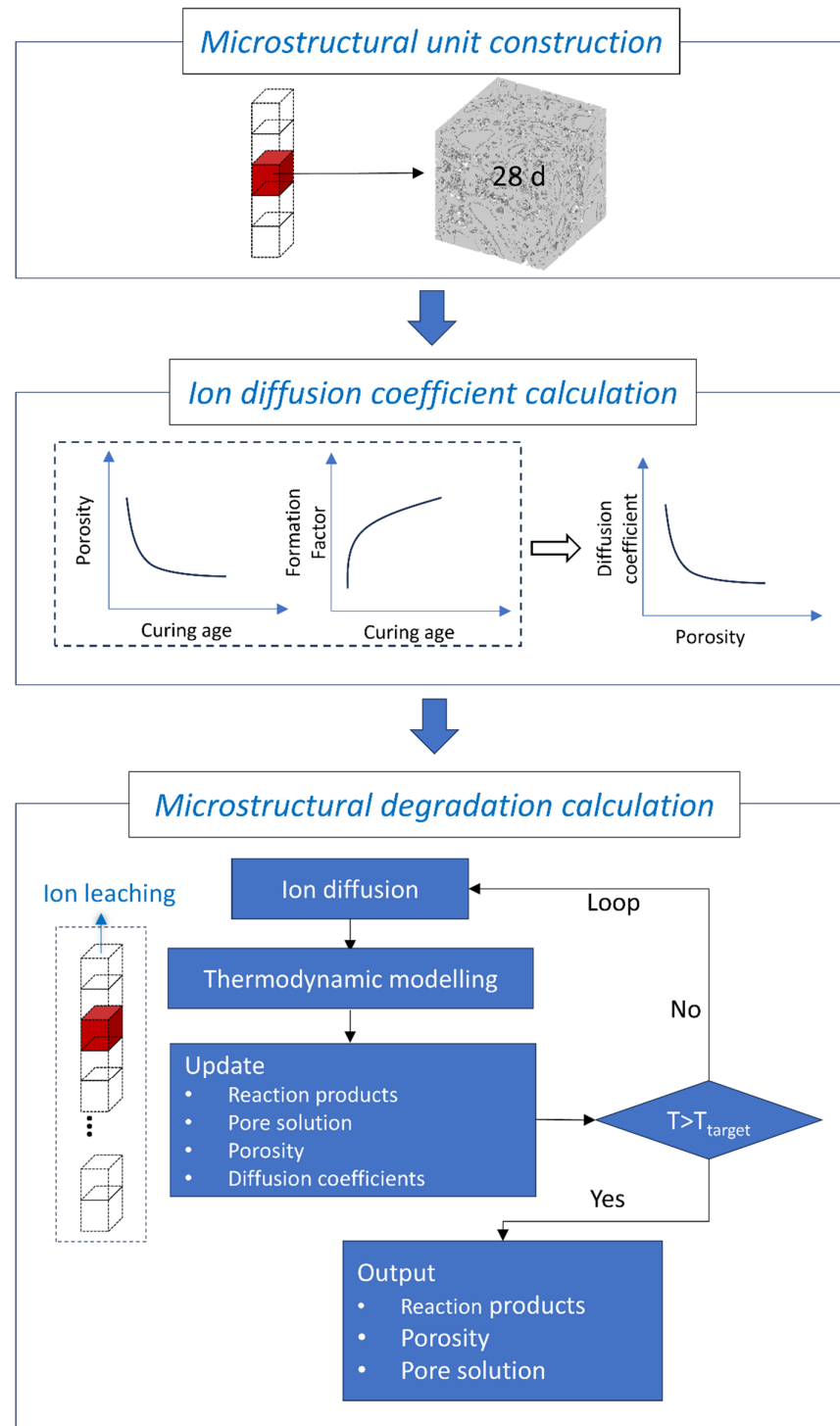


Figure 6.5. Flowchart of the modelling process for pore structure deterioration induced by leaching.

6.4 Experimental results and discussion

6.4.1 Pore structure analyses of AAS pastes subjected to water immersion

Figure 6.6 shows SEM images of the cross-sections of AAS pastes near the exposure front after 28 and 90 d of water immersion. The inner part of the NS paste exhibits no visible pores, indicating a denser microstructure compared to the NH paste. This increased density is attributed to the presence of soluble silicates in the NS activator, which facilitates the formation of C-(N-)A-S-H gels. This observation aligns with the MIP data in Chapter 8. Notably, the regions near the exposure front appear darker in all four pastes. This darkened area is more extensive in NH pastes than in NS pastes, and it increases over time, as demonstrated by the larger darkened region in NH_90d paste compared to NH_28d.

The grayscale level in BSE images corresponds to the intensity of the detected backscatter electrons, which are influenced by several factors: (1) Surface topography: raised areas emit more backscatter electrons and appear brighter. (2) Chemical composition: regions containing heavier elements (higher atomic mass) emit more electrons, resulting in brighter areas, whereas lighter elements or regions with lower atomic density appear darker. (3) Detector settings: parameters such as bias voltage and gain can affect the grayscale intensity, though these were kept consistent in this study.

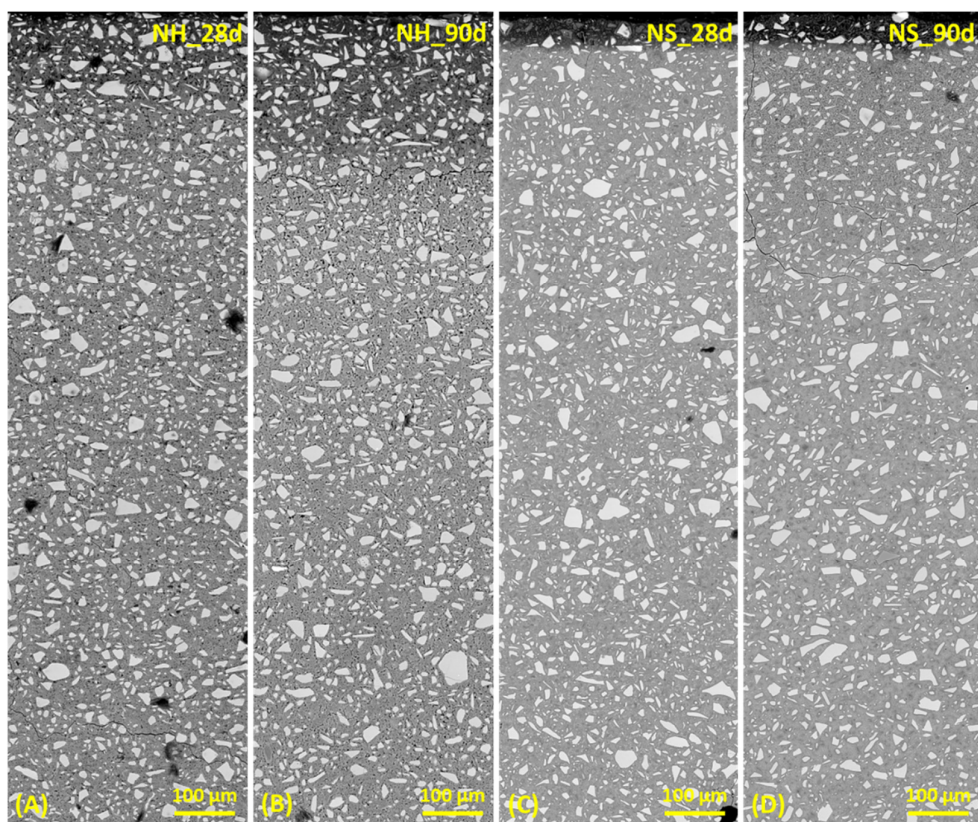


Figure 6.6. Representative BSE images of the cross-section of the exposure front of AAS pastes exposed to deionised water immersion for 28 and 90 d. (A) NH_28d; (B) NH_90d; (C) NS_28d; (D) NS_90d. The prefix denotes the type of alkaline activator, while the suffix refers to the duration of water immersion. The images have been adjusted to the same levels of brightness and contrast. The dirty black cluster indicates the presence of carbon from the coating process.

Given that the samples were thoroughly polished to ensure flatness at the local scale and imaged under identical conditions, the grayscale variations primarily reflect differences in the average atomic mass of the detected regions. The darker areas near the exposure front thus indicate a lower atomic mass. As mentioned in *Chapter 5*, the leaching of alkali ions lowers the pH of the pore solution of AAS pastes, which hinders further slag reactions and reaction product formation. On the other hand, continuous leaching can cause the decomposition of C-(N)-A-S-H gels. These processes result in a darker appearance (low greyscale intensity) in regions affected by leaching. Additionally, with the extension of exposure time, leaching progressively affects deeper regions of pastes, as evidenced by the more pronounced darkened region in NH_90d compared to NH_28d (*Figures 6.6A and B*).

Figure 6.7 shows the magnified images of the exposure front of NH and NS pastes after 28 and 90 d of water immersion. As shown in *Figures 6.7A and B*, the paste of NH_90d is more porous and appears darker than that of NH_28d, which is attributed to the longer exposure time. Additionally, the darkened region near the exposure front comprises not only visible pores but also areas of darkened paste, which indicate coarsening of undetectable small capillary and gel pores. At the magnification used (1000 \times), the pixel size in BSE images is approximately 400 nm, making pores smaller than this threshold indistinguishable. As shown in *Figures 6.7C and D*, the samples of NS_28d and NS_90d exhibit comparable depths of darkened pastes near the exposure front. However, the rim of slag in NS_90d is more evident than in NS_28d, probably due to the decomposition of gels or hydrotalcite-like phases around the slag particles [222].

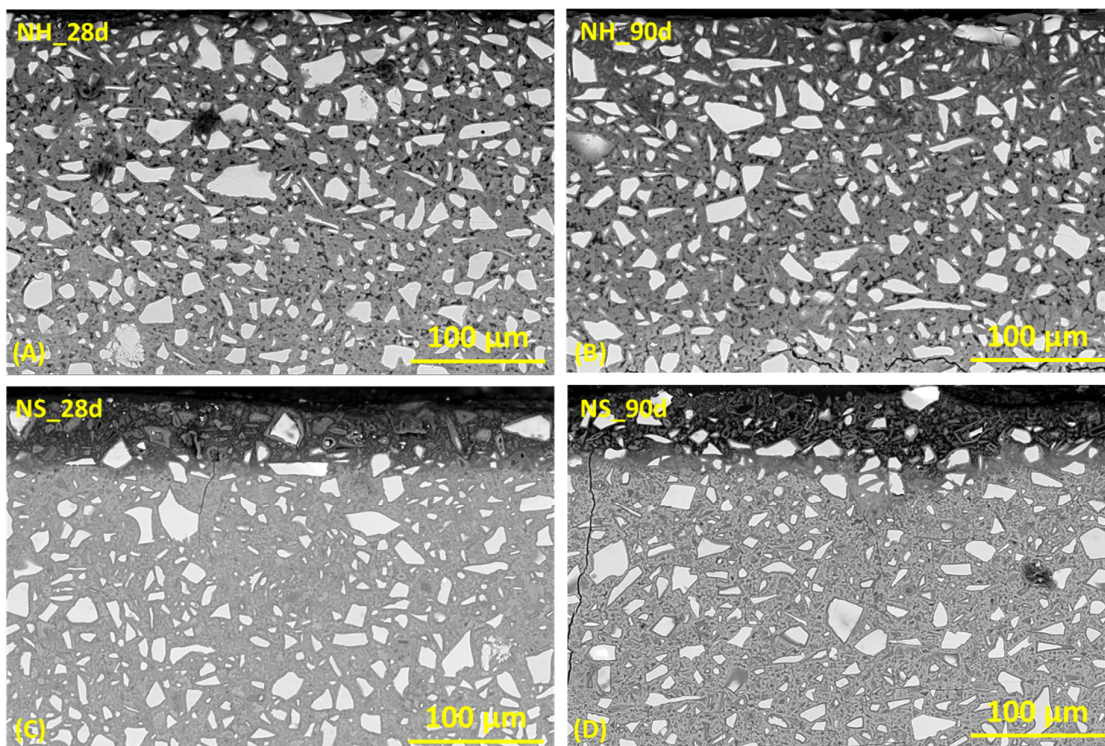


Figure 6.7. BSE images of the exposure front of NH and NS pastes after 28 and 90 d of water immersion. The images have been adjusted to the same levels of brightness and contrast.

To quantify porosity at different depths, an image processing method was applied to segment BSE images based on greyscale thresholds. This approach distinguishes visible pores and darkened paste, compensating for the pixel size limitations. *Figure 6.8* shows the segmentation process for the NH_90d sample using thresholds of 70 and 120. It is observed that different thresholds can screen different regions within the image. The region defined by a threshold below 70 (*Figure 6.8B*) encompasses the visible pores and cracks of the sample, along with a portion of the resin near the edge of the sample. In contrast, the region defined by a threshold below 120 (*Figure 6.8C*) is larger than that of 70, consisting exclusively of the darkened paste, as observed in *Figure 6.6*. These regions can be considered the coarsened small capillary and gel pores. Consequently, according to the thresholds of 70 and 120, the regions in AAS pastes can be segmented into three categories: 0 – 70 (large capillary pore), 70 – 120 (small capillary and gel pores), and 120 – 255 (dense paste region). Note that 255 is the upper limit of a greyscale image. This categorisation enables the quantification of porosity changes at varying depths and highlights the progression of microstructural deterioration due to leaching.

Figure 6.9A shows the content of large capillary pores in AAS pastes at different depths. The porosity of NH_28d and NH_90d pastes stabilises between 400 μm and 600 μm , approximately four to six times higher than that of NS_28d and NS_90d, which stabilises around 100 μm . This suggests that the matrix with a dense microstructure shows better resistance to water immersion.

Figure 6.9B shows the content of small capillary and gel pores at different depths. The NH_90d near the exposure front shows higher porosity than the NH_28d, indicating that the pore structure deterioration progresses over time. Both NS_28d and NS_90d show higher porosity near the exposure front than their inner parts, while their overall porosities are lower than those of NH_28d and NH_90d. This can be attributed to the decomposition of reaction products, as evidenced by the darkened slag (*Figure 6.7D*). Although NS pastes maintain a dense microstructure, the decomposition of reaction products occurs in the long term, increasing the small capillary and gel pores. Furthermore, the inner part of NH_90d shows lower porosity than NH_28d, attributed to the continued reaction of slag or the discrepancy of the general greyscale between the two pastes.

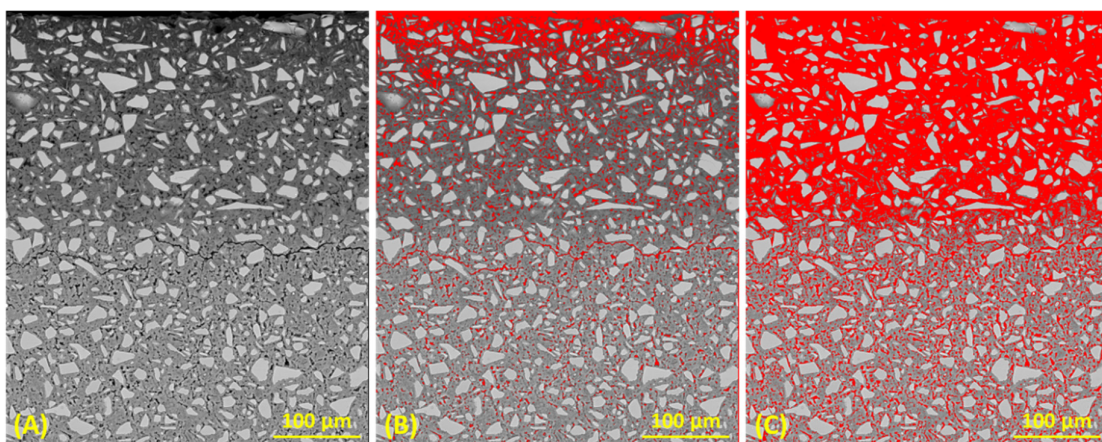


Figure 6.8. (A) Original BSE image of the exposure front of the NH_90d sample; (B) The image segmented by the greyscale threshold of 70; (C) The image segmented by the greyscale threshold of 120. The region highlighted in red represents that below the respective threshold values.

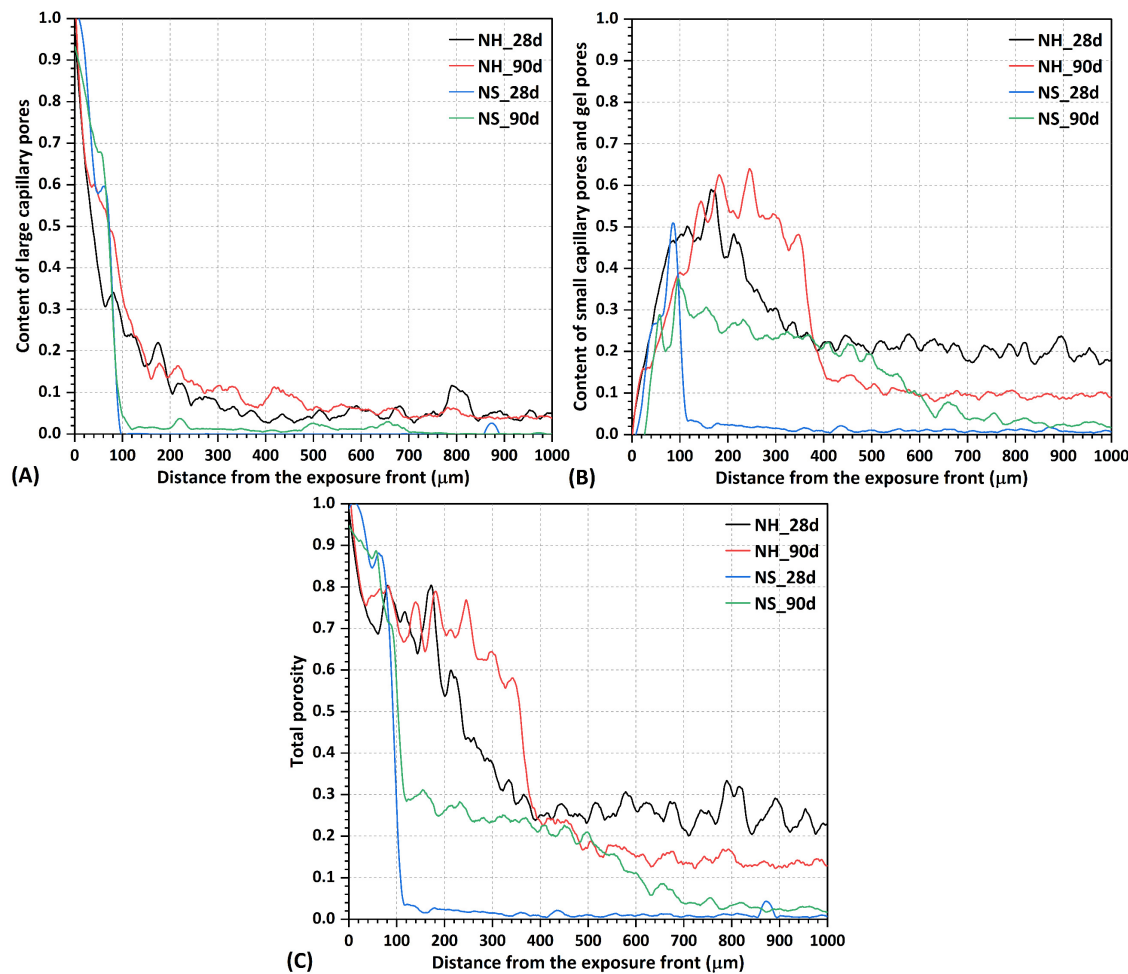


Figure 6.9. (A) porosity of large capillary pores; (B) porosity of small capillary and gel pores; (C) total porosity of AAS pastes at different depths from the exposure front. The porosities are determined by the greyscale range of 0 – 70, 70 – 120 and 0 – 120, respectively. It should be noted that the porosity at zero distance is nearly 1, attributed to the resin beyond the edge of the sample.

Figure 6.9C shows the total porosity of pastes, including both capillary and gel pores. The observed increase in total porosity is attributed to the synergistic effects of reduced reaction of slag and decomposition of reaction products. As discussed in Chapter 5, the leaching of alkali ions lowers the pH of the pore solution, inhibiting slag reactions and reducing the formation of reaction products. This results in a coarsened microstructure. In the meantime, the leaching of ions can disrupt the thermodynamic equilibrium between the reaction products and the pore solution, resulting in the decomposition of gels. Overall, the NS paste shows a better resistance to water immersion than the NH paste.

6.4.2 Elemental composition of AAS pastes subjected to water immersion

The EDX point analysis was conducted to examine the impact of leaching on the elemental composition of AAS pastes at three depths from the exposure front: “close” (0 – 360 µm), “medium” (360 – 720 µm), and “far” (720 – 1080 µm). *Figures 6.10A and B* show the relationship between the Na/(Si+Al) ratio and the Ca/(Si+Al) ratio in NH pastes. The Ca/(Si+Al) ratios remain relatively stable across the three regions in both NH_28d and NH_90d, ranging from 0.5 to 1.2, suggesting that 90 d of water immersion has little effect on this ratio. In contrast, the Na/(Si+Al) ratio shows greater variability. NH_90d pastes exhibit a lower Na/(Si+Al) ratio compared to NH_28d, indicating that Na ions are more susceptible to leaching than Ca ions in the gels. This finding aligns with MD simulation results from *Chapter 3*, where Ca demonstrated a higher dissolution free energy than Na in the same gel. Overall, no characteristic relationship between the Na/(Si+Al) and Ca/(Si+Al) ratios was observed.

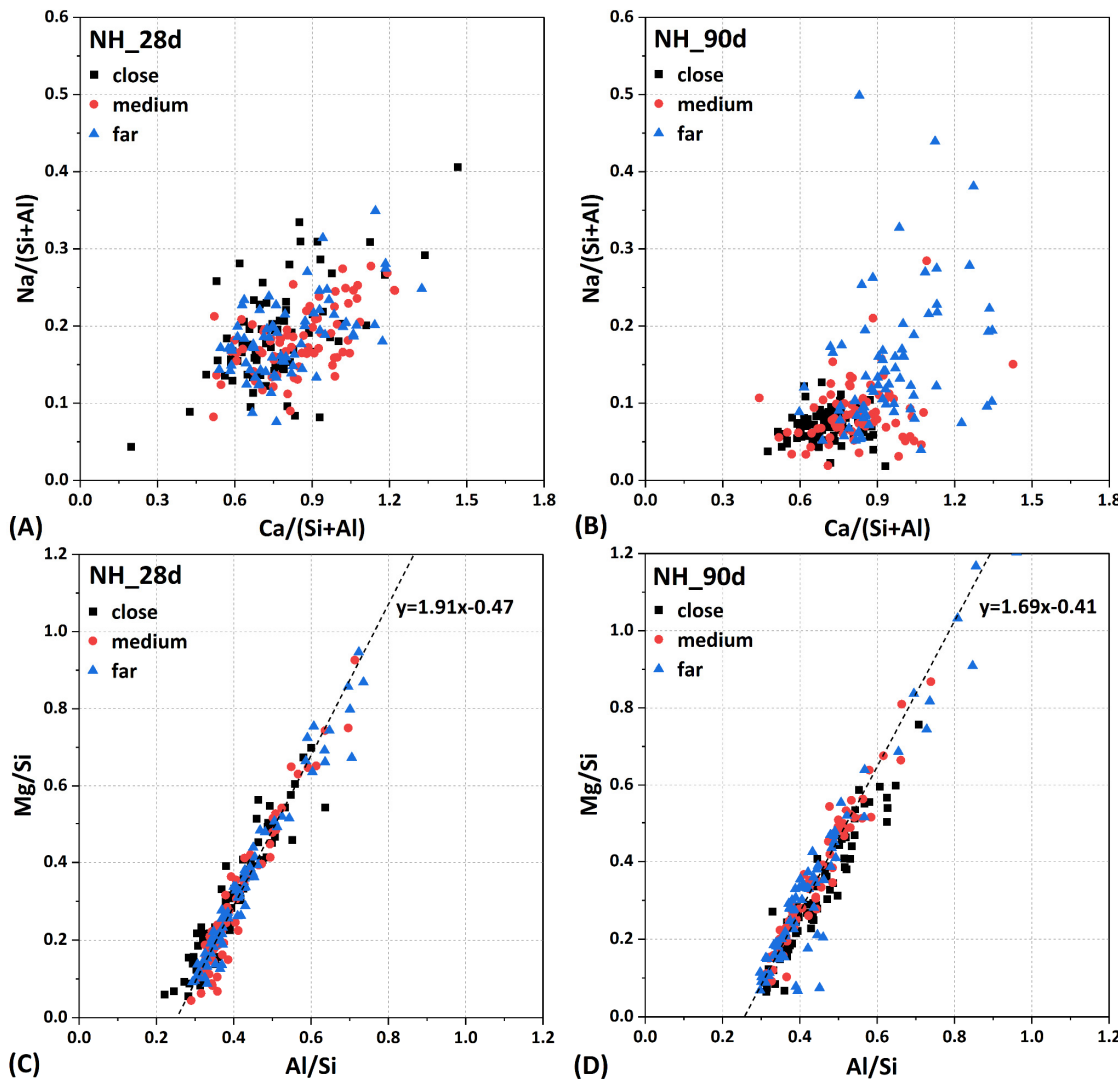


Figure 6.10. Elemental ratios of NH pastes at different depths from the exposure front after 28 d and 90 d of water immersion. The detected region ranges from 0 to 1080 µm away from the exposure front, which is further divided into three sections, namely “close” (0 – 360 µm), “medium” (360 – 720 µm) and “far” (720 – 1080 µm), respectively.

Figures 6.10C and D show the relationship between the Mg/Si ratio and the Al/Si ratio in NH pastes. A linear correlation between these ratios suggests the formation of hydrotalcite-like phases [222]. As described in *Chapter 5*, the slope of the trend line represents the Mg/Al ratio in the hydrotalcite, while the intercept on the X-axis reflects the Al/Si ratio in the rim of the slag. Data points from NH_28d and NH_90d overlap and follow a similar trend across all regions. The Mg/Al ratio decreases from 1.91 at 28 d to 1.69 at 90 d, indicating a reduction in the crystallization degree of hydrotalcite [222]. A similar phenomenon has also been observed in AAS paste under sealed conditions [194], though the underlying mechanism remains unclear. One possible explanation is the uptake of constantly dissolved Al by hydrotalcite. The Al/Si ratio of gels in the slag rim remains stable at approximately 0.25 for both NH_28d and NH_90d. This suggests the proportional dissolution of Si and Al from the gels.

Figures 6.11A and B show the Ca/(Si+Al) ratio of NH pastes at different depths after 28 and 90 d of water immersion. The Ca/(Si+Al) ratio of the NH_28d paste remains generally stable, with a slight reduction in the “0 – 120 µm” region compared to deeper regions. However, in NH_90d pastes, a more pronounced reduction is observed in the entire “close” region and the front portion of the “medium” region, indicating decalcification caused by the leaching of Ca ions. *Figures 6.11C and D* illustrate the Na/(Si+Al) ratio of NH pastes at different depths. In NH_28d pastes, the Na/(Si+Al) ratio is stable across all depths, fluctuating around 0.2. In contrast, NH_90d pastes show a noticeable decrease in the Na/(Si+Al) ratio compared to NH_28d, except in the “960–1080 µm” region, where the ratio is relatively higher. This trend confirms significant leaching of Na at 90 d, underscoring its lower stability compared to Ca.

Figures 6.10E and F show the Al/Si ratio of NH pastes at different depths. The Al/Si ratio remains stable during both 28 and 90 d of immersion, fluctuating around 0.4. This suggests a proportional dissolution of Si and Al from gels. Theoretically, the maximum Al/Si ratio in an aluminosilicate chain of gels should not exceed 0.33, as Al substitution can only occur at the bridging sites. The slightly higher observed Al/Si ratio (0.4) likely results from the coexistence of hydrotalcite and gel phases. *Figures 6.10G and H* show the Mg/Si ratio of NH pastes at different depths. The Mg/Si ratio remains relatively constant, ranging from 0.2 to 0.3. In AAS systems, the mobility of Mg is extremely low, being present in the slag rim (in the form of hydrotalcite-like phases) and in unreacted slag. Therefore, a constant Mg/Si ratio during 90 d of exposure implies a stable Si content in gels.

Figures 6.12A and B show the relationship between the Ca/(Si+Al) ratio and the Na/(Si+Al) ratio in NS pastes after 28 and 90 d of water immersion. In the NS_28d paste, the Ca/(Si+Al) ratio in the “medium” and “far” regions is comparable, ranging from 0.6 to 1.2, and is generally higher than in the “close” region. Some data points in the “close” region fall below 0.6, indicating paste decalcification. This decalcification is more pronounced in the NS_90d paste. Regarding the Na/(Si+Al) ratio, values in all regions of the NS_28d paste are comparable, ranging from 0.1 to 0.5, and are generally higher than those in NS_90d. The Na/(Si+Al) ratio in the close region of NS_90d is significantly lower than in the far region.

Figures 6.12C and D show the relationship between the Al/Si ratio and the Mg/Si ratio in NS pastes. The Mg/Al ratio in hydrotalcite decreases from 2.09 at 28 d to 1.63 at 90 d, consistent with the trend observed in NH pastes. The reduction is attributed to the uptake of Al by hydrotalcite [222]. The Al/Si ratio of gels in the slag rim is approximately 0.2 at both 28 and 90 d, slightly lower than the ratio observed in NH pastes (0.25). This difference is likely due to the additional Si introduced by the NS activators.

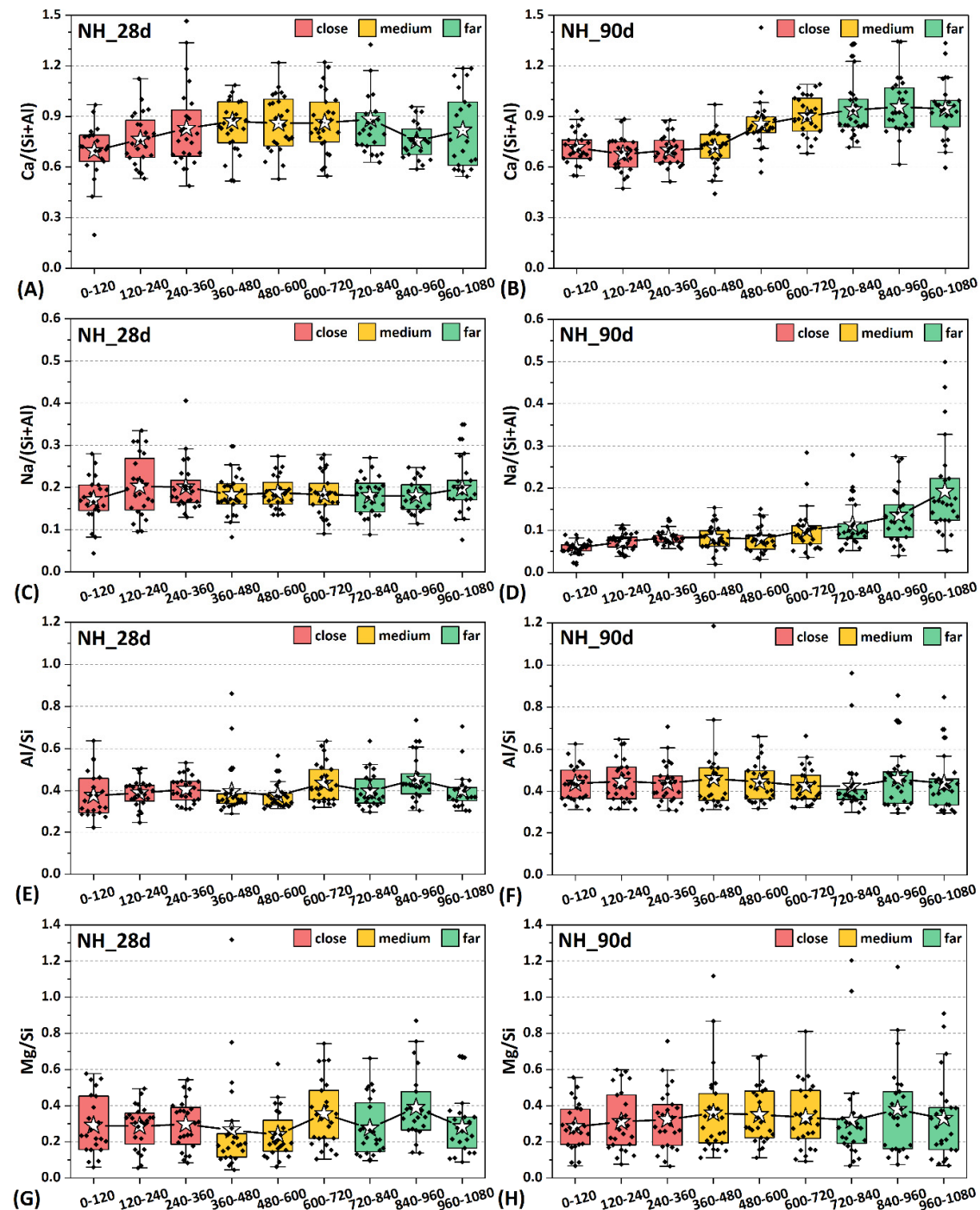


Figure 6.11. Box plot of the elemental ratio of NH pastes at different depths from the exposure front after 28 d and 90 d of water immersion. The top and bottom values of the box denote the 25th and 75th percentiles, respectively. The whiskers extend to the maximum and minimum data points, which are within the 1.5 times interquartile range. The white star in the box represents the average value of elemental ratios.

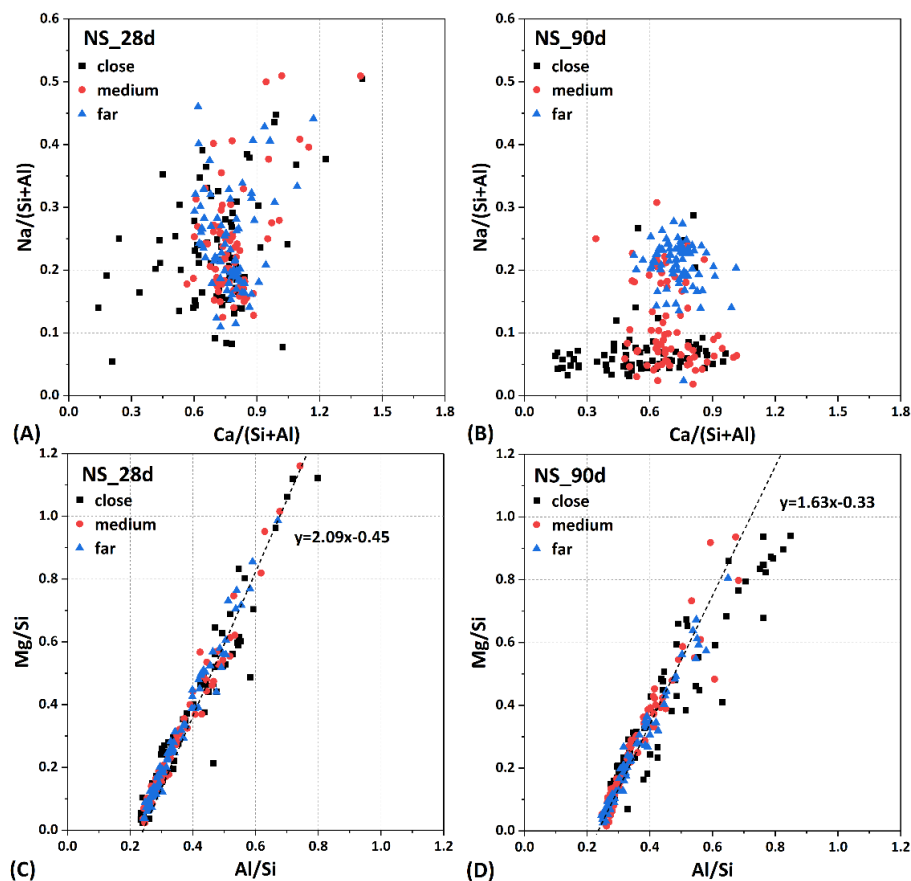


Figure 6.12. Elemental ratios of NS pastes at different depths from the exposure front after 28 d and 90 d of immersion. The detected region ranges from 0 to 1080 μm away from the exposure front, which is further divided into three sections, namely "close" (0 – 360 μm), "medium" (360 – 720 μm) and "far" (720 – 1080 μm), respectively.

Figures 6.13A and B show the Ca/(Si+Al) ratio of NS pastes at different depths after 28 and 90 d of water immersion. A notably lower Ca/(Si+Al) ratio of NS pastes is observed within 120 μm at 28 d, with a further decrease at 90 d at the same depth. This indicates progressive paste decalcification over time. The depletion of Ca, being a heavier element than Na, Al, and Si, prominently affects the greyscale of BSE images, contributing to the darkened areas near the exposure front of NS pastes (Figures 6.6C and D). Figures 6.13C and D show the Na/(Si+Al) ratio of NS pastes at different depths. At 28 d, the Na/(Si+Al) ratio remains stable, fluctuating between 0.2 and 0.3 across different depths. However, at 90 d, significantly lower values are observed in the "close" and "medium" regions, indicating substantial Na leaching. While Na can leach even through the dense structure of NS pastes, the depth of the leached region in NS pastes (0 – 720 μm) is shallower than in NH pastes (0 – 960 μm).

Figures 6.13E and F show the Al/Si ratio of NS pastes at different depths. At 28 d, the Al/Si ratio remains stable across all regions. However, at 90 d, higher values are observed at depths of "0 – 120 μm " region. A similar trend is noted for the Mg/Si ratio, as shown in Figures 6.13G and H. The darker appearance of NS pastes near the exposure front (Figure 6.7) is attributed to the predominance of slag rims and unreacted slag, with minimal outer reaction product gels. This darkened region is characterised by a high hydrotalcite content and a low gel content, resulting in elevated Al/Si and Mg/Si ratios within 120 μm . As discussed in Chapter

4, the synthetic C-(N-)A-S-H gel with a lower Ca/Si ratio shows a higher leaching loss of Si. Compared to NH pastes, the gel in NS pastes has a lower Ca/Si ratio, thereby leading to higher leaching losses of Si and higher Al/Si and Mg/Si ratios.

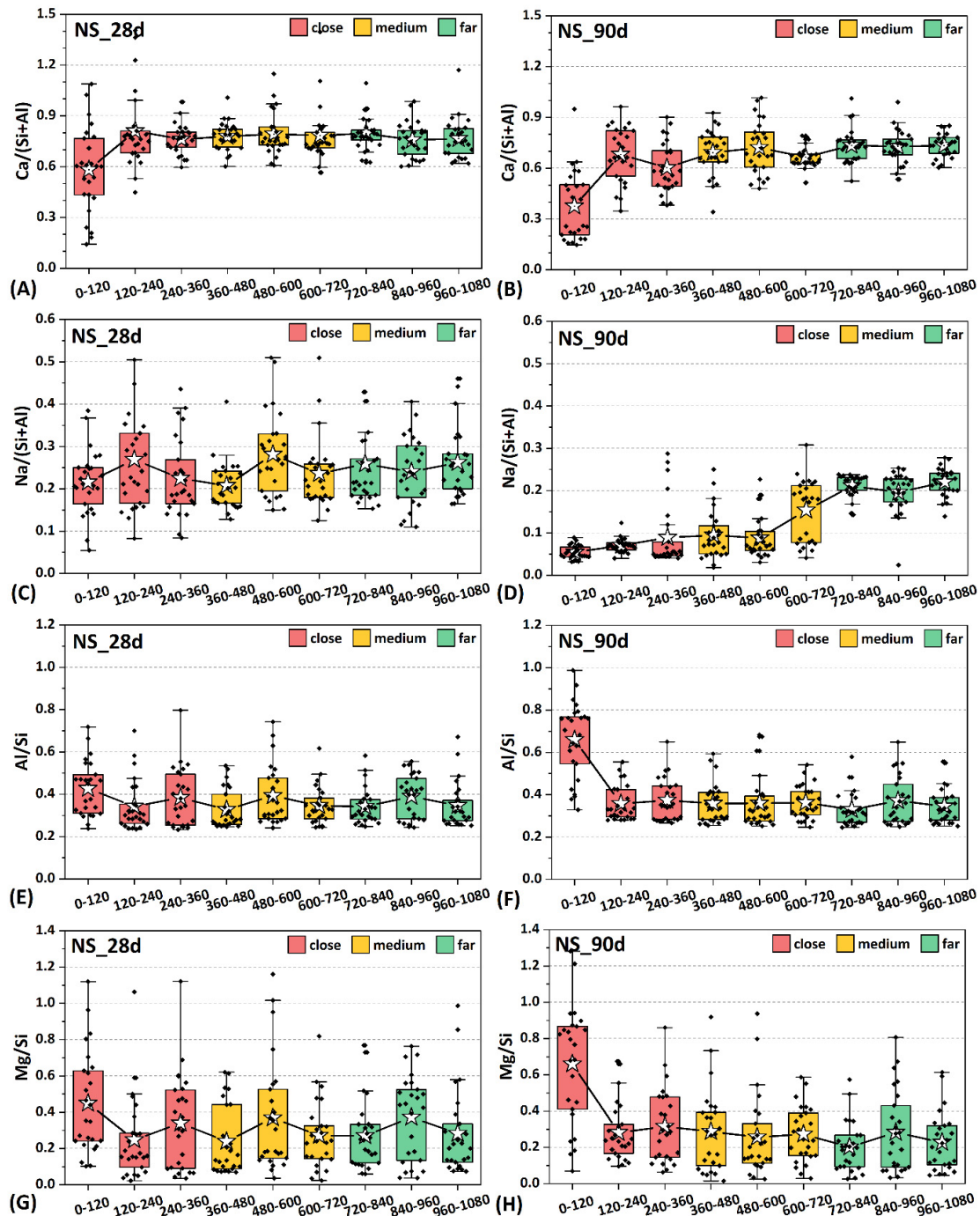


Figure 6.13. Box plot of the elemental ratio of NS pastes at different depths from the exposure front after 28 d and 90 d of water immersion. The top and bottom values of the box denote the 25th and 75th percentiles, respectively. The whiskers extend to the maximum and minimum data points, which are within 1.5 times interquartile range. The white star in the box represents the average value of elemental ratios.

6.5 Modelling results and discussion

6.5.1 Model validation

The chemical composition of the pastes, as measured in *Section 6.4*, consists of a mixture of different phases, making it challenging to compare the simulated phase composition with experimental data directly. To address this, porosity was used as the primary parameter for validating the model, as it is a critical indicator of microstructural degradation.

Figure 6.14 compares the simulated and experimental porosity of NH paste after 90 d of water immersion across different depths. It is observed that the porosities of the interior (or unaffected) part of the experimental and simulated pastes are comparable, demonstrating that Geomicro3D effectively simulates the porosity of NH pastes. However, the experimental porosity near the exposure front is significantly higher than the simulated porosity. This discrepancy could be attributed to a higher leaching rate of ions near the exposure front in experiments, leading to more severe degradation. Additionally, during sample preparation, solid particles at the edge of the sample might have been more extensively removed than those in the interior, leading to an uneven surface texture and artificially elevated porosity near the exposure front.

Despite these differences, the deterioration depths of the pore structure between the experimental and simulated results are consistent. This parameter is crucial for evaluating the extent of degradation caused by leaching. As shown in *Figure 6.14*, the depth at which porosity increases significantly is approximately 600 – 800 μm for both experimental and simulated results. Moreover, the porosity values in the inner regions of the paste are closely aligned between the two datasets. These findings confirm that the model is validated against experimental results, demonstrating its reliability for further analysis.

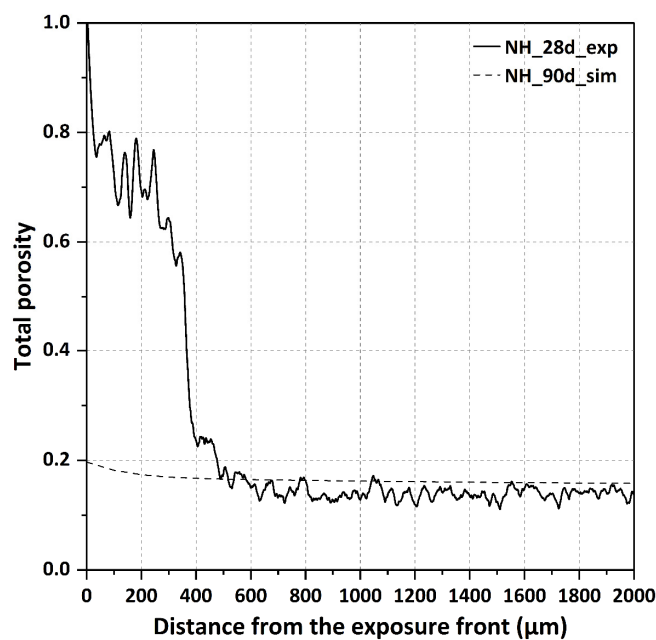


Figure 6.14. Comparison of simulated and experimental porosity of the NH paste at different depths from the exposure front. “exp”: experimental results; “sim”: simulated results. The porosity in this figure refers to the total porosity as shown in Figure 6.9C.

6.5.2 Pore solution

Directly measuring the ion concentration of the pore solution at different depths is challenging for experiments, but simulations provide a viable alternative. To determine ion concentrations at different depths, the initial ion concentrations of the NH paste at 28 d, without leaching, were first simulated using the Geomicro3D model. The simulated concentrations of key ions — Na, OH, Al, Si and Ca — are 2767, 2566, 6.96, 1.02 and 0.64 mmol/L, respectively. These values are comparable to the experimentally measured pore solution results of the NH paste in *Chapter 5*.

Figure 6.15 shows the simulated ion concentrations in the pore solution of NH pastes at different depths and exposure times. The concentrations of Na, OH and Al (Figures 6.15A–C) increase with depth while decreasing with exposure time. After 10 y of leaching, the ion concentrations in the simulated 100 mm of the NH paste are significantly lower than those of pastes without leaching. The trends in Si concentration (Figure 6.15D) follow a similar pattern to those of Na, OH and Al, whereas distinct peaks appear within the depth of 0.1–3 mm at 1, 5 and 10 y. These peaks become more pronounced over time, mainly due to the ion leaching from both the pore solution and reaction products. Specifically, in the early stages (before 180 d), the steep gradient of ion concentrations between the external water and the pore solution drives the leaching process, with ions in the pore solution contributing predominantly to leaching. However, with the extension of time, the chemical environment surrounding gels changes, probably leading to the decomposition and reorganisation of gels. The humps near the exposure front in *Figure 6.15D* can be attributed to the dissolved Si species released from gels. Similarly, the accumulation of Ca is observed near the exposure front, with a more pronounced effect than that of Si, suggesting the leaching of Ca from gels.

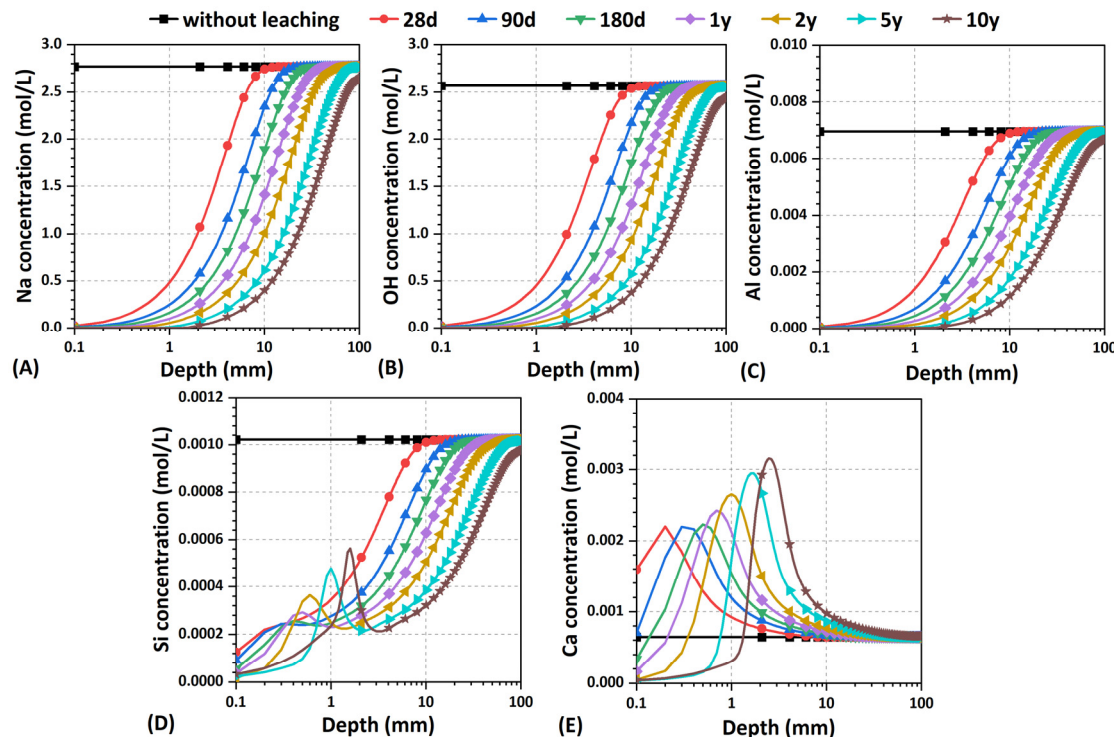


Figure 6.15. Simulated ion concentrations in the pore solution at different depths of the NH paste with leaching time. y: year.

6.5.3 Phase assemblage

Figure 6.16 shows the simulated phase assemblage of the NH paste at different depths from the exposure front with time. Generally, the volume of the aqueous solution increases with time, indicating the coarsening of the pore structure. This is attributed to the decomposition of reaction products (gels and hydrotalcite). The hydrotalcite-like phases remain relatively stable, with only slight reductions observed within 0.8 mm depth after 10 y of water immersion (Figure 6.16F). This stability aligns with the experimental results discussed above. On the contrary, gels are more prone to decomposition, initiating after 90 d of immersion (Figure 6.16B), consistent with the observation in Figure 6.6. By 10 y, gels have completely dissolved within the top 1 mm, leading to a reduction in both absorbed water and gel pore water contents.

The decomposition ratios of gels, absorbed water and gel water in the NH paste at different depths with time were calculated according to their initial contents before leaching, as shown in Figure 6.17. The decomposition behaviour of the gels closely resembles that of absorbed water due to the fixed proportion (*i.e.* 0.3 mol of water per mole of C-(N-)A-S-H gels). However, gel water shows a distinct trend, with a higher decomposition rate compared to gels and absorbed water at 90 d, 180 d and 1 y. This discrepancy suggests a volume change in gels caused by prolonged water immersion. To gain deeper insights, the evolution of gel phases with time was investigated.

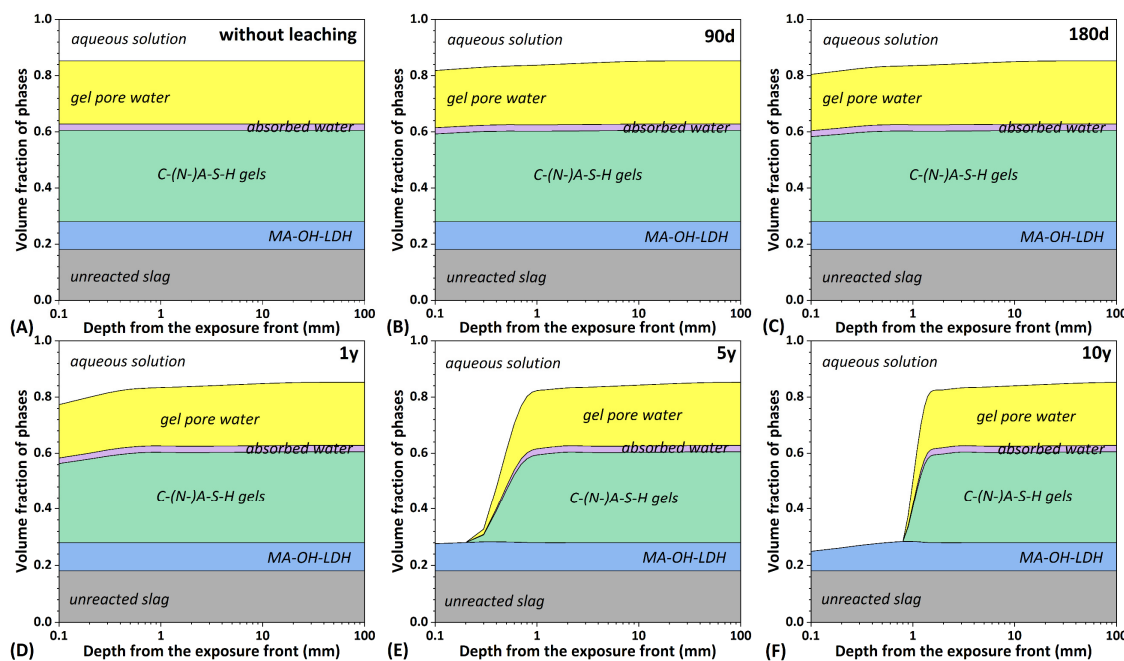


Figure 6.16. Simulated phase assemblage of the NH paste at different depths from the exposure front with time.

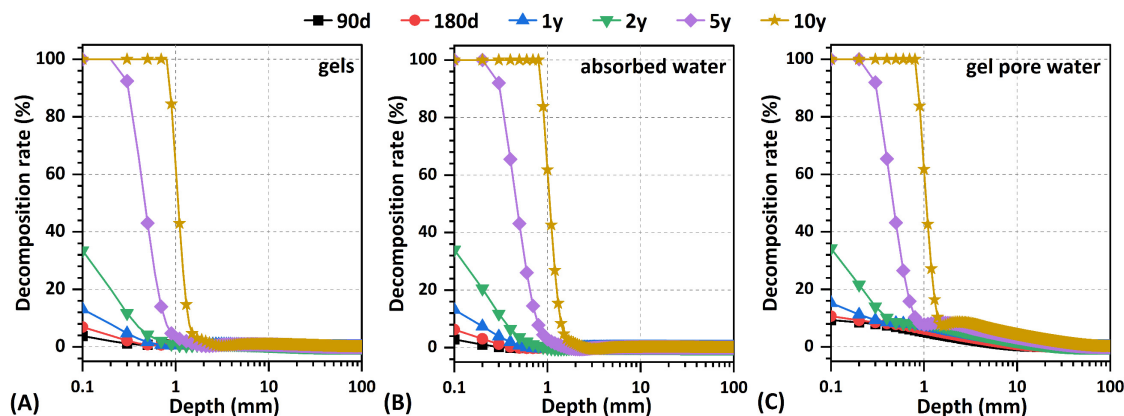


Figure 6.17. Decomposition ratio of gels, absorbed water and gel water in the NH paste at different depths from the exposure front with time.

Figure 6.18A shows the simulated volume of eight C-(N)-A-S-H end-members in the NH paste after 90 d of water immersion within a depth of 100 mm. The phase assemblage of gels changes with depth, stabilising at approximately 10 to 20 mm. Near the exposure front (within 20 mm), the paste shows lower contents of 5CNA, INFCNA, INFCN and T2C phases but higher contents of T5C, INFCA and 5CA phases compared to the inner part. According to the formulae and molar ratios of the eight C-(N)-A-S-H end-members in *Table 6.2*, this reorganisation of gel phases reflects the leaching of Na and Ca from gels. This finding is consistent with the EDX results presented in *Figures 6.11B and D*.

Moreover, as presented in *Table 6.2*, Na-containing gels show lower chemically bound water than other gels, indicating higher gel water content (the definition of simulated gel water is mentioned in *Section 6.3.1*). The leaching of Na triggers the transformation of gels into Na-free forms, which subsequently reduces the content of gel water. This reduction in gel water content explains the lower gel pore water contents observed in *Figure 6.17C*. Notably, the peaks in Ca and Si concentrations near the exposure front (*Figures 6.15D and E*) can also be attributed to this gel reorganisation process.

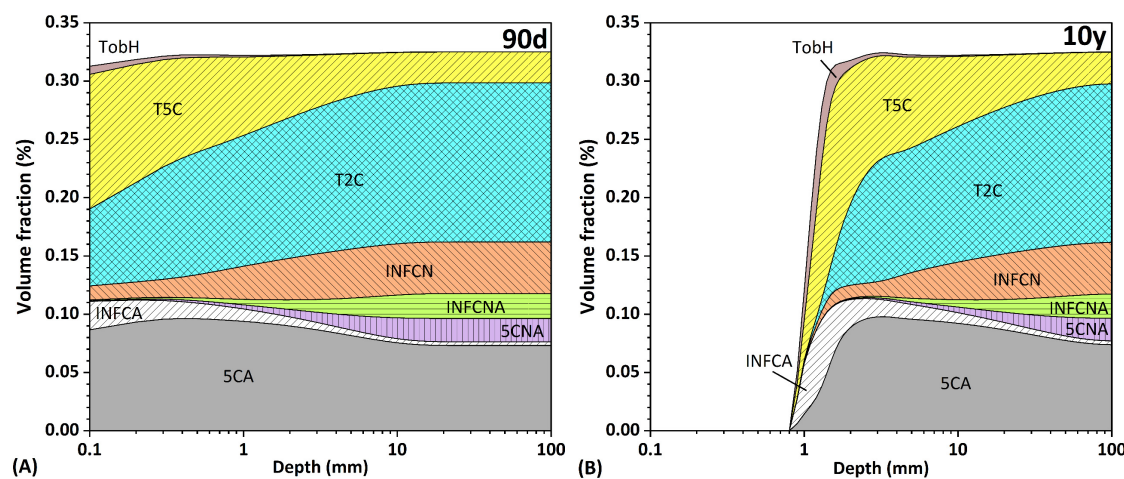


Figure 6.18. Simulated volume fraction of eight C-(N)-A-S-H end-members in the NH paste after (A) 90 d and (B) 10 y of water immersion within the depth of 100 mm.

Table 6.2. Formulae and molar ratios of eight C-(N-)A-S-H end-members.

	Names	Formulae	Molar ratios		
			Ca/Si	Al/Si	Na/Si
C-A-S-H gels	5CA	$(\text{CaO})_{1.25} \cdot (\text{Al}_2\text{O}_3)_{0.125} \cdot (\text{SiO}_2)_1 \cdot (\text{H}_2\text{O})_{1.625}$	1.25	0.25	0
	INFCA	$(\text{CaO})_1 (\text{Al}_2\text{O}_3)_{0.15625} (\text{SiO}_2)_{1.1875} (\text{H}_2\text{O})_{1.65625}$	0.84	0.26	0
C-N-A-S-H gels	5CNA	$(\text{CaO})_{1.25} (\text{Na}_2\text{O})_{0.25} (\text{Al}_2\text{O}_3)_{0.125} (\text{SiO}_2)_1 (\text{H}_2\text{O})_{1.375}$	1.25	0.25	0.5
	INFCNA	$(\text{CaO})_1 (\text{Na}_2\text{O})_{0.34375} (\text{Al}_2\text{O}_3)_{0.15625} (\text{SiO}_2)_{1.1875} (\text{H}_2\text{O})_{1.3125}$	0.84	0.26	0.58
	INFCN	$(\text{CaO})_1 (\text{Na}_2\text{O})_{0.3125} (\text{SiO}_2)_{1.5} (\text{H}_2\text{O})_{1.1875}$	0.67	0	0.42
C-N-S-H gels	T2C	$(\text{CaO})_{1.5} (\text{SiO}_2)_1 (\text{H}_2\text{O})_{2.5}$	1.50	0	0
C-S-H gels	T5C	$(\text{CaO})_{1.25} (\text{SiO}_2)_{1.25} (\text{H}_2\text{O})_{2.5}$	1.00	0	0
	TobH	$(\text{CaO})_1 (\text{SiO}_2)_{1.5} (\text{H}_2\text{O})_{2.5}$	0.67	0	0

Figure 6.18B shows the simulated volume of eight C-(N-)A-S-H gel phases in the NH paste after 10 y of water immersion within a depth of 100 mm. The content of gels shows a substantial reduction within a depth of 1 mm. The region affected by the gel reorganisation extends to approximately 80 mm, much broader than at 90 d. While this reorganisation has minimal impact on the overall porosity of the paste, it could potentially affect the mechanical integrity of the matrix, particularly in the presence of microcracks. Specifically, the redistribution of gel phases may contribute to microcrack propagation, a concern that will be further discussed in Chapter 7.

6.5.4 Pore structure

Figure 6.19 shows the simulated porosity of NH pastes at different depths from the exposure front over time. As shown in Figure 6.19A, the porosity increases both as the distance to the exposure front decreases and with prolonged exposure time, emphasising that leaching is a depth- and time-dependent issue. After 10 y of water immersion, the porosity within 1 mm of the exposure front is 6 to 7 times higher than that at 28 d. As indicated by Figure 6.16F, this significant increase in porosity is primarily attributed to gel decomposition, leaving only unreacted slag and hydrotalcite behind.

Additionally, Figure 6.19A shows substantially increased porosity of pastes within about 1.5 mm from the exposure front after 10 y of water immersion, implying significant microstructural deterioration. Beyond this depth, long-term immersion appears to have minimal visible impacts. However, Figure 6.19B, which plots porosity between 0.14 and 0.18 on a linear x-axis, reveals that long-term immersion affects the interior as well. After 10 y, the paste exhibits increased porosity throughout the simulated 100 mm depth than that without leaching, indicating subtle but measurable interior degradation.

As outlined in section 6.3.3, the diffusion coefficient of ions is closely correlated with porosity. The leaching of ions promotes the dissolution of reaction products, progressively coarsening the microstructure. This coarser microstructure further accelerates ion dissolution, which in turn exacerbates the coarsening process. In summary, prolonged water exposure leads to substantial degradation of the paste close to the exposure front, while inducing a minimal coarsening of the pore structure in the inner part.

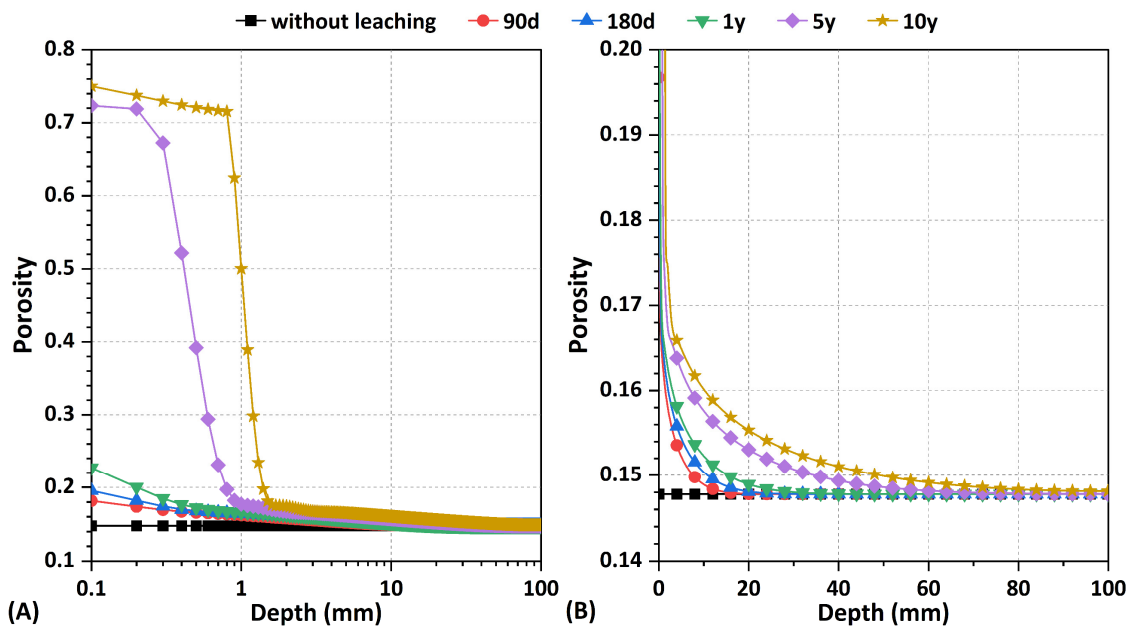


Figure 6.19. Simulated porosity of the NH pastes at different depths from the exposure front with time. (A) plotted on a logarithmic x-axis (Log10); (B) plotted on a linear x-axis.

6.6 Conclusions

In this chapter, the degradation of AAS pastes induced by water immersion at different depths was studied experimentally and numerically. In the experiments, NH and NS pastes were sealed for 28 d, followed by immersion in deionised water for up to 90 d. Pore structure deterioration was observed near the exposure front in both NH and NS pastes. For large capillary pores (those larger than 400 nm), the degraded depth in the NH paste after 90 d of water immersion reached 600 μ m, approximately 6 times higher than that of the NS paste. However, when small capillary and gel pores were included, the degraded depth of the two pastes became comparable at 90 d, though the total porosity of the NS paste was still lower than the NH paste. Additionally, significant reductions in the Na/(Si+Al) ratio and slight decalcification were identified near the exposure front in both pastes. Hydrotalcite remained generally stable, though with a reduction in the Mg/Al ratio. The stability of Si in the C-(N-)A-S-H gels of the NS paste was lower than that in the NH paste. Overall, NS pastes demonstrated better resistance to leaching compared to NH pastes.

A thermodynamics-based diffusion-dissolution model was developed to further understand and predict the impact of leaching on NH pastes to a depth of 100 mm. The ion concentration in the pore solution generally decreased over time, with the entire 100 mm depth being affected after 10 y of leaching. The leaching of ions disrupted the equilibrium between the reaction products and the liquid phases. Significant decomposition of gels was identified within the depth of 1.5 mm at 10 y, leading to substantial degradation of the paste close to the exposure front. While the leaching of Na induced the reorganisation of gel phases throughout the whole 100 mm depth at 10 y, it resulted in only minimal coarsening of the microstructure across the simulated region. Generally, the simulated results aligned with the experimental findings, making this model an effective tool for predicting the degradation of AAS materials subjected to water immersion.

Chapter 7

Cracking of AAS pastes induced by water immersion

7.1 Introduction

In *Chapter 5*, the degradation of AAS pastes subjected to water immersion has been investigated. Leaching was identified as the primary factor driving this degradation, as it reduces the pH of the pore solution, diminishes the reaction of slag and triggers the decomposition of gels. Building on this, *Chapter 6* introduces a diffusion-dissolution model to further explore the microstructural deterioration in AAS pastes with depth, offering essential insights for predicting the durability of these materials in aqueous environments. Additionally, as summarised in *Chapter 2*, previous studies [14,15,50] have documented cracking problems in AAS materials under humid conditions. However, the underlying mechanisms remain unclear.

In this chapter, the cracking mechanisms of AAS pastes induced by water immersion are studied by means of experiments and modelling. AAS pastes were produced using alkaline activators with different silicate moduli (0, 0.5, 1, 1.5). First, the compressive and flexural strength of pastes cured with and without water immersion were compared. Second, the chemical properties of AAS pastes before and after immersion were analysed, including phase assemblage, paste chemistry, gel structure and the leaching stability of gels. Transport properties, such as pore volume, pore size distribution, and saturation degree, served as inputs for modelling the water transport in AAS materials. Based on the experimental and modelling results, this chapter elucidates the chemical and physical mechanisms driving cracking in AAS pastes and proposes potential strategies to mitigate this issue.

7.2 Methodology

7.2.1 Outline of this chapter

The outline of *Chapter 7* is presented in *Figure 7.1*. In terms of chemical aspects, firstly, the phase assemblage of AAS pastes before and after immersion in deionised water was analysed using XRD, which was used to identify any newly formed phases during immersion. Secondly, the paste chemistry before water immersion was measured by SEM with EDX detectors. Thirdly, leaching tests on powdered AAS pastes were conducted to specifically investigate the leaching behaviour of gels in different AAS pastes. Finally, FTIR was performed to assess the structural change of gels in AAS pastes induced by leaching. As for physical aspects, the finite element method (FEM) was used to simulate water ingress via capillary suction in AAS pastes. To gain the input, the water content (or saturation degree) of AAS pastes before water immersion was measured. The porosity and pore size distribution of pastes were characterised by MIP and N₂ absorption tests. Eventually, based on experimental and simulated results, some potential mitigation strategies to address the cracking issue of AAS materials subjected to water-exposed conditions were proposed.

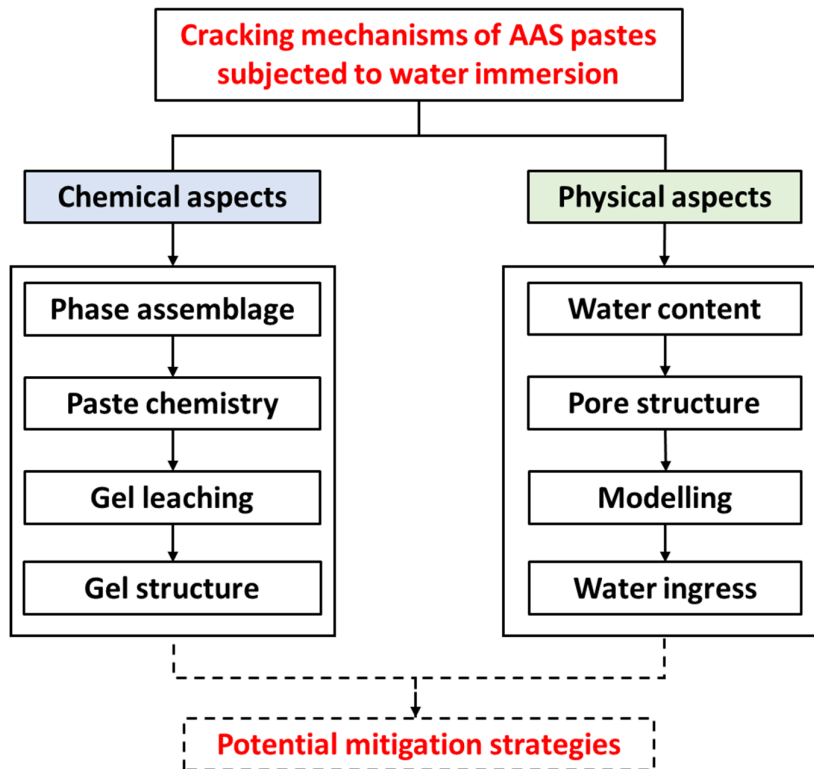


Figure 7.1. Outline of Chapter 7.

7.2.2 Materials and mixtures

The physical and chemical properties of slag used in this chapter are consistent with those in the above chapters (*Table 5.1*). Four types of alkaline activators with silicate modulus of 0, 0.5, 1 and 1.5 were prepared, using NaOH solution (50 wt.%), Na₂SiO₃ solution (8.25 wt.% Na₂O, 27.5 wt.% SiO₂, and 64.25 wt.% water), and deionised water. The mixture design of AAS pastes is presented in *Table 7.1*. The slag is activated using alkali activators with different silicate moduli, referred to as $m = 0, 0.5, 1$ and 1.5 , respectively. This aims to cover the range of silicate moduli used in AAS materials as much as possible. The fresh AAS pastes were prepared at room temperature using a Hobart mixer. The paste was then cast in 4 cm × 4 cm × 16 cm moulds for the flexural and compressive strengths and polyethene bottles (ϕ 35 mm × 70 mm) for other characterisations.

Table 7.1. Mixture proportions of AAS pastes.

	Slag (g)	SiO ₂ (mol)	Na ₂ O (mol)	Water (g)
$m=0$	1000	0	0.8	430
$m=0.5$	1000	0.4	0.8	430
$m=1$	1000	0.8	0.8	430
$m=1.5$	1000	1.2	0.8	430

7.2.3 Experimental methods

Flexural and compressive strength tests

The 4 cm × 4 cm × 16 cm AAS prisms were initially sealed for 7 d and subsequently exposed to either sealed or water-immersed conditions for an additional 7 d. The strength of specimens labelled as “7 s”, “7 s + 7 s” and “7 s + 7 w” was measured. These labels refer to “7 d of sealed curing”, “7 + 7 d of sealed curing” and “7 d of sealed curing followed by 7 d of water immersion”, respectively. For flexural strength, a loading rate of 0.05 kN/s was applied, with three replicates per mixture. Following the flexural strength test, the six halves of the prisms were used to measure compressive strength, using a loading rate of 2.4 kN/s. Detailed procedures of flexural and compressive strengths were shown in [167].

XRD tests

AAS samples were first sealed in the aforementioned polyethylene bottles for 7 d. Then, the samples were crushed into approximately 2 – 4 mm pieces before being exposed to deionised water for 7 d. Finally, the piece samples after exposure were immersed in isopropanol and ground into fine powder to stop the reaction. After being dried in a vacuum oven at 25 °C for 7 d, the powdered sample underwent scanning within the range of 5 – 70° with a step size of 0.02° and a swell time of 5s per step.

SEM and EDX tests

The elemental composition of AAS pastes sealed for 7 d was analysed. The sample preparation process and equipment used were identical to those described in *Chapter 6*.

ICP-OES and FTIR tests

ICP-OES was performed to investigate the leaching behaviour of gels in AAS pastes using a PerkinElmer Optima 5300DV. To isolate the effects of gel leaching from the influence of pore solution, reaction-arrested powdered samples (sealed for 7 d) were employed. As for leaching tests, precisely 0.500 g (± 0.03) of the samples was added to a polyethylene bottle containing 30.0 g (± 0.1) of deionised water. After standing for 7 d, the leachate was filtered and the concentration of Si, Al, Ca and Na was measured. The solid residue was dried in a vacuum oven at 25 °C. After that, FTIR was carried out to detect the structural change of gels with and without leaching.

MIP and N₂ absorption tests

MIP was conducted using a Micrometrics PoreSizer 9500 to obtain the open porosity and pore size distribution of AAS pastes. The correlation between pore diameter (D) and pore pressure (P) is built by the Washburn equation [223] as presented in *Equation 7.1*.

$$P = -\frac{4\gamma \cos \theta}{D} \quad (7.1)$$

where the γ is the surface tension of mercury, 0.485 N/m at 25 °C; θ is the contact angle between samples and mercury, 141° in this work.

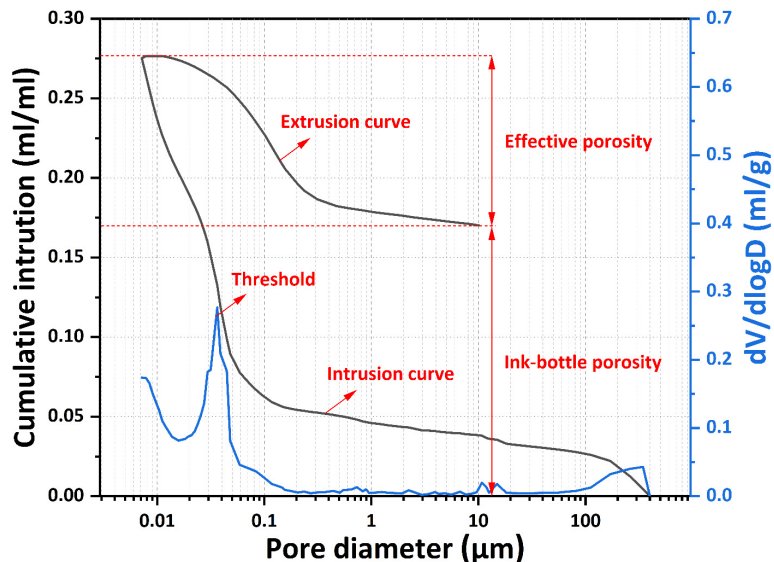


Figure 7.2. Schematic representation of effective porosity, ink-bottle porosity and threshold pore diameter obtained from MIP results.

Three procedures were involved in each measurement, including mercury intrusion at low pressure from 0 to 0.170 MPa; mercury intrusion at high pressure from 0.170 to 210 MPa; and mercury extrusion. According to *Equation 7.1*, the pore diameter detectable by this method ranged from 7 nm to 400 μm . The “effective porosity”, “threshold/critical pore diameter”, and “ink-bottle porosity” can be deduced from the MIP results as presented in *Figure 7.2*. Effective porosity refers to pore volume that is interconnected and capable of contributing to fluid flow or permeability. “Ink-bottle” is connected to the surface or other pores through narrower throats. These pores can retain mercury due to the smaller throats that prevent its egress during pressure release. The threshold/critical pore diameter corresponds to the point on the intrusion curve where a significant increase in cumulative intrusion is observed, indicating the entry of mercury into a dominant pore size range. Since the pore diameter of $m = 1$ and $m = 1.5$ AAS pastes was below the detection limit of MIP equipment, N_2 absorption tests were conducted by a Micrometrics Gemini VII 2390 V1.03 to identify pores ranging from 0.3 nm to 300 nm. The detailed N_2 absorption test method can be found in *Chapter 5*.

Water content tests

The water content (or saturation degree) of AAS pastes was measured before water immersion. The samples were sealed for 7 d, crushed into 2 – 4 mm pieces, and their initial mass (m_i) was recorded with an accuracy of 0.001 g. Then, the samples were dried in an oven at 40 °C to a constant mass (m_d). Finally, the samples were fully submerged in deionised water under vacuum conditions until saturation, with the saturated mass (m_s) recorded. Notably, the leaching loss of Na (m_{Na}) was also taken into account during the test, due to its significant leaching as observed in previous chapters. The ion concentration of Na in the leachate was measured, and the leaching amount was incorporated. As a result, the saturation degree of AAS samples was calculated using *Equation 7.2*.

$$S = \frac{m_i - m_d}{m_s - m_d + m_{\text{Na}}} \times 100\% \quad (7.2)$$

Using this method, the saturation degrees of AAS pastes with silicate moduli of 0, 0.5, 1 and 1.5 after 7 d of sealed curing were determined to be 94.6%, 93.8%, 92.3% and 90.2%, respectively.

7.2.4 Numerical simulation

7.2.4.1 Governing equations

Richards' equation describes the water flow in an unsaturated porous medium, driven by gravity and capillary force while neglecting the movement of the non-wetting phase, typically air [224,225]. Richards' equation is a simplified form of the standard two-phase flow model for gas and liquid phases in a porous medium. It assumes that the pressure gradient needed to drive the flow of the gas phase can be neglected, owing to the significant mobility contrast between the water and gas phases. Generally, Richards' equation is presented in three different forms: (1) the "mixed form", which incorporates both water saturation and pressure head; (2) the "head-based form", which is expressed entirely in terms of pressure head; and (3) the "saturation-based form", which focuses on water saturation rather than pressure head. In this case, water movement in AAS pastes is driven by the capillary suction (pore pressure). The pressure head was not considered in this study, as it was negligible compared to the capillary pressure. The transient state formulation of Richards' equation used in this study is expressed as:

$$\frac{\partial \theta}{\partial t} = \nabla \cdot (K_\theta \nabla p) \quad (7.3)$$

where θ is the water content (m^3/m^3), K_θ is the unsaturated water permeability of pastes (m^2/s), and p is the pore pressure (N/m^2).

If the capillary diffusivity (D_θ) is defined as *Equation 7.4* [226], the Richards' equation can also be formulated as *Equation 7.5*.

$$D_\theta = K_\theta \frac{\partial p}{\partial \theta} \quad (7.4)$$

$$\frac{\partial \theta}{\partial t} = \nabla \cdot (D_\theta \nabla \theta) \quad (7.5)$$

Zhou et al. [229] studied the correlation between unsaturated water permeability (K_θ), open porosity (φ) and water content (θ) in PC-based materials. Given that AAS materials share a similar morphology of pore distribution with PC-based materials [230], K_θ of AAS pastes can be calculated via *Equation 7.6*.

$$K_\theta = \frac{\varphi^2}{50B^2\mu} \left(1 - \left[1 - \ln\left(1 - \frac{\theta}{\varphi}\right)\right] \left(1 - \frac{\theta}{\varphi}\right)\right)^2 \quad (7.6)$$

where μ is the dynamic viscosity of water.

By substituting *Equations 7.5* and *7.6* into *Equation 7.4* and performing some algebraic manipulations, the resulting expression for the capillary diffusivity (D_θ) is obtained:

$$D_\theta = \frac{C\gamma \cos \theta_c}{25B\mu} \frac{\varphi^2}{(\varphi - \theta) \ln^2(1 - \frac{\theta}{\varphi})} \left(1 - \left[1 - \ln\left(1 - \frac{\theta}{\varphi}\right)\right] \left(1 - \frac{\theta}{\varphi}\right)\right)^2 \quad (7.7)$$

7.2.4.2 Numerical implementation

A 2D finite element model was developed to simulate water transport across a 4 cm \times 4 cm cross-section in the middle of the prism. This model was implemented using ABAQUS software, which has been validated in previous studies for simulating water and chloride diffusion in cementitious materials [227,228]. Water transport in porous media was modelled using the heat transfer module in ABAQUS. This approach leveraged the similarity between water transport (based on Fick's second law) and heat transfer phenomena. The comparison between heat transfer and water transport is shown in *Appendix A Equations A1 and A2*, and *Table A1*.

The non-steady state of unsaturated water transport was simulated using a 4-node linear quadrilateral element. The porosity and water content of AAS pastes obtained from experiments were used as inputs. Since the samples were initially cured under sealed conditions before being exposed to water, the porosity and water content were assumed to be homogeneously distributed across the entire simulated cross-section. The pore structure was also assumed to be constant, and all the pores in the media were permeable during capillary suction.

According to *Equation 7.7*, the capillary diffusivity (D_θ) of AAS pastes was calculated based on variations in water content (θ). Since the saturation degree (θ/φ) in *Equation 7.7* cannot reach 1, it is capped at 0.999 for calculations. *Appendix A Figure A2* shows the relationship between D_θ and θ of AAS pastes with different silicate moduli. Detailed input parameters for the water transport model of four AAS pastes are listed in *Appendix A, Table A2*. Given the observed cracking in $m = 1.5$ AAS paste prisms after 1 h of water immersion (*Appendix A, Figure A1*) and the rapid nature of the capillary suction process, I will concentrate on simulating the water content distribution during the first hour for all four pastes. In this modelling, an iterative nonlinear solver based on the Newton-Raphson method was implemented in ABAQUS to address the material nonlinearity problem.

7.3 Experimental results

7.3.1 Strength

Figure 7.3A shows the flexural strength of AAS pastes under different conditions. Under sealed conditions, the flexural strength of all four pastes increases with time but does not show an increasing trend with the increase of silicate modulus. In principle, a higher silicate modulus provides a higher content of soluble Si, promoting gel formation and microstructural densification [126]. This densification is theoretically associated with higher flexural strength. However, the finer microstructure resulting from higher silicate moduli also generates significant pore pressure from unsaturated menisci, leading to high internal stress and shrinkage [229,230]. Consequently, microcracks frequently develop in pastes with higher silicate moduli. As the flexural strength is sensitive to microcracks, the flexural strengths of $m = 1$ and $m = 1.5$ are lower than those of $m = 0.5$ at the same ages. Additionally, the paste of $m = 0$ exhibits the lowest flexural strength among all groups, attributed to its relatively porous microstructure.

The flexural strength of AAS pastes after water immersion exhibits different trends compared to those under sealed conditions. For the $m=0$ paste, the flexural strength under “7 s + 7 w” is higher than that under “7 s + 7 s”, while the flexural strength of the other three prisms activated by sodium silicate is lower than that before immersion. This is because water ingress into the relatively porous paste ($m = 0$) can mitigate the shrinkage, reducing internal stress and minimising the development of microcracking. As a result, water immersion is conducive to the flexural strength development of pastes with a low silicate modulus at early ages. In contrast, the flexural strength of the other three pastes ($m = 0.5$, $m = 1$, $m = 1.5$) decreases after immersion, with the extent of the reduction correlating with an increase in silicate modulus.

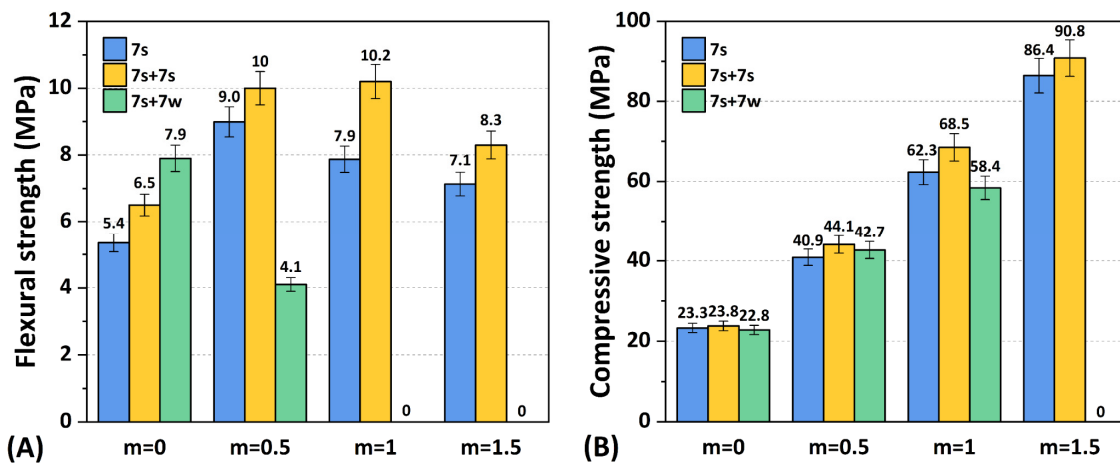


Figure 7.3. Flexural and compressive strengths of AAS pastes under sealed and water-immersed conditions. The “7 s” indicates 7 d of sealed curing, while the “7 w” refers to 7 d of water immersion.

As shown in *Figure 7.4*, the $m = 1$ paste fractures into two halves, while the $m = 1.5$ paste completely fragments into smaller pieces after 19 h of water immersion. Both pastes show no measurable flexural strength after immersion, clearly demonstrating the detrimental impact of water immersion on sodium silicate-based AAS pastes. This trend is consistent with the findings from previous works [14,47,126,231]. Interestingly, pastes with $m = 1.5$ are not only fragmented into several sections like the prisms of $m = 1$ but even into smaller pieces, especially at the corners of prisms (highlighted in dashed red circles in *Figure 7.4*). Similar observations have been reported in [15]. This phenomenon indicates severe structural problems of AAS pastes under immersed conditions, which have been scarcely reported in previous research and warrant significant attention.

Figure 7.3B shows the compressive strength of AAS pastes under sealed and water-immersed conditions. Unlike flexural strength, the compressive strength of AAS pastes increases with both curing time and silicate modulus under sealed conditions. This behaviour can be attributed to the fact that compressive strength is predominantly influenced by the porosity of the microstructure instead of microcracks. As the silicate modulus increases, the formation of gels densifies the matrix, reducing porosity and enhancing compressive strength. Moreover, water immersion for 7 d results in only a slight reduction in compressive strength compared to sealed conditions at the same age. This suggests that short-term water immersion does not significantly change the overall porosity of AAS prisms. Due to the complete damage of the prismatic samples, the compressive strength of $m = 1.5$ prisms after immersion is unmeasurable.

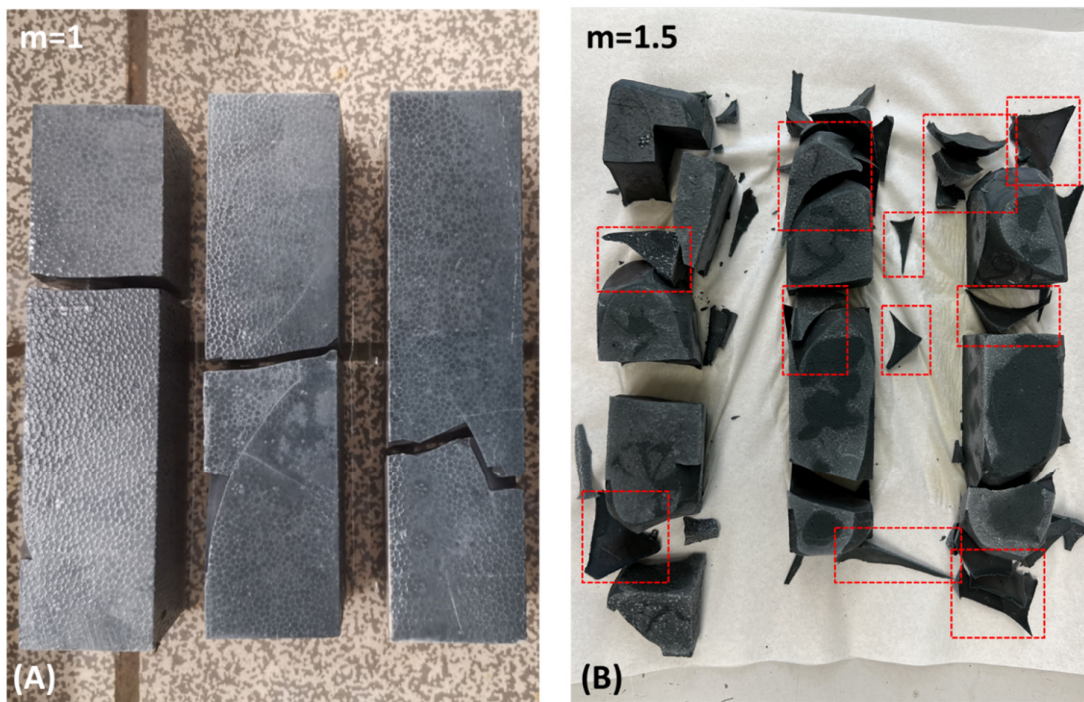


Figure 7.4. Fracture of the AAS prismatic pastes with $m = 1$ and $m = 1.5$ after 19 h of water immersion. The photo was taken immediately after the samples were removed from water, without undergoing the drying process.

7.3.2 Phase assemblage

Figure 7.5 shows the XRD pattern of AAS pastes with different silicate moduli under sealed and immersion conditions. Generally, gels and hydrotalcite are the two main reaction products in an AAS paste, consistent with the results in Chapter 5. The characteristic peaks of gels are more pronounced in the paste with a low silicate modulus. This is because the gel in a high-modulus paste normally shows a low Ca/Si ratio, resulting in a more crosslinked and amorphous structure, which obscures the reflections of some representative crystal planes in the Si-Al tetrahedra. Additionally, the characteristic peaks of hydrotalcite diminish with the increase of silicate modulus, indicating that a high silicate content hinders the formation of crystalline hydrotalcite.

In the comparison of sealed and water-immersed samples, the phase assemblage of pastes remains stable. However, in the $m = 0$ paste, the characteristic peak of gels “*” becomes less evident after 7 d of water immersion, suggesting partial decomposition of some chemical units within the gels. Despite this, no secondary phases are identified in any paste after 7 d of immersion, eliminating the possibility of cracking caused by the expansion of crystalline phases.

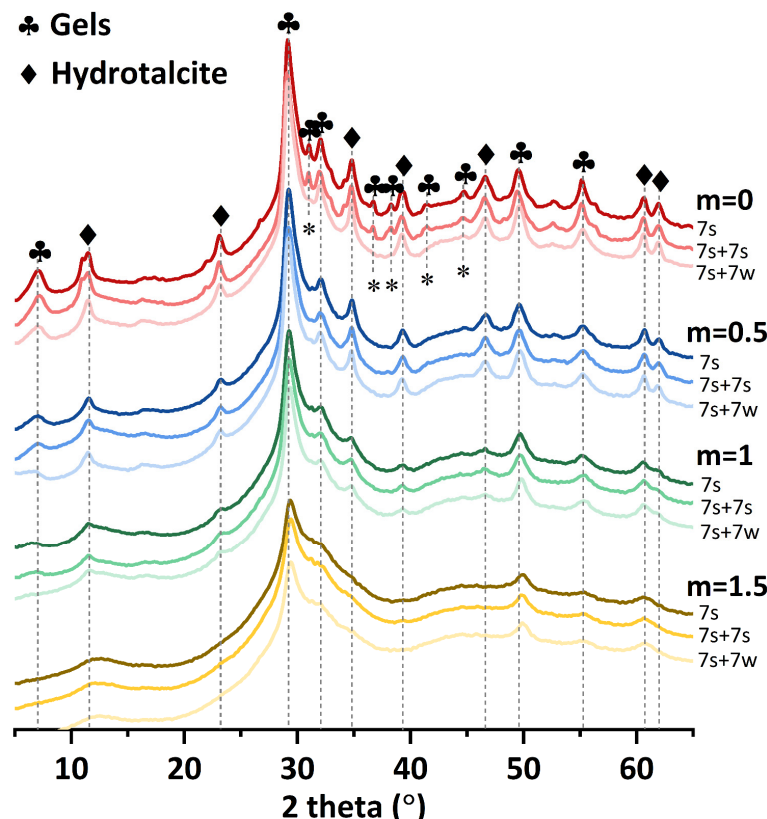


Figure 7.5. XRD pattern of AAS pastes with different silicate moduli under sealed and water-immersed conditions. The curves with colours from dark to shallow in each group represent the sample of “7 s”, “7 s + 7 s” and “7 s + 7 w”, respectively. The “*” marks the characteristic peak of gels only existing in the $m = 0$ paste.

7.3.3 Paste chemistry

Figure 7.6A shows a representative BSE image of the AAS paste with $m = 1$ after 7 d of sealed curing. The microstructure typically contains unreacted slag, inner products, outer products and pores. The inner products, identifiable as the dark rim of slag, are predominantly composed of hydrotalcite-like phases, along with C-(N-)A-S-H gels [222]. Due to the dissolution and diffusion of Ca and Si species from slag, the greyscale of these rims is usually higher than slag particles [222,232]. In contrast, the outer products consist exclusively of C-(N-)A-S-H gels due to the limited mobility of Mg [232,233]. Therefore, to focus on the chemical composition of gels, the outer product regions were selected for point analysis.

Figure 7.6B shows the atomic ratio of Ca/Si versus Na/Si in the outer product of AAS pastes. A negative correlation is observed between these ratios, attributed to the competitive role of Ca and Na in charge balancing [58]. The gel in the paste with a higher modulus shows a lower Ca/Si ratio and a higher Na/Si ratio. This can be ascribed to the additional soluble Si ions supplied by sodium silicate-based activators, which react directly with dissolved Ca and Al from the slag to form gels. The extensive gel formation results in higher absorption of Na in the pore solution. Consequently, this results in a heightened Na/Si ratio of gels in the outer products of the $m = 1$ and $m = 1.5$ matrices. As reported in [234], the bulk modulus of gels is partially determined by the interlayer density, with higher interlayer Ca content contributing to increased bulk stress at a comparable basal spacing. This means that the gel with a lower Ca/Si ratio shows a lower intrinsic mechanical property. Therefore, it can be inferred that the gels in $m = 1.5$ and $m = 1$ pastes are mechanically weaker than those in $m = 0.5$ and $m = 0$ pastes. This reduced mechanical strength of gels likely promotes the propagation of cracks.

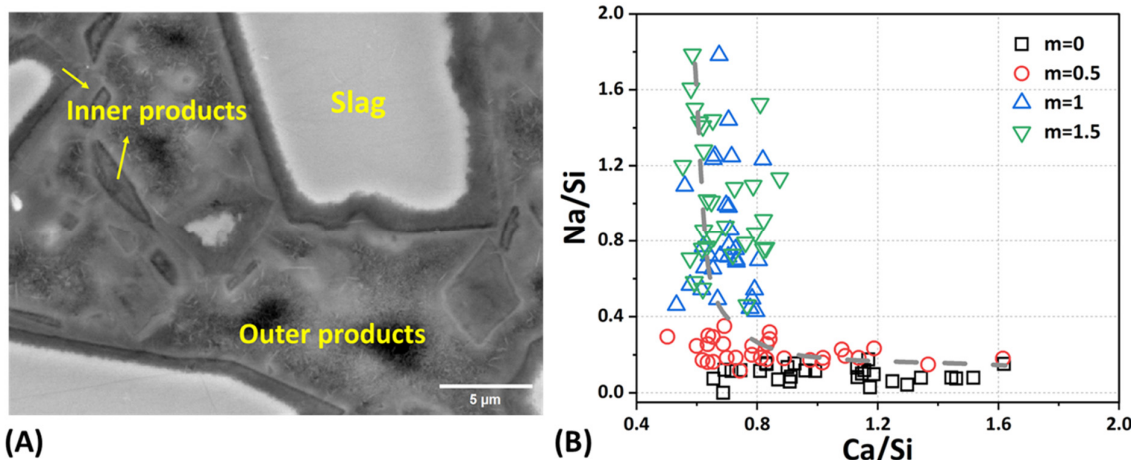


Figure 7.6 (A) A representative BSE image of AAS paste with $m = 1$ sealed for 7 d; (B) Atomic ratios of Ca/Si against Na/Si in the outer products of 7 d sealed AAS pastes with different silicate moduli.

7.3.4 Leaching behaviour

The leaching behaviour of powdered AAS pastes can reflect their thermodynamic stability during water immersion. Considering the minimal dissolution loss of slag and hydrotalcite in deionised water [126], the ions leached into the solution mainly originate from the decomposition of C-(N-)A-S-H gels. *Figure 7.7* shows the concentrations of Si, Al, Ca and Na in the leachate of AAS powdered samples after 7 d of water immersion. The concentrations of Si and Ca are comparable across the four samples, with pastes containing higher silicate moduli generally showing higher values. Si and Ca are essential components of gel structures, the leaching of which is detrimental to the stability of gels [20]. This indicates that the gels in the pastes with high silicate moduli are more vulnerable to leaching.

Furthermore, the concentration of Al in the leachate decreases with increasing silicate modulus. This trend is likely due to the lower content of Al in the paste with a higher silicate modulus. A higher content of sodium silicate in the activator reduces the pH at a constant Na dosage, which would impede the decomposition of slag and the dissolution of Al. Additionally, the leached ions are predominantly composed of Na, as an indicator of its weak bond with gels and high mobility in aqueous conditions. The concentration of Na in the leachate of the paste with a higher silicate modulus exhibits a higher Na/Si ratio in gels (*Figure 7.6B*). As discussed in *Chapter 4*, the leaching of Na in the interlayer can trigger the migration of intralayer Ca to the interlayer for charge compensation. This subsequently results in the decalcification of the intralayer and the formation of a more crosslinked gel structure. Therefore, this considerable leaching of Na in the paste of $m = 1.5$ could suggest a substantial change in its gel structure. To further understand the structural change of gels induced by leaching, FTIR tests were performed.

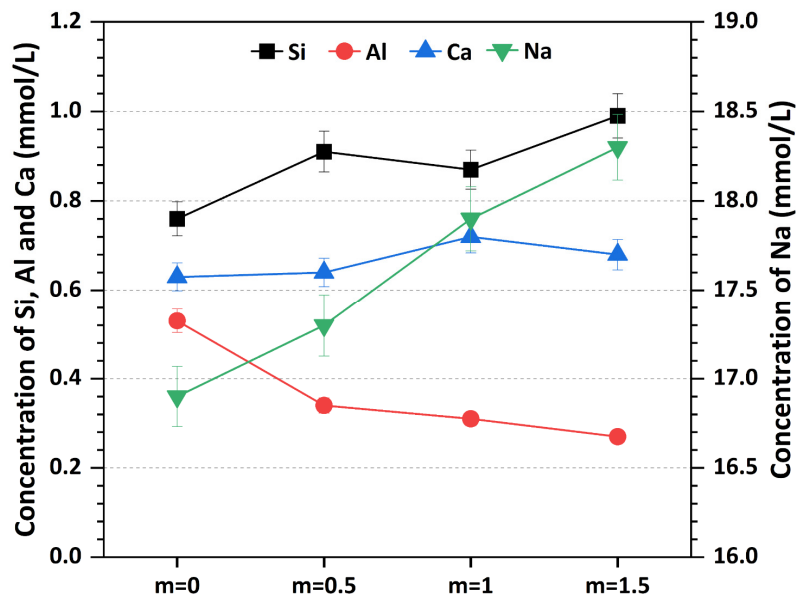


Figure 7.7. Ion concentration of Si, Al, Ca (on the left Y) and Na (on the right Y) in the leachate of AAS powdered samples after 7 d of water immersion.

7.3.5 Gel stability

The infrared spectra of AAS pastes are depicted in *Figure 7.8*. As demonstrated in *Figure 7.8A*, the paste with a higher silicate modulus exhibits a less pronounced absorption peak compared to that with a lower modulus, particularly near 890 cm^{-1} . This finding matches the XRD results, indicating that the gel in high-modulus pastes is less ordered, with less distinct chemical group features. 7 d of water immersion has a limited impact on the main gel structure, which is consistent with *Chapter 5*. However, there are subtle variations with regard to the wavenumber of Q^2 units.

Figure 7.8B shows the peak value of the Q^2 unit in the four AAS pastes before and after water immersion. A higher wavenumber of the Q^2 peak indicates a higher degree of polymerisation of gels. The wavenumber of the Q^2 peak increases with the increase of silicate moduli, which suggests that the gel in the high-modulus paste has a more crosslinked structure [235]. As shown in *Figure 7.6B*, the gel in the pastes of $m = 1$ and $m = 1.5$ shows a lower Ca/Si ratio, which implies a lower content of Ca in the Ca-O of the intralayer. A lower content of Ca in the intralayer is conducive to a prolonged silicate chain. In contrast to the sealed AAS pastes, the gel in pastes after water immersion shows a higher wavenumber, indicating a higher polymerisation degree. As discussed above, this is mainly due to the leaching of Na. Moreover, the increase in the wavenumber of the Q^2 unit is more pronounced in $m = 1$ and $m = 1.5$ pastes compared to $m = 0$ and $m = 0.5$ pastes. This discrepancy can be ascribed to the variation in Na leaching across different systems (*Figure 7.7*). A greater loss of Na corresponds to a more significant structural evolution. Among these four pastes, the gel in the $m = 1.5$ paste shows the highest Na loss and thereby undergoes the most severe structural change when subjected to water exposure. This structural evolution of gels can promote the development of microcracks, compromising the underwater stability of the materials.

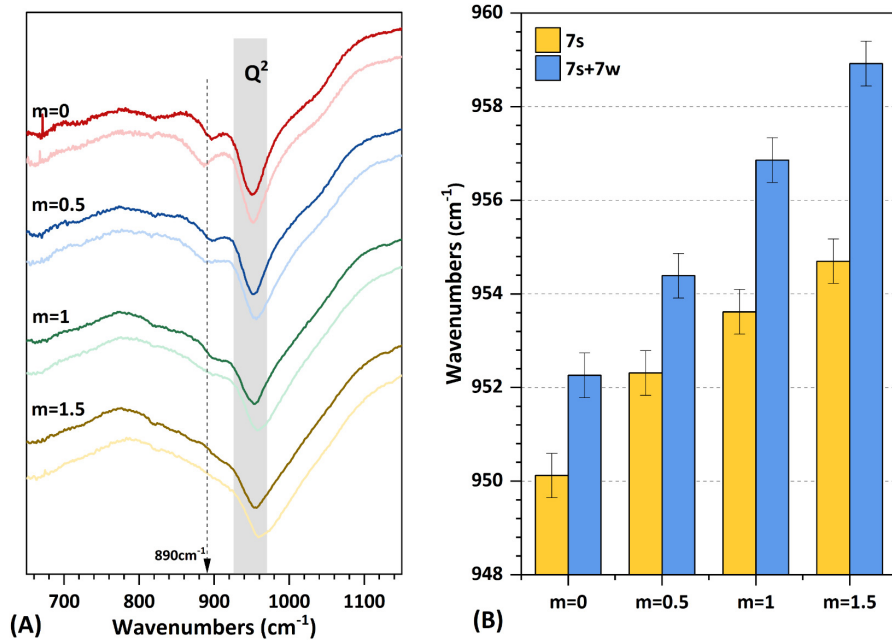


Figure 7.8. (A) FTIR pattern of powdered 7 d AAS pastes before and after 7 d of water immersion. The curves in dark and light colours represent the sample with and without exposure, respectively. (B) The peak value of wavenumbers of the Q^2 units in gels of different AAS pastes.

7.3.6 Pore structure

Figure 7.9 shows the cumulative mercury intrusion and pore size distribution of 7 d AAS pastes. It is observed that the open porosity of pastes decreases from 26.5% to 7.9% as the silicate modulus increases from 0 to 1.5. This indicates that the presence of soluble Si in initial activators can effectively densify the microstructure. The effective porosity, referring to the ratio of interconnected pores allowing fluid flow, is also lower in the paste with a higher silicate modulus, further declining as the modulus increases. This implies that a high-modulus paste has low water permeability.

Moreover, the threshold pore diameter, defined as the pore diameter with the highest rate of mercury intrusion per change in pressure or diameter (dV/dP or dV/dD), also decreases with increasing silicate modulus. It drops from 36.25 nm in $m = 0$ to 2.63 nm in $m = 1.5$. Powers et al [236] found that the permeability of cement pastes dramatically decreases when the threshold pore diameter falls below a critical value. In such cases, water transport shifts from capillary pores (10 nm – 100 μ m) to gel pores (1 – 10 nm), which are over an order of magnitude smaller [237]. Therefore, the water transport in $m = 1$ and $m = 1.5$ pastes is considerably lower than that in the $m = 0$ and $m = 0.5$ pastes, since the water flow in the former two systems is governed by gel pores while that in the latter two is controlled by small capillary pores. The distinct pore structures in different pastes will result in different behaviours of water transport.

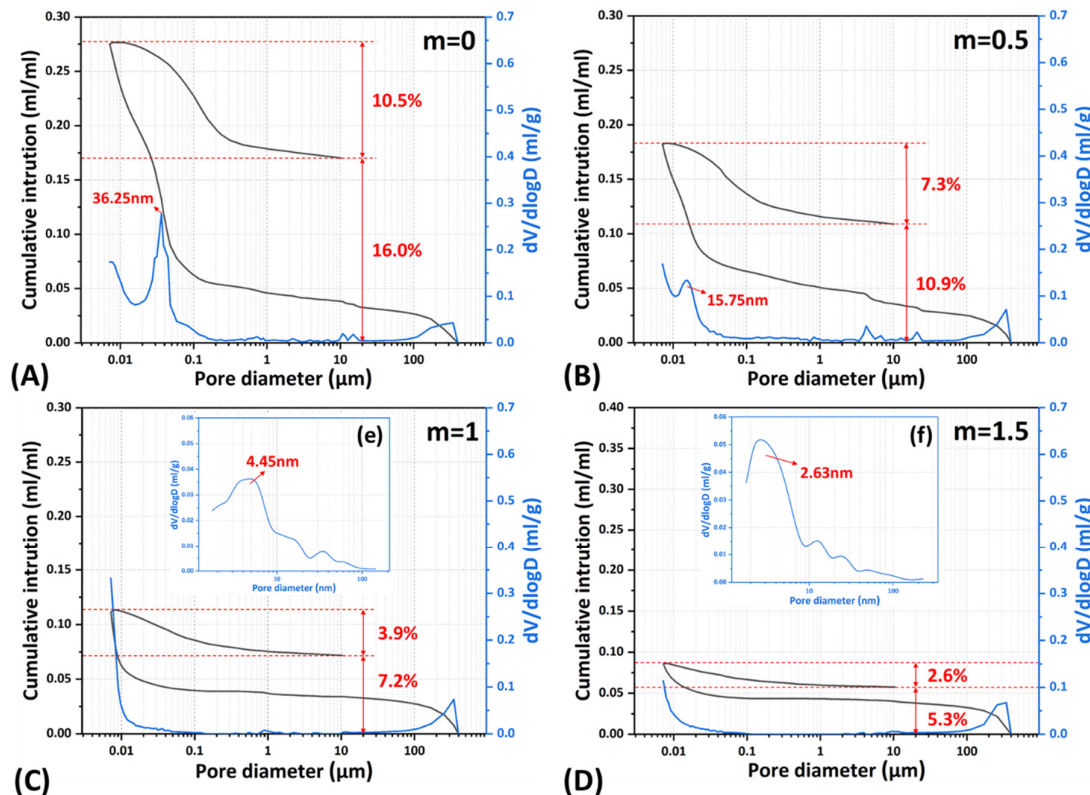


Figure 7.9. Pore structure information of AAS pastes obtained from MIP (A–D) and N_2 absorption ((e) and (f)) results. The percentages in each inset indicate the effective porosity and ink-bottle porosity.

7.4 Simulation results

With the reaction of slag in AAS pastes, the water content within the pore structure decreases over time. After 7 d of sealing, the initial water content of the four pastes was measured at 94.6%, 93.8%, 92.3%, and 90.2%, respectively. The paste with a higher silicate modulus exhibited lower initial water content. This trend is attributed to the increased Si content in activators, which consumes more water during gel formation. As water is consumed, the pores become unsaturated, enabling water ingress through capillary suction. However, conventional experimental methods like CT struggle to capture the rapid capillary-driven water movement. To address this, simulations were conducted on the cross-section of AAS pastes within 1 h (*Figure 7.10*). The results revealed that water content increased over time, with pastes of higher silicate moduli (e.g., $m = 1$ and $m = 1.5$) showing slower water ingress rates. After 1 h of exposure, the pastes with $m = 0$ and $m = 0.5$ reached near saturation, while those with $m = 1$ and $m = 1.5$ remained largely unsaturated in the centre, indicating an uneven spatial distribution of water.

This non-uniform water distribution poses challenges for AAS materials. As noted in [240], C-S-H gels in PC-based materials initially shrink during water loss and swell upon rehydration, suggesting that water ingress and swelling are interdependent processes. Quantifying this expansion experimentally is challenging, and specific parameters for simulating such behaviour remain unavailable. To conceptualise the phenomenon, a schematic diagram (*Figure 7.11*) illustrates how uneven water-induced swelling could generate localised stresses within the matrix.

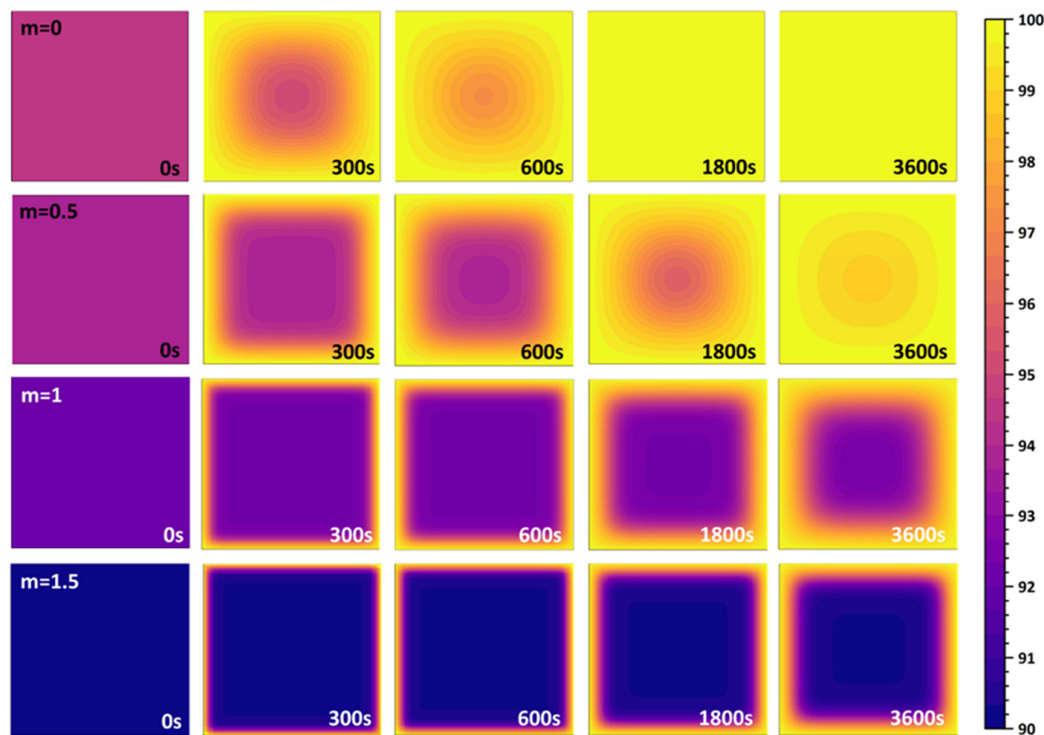


Figure 7.10. Distribution of the water content (unit: %) of the cross-section (4 cm × 4 cm) of AAS prisms subjected to water immersion within 1 h. The water content of 7 d pastes of $m = 0, 0.5, 1$ and 1.5 before water immersion was measured as 94.6%, 93.8%, 92.3% and 90.2%, respectively.

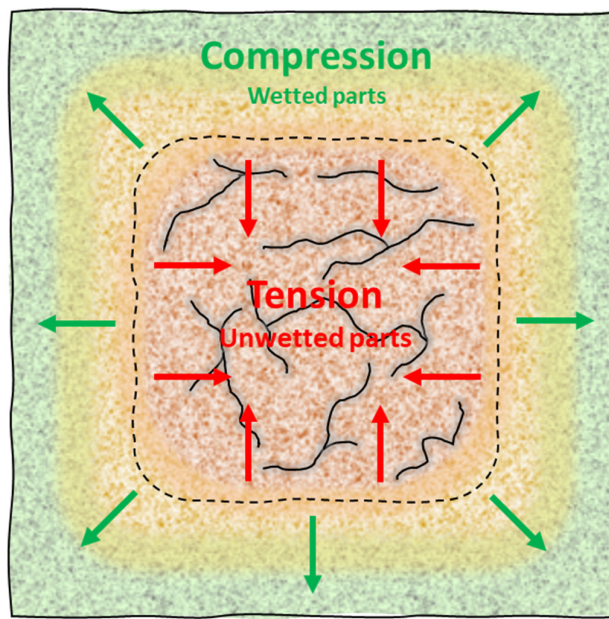


Figure 7.11. Schematic diagram of the cross-section of AAS pastes induced by water ingress.

Figure 7.11 shows a schematic representation of the cross-section of AAS pastes induced by water immersion. In a high silicate modulus paste (e.g., $m = 1$ and $m = 1.5$), the dense pore structure hinders rapid inward water penetration via capillary suction (Figure 7.10). This result creates a pronounced gradient of water content between the surface and the centre of the matrix. The wetted part relaxes pore pressure locally, inducing compressive stress at the surface and tensile stress at the centre. Cementitious materials, being inherently weaker in tension than compression, are particularly vulnerable to such tensile stresses. When the tensile stress exceeds the material's tensile strength, cracking initiates at the centre, as observed in Figure 7.4 for the $m = 1$ paste, where fractures perpendicular to the prism's cross-section are evident. In severe cases (notably for $m = 1.5$), these central cracks propagate outward toward the surface, leading to corner spalling—a phenomenon where fragments break away from the corner of the sample.

7.5 Discussion

7.5.1 Cracking mechanisms of AAS materials underwater

7.5.1.1 Chemical perspective

Although no expansive reaction product forms and no evident phase decomposition are identified in AAS pastes after short-term water immersion, the C-(N-)A-S-H gels can undergo structural evolution due to the leaching of Na ions. This structural change is dependent on the chemical composition of gels. With the increase of silicate modulus, the content of Si in the gels increases, resulting in a lower Ca/Si ratio and a higher Na/Si ratio. These gels are more amorphous and exhibit lower intrinsic mechanical properties [234]. More importantly, gels in the paste with high silicate moduli lose more Na ions when exposed to water immersion, leading to more severe structural changes. It is plausible that the cracking propagation in the paste with high silicate moduli is more likely to happen since the gels experience more significant structural changes underwater.

7.5.1.2 Physical perspective

As discussed in *Section 7.4*, the cracking mechanisms from a mechanical perspective are primarily driven by centre tension induced by surface swelling. To simplify the modelling process, it is assumed that the pores in the media are fully interconnected and can be entirely percolated over a sufficient period. However, in a real AAS paste, especially those with high silicate moduli, some small capillary pores or gel pores remain disconnected and impermeable. These impermeable pores retain high pore pressure even after water ingress into surrounding areas, as depicted in *Figure 7.12*. In the case of the paste with low silicate modulus, the material is porous and the pores are interconnected (*Figure 7.12A*). After water ingress, the pores on the surface of the material become saturated and the pore pressure can decrease to almost zero (*Figure 7.12B*). However, in pastes with high silicate moduli, the material is dense and some pores are impermeable (*Figure 7.12C*). Even after water ingress, these pores remain unsaturated with high pore pressure (*Figure 7.12D*), contributing to internal gradients. Besides, as implied in flexural strength results (*Figure 7.3A*), some microcracks might exist in sealed pastes with high silicate moduli. If the residual stress in the impermeable pore exceeds the limit of the paste, it will promote microcrack propagation. This can also explain why the paste with $m = 1.5$ fractures into pieces after water immersion.

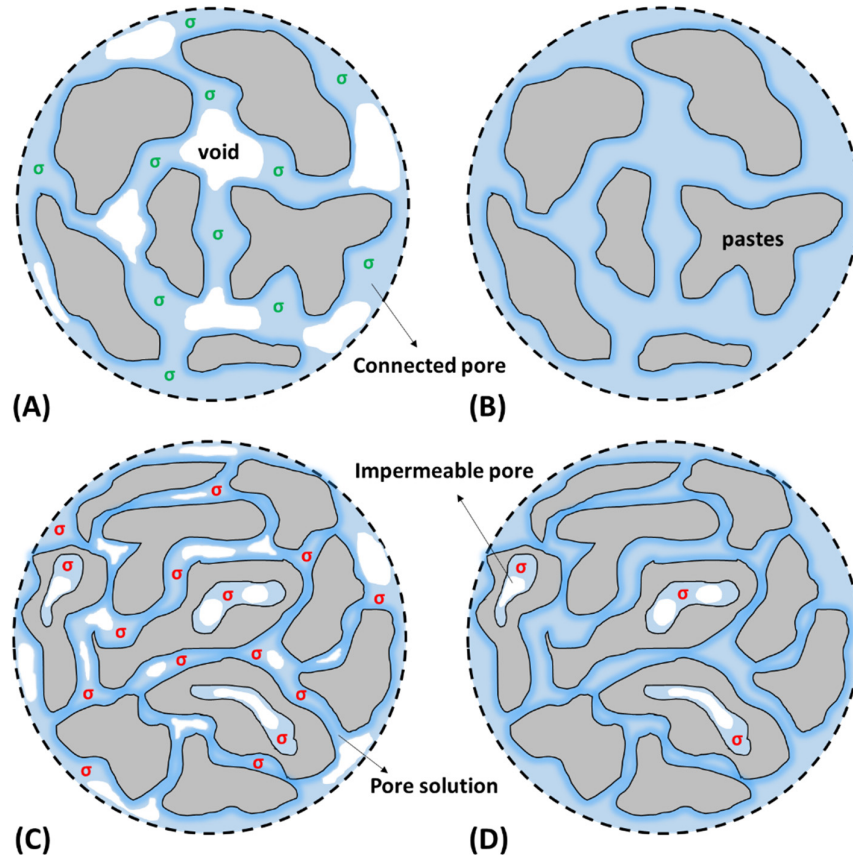


Figure 7.12. Representation diagrams of AAS pastes with low (A and B) and high (C and D) porosities before and after water percolation. The unreacted slag and reaction products are omitted from the paste. The pore pressure of σ in red is higher than that in green due to the different radii of the menisci in different matrices.

7.5.2 Potential mitigation strategies

Based on the identified cracking mechanisms, some potential strategies can be proposed to mitigate this problem. From the chemical perspective, it is imperative to increase the Ca/Si ratio of C-(N)-A-S-H gels for the reduction in the leaching of Na and structural evolution of gels. For plain slag systems, decreasing the silicate modulus is an effective approach to decreasing the content of Si and increasing the Ca/Si ratio in gels. For slag blended systems, incorporating a high proportion of slag, which is richer in Ca than other precursors, can further elevate the Ca/Si ratio of C-(N)-A-S-H gels. From the physical perspective, while denser matrices may improve mechanical properties under sealed conditions, they are not necessarily ideal for mitigating cracking problems caused by water immersion. Moderate dosages of sodium silicate and slag can result in a matrix with sufficient permeability to reduce stress gradients while avoiding overly dense or highly porous structures. Incorporating relatively inert aluminosilicate precursors, such as fly ash, can moderate reaction rates and coarsen the microstructure. This enhances the material's ability to accommodate water transport without excessive stress buildup.

Additionally, the addition of fine aggregate can partially address this problem. Given that flexural strength is highly sensitive to cracks, it serves as a reasonable indicator for evaluating cracking problems. In this chapter, the flexural strength of AAS mortars with different silicate moduli (*Appendix A Figure A3*) was also measured. The flexural strength of $m = 1.5$ mortars subjected to water immersion was measurable but lower than that under sealed conditions. This indicated that cracking problems persisted in mortars, even though they were less evident than in pastes. In my previous work [241], the $m = 1$ mortar showed a decreasing flexural strength trend under high-humidity conditions with time, while showing an increasing trend under ambient and sealed conditions. These findings suggested that while the addition of aggregates mitigates cracking to some extent, it does not completely eliminate this problem. The optimal solution lies in refining the mixture design, considering both the paste chemistry and pore structure. In terms of experimental and computational results, a silicate modulus of no higher than 0.5 is recommended for plain AAS materials.

7.6 Conclusions

In this chapter, the behaviour of AAS pastes with varying silicate moduli subjected to water immersion was investigated. The experimental and simulation results revealed that the pastes with high silicate moduli are prone to cracking and even fragmentation under such conditions. The mechanisms behind these phenomena were unveiled chemically and physically. Some conclusions can be drawn as follows:

1. Apart from the prism with $m = 0$, the flexural strength of the other three AAS prisms ($m = 0.5$, $m = 1$ and $m = 1.5$) decreased to varying extents after 7 d of water immersion. Notably, the prisms of $m = 1$ fractured into halves, while those of $m = 1.5$ were fragmented, resulting in no measurable flexural strength. However, other than the prism of $m = 1.5$, AAS pastes exhibited minimal adverse effects from water immersion in terms of compressive strength.
2. The phase assemblage of all four AAS pastes before and after 7 d of water immersion was comparable, without the formation of new crystals being observed. The gel in the paste with a higher silicate modulus showed a higher leaching loss of Na, due to initially higher Na contents. The heightened leaching of Na can trigger more severe structural change and deterioration of gels, potentially contributing to crack propagation.
3. Simulated results indicated that the pastes with $m = 1$ and $m = 1.5$ showed significantly lower permeability than those with $m = 0$ and $m = 0.5$. This led to an uneven spatial distribution of water content in the matrix. The wetted part relaxed pore pressure locally, generating compressive stress at the surface and tensile stress at the centre. Once the tensile stress exceeded the material's inherent tensile strength, cracking initiated at the centre. In severe cases, particularly for $m = 1.5$, these central cracks propagated outward, culminating in extensive fractures and corner spalling.
4. Considering both chemical and physical perspectives, a low silicate modulus (no higher than 0.5) was recommended to address the cracking issue of AAS materials underwater. In such a system, the gel would show fewer structural changes and the matrix may show lower internal stress subjected to water immersion.

Chapter 8

Efflorescence mechanisms of AAS pastes

8.1 Introduction

As mentioned in *Chapter 2*, efflorescence refers to the formation of fluffy white deposits on the surface of materials, posing both aesthetic and structural problems. In general, efflorescence is considered a derivative problem of leaching, caused by the leaching of Na and its reaction with CO₂ in the atmosphere. However, the mechanism of efflorescence of AAS materials is not fully understood. The environmental factors influencing the efflorescence of AAMs, such as relative humidity, have been rarely reported. Additionally, there is a lack of research on the efflorescence of plain slag-based AAMs. Most studies focus on fly ash- or metakaolin-based materials [21,22,25], as they are considered more porous and vulnerable to efflorescence problems compared to AAS materials. However, significant efflorescence, accompanied by cracks, has been observed in previous work [72]. The underlying cracking mechanisms and their relationship with efflorescence seem to be unknown. Additionally, an effective quantification method for efflorescence is still lacking, which inhibits a precise assessment of this phenomenon.

To address these issues, efflorescence experiments were conducted on cylindrical AAS pastes with their bottom in contact with water. First, the effects of alkalinities (Na₂O content of 3%, 5% and 7% to slag) and alkali activators (NH and NS), exposure atmospheres (ambient, N₂ and 0.2 vol.% CO₂) and relative humidities (40%, 60% and 80%) on visual efflorescence of AAS pastes were investigated. Then, leaching tests of AAS pastes in different sizes under different conditions were examined. The Na amount in efflorescence products of AAS pastes was quantitatively determined. The distributions of absolute amount and relative proportion of Na in AAS cylinders were calculated. The relationship between efflorescence and leaching was then established. Subsequently, the phase assemblage of efflorescence products of NH and NS pastes under ambient conditions and the impacts of efflorescence on the phase assemblage, gel structure and pore structure of AAS cylinders at different heights were comprehensively studied. The compressive strengths of AAS pastes with and without efflorescence were compared. Finally, the efflorescence process of AAS pastes was specified and the mechanism of efflorescence of AAS pastes has been clarified.

8.2 Methodology

8.2.1 Materials and mixtures

Slag and commercial alkali activators used in this chapter were the same as those in previous chapters. The mix proportions of AAS pastes are shown in *Table 8.1*. To compare the impact of alkali activators on the efflorescence of AAS pastes, sodium hydroxide and sodium silicate were used, both with an alkali dosage of 5% to the weight of slag, denoted as the “NH” and “NS” groups. To assess the effect of alkali dosage on the efflorescence of AAS pastes, NH pastes with alkali dosages of 3% and 7% were also prepared, referred to as “NH_3%” and “NH_7%”, respectively.

Table 8.1. Mix proportions of AAS pastes.

AAS	Slag (g)	SiO ₂ (mol)	Na ₂ O (mol)	Water (g)	Na ₂ O dosage (wt.%)
NH_3%	1000	0	0.48	430	3%
NH (NH_5%)	1000	0	0.8	430	5%
NH_7%	1000	0	1.13	430	7%
NS (NS_5%)	1000	0.8	0.8	430	5%

The AAS pastes were prepared at room temperature (about 20 °C) with a Hobart mixer. The freshly prepared pastes were poured into polyethene cylindrical moulds (with dimensions of ϕ 35 mm × 70 mm) for efflorescence and leaching tests, and 4 cm × 4 cm × 16 cm prism moulds for compressive strength tests.

8.2.2 Efflorescence tests under different conditions

AAS cylindrical samples were first sealed for 7 d and then cut into the shape of ϕ 35 mm × 50 mm. The cut side of the cylinders was submerged in deionised water, maintaining a depth of 10 ± 1 mm in a glassy dish until 28 d. The environmental conditions for efflorescence tests are shown in *Figure 8.1*, including (A) ambient condition (air, T = 20 °C and RH = 55%), (B) N₂ condition in a glove box (N₂, T = 20 °C and RH = 55%, 1 atm), (C) CO₂ condition in a CO₂ chamber (0.2% CO₂, T = 20 °C and RH = 55%, 1 atm) and (D) different RH conditions in a tank with vents (air, T = 20 °C and RH = 40%, 60% and 80%).

The RH of N₂ and CO₂ conditions were controlled by an oversaturated Mg(NO₃)₂ solution. The different RH conditions were controlled using oversaturated solutions of MgCl₂, Mg(NO₃)₂, and KCl in a tank, respectively, and vents located on the cover of the tanks allowed the exchange of CO₂ with outside air. The RH inside the tank was monitored using an Extech® humidity/temperature data logger. RH levels of approximately 40%, 60% and 80% at 20 °C were achieved by the three solutions. The efflorescence of AAS cylinders was captured by a mobile phone for up to 28 d.

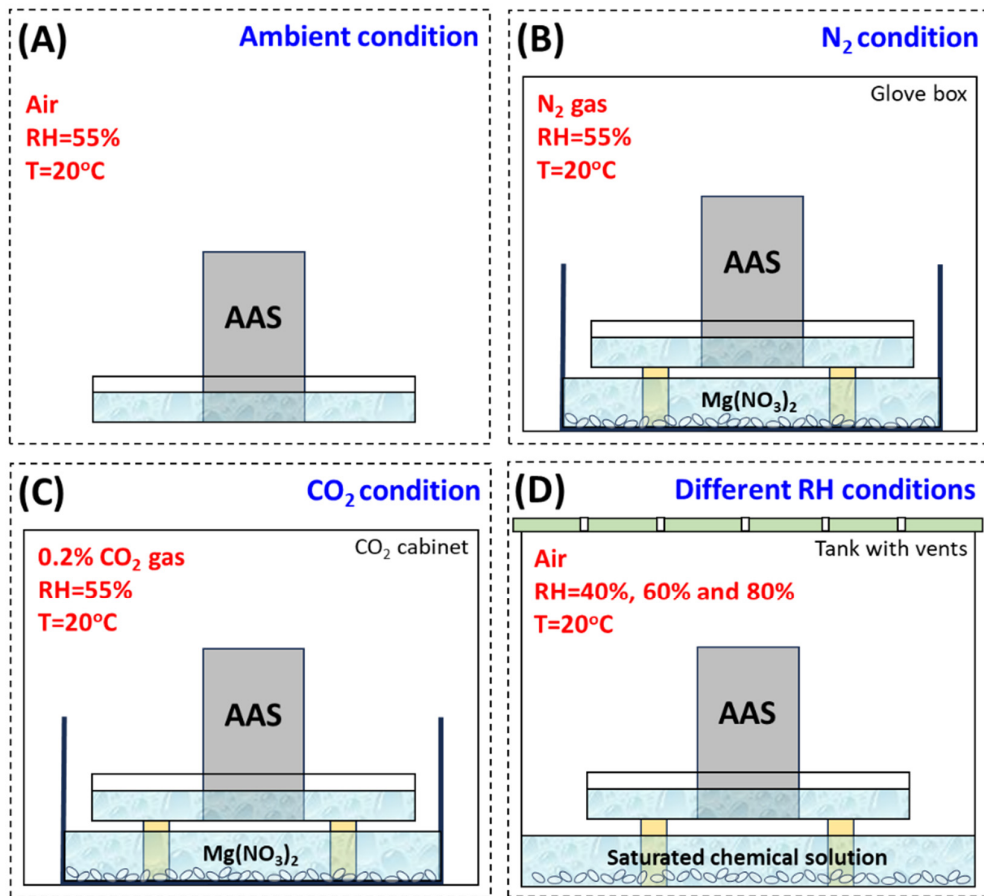


Figure 8.1. Schematic diagram of the efflorescence tests for AAS cylindrical pastes exposed to different atmospheres. The samples were sealed for 7 d and then exposed to the above conditions for another 28 d. (A) ambient condition (air, $T = 20^\circ\text{C}$ and $\text{RH} = 55\%$), (B) N_2 condition in a glove box (N_2 , $T = 20^\circ\text{C}$ and $\text{RH} = 55\%$, 1 atm), (C) CO_2 condition in a CO_2 chamber ($0.2\% \text{CO}_2$, $T = 20^\circ\text{C}$ and $\text{RH} = 55\%$, 1 atm) and (D) different RH conditions in a tank with vents (air, $T = 20^\circ\text{C}$ and $\text{RH} = 40\%, 60\%$ and 80%).

8.2.3 Leaching tests

Leaching tests of AAS pastes were carried out to establish the relationship between leaching and efflorescence and quantitatively determine the efflorescence of AAS pastes. The ion concentration of Na in different leachates (Figure 8.2) was measured using a PerkinElmer Optima 5300DV ICP-OES spectrometer. In Figure 8.2A, a cylindrical sample ($\phi 35 \text{ mm} \times 50 \text{ mm}$, $80 \pm 1 \text{ g}$) was first sealed for 7 d and then directly immersed in 150 ml of deionised water for 28 d. The leachate was referred to as "lea_cyl". In Figure 8.2B, AAS pastes were first sealed for 7 d and then crushed into 2 – 4 mm pieces. 15 g of the pieces were submerged in 150 ml of deionised water for 28 d, with the resulting leachate labelled as "lea_pie". The above two leachates were used to determine the relationship between leaching and efflorescence.

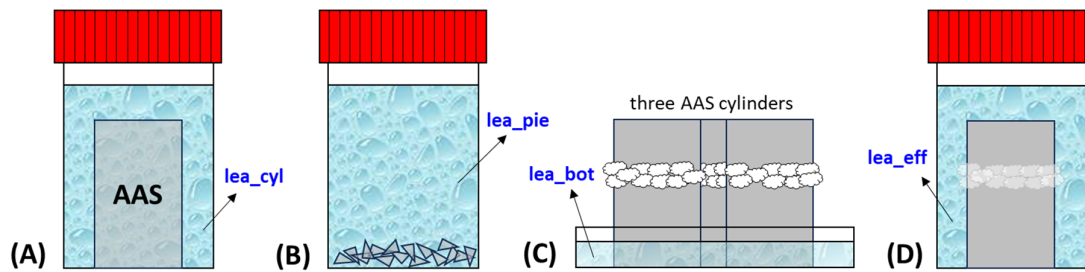


Figure 8.2. Four types of leachates for the measurement of the ion concentration of Na in the leaching tests. (A) An AAS cylinder is immersed in 150 ml of deionised water for 28 d. The leachate is denoted as “lea_cyl”. (B) 15 g of piece AAS pastes are immersed in 150 ml of deionised water for 28 d. The leachate is denoted as “lea_pie”. (C) The bottom leachate of three AAS cylinders after 28 d of efflorescence under ambient conditions is referred to as “lea_bot”. (D) The solution that dissolves the efflorescence products of three AAS cylinders is labelled as “lea_eff”.

Figure 8.2C illustrates the efflorescence test of three 7 d AAS cylinders under ambient conditions (*Figure 8.1A*). After 28 d of efflorescence, the solution in the dish was collected and diluted to a total volume of 150 ml, which was denoted as “lea_bot”. After the collection of the bottom solution, the three AAS cylinders attached by efflorescence products were immersed in 150 ml of deionised water sequentially for ultrasonic cleaning, as shown in *Figure 8.2D*. This process aimed to dissolve the efflorescence products on or beneath the surface of the cylinders. The resultant leachate was labelled as “lea_eff”. It should be noted that the cleaning process lasted only 30 s to minimise the influence of excessive Na leached from AAS cylinders. The amount of Na in the efflorescence products can be calculated, which was considered a quantitative approach to evaluating efflorescence.

The Na concentration of four leachates was used to quantify the amount of leached Na from AAS pastes and the amount of Na in the efflorescence products. Then, I can use these values to further calculate the distribution of Na in a cylinder during the efflorescence process. Prior to this, the Na amount in the leachate per cylinder should be known. The calculation is shown as follows. Noted that “[lea_xxx]” refers to the Na concentration in the leachate of “lea_xxx”.

$$\text{Na amount in the leachate of “lea_cyl” per cylinder} = [\text{“lea_cyl”}] \times 0.15$$

$$\text{Na amount in the leachate of “lea_pie” per cylinder} = [\text{“lea_pie”}] \times 0.15 \div 15 \times 80$$

$$\text{Na amount in the leachate of “lea_bot” per cylinder} = [\text{“lea_bot”}] \times 0.15 \div 3$$

$$\text{Na amount in the leachate of “lea_eff” per cylinder} = [\text{“lea_eff”}] \times 0.15 \div 3$$

The Na amount in the leachate of “lea_pie”, “lea_bot” and “lea_eff” per cylinder was used to calculate the distribution of Na. More specifically, the total amount of leachable Na in a cylinder was equal to the ‘Na amount in the leachate of “lea_pie” per cylinder’, assuming that all the free and weakly bound Na in the pore solution and gels can be leached away from the piece samples after 28 d of immersion. The Na distributed in the efflorescence products per cylinder was equal to the ‘Na amount in the leachate of “lea_eff” per cylinder’, while the amount of Na leached away from the bottom per cylinder was equal to the ‘Na amount in the leachate of “lea_bot” per cylinder’. Finally, the distribution of the relative proportion of Na (wt.%) in a cylinder was calculated using the obtained distribution of the absolute amount of Na per cylinder.

8.2.4 Paste characterisations

The impacts of efflorescence on the properties of AAS cylinders at different heights under ambient conditions (*Figure 8.1A*) were investigated. Similarly, the samples were first sealed for 7 d and then exposed to ambient conditions for 28 d. Subsequently, the cylinders were ultrasonically cleaned (*Figure 8.2D*) and evenly sliced into 4 thick sections, namely “bot”, “low”, “med”, and “top”, from the bottom upwards, as shown in *Figure 8.3*. The exposed slices were immersed in isopropanol for 7 d to arrest the reaction, and then dried in a vacuum oven until constant weight. Some of the slices were crushed into 4 – 6 mm pieces for MIP tests using a Micrometrics PoreSizer 9500. A high-pressure mercury intrusion process ranging from 0.17 to 210 MPa, with a contact angle of 141°, enabling the pore size distribution ranging from 400 µm to 7 nm. Some of the slices were crushed into pieces and then ground into powder for chemical characterisations, including XRD, TGA and FTIR. It is noted that the AAS pastes under sealed conditions were also characterised as the reference, namely “seal”. XRD, TGA and FTIR tests were conducted on AAS pastes at different heights. The detailed testing procedures are described in *Chapter 5*.

The compressive strength of AAS prisms was measured under three conditions: (1) ambient condition, (2) ambient condition with one side of the prism (4 cm × 16 cm) in contact with water at a depth of 10 mm, and (3) N₂ condition with one side of the prism in contact with water. The specimens sealed for 7 d and then exposed to the aforementioned three conditions for an additional 7 d (labelled “7 d”) and 28 d (labelled “28 d”) were measured. The measuring procedures were in accordance with NEN-196-1 [242].



Figure 8.3. Sample preparation before paste characterisations. The 7 d sealed cylinders after 28 d of efflorescence under ambient conditions are first ultrasonically cleaned, and then are sliced into four sections, designated “bot”, “low”, “med” and “top”.

8.3 Results

8.3.1 Visual observation of efflorescence

8.3.1.1 Effect of alkali dosages in the activator

To investigate the impact of alkali dosages on the efflorescence of AAS pastes, NH cylinders with varying alkali dosages of 3%, 5% and 7% were sealed for 7 d and then exposed to ambient conditions (*Figure 8.1A*). As shown in *Figure 8.4*, the NH_3% group exhibits a lower severity of efflorescence compared to the NH_5% and NH_7% groups at both 7 d and 28 d, which indicates that the paste with a lower alkali content shows less efflorescence. This finding agrees with previous research [25,71,72], which is ascribed to a lower Na content in the

cylinder of NH_3%. Additionally, it is interesting to observe that the “efflorescence front” (the position at which the white deposits begin to form) of the NH_3% cylinder is higher than that of the NH_5% and NH_7%. The height of the efflorescence front might be associated with the transport of water and ions in the cylinder. A decreased alkali dosage leads to a more porous and permeable pore structure of AAS materials, allowing an increased amount of water at the bottom to be absorbed upwards. This may result in a higher water penetration height in the NH_3% than in the NH_5% and NH_7%. With a constant temperature and sufficient raw ions supply, a proper RH for the formation of efflorescence should be the same in three cylinders and an excessive RH can dissolve the efflorescence products (sodium (bi)carbonate). Therefore, due to a higher water penetration level, the efflorescence front of NH_3% is higher than NH_5% and NH_7%.

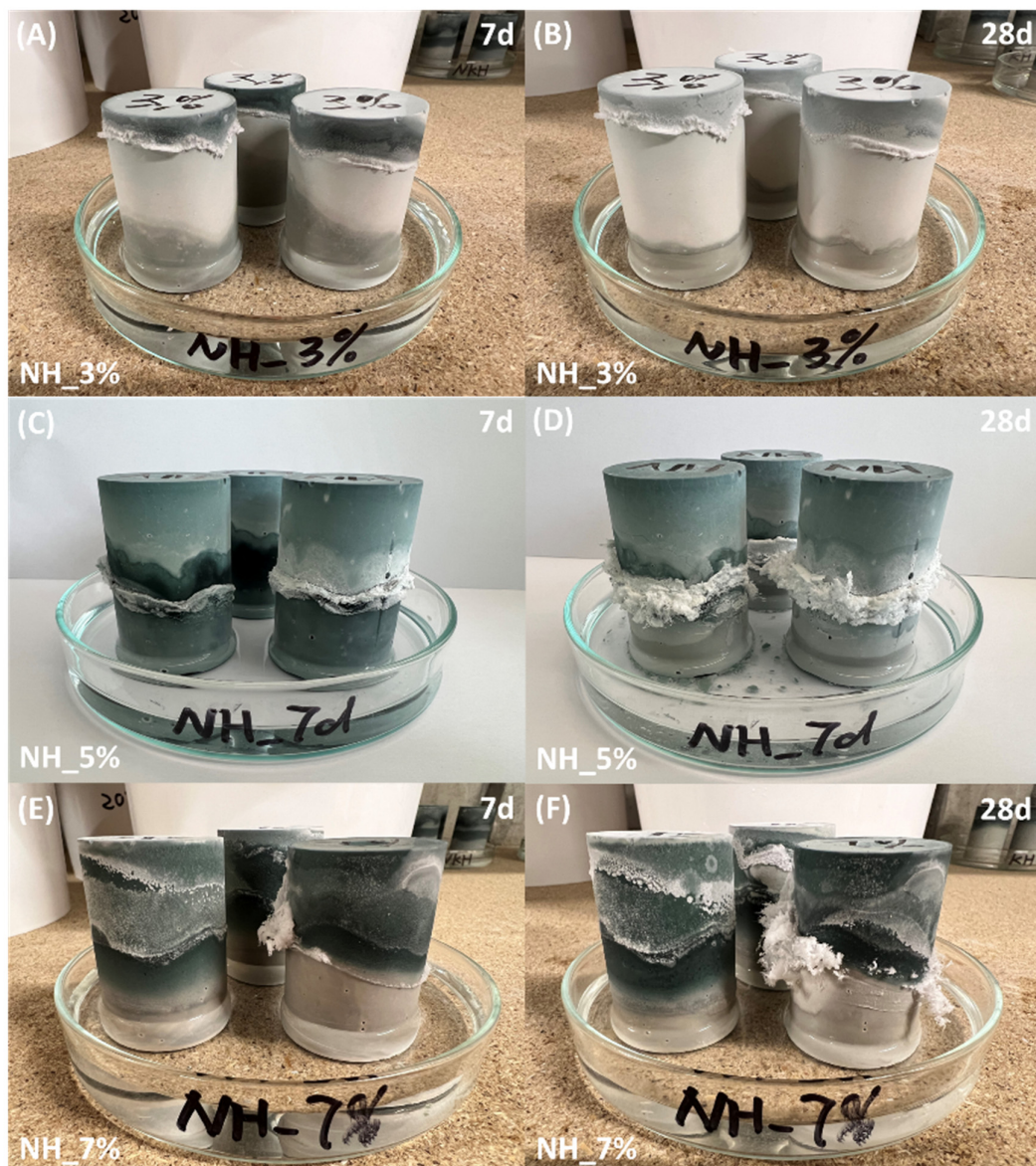


Figure 8.4. Visual observation of efflorescence of NH cylinders with alkali dosages of 3%, 5% and 7% exposed to ambient conditions for 7 d and 28 d.

8.3.1.2 Effect of activator types

Figure 8.5 shows the efflorescence of NH and NS cylinders under ambient conditions. The severity of efflorescence in both groups increases over time, with NH pastes exhibiting a more rapid development than NS pastes, as evident from photos captured after 1 d of exposure. These observations are consistent with an earlier work [22]. The presence of soluble silicate promotes the formation of gels, which is effective in reducing the porosity and pore connectivity of the matrix. A dense microstructure can impede the transport of water and Na, resulting in a lower efflorescence rate of NS samples.

In addition to the efflorescence rate, NH and NS cylinders also show distinct growth patterns of efflorescence products. As indicated in Figure 8.5 at 3 d, white deposits on NH cylinders initiate from the second red line from the bottom, higher than that of NS cylinders beginning from the middle between the first and second red lines. In conjunction with the preceding observations illustrated in Figure 8.4, the lower efflorescence front of the NS cylinder is due to a denser microstructure. Additionally, on NH samples, fluffy white deposits only progressively accumulate around the second red line, whereas those on NS samples can spread upwards until the top. Significant cracks are also observed at the top of NS cylinders. Similar observations regarding the efflorescence of alkali-activated phosphorus slag were also reported in [72]. While the amounts of deposits grown on NH samples differ apparently with different alkali contents (Figure 8.4), those on NH and NS samples are hard to compare quantitatively. The white deposits on NH samples are more concentrated, while those on NS samples cover a larger area but are thinner. Therefore, a quantitative manner for assessing the severity of efflorescence is necessary.

After 28 d of efflorescence, the samples were cleaned with an ultrasonic bath to remove the white deposits. The appearance of the side and top surfaces of AAS cylinders is presented in Figure 8.6. Interestingly, as shown in Figure 8.6A, discolouration is identified on both NH and NS cylinders. The middle section of the NH cylinders, as well as the entirety of the NS cylinder above the immersed portions, displays a darker colour than the immersed sections.

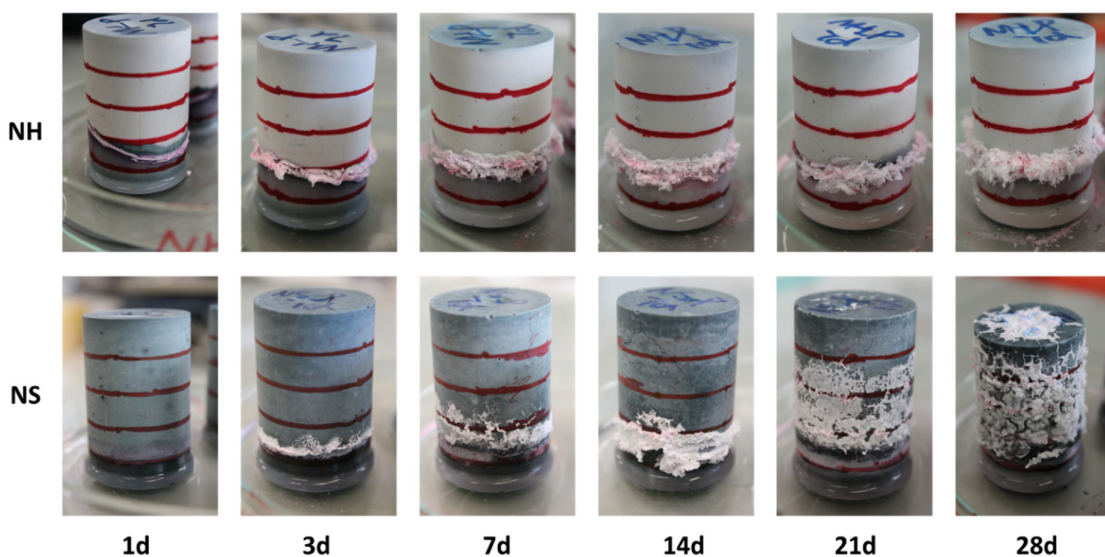


Figure 8.5. Visual observation of efflorescence of NH and NS cylinders under ambient conditions with time. The cylindrical samples are marked by parallel red lines at 1 cm intervals to clearly show the location of efflorescence products.

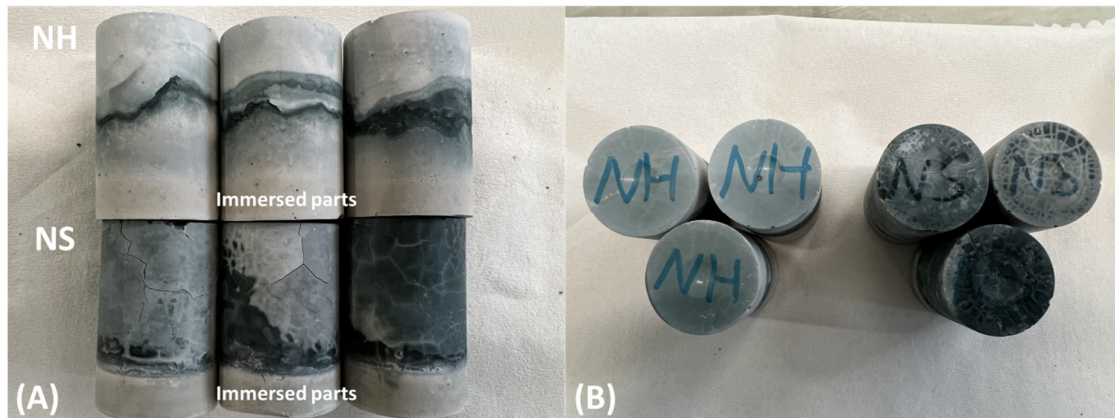


Figure 8.6. Side and top surfaces of ultrasonically cleaned NH and NS cylinders after 28 d of efflorescence under ambient conditions.

As reported in [243], the dark colour (dark green/blue) of slag-based materials is attributed to the presence of trisulfur radical anion (S_3^-). These ions are vulnerable to oxidation under ambient conditions, resulting in surface discolouration. Compared with *Figure 8.5*, the blue/green regions in *Figure 8.6A* are exactly the regions where efflorescence forms. So far, no research has claimed the underlying mechanisms behind this phenomenon. It can be considered that there is a competition between efflorescence formation and oxidation of trisulfur anions, and the latter reaction might be hindered by the former.

Moreover, it can also be seen that more significant cracks are observed on both the top and sides of the NS cylinders. In fact, large drying shrinkage of AAS materials has been extensively confirmed in early studies [244,245], which can lead to severe cracking problems under ambient conditions. In addition, the magnitude of dry shrinkage is dependent on the RH of exposure conditions, with a lower RH exhibiting a more substantial shrinkage. The scenario of the bottom of cylinders in contact with water can induce an uneven distribution of RH and thus an uneven distribution of shrinkage, which in turn, significantly heightens the cracking potential of AAS cylinders. As reported in [72], similar cracks on the upper sides of the phosphorus slag activated by sodium silicate are also observed during efflorescence. They hypothesise this phenomenon to the growth of efflorescence products. To better understand this cracking issue, I conducted the efflorescence tests under N_2 conditions as well.

8.3.1.3 Effect of exposure to atmospheres

N_2 atmospheres can eliminate the influence of CO_2 and efflorescence formation on AAS cylinders. As shown in *Figure 8.7*, no efflorescence products but some cracks are observed on AAS cylinders under an N_2 atmosphere. In addition, the magnitude of cracks appears to be smaller than that under ambient conditions (*Figure 8.6*). This indicates that the semi-immersed condition is the main reason triggering the cracking of NS cylinders, and the accumulation of efflorescence products along the cracks under ambient conditions can further exacerbate the cracking problems.

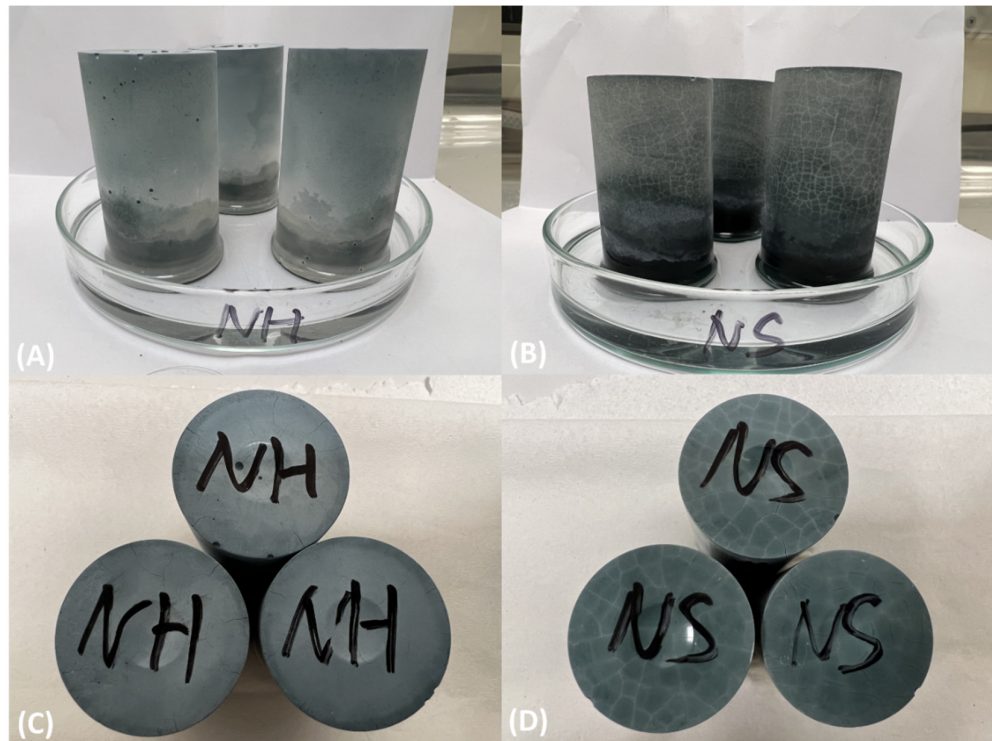


Figure 8.7. (A) and (B): NH and NS cylinders exposed to N_2 atmosphere under semi-contact water conditions. (C) and (D): Top surfaces of NH and NS cylinders after exposure for 28 d.

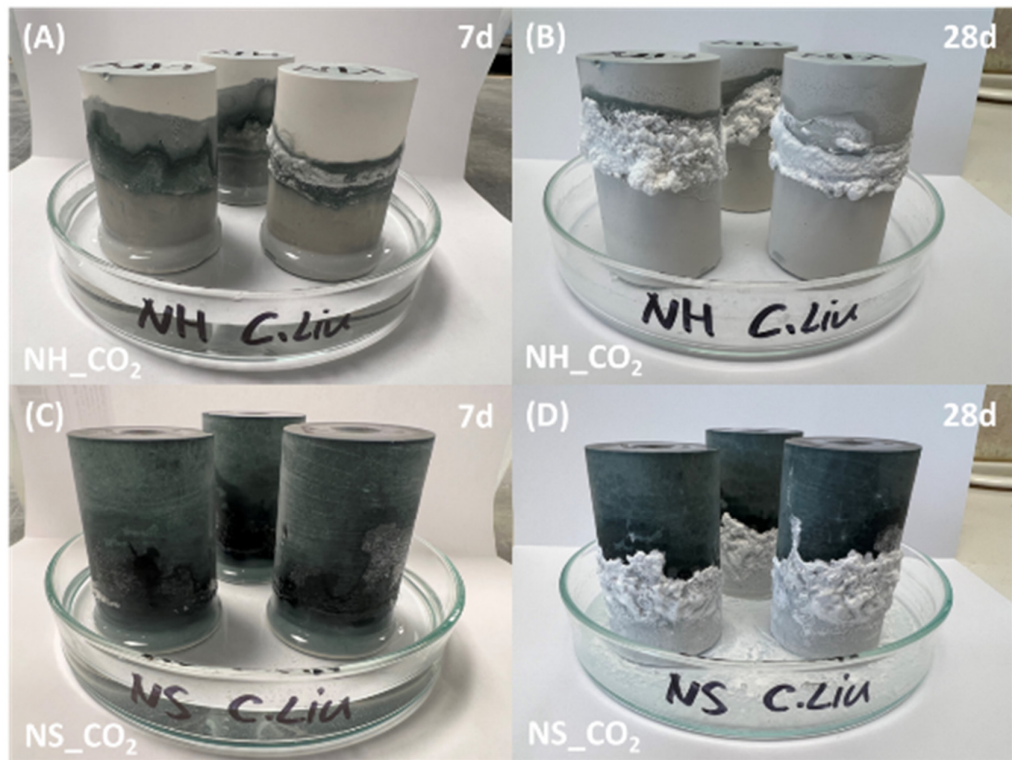


Figure 8.8. Visual observation of efflorescence of NH and NS cylinders exposed to 0.2% CO_2 conditions for 7 and 28 d.

To understand the impact of CO₂ concentration on the efflorescence of AAS pastes, cylinders exposed to a 0.2% CO₂ atmosphere are also observed, as shown in *Figure 8.8*. Consistent with the observations in *Figure 8.5*, the efflorescence front of NH cylinders is higher than that of NS ones. However, the white deposits appear thicker and denser on both types of cylinders under CO₂ conditions than under ambient conditions. This indicates that an elevated CO₂ concentration can promote the formation of efflorescence products. Additionally, it can be seen that the white deposits on NS cylinders under CO₂ conditions tend to accumulate at low positions rather than developing towards the top, as observed under ambient conditions (*Figure 8.5*), while cracks are also observed on NS cylinders. A possible reason for this phenomenon could be the internal circulation system in the CO₂ cabinet, which may provide a more significant drying process on the top of samples than under ambient conditions. The top sections of NS cylinders with cracks in the CO₂ chamber can be dried more quickly and intensively than under ambient conditions. However, efflorescence products fail to form under dry conditions. Therefore, the white deposits can predominantly form at the low and medium parts of NS cylinders.

8.3.1.4 Effect of relative humidities

Figure 8.9 displays the efflorescence of NH cylinders under different RH conditions. As observed in *Figures 8.9A–C*, the NH cylinder under RH = 40% has already shown efflorescence after 1 d of exposure, whereas those stored under RH of 60% and 80% do not. This indicates that the sample exposed to a lower RH environment undergoes a more rapid efflorescence process. With the extension of exposure time, white deposits gradually emerge and accumulate on cylinders under RH of 60% and 80%. During 28 d of exposure, the efflorescence on NH_40% samples is constantly more intensive than that on NH_60% and NH_80% ones. In addition, some drops of liquid are discernible on NH_80% samples (*Figures 8.9F and I*). This implies that moisture under high RH environments may condense on the surface of cylinders, which results in a reduced formation of visible efflorescence. Therefore, it is evident that RH plays a significant role in both the rate and severity of efflorescence.

It should be noted that the white deposits on NH cylinders in *Figure 8.9* develop at both the medium and top sections of the cylinder, contrasting with the observation in *Figure 8.5*. This distinction probably arises from the distribution of CO₂ within the experimental setups. Under ambient conditions (*Figure 8.1A*), cylinders are exposed to fresh air, among which CO₂ is evenly and constantly distributed around the cylinders at different heights. However, under different RH conditions, fresh CO₂ is only supplied through the vents of the tank (*Figure 8.1D*), potentially resulting in a higher concentration of CO₂ at the top of the cylinders than at low positions. This uneven distribution of CO₂ contributes to a preferential formation of efflorescence products at the upper regions of cylinders.



Figure 8.9. Visual observation of efflorescence of NH cylinders subjected to different RH conditions of 40%, 60% and 80% for 1, 7, and 28 d.

8.3.2 Leaching tests of AAS pastes

8.3.2.1 Na amount in different leachates

Leaching is regarded as a derivative problem of efflorescence, which partly reflects the efflorescence potential of materials [22]. Figure 8.10 shows the Na amount in four types of leachates per cylinder calculated from Na concentration tested by ICP-OES (Section 8.2.3). The “lea_cyl” and “lea_pie” refer to the leachates of AAS pastes in cylinder and piece shapes, respectively. The Na amount in the leachate of “lea_pie” is significantly higher than that of “lea_cyl”, attributed to the size effect of materials. Additionally, the paste with a higher alkali dosage shows a higher leaching amount of Na, consistent with the above efflorescence observation (Figure 8.4). Interestingly, the Na amount in the “lea_pie” of NS_5% is slightly lower than that of NH_5%, while the Na amount in the leachate of “lea_cyl” of NS_5% is much higher than NH_5% and even NH_7%. Regarding the former result, it is due to the higher content of C-(N)-A-S-H gels in NS pastes than in NH pastes. These gels require more Na ions to counterbalance the charge in the interlayer, resulting in a lower concentration of free Na ions in the pore solution (Chapter 5). As for the latter result, the leaching of cylinders is a transport issue, closely correlated with surface microstructure. While a higher silicate modulus results in reduced porosity, the surface of the NS cylinder suffers from the cracking problem under immersed conditions, which is the main reason why the cylinder of NS_5% exhibits a higher leaching amount of Na than NH_5%.

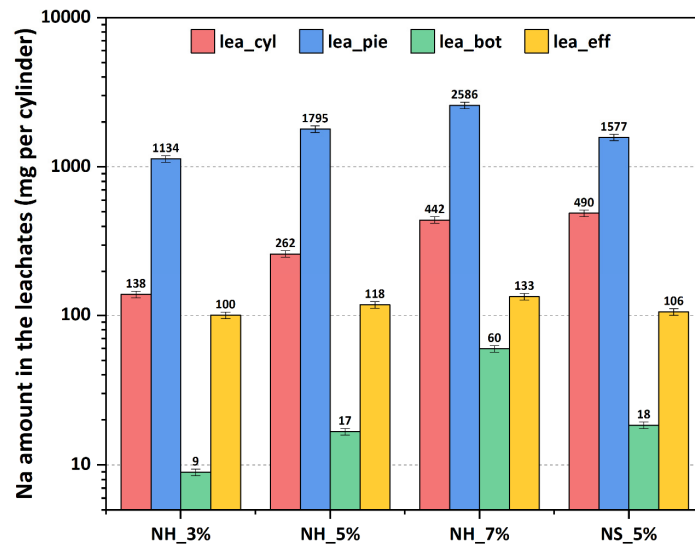


Figure 8.10. Na amount in different leachates of AAS pastes per cylinder.

The leachate of “lea_{bot}” refers to the solution in contact with the bottom of the cylinders. It is shown in *Figure 8.10* that the leached Na amount increases with the increase in alkali dosages in NH pastes. Different types of pastes with the same alkali dosage show comparable leaching amounts of Na in the leachate of “lea_{bot}”. This indicates that the leached amount of Na from the bottom of cylinders during efflorescence depends on the initial alkali contents. The Na amount in the leachate of “lea_{eff}” indicates the amount of Na in the efflorescence products (sodium (bi)carbonate), serving as a quantitative indicator for evaluating the severity of efflorescence of AAS cylinders. As can be expected, the NH_7% paste shows a higher Na amount than NH_5%, followed by the NH_3% paste, which aligns with the observations presented in *Figure 8.4*. Moreover, the Na amount in the leachate of “lea_{eff}” per NH cylinder (NH_5%) subjected to different RH conditions is shown in *Figure 8.11*. It is evident that the Na amount in the leachate of “lea_{eff}” increases with the decrease of RH, which matches the observation in *Figure 8.9*. The feasibility of this quantitative method is validated again. It is also seen that the Na amounts in the leachate of “lea_{eff}” under different RH conditions are all lower than that of NH_5% under ambient conditions. This is probably due to an insufficient CO₂ supply from the vents of the tank.

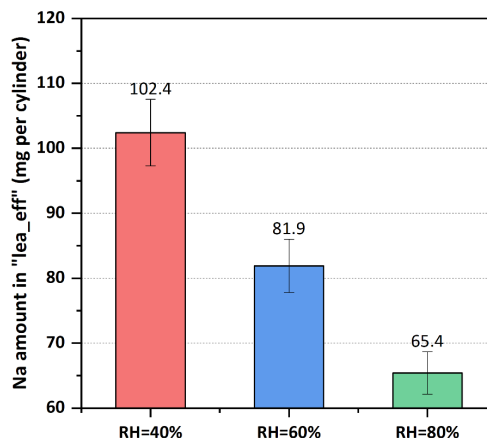


Figure 8.11. Na amount in the leachate of “lea_{eff}” per NH cylinder (NH_5%) under RH = 40%, 60% and 80% conditions.

8.3.2.2 Na distribution in AAS cylinders during efflorescence

Figure 8.12A shows the distribution of the absolute amount of Na in an AAS cylinder by mass. It is observed that the total leachable Na (“bottom-leached” + “efflorescence” + “remained”) in NH cylinders increases with the increase of the alkali content in the activator. The remained amount of leachable Na in the paste with a higher alkali dosage is also higher than that with a lower alkali dosage. This part of Na can be regarded as the efflorescence potential, and it is recommended to utilise this method for predicting the efflorescence potential of AAS materials.

Figure 8.12B shows the distribution of the relative proportion of Na in AAS cylinders under ambient conditions. It can be seen that the majority of leachable Na (90.5 – 92.6%) remains in the cylinder after 28 d of efflorescence. A minor fraction of Na (5.1 – 8.7%) is present in the efflorescence products, while a small proportion of Na (0.8 – 2.3%) leaches from the bottom. Compared with NH_5% and NS_5%, the fractions of “bottom-leached”, “efflorescence” and “remained” Na are comparable. Even though the presence of Si can densify the microstructure, it appears that it fails to significantly hinder the leaching of Na. As for the three NH pastes, it is interesting to note that the proportion of Na in the “efflorescence” part decreases with an increase in alkali dosages, while the proportion of Na in the “bottom-leached” part increases with the increase in alkali dosages.

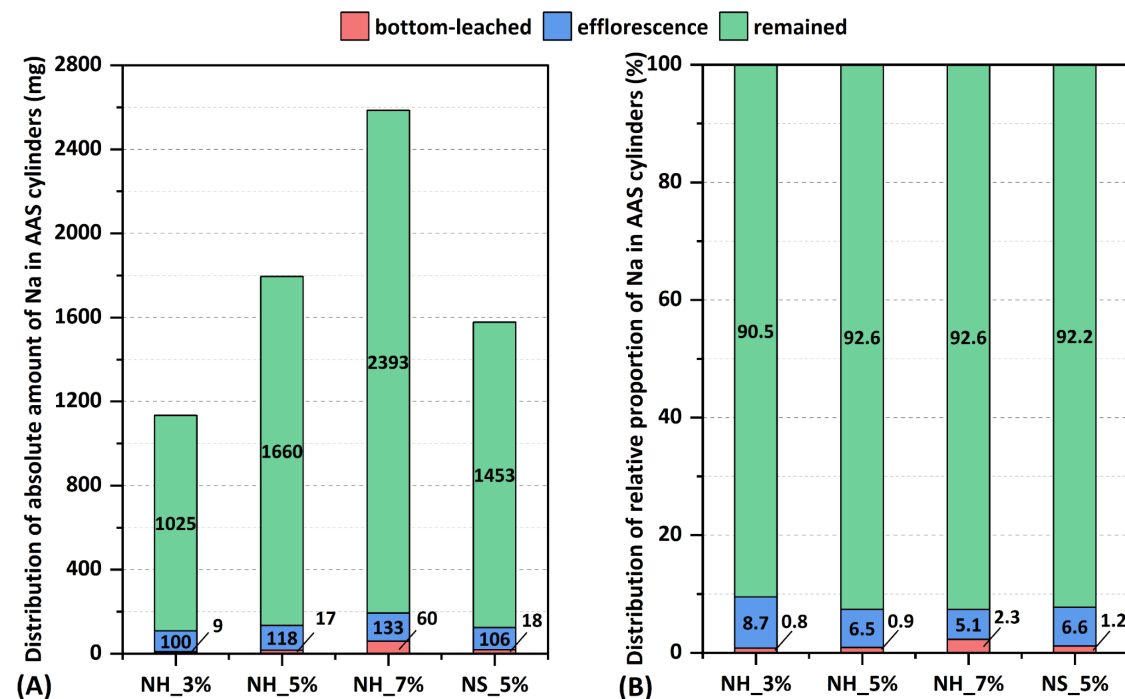


Figure 8.12. (A) Distribution of the absolute amount of Na in AAS cylinders under ambient conditions. (B) Distribution of the relative proportion of Na in AAS cylinders under ambient conditions. “bottom-leached” indicates the Na leached away from the bottom of the cylinder during efflorescence tests. “efflorescence” denotes the Na in efflorescence products. “remained” refers to the Na remaining in the cylinder after efflorescence tests. The sum of “bottom-leached”, “efflorescence” and “remained” Na is the total leachable Na in an AAS cylinder.

In fact, the relative Na distribution in AAS cylinders can reflect the mobility of Na, with a higher proportion of Na indicating a higher mobility of Na. It is plausible that the porosity contributes more than alkali dosages to impacting the mobility of Na in terms of efflorescence. Conversely, the alkali dosages have a greater influence on the mobility of Na concerning leaching than the porosity does. This indicates different main driving forces between leaching and efflorescence. The former is more related to the gradient of ion concentration, while the latter is more dependent on the transport of moisture and ions.

8.3.2.3 Relationship between leaching and efflorescence

Figure 8.13 shows the relationship between the Na amount in the efflorescence products and the leachate of “lea_pie” and “lea_cyl”. As shown in Figure 8.13A, the Na amount in the leachate of NH pieces shows a positive linear relationship with that in efflorescence products. This suggests that the leaching of Na from piece pastes can reflect the severity of the efflorescence of AAS cylinders. The leaching amount of Na of NS_5% is slightly lower than that of NH_5%, due to a lower porosity of NS_5%. As shown in Figure 8.13B, the Na amount in the leachate of cylinders is also positively related to that in the efflorescence products. However, the Na amount in the leachate of NS_5% is significantly higher than that of NH_5%, although both of the pastes show the same alkali dosage. As mentioned above, this is mainly attributed to the cracking of NS cylinders when subjected to water immersion (Chapter 7), which increases the permeability of the surface pastes and promotes the leaching of Na. Therefore, it is better to use the leaching result of piece samples to compare the efflorescence potential of AAS materials to minimise the size effect and cracking problems.

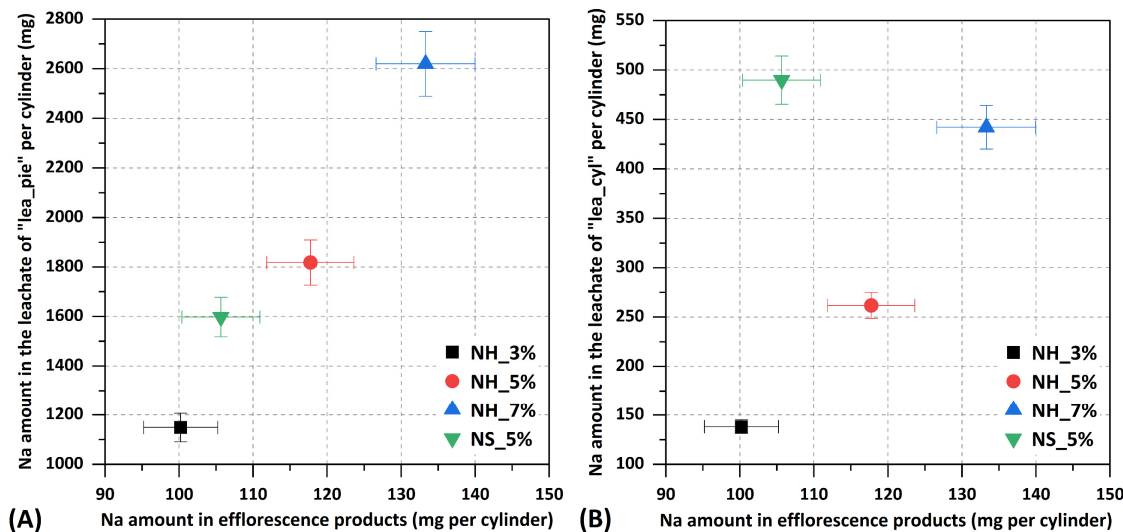


Figure 8.13. Relationship between the Na amount in efflorescence products per cylinder and the Na amount in the leachate of “lea_pie” and “lea_cyl” per cylinder. The Na amount in efflorescence products is obtained from the leachate of “lea_eff”.

8.3.3 Characterisations of AAS pastes

In this section, the impact of efflorescence on the properties of NH and NS cylinders with an alkali dosage of 5% under ambient conditions was investigated, representing two typical types of AAS materials. First, the component of efflorescence products of NH and NS cylinders was identified. Then, the phase assemblage, gel structure and pore structure of AAS cylinders at different heights after 28 d of efflorescence were examined. Finally, the compressive strength of AAS pastes with and without efflorescence was compared.

8.3.3.1 XRD

Figure 8.14 shows the XRD pattern of the white deposits on NH and NS cylinders after 28 d of efflorescence under ambient conditions. In agreement with previous works [22,24,74,79,91,95,246], the primary efflorescence product of both groups is identified as hydrated sodium carbonate. However, the efflorescence product of the NH pastes is dominated by $\text{Na}_2\text{CO}_3 \cdot 7\text{H}_2\text{O}$, whereas that of NS pastes is $\text{Na}_2\text{CO}_3 \cdot \text{H}_2\text{O}$. This indicates a higher presence of chemically bound water in the white deposits of NH cylinders. As stated in [247], the chemically bound water of sodium carbonate is dependent on the humidity of its growth environments. As both types of pastes are exposed to the same ambient conditions (Figure 8.1A), the distinction of chemically bound water in efflorescence products is mainly due to the water supply from the bottom of the cylinder. Specifically, the NH paste shows a more porous structure, allowing it to absorb more water from the bottom. A higher water content in the pore structure is therefore conducive to the increase of chemically bound water in efflorescence products.

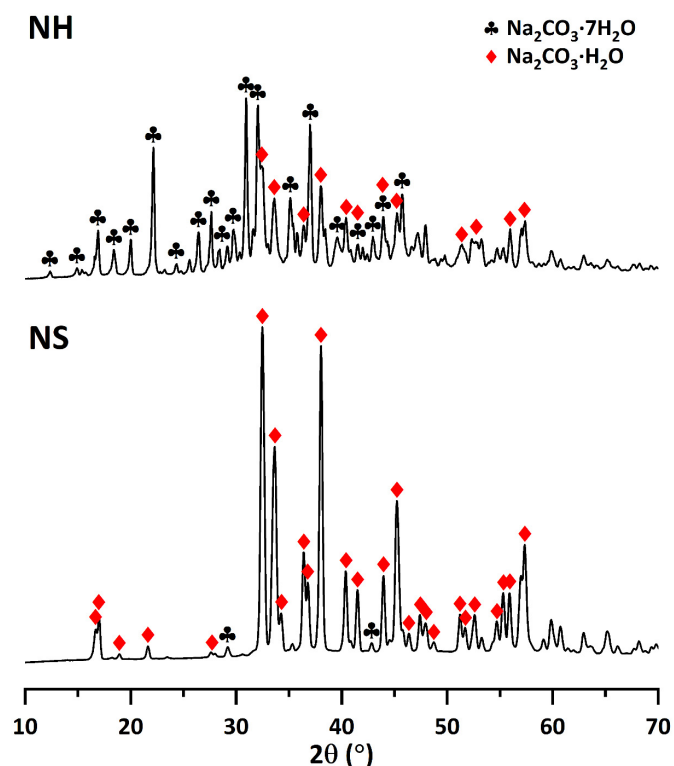


Figure 8.14. XRD patterns of the efflorescence products on the NH and NS cylinders under ambient conditions for 28 d.

Figure 8.15A shows the XRD pattern of 7 d NH pastes subjected to 28 d of efflorescence under ambient conditions and 28 d of sealed conditions, respectively. In general, C-(N)-A-S-H gels [248] and hydrotalcite-like phases [60] are the two main phases dominated in NH pastes under sealed conditions, while calcite and vaterite, two CaCO_3 polymorphs [183], are the CO_2 -bearing phase detected in the sample under ambient conditions. Additionally, the phase assemblage of the pastes exhibits slight differences at different heights of cylinders. For instance, while the “top”, “med”, “low” and “bot” pastes are all exposed to ambient conditions, they experience carbonation to different degrees. It appears that the top of the cylinder is subjected to more severe carbonation than the other parts, as indicated by more pronounced characteristic peaks. This is due to different mechanisms between dry and wet carbonations. In the “bot” part, the paste is submerged in deionised water. Due to the gradient of ion concentration, Ca, Na and OH ions can leach away from the bottom of cylinders, which increases the pH of the leachate. Under alkaline conditions, gaseous CO_2 can hydrolyse to CO_3^{2-} , which then reacts with Ca ions to the precipitation of CaCO_3 on the surface of cylinders or in the leachate (Chapter 5).

In the “low” part, despite not being fully immersed in water, the paste at this location also has a relatively high saturation degree, which may follow the same wet carbonation mechanism as that in the “bot” part. However, on the “top” part of the cylinders, the paste is situated at a relatively high position and exposed to dry air, which is vulnerable to dry carbonation [191,249,250]. As reported in [251], calcium carbonate and carbonated hydrotalcite-like phases are the two main CO_2 -bearing phases upon dry or ambient carbonation. Due to a probably higher concentration of CO_2 in the air than in the leachate and the higher diffusion coefficient of CO_2 in the dry matrix, dry carbonation appears to be more intensive than wet carbonation during the same exposure time. This is supported by more evident peaks of calcite in the “top” paste.

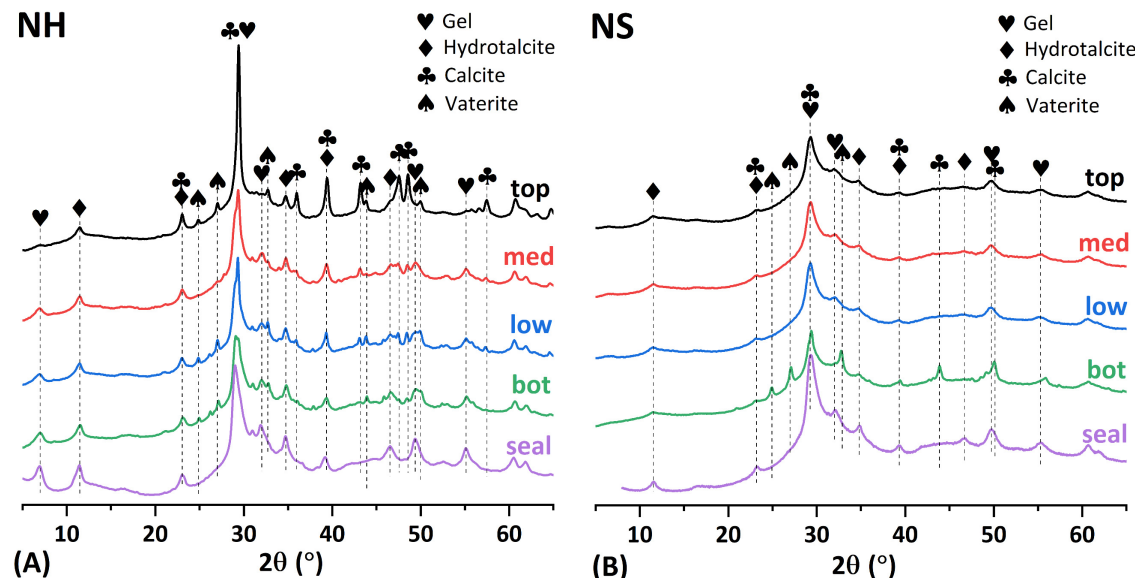


Figure 8.15. XRD pattern of 7 d (A) NH and (B) NS pastes subjected to 28 d of efflorescence under ambient conditions and 28 d of sealed conditions. The labels “top”, “med”, “low” and “bot” represent the top, medium, low and immersed parts of the AAS cylinder under ambient conditions, respectively. The label “seal” denotes the AAS paste under sealed conditions.

Interestingly, calcium carbonate is rarely detected in the paste located at the “med” position, at which the efflorescence product of sodium carbonate emerges (*Figure 8.5*). This implies that the dissolved or dried CO₂ in this region has an affinity for the formation of Na₂CO₃ rather than CaCO₃. This is likely due to a conducive RH for the growth of Na₂CO₃ in the “med” region and a considerably higher concentration of Na ions than Ca ions in an AAS system. Furthermore, the characteristic peaks of gels in the pastes under sealed conditions remain more evident than those under ambient conditions, and the reflection of gels of paste at the “top” is less intense than the others. These can be attributed to gel decalcification caused by wet and dry carbonation to different extents. As for hydrotalcite-like phases, no significant differences are identified among the five pastes, as the characterisation peak of hydrotalcite is almost the same as that upon carbonation [252]. This indicates that hydrotalcite is stable to wet or dry carbonation.

Figure 8.15B shows the XRD pattern of 7 d NS pastes subjected to 28 d of efflorescence under ambient conditions and 28 d of sealed conditions, respectively. Despite the two phases of gels and hydrotalcite being the same as identified in NH pastes, their characteristic peaks in NS pastes are less evident, indicating a more amorphous structure of reaction products in the NS system [61,104]. Different from that in NH samples, calcium carbonate is only identified in the “bot” part of the NS cylinder. On one hand, this suggests that NS pastes are less susceptible to dry carbonation, consistent with results reported in [253,254]. The primary reason is a lower content of free Ca ions in both the pore solution and interlayer of gels [104,126], leading to reduced formation of calcium carbonate compared to NH systems. In addition, calcium carbonate formed in the interlayer of gels is more amorphous, which is hardly detected by XRD. On the other hand, as shown in *Figure 8.5*, the efflorescence products on NS cylinders initiate from the “low” position and develop to the top gradually. This observation again proves that CaCO₃ does not form in the region where efflorescence happens. Regarding the gel and hydrotalcite-like phases, NS pastes at different levels show limited discrepancies.

8.3.3.2 TGA

Figure 8.16 shows the TG and DTG curves of 7 d NH and NS pastes subjected to 28 d of efflorescence under ambient conditions and 28 d of sealed conditions. According to the literature [255], weight loss below 200 °C corresponds to the release of water from gels, while hydrotalcite-like phases mainly undergo decomposition at around 200 – 250 °C and 300 – 400 °C [252]. Due to the different chemical structures of calcium carbonate, amorphous/poorly-crystallised CaCO₃, aragonite, vaterite, and calcite are decomposed at temperatures around 450 – 530 °C, 530 – 650 °C, and 650 – 950 °C, respectively [183,256].

Figure 8.16A shows the TG and DTG curves of NH samples. The peak of gels is more significant in the sealed sample than in the exposed samples. This weight loss in gels is associated with both a higher content of gels and a higher content of chemically bound water in gels. The former lies in the fact that the sealed condition is conducive to the reaction of slag and the formation of gels, while the latter results from the reduction of interlayer Ca or Na in gels caused by carbonation or efflorescence, which subsequently decreases the chemically bound water in the gels. In addition to the sealed condition, the cylinder under ambient conditions contains different contents and types of CaCO₃ at different heights. Specifically, the decomposition peak of calcium carbonate in the “top” of NH cylinders ranges from 450 °C to 750 °C. Combined with the above XRD results (*Figure 8.15A*), this indicates the presence of

amorphous CaCO_3 , vaterite and calcite, which resembles that in NH pastes upon natural carbonation [179,254,255].

In the “bot” and “low” parts, the pastes undergo wet carbonation, and the decomposition peak of calcium carbonate is much higher than that in the “top” region, indicating a more stable polymorph. The formation of different polymorphs of CaCO_3 under dry and wet carbonation is probably dependent on the specific location of the carbonation reaction. In a dry condition, the pore structure is less saturated. The carbonation reaction happens in both the pore solution and gel structure. The free Ca ions in the pore solution have a relatively large space for the formation of CaCO_3 , which contributes to the formation of crystallised CaCO_3 , like vaterite and calcite (*Figure 8.15A*). However, the interlayer Ca located in the basal spacing of gels has less space for CaCO_3 formation, allowing only the formation of amorphous CaCO_3 with a smaller size than crystallised CaCO_3 [257]. Under wet conditions, the water content in pores becomes higher, which leads to the leaching of interlayer Ca in gels. The leached Ca migrates to the pore solution and promotes the formation of vaterite and calcite. Moreover, the content of CaCO_3 in the “top” part is much higher than that in the “bot” and “low” parts and no evident decomposition peak of calcium carbonate is found in “med”. These observations align well with the above XRD results (*Figure 8.15A*).

Figure 8.16B shows the TG and DTG curves of NS pastes. Generally, the total weight loss of NS pastes is comparable to that of NH pastes. Two decomposition peaks corresponding to gels and hydrotalcite-like phases are observed in sealed NS pastes, and the intensity of the gel peak is also higher than the others, similar to NH pastes. Additionally, CaCO_3 is exclusively detected in the “bot” part of cylinders, which matches well the XRD results (*Figure 8.15B*). Interestingly, the water-immersed part of the cylinder (“bot”) exhibits a lower content of gels than the other three groups. This is probably due to the leaching and carbonation of gels [20,126].

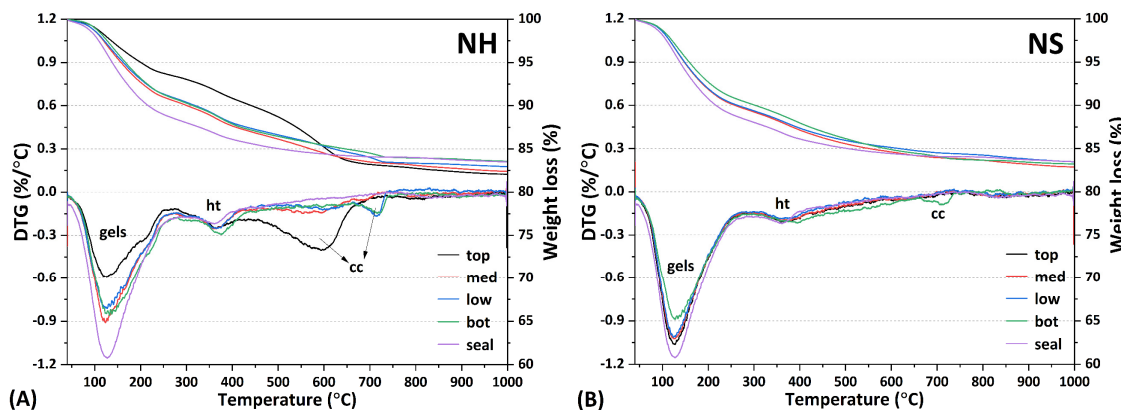


Figure 8.16. TG and DTG curves of 7 d (A) NH and (B) NS pastes subjected to 28 d of efflorescence under ambient conditions and 28 d of sealed conditions. Ht: hydrotalcite-like phases; cc: calcium carbonate.

8.3.3.3 FTIR

Figure 8.17 shows the FTIR pattern of AAS pastes subjected to 28 d of efflorescence under ambient conditions and 28 d of sealed conditions. It is observed that all the FTIR pattern is dominated by a hump around 950 cm^{-1} , which is associated with the asymmetric stretch of Si-O bonds generated by Q^2 units in gels [254]. A shoulder on the low-frequency side of this hump is located at 895 cm^{-1} , referring to the bending vibration of Si-O. In addition, the peak at around 875 cm^{-1} is assigned to the out-of-plane bending of CO_3^{2-} in calcium carbonate.

Figure 8.17A shows the FTIR pattern of NH pastes. It is observed that the peak value of Q^2 units ranges from 943 cm^{-1} to 960.9 cm^{-1} in the five pastes. A higher wavenumber of the Q^2 peak indicates a higher polymerisation degree of gel structure [235]. The peak value of Q^2 units in the “top” paste is much higher than that in the remaining four pastes. This is mainly due to gel decalcification caused by dry carbonation [258]. Additionally, the peak values of the “med”, “low” and “bot” pastes are comparable and higher than those of the paste under sealed conditions. The elevated polymerisation of gel structure in “low” and “bot” can be attributed to gel decalcification caused by wet carbonation. However, in the “med” part, carbonation of pastes is rarely detected in XRD, TGA and FTIR results, thereby this phenomenon cannot be directly ascribed to carbonation. As discussed in Chapter 4, the leaching of interlayer Na prompts the movement of Ca from intralayer to interlayer, which results in the decalcification of the Ca-O sheet in silicate chains. In the “med” region of NH cylinders, efflorescence products form considerably, as shown in Figure 8.5. The leaching of Na in gels may occur for the formation of sodium carbonate, resulting in an increased length of gels. Moreover, the reflection of C-O units at 875 cm^{-1} is prominently present in the “top” part of the NH cylinder, as an indicator of a substantial presence of calcium carbonate. The presence of C-O units in “low” and “bot” pastes is also identified, but the content is very low. These observations are all in agreement with XRD and TGA results.

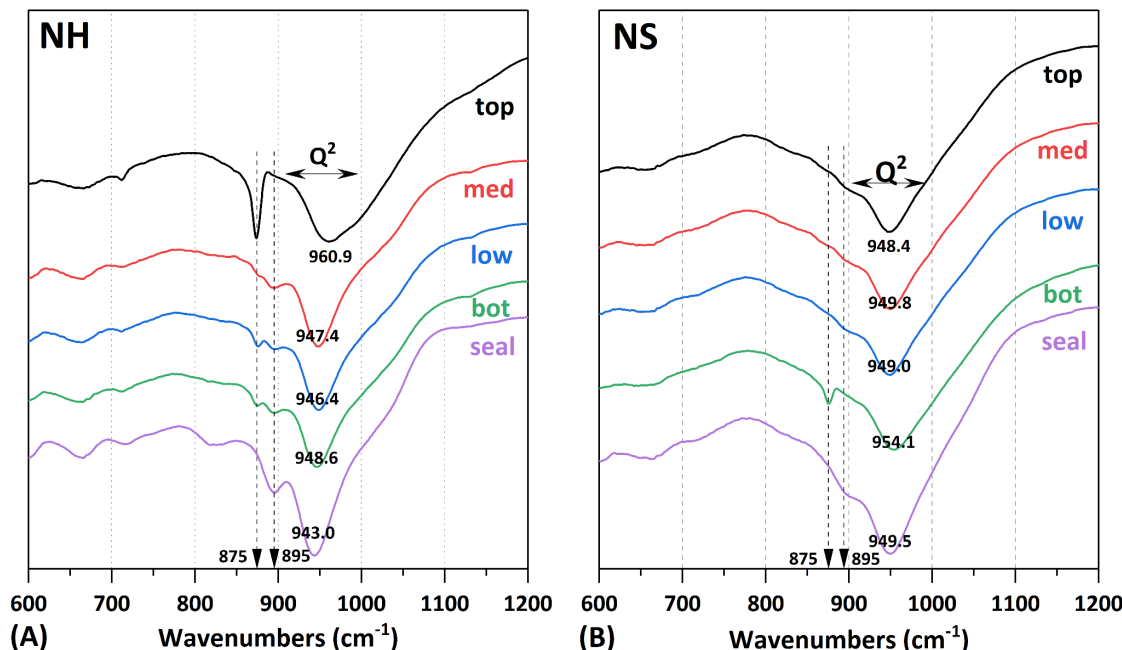


Figure 8.17. FTIR pattern of 7 d (A) NH and (B) NS pastes subjected to 28 d of efflorescence under ambient conditions and 28 d of sealed conditions.

Figure 8.17B shows the FTIR pattern of NS cylinders. The peak value of Q^2 units ranges from 948.4 cm^{-1} to 954.1 cm^{-1} in the five NS pastes, which is generally higher than that of NH pastes, except for the “top” of NH cylinders. With equivalent alkali dosage, gels in NS pastes have a lower Ca/Si ratio than NH pastes, resulting in a higher polymerisation of gels in NS pastes [126]. Additionally, the peak values of “top”, “med”, “low” and “seal” are comparable, which are lower than that of “bot”. Integrating the results of XRD, TGA and FTIR, it can be found that calcium carbonate is only identified in the “bot”, which is immersed in water. Therefore, the elevated polymerisation degree of gels is due to the wet carbonation of gels and the leaching of Na. The out-of-plane bending of C-O in calcium carbonate is detected in the “bot” part of NS cylinders, consistent with XRD and TGA results.

8.3.3.4 MIP

Figure 8.18 shows the cumulative pore volume and pore size distribution of 7 d NH and NS pastes subjected to 28 d of efflorescence under ambient conditions and 28 d of sealed conditions. *Table 8.2* presents the porosity of AAS pastes, considering the pores ranging from 7 nm to 400 μm . Normally, pores in building material are broadly categorised into gel pores ($0.001 - 0.01\text{ }\mu\text{m}$), small capillary pores ($0.01 - 1\text{ }\mu\text{m}$), big capillary pores ($1 - 100\text{ }\mu\text{m}$) and voids or cracks ($>100\text{ }\mu\text{m}$) [237]. Generally, the porosity of NS pastes is significantly lower than that of NH pastes, due to the presence of silicates in the activator of NS systems.

In terms of NH pastes, the porosity of “top”, “med”, “low” and “bot” is comparable, ranging from 22% to 24%, which is lower than that of “seal”. This result is consistent with findings reported in [47,254], where the NH paste under ambient conditions shows lower porosity than under sealed conditions. This is attributed to the presence of Ca in the pore solution, which promotes the formation of calcium carbonate under ambient conditions — a volume expansion reaction that subsequently densifies the pore structure. This might be validated by *Figure 8.18B*, in which the paste under sealed conditions shows a higher volume of large pores ($0.1 - 0.01\text{ }\mu\text{m}$) than that under ambient conditions. These pores are probably due to the formation of calcium carbonate under ambient conditions.

The total porosity of NS paste under sealed and ambient conditions is comparable (*Figure 8.18C* and *Table 8.2*). However, the pore size distribution between them is different, as shown in *Figure 8.18D*. Specifically, the NS paste under sealed conditions shows a high volume of large pores but a lower volume of small capillary pores and gel pores, which is also consistent with the pore size distribution of NH paste. This indicates that the refinement of voids and cracks is compromised by the coarsening of small capillary pores and gel pores. However, the pore refinement by carbonation is not that efficient in NH pastes, since there is less Ca available to be carbonated to form calcium carbonate, as presented in XRD, TGA and FTIR results. Even worse, as discussed above, the cracking of NS cylinders can be exacerbated by the formation of efflorescence products, which may further compromise the positive effect of calcium carbonate formation. Overall, 28 d of efflorescence shows limited influence on the total porosity of both NH and NS pastes, but can affect their pore size distributions.

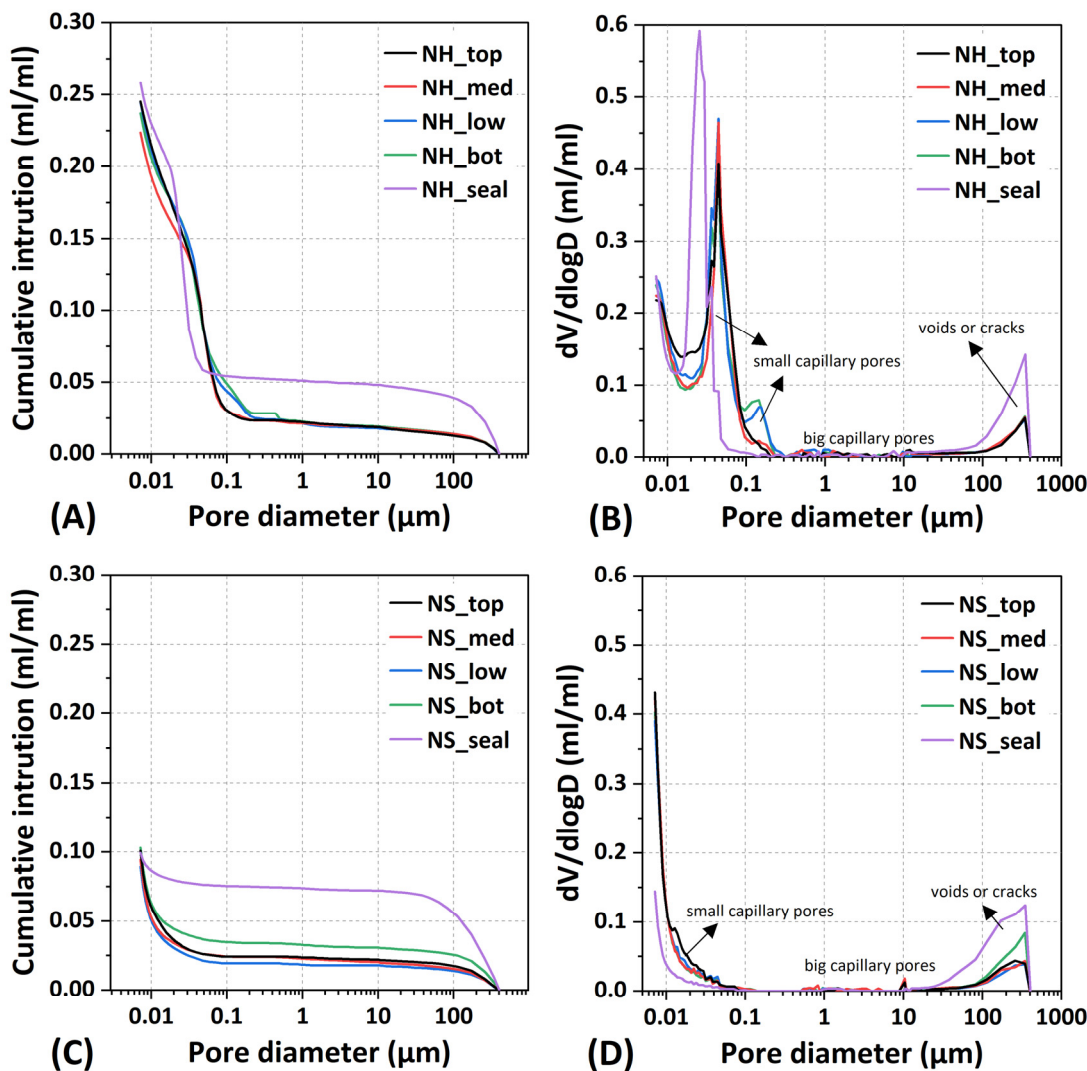


Figure 8.18. Cumulative pore volume and pore size distribution of 7 d NH and NS pastes subjected to 28 d of efflorescence under ambient conditions and 28 d of sealed conditions.

Table 8.2. Porosity of NH and NS pastes considering the pores ranging from 7 nm to 400 μm .

	Porosity (%)		Porosity (%)
NH_top	23.7	NS_top	10.3
NH_med	24.5	NS_med	8.9
NH_low	22.4	NS_low	9.4
NH_bot	24.5	NS_bot	10.1
NH_seal	25.9	NS_seal	9.9

8.3.3.5 Compressive strength

Figure 8.19 shows the compressive strength of NH and NS pastes under ambient, “ambient_bot” and “N₂_bot” conditions. Generally, the compressive strength of NS pastes is significantly higher than that of NH pastes, corresponding to the MIP results. As shown in Figure 8.19A, the compressive strengths of NH prisms exposed to three conditions all increase with time. The compressive strengths of NH prisms exposed to the “ambient_bot” condition

at 7 and 28 d are slightly lower than those under ambient and “N₂_bot” conditions, which suggests that efflorescence barely shows an adverse impact on the compressive strength of NH pastes. As shown in *Figure 8.6*, the NH cylinders, after exposure to “ambient_bot” and “N₂_bot” conditions for 28 d, exhibit no visible surface cracks. These results imply that neither the uneven distribution of humidity nor the crystallisation pressure induced by efflorescence formation leads to significant structural problems in the matrix of NH pastes.

However, efflorescence shows significantly adverse impacts on the compressive strength of NS pastes. As shown in *Figure 8.19B*, the compressive strength of NS specimens under the “ambient_bot” condition is significantly lower than that under ambient conditions. This decline is mainly due to the problem of cracking. On one hand, the “ambient_bot” condition can induce an uneven distribution of water content, which further leads to an uneven distribution of internal stress and the formation of cracks [14,50,126]. On the other hand, excessive formation of efflorescence products along the cracks results in volume expansion and crack propagation. The compressive strength of NS pastes under the “N₂_bot” condition can support this statement. At 7 d, the compressive strength of prisms under the “N₂_bot” condition is lower than that under both the “ambient” and “ambient_bot” conditions. This indicates that even without efflorescence, the semi-contacted water condition has already induced significant reductions in compressive strength. In addition, the slightly lower value of “N₂_bot” compared to “ambient_bot” at 7 d is probably because the early-formed efflorescence products can partially densify the cracks. Noted that the samples with efflorescence products were not ultrasonically cleaned before compressive tests. However, at 28 d, the compressive strength of NS samples exposed to the “ambient_bot” condition is lower than that under the “N₂_bot” condition. This implies that prolonged formation of efflorescence products can exacerbate the cracking issue. Therefore, AAS paste with a high silicate modulus is more susceptible to efflorescence in terms of compressive strength.

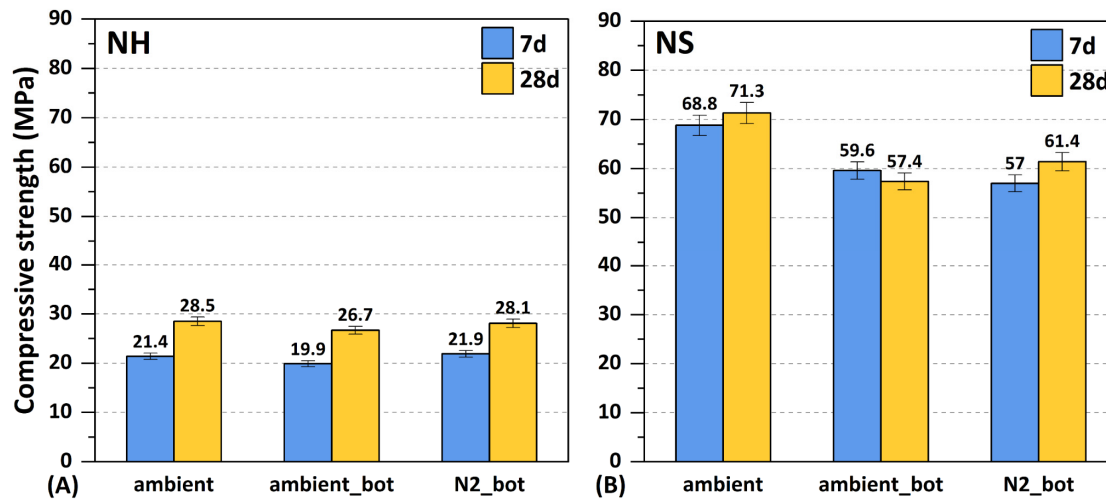


Figure 8.19. Compressive strength of NH and NS pastes sealed for 7 d followed by exposure to ambient, “ambient_bot”, and “N₂_bot” conditions for 7 and 28 d. “ambient” represents a room environment with T = 20 °C and RH = 55%. “ambient_bot” refers to the bottom of prisms in contact with water under ambient condition. “N₂_eff” denotes the bottom of prisms in contact with water under N₂ conditions.

8.4 Discussion

8.4.1 Efflorescence process of AAS pastes

Accordingly, the efflorescence of AAS cylinders under ambient conditions is observed, and the impact of efflorescence on AAS pastes is investigated. Based on these findings, the efflorescence process of NH and NS pastes can be deduced. *Figure 8.20* depicts a schematic representation of the process of efflorescence of AAS pastes under ambient conditions. Given the different chemical composition and pore structure between the NH and NS pastes, it is necessary to discuss them separately.

Figure 8.20A demonstrates the efflorescence process of NH pastes. Generally, the paste with its bottom in contact with water can be divided into underwater and overwater parts by the waterline. In the underwater part, the paste is subjected to leaching. Due to the gradient of ion concentration, Na, Ca and OH ions in the pore solution can leach away from the bottom, which can increase the pH of the leachate. An alkaline condition facilitates the dissolution of gaseous CO_2 and contributes to the formation of CO_3^{2-} by hydrolysis. The resulting CO_3^{2-} can further react with Ca ions to the precipitation of CaCO_3 attached to the “bot” of the samples.

Once the underwater region has been entirely infiltrated, moisture continues to migrate upward. In the area nearly above the waterline (“low” sections), a water film on the surface of the sample forms. Gaseous CO_2 can dissolve into this water film and hydrolyse to CO_3^{2-} ; in the meantime, Na and Ca ions can migrate to the surface from the matrix, contributing to the formation of Na_2CO_3 and CaCO_3 . However, as a result of the high humidity at the “low” position, the efflorescence product of Na_2CO_3 crystals is soluble in this zone, hence the main CO_2 -bearing phase is CaCO_3 .

As the increase of the height of the cylinder, the RH around the pastes would gradually diminish. There is an area in which sodium carbonate is more likely to form. In the case of the NH pastes, the efflorescence front is located in the medium part, while that of the NS paste is located at a lower position. This is due to a more porous structure of the NH paste, contributing to an increased water sorptivity of cylinders and a higher fraction of high-humidity regions. Additionally, CaCO_3 is barely identified at the region where efflorescence emerges, which indicates a preferential formation of Na_2CO_3 over CaCO_3 . NH pastes after 28 d of efflorescence show limited cracks on the surface. The efflorescence products accumulate progressively around the efflorescence front. As for the “top” part, the paste at this location is relatively dry, akin to dry carbonation, where CaCO_3 emerges as the main CO_2 -bearing product.

Figure 8.20B depicts the efflorescence process of NS paste. Similar to the NH pastes, calcium carbonate is detected in the “bot” of the NS cylinder, resulting from the leaching of Ca ions in the matrix and the solvent CO_3^{2-} from the air. Due to the lower porosity of the matrix, the efflorescence front of the NS paste is lower than that of the NH paste. However, the efflorescence product of NS pastes can develop toward a higher position than NH pastes. This phenomenon is probably attributed to the cracking of NS cylinders under such semi-contact water conditions, which can promote the transport of water and alkali ions. Additionally, the crack problem can be exacerbated by the formation of efflorescence products. Similar to NH pastes, calcium carbonate is absent in the efflorescence regions of NS cylinders (“low”, “med” and “top”). This again indicates a competition between efflorescence and carbonation.

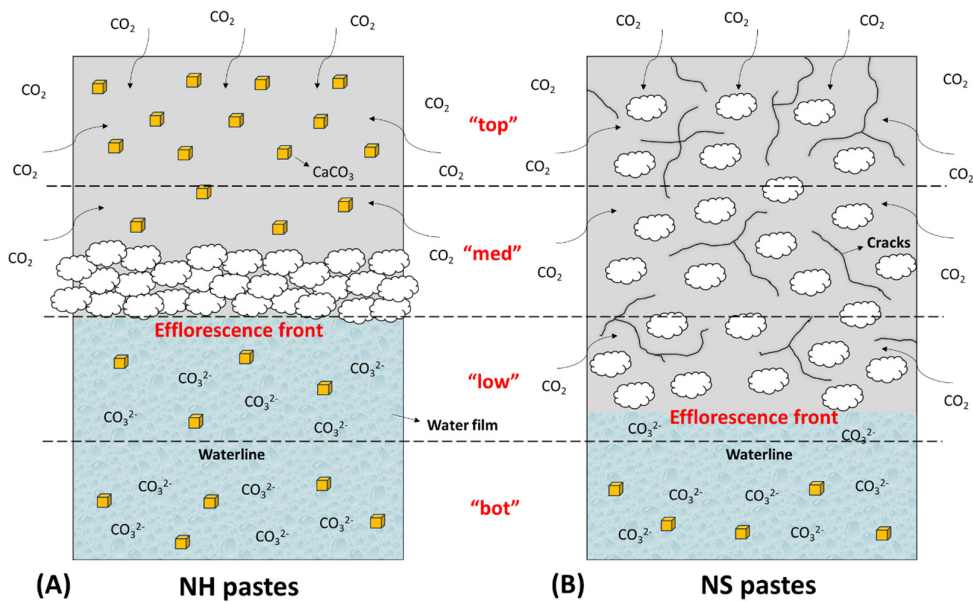


Figure 8.20. Schematic representation of the process of efflorescence of NH and NS pastes under ambient conditions. The white cloud-like shape refers to the efflorescence products (sodium carbonate), and the golden cubic shape refers to the carbonation products (calcium carbonate).

8.4.2 Efflorescence mechanisms of AAS pastes

For a better understanding of the mechanisms of efflorescence of AAS pastes, it is essential to focus on the formation of efflorescence products (hydrated sodium carbonate). Figure 8.21 shows the chemical reaction of efflorescence formation. It can be seen that Na^+ , CO_3^{2-} and H_2O are the three main components contributing to the formation of sodium carbonate. Their availability is influenced by alkali dosages, pore structure and environmental conditions.

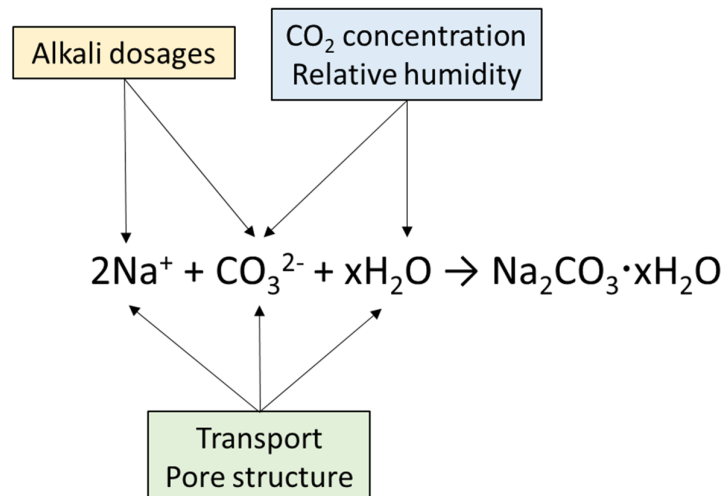


Figure 8.21. Formation mechanisms and influential factors of efflorescence products of AAS pastes.

Alkali metal ion (Na)

The Na in efflorescence products stems from the leaching of Na in AAS pastes, with most of the Na ions deriving from the pore solution and a minor portion from C-(N-)A-S-H gels [72]. The overall amount of Na that can reach the water film surrounding the paste is governed by both the alkali content in the pore solution (or the initial alkali dosage in activators) and the transport of Na within the pore structure. As for the same type of AAS pastes, although a higher alkali content contributes to a denser microstructure, which can partly hinder the transport of Na ions, the alkali content seems to play a more significant role than the pore structure as observed in efflorescence experiments among "NH_3%", "NH_5%" and "NH_7%". Additionally, at the same alkali dosage, a compact microstructure can impede efflorescence during early ages. Nevertheless, due to the cracking of NS pastes, the transport of Na is enhanced and the severity of efflorescence of NH and NS cylinders at 28 d becomes comparable. This highlights the importance of pore structure in influencing the efflorescence.

CO₂

The concentration of CO₂ remains constant in the air at around 0.04% by volume, while that in a liquid is not fixed. As for efflorescence, it is important to understand the dissolution of CO₂ in the water film on the surface of pastes. Therefore, it is imperative to understand the dissolution behaviour of CO₂ in an aqueous condition. Typically, CO₂ can first react with water to form H₂CO₃ molecules slowly, as shown in *Equation 8.1* [174,175]. Under weak alkali conditions with a pH < 8, these H₂CO₃ molecules react with OH⁻ to yield bicarbonate ions (HCO₃⁻), as expressed in *Equation 8.2* [259]. In cases where the alkali solution is fairly concentrated with a pH > 10, CO₂ can directly react with OH⁻ to form HCO₃⁻, which further reacts with OH⁻ to form CO₃²⁻, as shown in *Equation 8.3*. If the alkali is depleted or the atmospheric CO₂ is in high concentration, the CO₃²⁻ can react with CO₂ once again, forming HCO₃⁻ again, leading to the decrease of pH of solutions (*Equation 8.4*) [174,260].



According to these equations, it can be found that the type and amount of hydrolysed CO₂ species are closely dependent on the pH of the water film and the concentration of gaseous CO₂. Under ambient conditions, external CO₂ concentration is relatively low and can be regarded as a constant, thereby the pH of the water film on the paste plays a more vital role. The pH level is altered by the leaching of OH⁻ from the matrix, which is associated with both the alkali dosage and transport. Additionally, the phase assemblage of efflorescence products is also impacted by the concentration of CO₂. As shown in *Appendix Figure B1*, Trona (Na₃H(CO₃)₂·2H₂O), considered a combination of NaHCO₃ and Na₂CO₃, is identified on NH cylinders under 0.2% CO₂ conditions. This indicates that a higher CO₂ concentration is conducive to the conversion from Na₂CO₃ to NaHCO₃. Therefore, considering the complexity of the anions of efflorescence products, it is better to quantify efflorescence by determining the amount of Na.

Water (or RH)

Water serves as the medium of chemical reactions, significantly impacting the visibility and chemically bound water of efflorescence products. A relatively low RH is favourable for both the rate and severity of efflorescence formation of AAS pastes, particularly when the bottom of the samples is in contact with water, as observed in the efflorescence tests among "NH_40%", "NH_60%" and "NH_80%". Conversely, a high RH results in the dissolution of efflorescence products and a reduction in visible efflorescence. Additionally, water transport can affect the chemically bound water of efflorescence products. Sodium carbonate on the NH paste shows a higher content of chemically bound water compared to the NS one. This is related to the porous pore structure of the NH pastes, which can provide the crystallisation of sodium carbonate with more water.

8.5 Conclusions

In this chapter, the effects of alkali dosages, activator types, exposure atmospheres, and relative humidity on the efflorescence of AAS pastes were observed. The leaching tests of pastes in different sizes were performed. The influence of efflorescence on phase assemblage, gel structure, pore structure and compressive strength of AAS pastes was examined as well. Based on the above results, the process and mechanism of efflorescence of AAS pastes have been clarified. The conclusions are summarised as follows.

1. At the same alkali dosage, NH pastes had more porous microstructures and showed faster efflorescence rates than NS pastes. The NH paste with a higher alkali dosage showed more severe efflorescence. The NH paste subjected to a lower RH environment showed a more rapid and significant efflorescence. NS pastes suffered from cracking problems when the bottom contact with water under both N_2 and ambient conditions. Furthermore, the formation of efflorescence products can exacerbate this cracking problem.
2. The efflorescence front of AAS pastes was associated with the pore structure. The paste with a higher porosity shows a higher efflorescence front. The efflorescence products of NH pastes accumulated near the efflorescence front, while those of NS pastes can develop on the top. This was attributed to the cracking of NS cylinders, which promoted the transport of water and alkali ions and the formation of efflorescence products.
3. It was feasible to quantitatively determine the efflorescence of AAS pastes by calculating the amount of Na in efflorescence products. The quantitative results were not only consistent with visual observations but also correlated with the leaching results of AAS pastes. However, it should be noted that the leaching results of NS cylinders failed to establish a good relationship with efflorescence due to the cracking problem under immersed conditions. Therefore, to evaluate the efflorescence potential of AAS pastes, it was recommended to use the leaching results of piece samples.
4. While the efflorescence products of NH and NS pastes were both dominated by sodium carbonate, their chemically bound water was different. Sodium carbonate in NH pastes had a higher content of chemical-bound water. This was due to a more porous structure of NH pastes, which allowed for a greater supply of water from the bottom of cylinders for the formation of sodium carbonate. A higher CO_2 concentration was conducive to the conversion of sodium carbonate to sodium bicarbonate.
5. The water-immersed part of the pastes was subjected to wet carbonation, while the overwater part was subjected to both efflorescence and dry carbonation. However, these two chemical processes seemingly cannot happen simultaneously and appear to compete

with each other. Calcium carbonate was rarely found in the efflorescence region where sodium carbonate formed. Additionally, 28 d of efflorescence showed limited influence on the total porosity but can affect the pore size distribution of AAS pastes.

6. The impact of efflorescence on the compressive strengths of NH pastes was minimal, but it was significant for NS pastes. The compressive strength of NS specimens after 28 d of efflorescence was lower than that under ambient conditions, which was even lower than that after 7 d of efflorescence. The reduction was owing to cracking by heterogeneous internal stress coupled with the expansion caused by the formation of efflorescence products. Since efflorescence was detrimental to the development of long-term mechanical properties of AAS materials, a mitigating method will be proposed in the next chapter to address this problem.

Chapter 9

Mitigating the efflorescence of AAS mortars by aluminosilicate-based lightweight fine aggregates

9.1 Introduction

According to *Chapter 2*, various mitigation strategies for efflorescence have been developed. Among these, the most commonly employed and effective approach is the addition of admixtures, which can be classified into Al-rich admixtures [50,81], cation exchange admixtures [84,85], nanoparticles [86,90], hydrophobic agents [24,93] and other chemical admixtures [95,96]. All of these methods focus on the modification of the paste or binder, while mitigation strategies at an upper level, such as sand or gravel, are rarely considered. Given the substantial volume and quantity of aggregates used in real constructions, it is promising to address this issue from the perspective of aggregates. However, conventional fine aggregates employed in mortar and concrete include river sand [261], sea sand [262] or manufactured sand [263], primarily composed of quartz. Quartz is highly crystalline and exhibits inert chemical properties under even high alkalinity conditions. Lightweight fine aggregates (LWFA) are manufactured by sintering selected clay, shale or fly ash, followed by rapid cooling treatment. This special aluminosilicate-based aggregate not only exhibits an internal curing effect [264,265] due to its porous structure but also pozzolanic reactivity [266–268]. Considering the depletion of natural sand resources, despite being relatively expensive, LWFA is a promising candidate for mitigating the efflorescence problem, based on the experience in *Chapters 3 and 8*.

In this chapter, AAS mortars with 0%, 20% and 50% volume substitutions of sand by LWFA were prepared using NH solutions. Efflorescence was observed under controlled conditions, with the bottoms of the cylindrical mortars in contact with water. Leaching tests were conducted to assess Na leachability from both pore solutions and gels. Additionally, the dissolution behaviour of various ions from LWFA in alkali activators was examined. Finally, the impact of LWFA on the pore solution, reaction products, gel structure, chemistry, pore structure, and mechanical strengths (compressive and flexural) was analysed. The mitigation mechanisms of LWFA on the efflorescence of AAS mortars from the aspects of gels, pore solution and microstructure were examined. The potential for LWFA application in AAMs was also critically assessed.

9.2 Materials and methods

9.2.1 Raw materials

The slag used was the same as that referenced in previous chapters. Standard sand (EN 196-1) and LWFA with particle sizes ranging from 0 and 4 mm were used. The chemical composition of aluminosilicate-based LWFA is presented in *Table 9.1*, while *Figure 9.1* shows the phase assemblage determined by XRD.

Part of this chapter is published on:

C. Liu, Z. Li, G. Ye. (2025) Mitigating the efflorescence of alkali-activated slag mortars by aluminosilicate-based lightweight fine aggregate. *Cement and Concrete Research*.

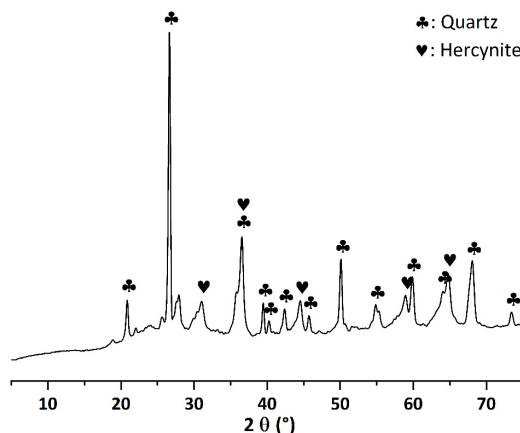


Figure 9.1. XRD pattern of LWFA.

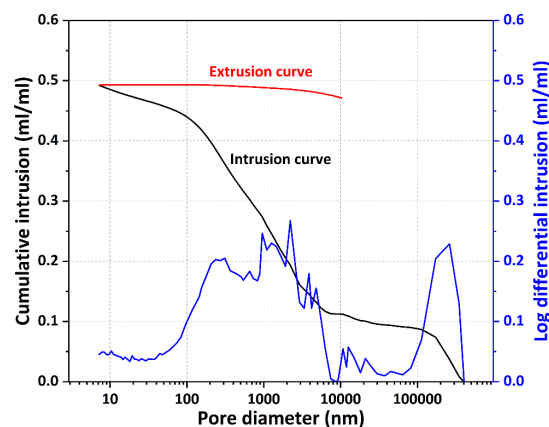


Figure 9.2. Pore structure of LWFA.

Table 9.1. Chemical composition of aluminosilicate-based LWFA. (wt.%)

	CaO	Al ₂ O ₃	SiO ₂	MgO	Fe ₂ O ₃	K ₂ O	Na ₂ O	TiO ₂	other
LWFA	3.8	18.4	58.2	3.8	9	3.4	1.2	1.1	1.1

The aluminosilicate-based LWFA employed in this study was a kind of expanded shale, mainly consisting of quartz (SiO_2) and hercynite (FeAl_2O_4). A small hump ranging from 20° to 35° suggested the presence of amorphous phases. Figure 9.2 shows the pore volume and pore size distribution of LWFA determined by MIP. The total pore volume of LWFA was around 49%, with the pores primarily distributed across two size ranges: $0.1 - 10 \mu\text{m}$ and $\geq 100 \mu\text{m}$. The extrusion curve indicated a significant volume of ink-bottle pores, contributing to the excellent water retention properties of LWFA. The saturated water absorption of LWFA was approximately 14% by mass. The bulk densities of sand and LWFA were 2600 kg/m^3 and 1530 kg/m^3 , respectively. Since efflorescence tended to occur more rapidly in porous materials, as noted in Chapter 8, an NH solution was used as the alkali activator. The use of NH solution also provided a simplified AAS system, allowing for a focused analysis of the effects of LWFA without interference from other anions such as silicate, carbonate, or sulfate, which were often present in alkaline activators.

9.2.2 Mortar preparation

The mixture design of AAS mortars is presented in Table 9.2. The alkali dosage was 5%. Fine aggregate, consisting of sand and LWFA (55 vol.% of the total mixture). The percentage indicated on the label refers to the volume of LWFA within the total fine aggregate. For example, "LWFA_20%" means that 20% of the fine aggregate in the AAS mortars was LWFA.

Table 9.2. Mixture design of AAS mortars.

	Slag (g)	Sand (g)	Dry LWFA (g)	Activator (g)	w/b
LWFA_0%	1000	2500	0	554.6	0.505
LWFA_20%	1000	2000	294.2	554.6	0.505
LWFA_50%	1000	1250	735.6	554.6	0.505

Prior to casting, dry LWFA was immersed in water for 1 d to prevent excessive water absorption during mixing, which could otherwise affect the workability of fresh mortars [176,269,270]. After 1 d of water immersion, the wet LWFA was surface-dried with a towel. The slag, sand and wet LWFA were mixed in a Hobart mixer for 1 min at a slow speed. Then, the NH solution was added, followed by 1 min of slow mixing and 1 min of fast mixing. The fresh mortar was cast into polyethene bottles (ϕ 35 mm \times 70 mm) and prismatic moulds (4 cm \times 4 cm \times 16 cm) for further measurements. The densities of three mortars sealed for 28 d were measured, resulting in values of 2191.4 kg/m³, 2080 kg/m³ and 1928.4 kg/m³, respectively.

9.2.3 Efflorescence and leaching tests

Efflorescence tests

The fresh mortars contained in polyethene bottles (ϕ 35 mm \times 70 mm) were sealed for 28 d and then cut into cylinders with a height of 50 mm. The cutting side of each cylinder was immersed in deionised water to a depth of 10 ± 1 mm within a glassy dish. The cylinders with dishes were exposed to ambient conditions ($T = 20^\circ\text{C}$ and $\text{RH} = 55\%$) for 28 d. The efflorescence of AAS mortars was observed with time.

Leaching tests

To quantify the efflorescence of AAS mortars, Na in the leachate of efflorescence products was measured. The cylinders were immersed in 150 ml of deionised water and were cleaned ultrasonically for 30 s to remove the efflorescence products. The concentration of Na in the resulting solution was measured using a PerkinElmer Optima 5300DV ICP-OES spectrometer. The Na amount in the efflorescence product per cylinder was calculated based on this concentration. The detailed experimental setup for the efflorescence tests is described in *Chapter 8*.

Moreover, leaching tests were also conducted using both AAS mortar pieces and powdered samples. The tests with mortar pieces aimed to evaluate the leaching stability of Na in fresh bulk AAS mortar (containing pore solution), while the tests with powdered samples focused on the leaching stability of Na in C-(N-)A-S-H gels. For mortar species, AAS mortars sealed for 28 d were crushed into 4 – 6 mm pieces and 10.00 g (± 0.01 g) of pieces were immersed in 100.0 g (± 0.1 g) deionised water for 28 d, and the Na concentration in the leachate was measured. For powdered samples, the AAS mortars sealed for 28 d were crushed into powder using isopropanol to stop the reaction. Then, the powder was treated with ether and dried in a vacuum oven. 1.000 g (± 0.005 g) powder sample was immersed in 50.0 g (± 0.1 g) deionised water for 28 d, and the Na concentration in the leachate was measured. Additionally, to evaluate the pozzolanic reactivity of LWFA, the leaching test of sand and LWFA subjected to NH activator immersion was conducted. The aggregate/liquid ratio followed that specified in *Table 9.2*. The concentrations of Na, Si, Al and Ca were measured by ICP-OES, while the concentration of OH⁻ ions in the leachate was obtained by titration tests using a 0.1 mol/L HCl solution.

9.2.4 Characterizations

9.2.4.1 ICP-OES, XRD, TGA and FTIR

The pore solution of AAS mortar sealed for 28 d was extracted using the steel-die method as described in *Chapter 5*. The ion concentrations of Na, Al, Si and Ca in the pore solution were

measured by ICP-OES, while the concentration of OH⁻ ions was determined through titration as mentioned in *Chapter 5*. XRD analysis was carried out to determine the phase assemblage of efflorescence products and AAS mortars. TGA was conducted to assess the thermal stability and decomposition behaviour of the samples, while FTIR was conducted to analyse the molecular structure and functional groups in AAS mortars. The experimental setups and parameters were the same as mentioned in the above chapters.

9.2.4.2 SEM and EDX

SEM with a solid-state EDX detector was used to observe the morphology and characterise the elemental composition of the pastes surrounding sand and LWFA. Bulk AAS mortars, sealed for 28 d, were first immersed in isopropanol for 7 d to stop the reaction, then dried in a vacuum oven. The dried sample was impregnated with low-viscosity epoxy resin. After the epoxy had dried, the sample was polished with sandpaper and cloth with diamond pastes, followed by carbon coating to enhance conductivity and improve imaging quality. The detailed experimental conditions and parameters were the same as mentioned in the previous chapters.

9.2.4.3 MIP and sorptivity tests

The pore structure of AAS mortars was evaluated using MIP analysis and a modified capillary sorptivity test. MIP was used to determine the total porosity of AAS mortars, while the modified sorptivity test assessed the water absorption capacity before efflorescence tests. The reaction-arrested and dried mortar pieces, approximately 4 – 6 mm in size, were subjected to MIP analysis. A modified sorptivity test was conducted using cylindrical mortars with dimensions of ϕ 55 mm \times 50 mm. Unlike the standard sorptivity test in ASTM C1585-13 [271], where samples are dried before testing, in this study, the samples were tested directly after 28 d of sealed curing without preconditioning. The side and top of the cylinders were covered with an aluminium tape, while the bottom was immersed in deionised water to a depth of 10 mm (\pm 1 mm). Mass changes were recorded at specific intervals of 5 min, 10 min, 20 min, 30 min, 1 h, 6 h, 1 d, 3 d, 4 d, 5 d, 6 d, and 7 d. Three replicates were measured for each group. The water sorptivity I ($\text{mm}/\text{s}^{1/2}$) of the specimens was calculated using *Equation 9.1*:

$$I = \frac{m_t}{a \times \rho} \quad (9.1)$$

where m_t (g) is the mass of samples at moment t , a (mm^2) is the exposed area of the specimen, ρ (10^{-3} g/ mm^3) is the density of water.

9.2.4.4 Flexural and compressive strengths

Flexural and compressive strengths of AAS mortars were measured to study the effect of LWFA substitution on the mechanical properties of mortars. The 4 cm \times 4 cm \times 16 cm samples were sealed for 7 d before being exposed to ambient conditions up to 28 d. Strength measurements were conducted at 7 d and 28 d. The testing procedures and loading parameters were the same as mentioned in the previous chapters.

9.3 Results

9.3.1 Efflorescence tests

9.3.1.1 *In-situ* observation

Figure 9.3 shows the visual observation of the efflorescence of AAS mortar under ambient conditions with time. Efflorescence deposits accumulate with time, with the mortars without LWFA showing more serious efflorescence at early ages (1 d and 7 d). Normally, efflorescence products mainly consist of sodium (bi)carbonates, with Na primarily sourced from the pore solution. Both a higher Na concentration in the pore solution and a porous microstructure can increase the supply of Na and enhance the efflorescence potential of materials [71,72]. In addition to Na ions, OH⁻ also significantly influences the formation of efflorescence products as discussed in Chapter 8.



Figure 9.3. Visual observation of the efflorescence of AAS mortar cylinders with time.

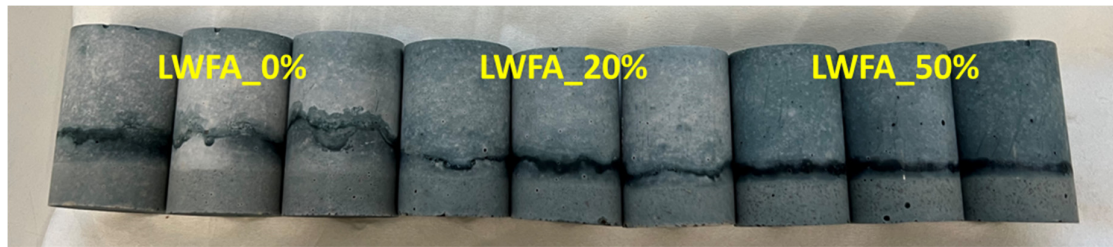


Figure 9.4. Ultrasonically cleaned AAS mortar cylinders after 28 d of efflorescence. From left to right, the three cylinders as a group refer to “LWFA_0%”, “LWFA_20%” and “LWFA_50%”, respectively. The darker green/blue trace indicates the “efflorescence front” of AAS cylinders.

As reported in [272], gaseous $\text{CO}_{2(\text{aq})}$ dissolves in water to form $\text{H}_2\text{CO}_{3(\text{aq})}$, which remains stable under neutral conditions. However, in the presence of OH^- , $\text{H}_2\text{CO}_{3(\text{aq})}$ becomes unstable and hydrolyses to $\text{HCO}_{3^{-}(\text{aq})}$ and $\text{CO}_{3^{2-}(\text{aq})}$ to varying extents, depending on the pH level [272]. Therefore, the reduced efflorescence of AAS mortar with LWFA is probably attributed to a decreased supply of Na^+ and OH^- .

After 28 d of exposure, mortars containing LWFA show less efflorescence compared to those without LWFA. This effect is more pronounced in mortars with a higher LWFA content (LWFA_50%). This indicates that the incorporation of LWFA can effectively mitigate the efflorescence of AAS mortars. Additionally, the efflorescence front (dark green/blue traces) in cylinders of “LWFA_20 %” and “LWFA_50%” is lower than that of the “LWFA_0%”, as shown in *Figure 9.4*. As stated in *Chapter 8*, the efflorescence front is correlated with the porosity of materials. Lower porosity results in a lower efflorescence front. This is because the formation of efflorescence involves not only Na and CO_2 but also H_2O (within a specific range of relative humidity). At a given temperature, sodium (bi)carbonate forms within a particular range of relative humidity. Due to capillary suction, relative humidity decreases with the height of the cylinder. A more porous structure allows water to rise to a higher level, thereby resulting in a higher efflorescence front. Thus, the lower efflorescence front observed in *Figure 9.4* suggests reduced water absorption in AAS mortars blended with LWFA. *Section 9.3.3.4* will further clarify this issue through MIP and sorptivity tests. Overall, the observation in this section indicates the excellent efficacy of LWFA in mitigating efflorescence.

9.3.1.2 Efflorescence products

Figure 9.5 shows the phase assemblage of efflorescence products on the mortar cylinders. Thermonatrite ($\text{Na}_2\text{CO}_3 \cdot \text{H}_2\text{O}$) is identified as the main phase in the efflorescence product of three mortar samples. This suggests that the substitution of LWFA shows a limited impact on the phase assemblage of efflorescence products. Traces of quartz are also found in the LWFA_0% and LWFA_20% groups, likely originating from sand or LWFA particles during the scraping of the efflorescence products. As discussed in *Chapter 8*, the primary efflorescence product in NH pastes is sodium carbonate heptahydrate ($\text{Na}_2\text{CO}_3 \cdot 7\text{H}_2\text{O}$). The appearance of thermonatrite instead suggests reduced hydrated water in the efflorescence product of the mortar samples.

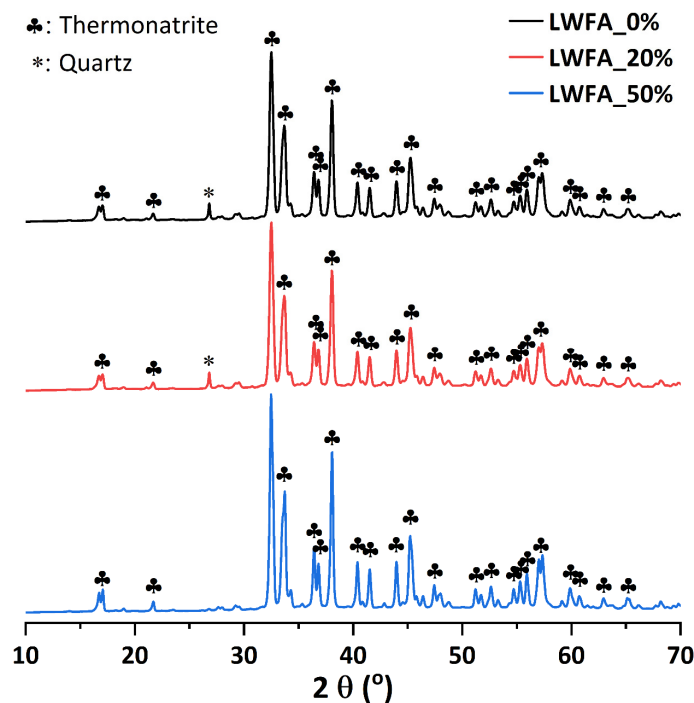


Figure 9.5. XRD pattern of efflorescence products on the three AAS mortars.

Typically, the presence of sand has two effects on the system. On one hand, sand is considered impermeable, and its introduction can densify the material. On the other hand, sand introduces interfaces with the paste, which tends to have high water/binder ratios and is generally more porous than the matrix [265]. In this chapter, the densifying effect of sand appears to be more significant than its impact on increasing porosity. The incorporation of sand likely reduces water transport within the material, thereby lowering the content of hydrated water in the efflorescence products.

9.3.2 Leaching tests

9.3.2.1 Leaching of efflorescence products

The efflorescence of AAS mortars, as evaluated using the quantification method proposed in *Chapter 8*, is shown in *Figure 9.6*. In *Chapter 8*, it was demonstrated that the Na amount in the efflorescence product of NH pastes is 118 mg per cylinder, indicating that the efflorescence of AAS pastes is more severe compared to AAS mortars. The inclusion of fine aggregates efficiently reduces efflorescence [72], due to the lower concentrations of Na^+ and OH^- in the same volume as pastes. Compared to the reference mortar, LWFA substitutions of 20% and 50% result in efflorescence reduction of 14.6% and 43%, respectively. This is consistent with the observation in *Figure 9.3*, further supporting the mitigating effect of LWFA on efflorescence in AAS mortars.

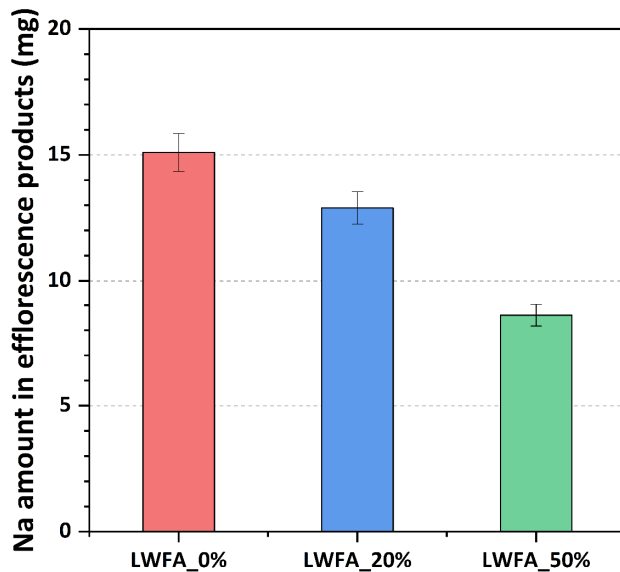


Figure 9.6. Na amount in efflorescence products per AAS mortar cylinder after 28 d of exposure.

9.3.2.2 Leaching of AAS mortar pieces and powder

Given the lower density of LWFA-based mortars than normal mortars, it is rational to compare the leaching result by volume. Therefore, I normalised the leaching data by volume, as depicted in *Figure 9.7A*. The results indicate that the Na concentration in the leachate decreases as LWFA dosages increase, suggesting that the presence of LWFA hinders the leaching of Na. Generally, Na in mortars can be categorised into three types: free Na ions in the pore solution, weakly bonded Na in C-(N-)A-S-H gels and strongly bonded Na in C-(N-)A-S-H gels [20,72]. Free Na is associated with the alkalinity of the pore solution, while weakly and strongly bonded Na are incorporated into the C-(N-)A-S-H gels. Given the use of fresh AAS mortar pieces, it is plausible that free Na in the pore solution contributed significantly to the leaching results.

Figure 9.7B shows the Na concentration in the leachate of powdered mortars. As described in *Section 9.2*, the reaction of powdered samples was arrested in isopropanol, meaning that all Na in the leachate originated from C-(N-)A-S-H gels. Interestingly, the Na concentration in the leachate increases with the LWFA dosage, contrary to the trend observed for mortar pieces (*Figure 9.7A*). As discussed in *Chapters 3 and 4*, Na is the predominant ion leached from synthetic C-(N-)A-S-H gels subjected to water immersion, due to its weak bonding within the interlayer of the gels. The leaching amount of Na increases with its initial content in the gels, implying that the gels in mortars with LWFA have a higher Na uptake. As shown in *Chapter 3*, the gel with a lower Ca/Si ratio and a higher Al/Si ratio shows a higher Na/(Al+Si) ratio due to increased charge negativity on gel substrates. This suggests that the addition of LWFA may alter the gel chemistry, potentially enhancing the Na uptake by the gels.

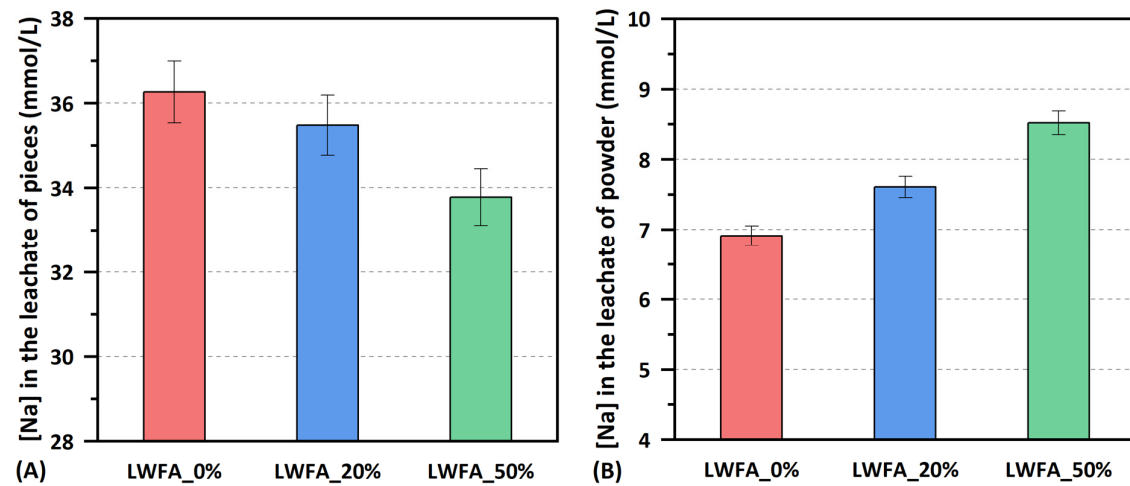


Figure 9.7. Na concentration in the leachate of AAS mortar pieces and powder. [Na] refers to the concentration of Na.

9.3.2.3 Ion Concentrations in the Leachate of LWFA after Immersion in NH Activator

Figure 9.8 shows the ion concentrations of Na, OH, Si, Al and Ca in the leachate of LWFA after immersion in the NH activator for 28 d. The solution is dominated by Na^+ and OH^- , with the OH^- concentration slightly lower than that of Na. The concentrations of both Na^+ and OH^- are slightly lower than those in the initial activator, with a more significant reduction observed in solutions containing higher amounts of LWFA. This suggests that the pozzolanic reaction of LWFA reduces the alkalinity of the solution. Simultaneously, Si and Al species are dissolved from LWFA, and their concentrations increase with the content of LWFA. Interestingly, although sand is generally considered inert, it can also release some amount of Si and even Al under alkaline conditions. However, the quantities released from sand are considerably lower than those from LWFA. The concentration of Ca remains relatively low compared to other elements and shows little variation between them. Overall, these dissolution tests indicate the pozzolanic reactivity of LWFA, which can supply extra Si and Al to the system.

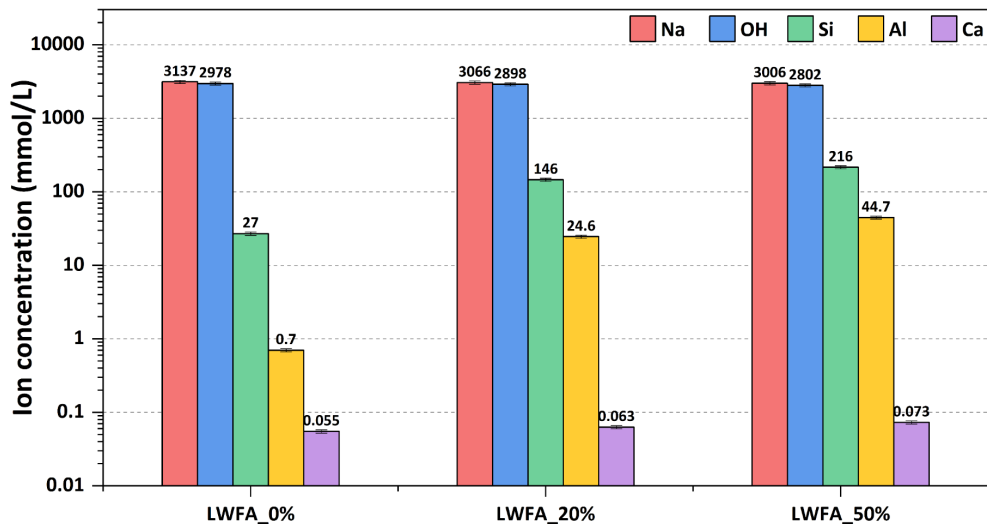


Figure 9.8. Ion concentration of Na, OH, Si, Al and Ca in the leachate of LWFA subjected to immersion of the NaOH activator for 28 d. The concentrations of Na^+ and OH^- ions of the fresh NH activator are 3297 and 3271 mmol/L, respectively.

9.3.3 Impacts of LWFA on AAS mortars

9.3.3.1 Pore solution

The ion concentrations of Na, OH, Si, Al and Ca in the pore solution of AAS mortars sealed for 28 d are shown in *Figure 9.9*. Similar to *Figure 9.8*, Na⁺ and OH⁻ dominate the pore solution, but their concentrations are lower, primarily due to the reaction of slag and the formation of C-(N)-A-S-H gels. Additionally, it is observed that both Na⁺ and OH⁻ concentrations decrease with increasing LWFA dosage. Specifically, substituting 20% and 50% LWFA results in Na concentration reductions of 7.7% and 15.5% respectively, and OH⁻ concentration reductions of 8.3% and 10.4%. These decreases can be attributed to the pozzolanic effect of LWFA, as well as the introduction of additional water through the pre-moistened LWFA. The concentration of Si increases with the increase of LWFA dosage, attributed to the dissolution of extra Si species from LWFA (*Figure 9.8*). The concentrations of Al are comparable across three pore solutions, with the two LWFA mortars exhibiting slightly higher values than the reference mortar. The concentration of Ca remains relatively low in comparison to the other ions, due to the low solubility of Ca under high alkalinity conditions.

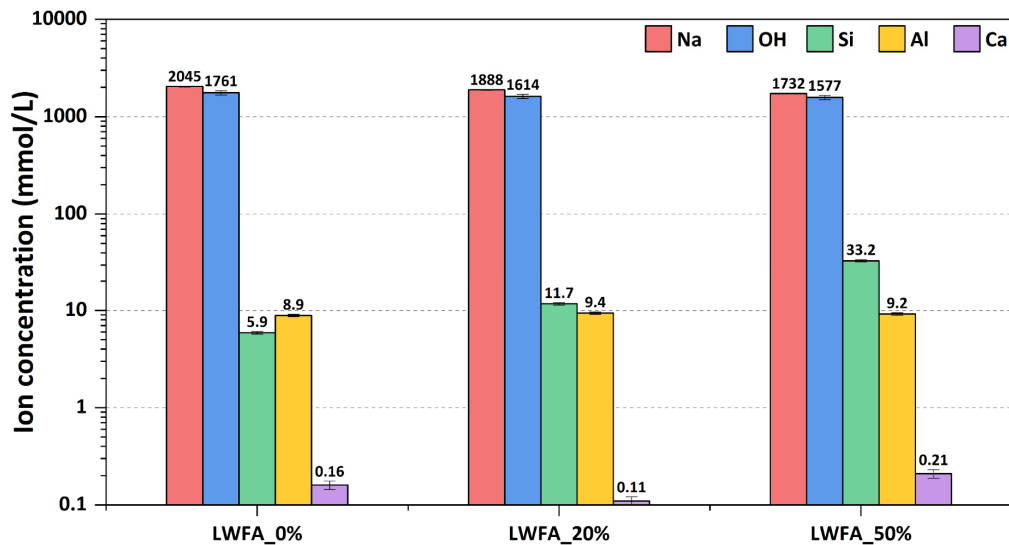


Figure 9.9. Ion concentrations of Na, OH, Si, Al and Ca in the pore solution of AAS mortars sealed for 28 d.

9.3.3.2 Reaction products

Figure 9.10 shows the XRD, TGA and FTIR results for AAS mortars. In *Figure 9.10A*, the XRD pattern is dominated by quartz, the main phase in both sand and LWFA. The intensity of the quartz signal decreases with the LWFA dosage, which probably indicates a higher content of quartz in sand than in LWFA. Additionally, a characteristic gel peak appears near 30°, but the intensity is too low to reveal significant differences among the three mortars, due to the high content and crystallinity of quartz masking the signal. *Figure 9.10B* shows the TG and DTG curves for the AAS mortars. The total weight loss of the samples increases with LWFA content, indicating an increasing content of reaction products. The DTG curves are mainly dominated by two peaks: the first corresponds to the weight loss of C-(N)-A-S-H gels between 40 – 250 °C and the second to hydrotalcite-like phases (ht) between 300 – 400 °C. The weight loss of Ht in the three mortars appears to be comparable, while that of the gels shows some distinctions. The mortar with a higher LWFA content shows a higher weight loss of gels. The

weight loss in gels is mainly due to chemically bonded or physically absorbed water, which is closely related to the amount and chemistry of the gels, as well as the drying method. In this study, the drying of powdered samples strictly followed the standard [273], ensuring that the level of free water and physically absorbed water was consistent across samples. Hence, this discrepancy can be attributed to a higher content of gels in the LWFA-blended mortar. As shown in *Figure 9.8*, Si and Al species can be dissolved from LWFA during the immersion of the alkali activator. These ions can serve as the raw materials for the formation of gels. Additionally, the internal curing effect of LWFA may create a high-humidity environment within the matrix, promoting the reaction of slag and enhancing the formation of gels. Furthermore, as reported in [57], gels with a higher alkali metal ion content tend to contain more chemically bound water. This suggests that the higher weight loss of gels in LWFA-blended mortars may be attributed to the higher Na content in the gels. This finding aligns with the results of the leaching test on powdered AAS mortars, as shown in *Figure 9.7B*.

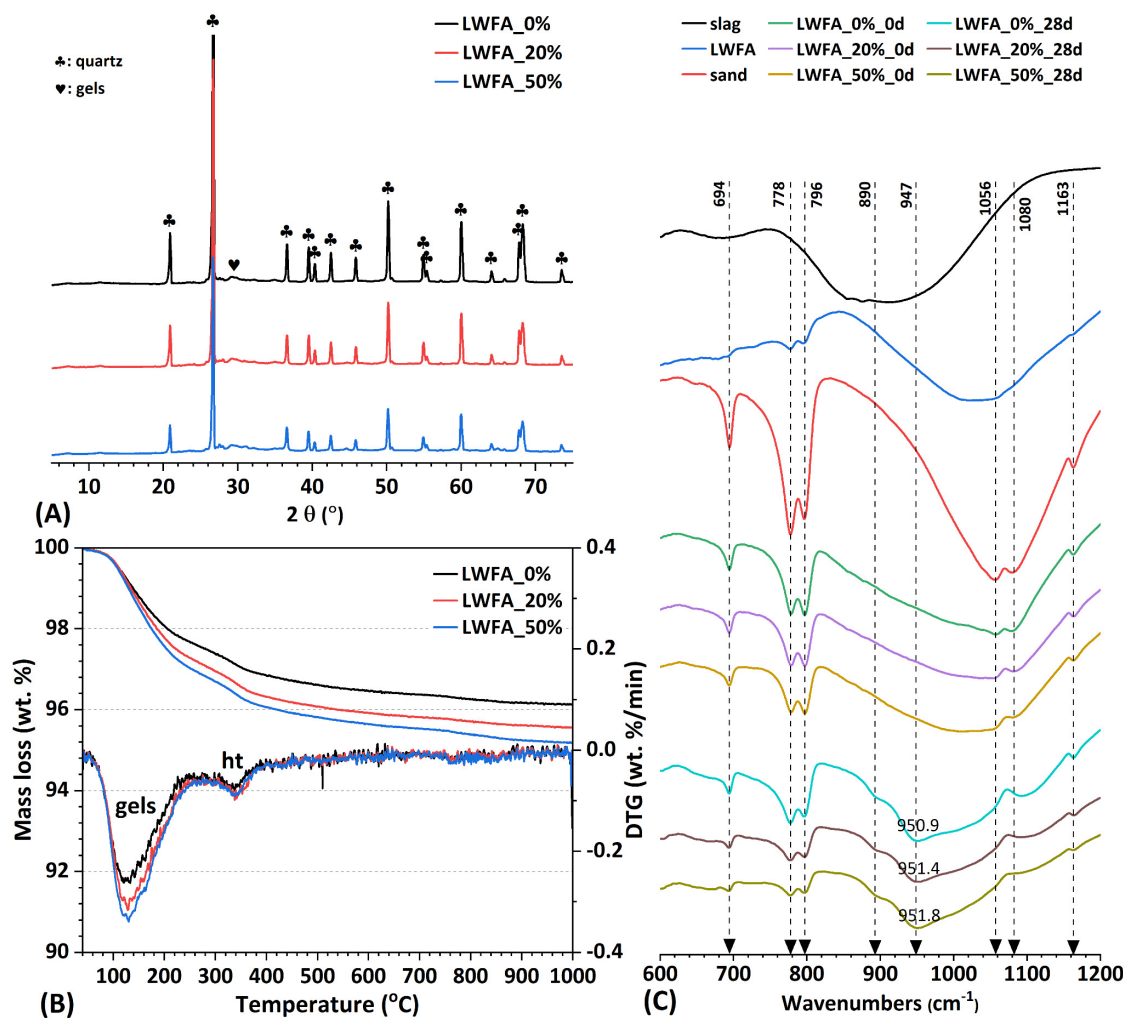


Figure 9.10. XRD pattern, TGA curves and FTIR curves of 28 d sealed AAS mortars. "ht" in (B) refers to hydrotalcite-like phases. "0 d" in the legend of (C) indicates the unreacted mixture consisting of unreacted slag, sand and LWFA.

Figure 9.10C shows the FTIR analysis results for slag, sand, LWFA and AAS mortars. There are no sharp absorption peaks but rather broad humps in slag and LWFA. Considering that both slag and LWFA are silicate-based materials, the higher wavenumber of the hump of LWFA indicates a more crosslinked structure. This is consistent with the NMR findings in [62,176], where the chemical environment of Si in slag is dominated by Q⁰ and Q¹, while LWFA is primarily composed of Q³ and Q⁴, indicating that slag has significantly higher reactivity. The main hump in sand shows even higher wavenumbers than LWFA, suggesting a more crosslinked network and, consequently, lower reactivity. As a result, LWFA can dissolve more Si than sand. The peaks at 694 cm⁻¹, 778 cm⁻¹, 796 cm⁻¹, 1056 cm⁻¹, 1080 cm⁻¹ and 1163 cm⁻¹ in the infrared pattern of sand are assigned to the vibration of Si-O-Si in quartz [274]. The spectra of “LWFA_0%_0d”, “LWFA_20%_0d” and “LWFA_50%_0d” represent combinations of the raw materials in each mixture, showing minimal differences between them. However, after 28 d of reaction, a newly formed hump in the range of 850 cm⁻¹ to 1100 cm⁻¹ is observed in all three mortars. The peak near 950 cm⁻¹ corresponds to the asymmetrical stretching vibration of Si-O-Si(Al) in Q² units within the gels. Additionally, a small shoulder at around 890 cm⁻¹ is assigned to the bending vibration of Si-O in gels. The average peak wavenumber of Q² units in the three mortars is 950.9, 951.4 and 951.8 cm⁻¹, respectively. This slight variation suggests that the gels in mortar with higher LWFA dosage show a higher degree of polymerisation, which can be primarily attributed to the additional Si and Al dissolved from LWFA.

9.3.3.3 Mortar morphology and paste chemistry

Figure 9.11 shows the typical morphology of pastes around sand and LWFA. The interface between sand and pastes is distinct, with the paste surrounding the sand appearing coarser than the matrix. In contrast, the interface between LWFA and pastes is less pronounced, and the paste surrounding LWFA appears denser than that around sand. This difference can be explained by the capillary effect of aggregates [275]. The water/binder ratio of pastes around normal aggregates is typically higher than the matrix, resulting in a more porous pore structure [276]. The capillary effect is more pronounced in LWFA due to its porous structure and pre-absorbed water. However, unlike sand, LWFA shows reactivity under alkali conditions [266,269], which leads to the release of extra Si and Al species. These species react with Ca and Na in the pore solution, contributing to the formation of additional gels and the densification of the surrounding pastes. This observation is also supported by the higher water loss in the gels of LWFA blended mortars as shown in the DTG curve (*Figure 9.10B*). As reported in [277], the interfacial transition zone (ITZ) in normal concrete tends to be thicker than that in LWFA-blended concrete. The impact of LWFA on the microstructure of AAS pastes will be further discussed in the following sections.

Figure 9.12A shows the Si/Ca versus Al/Ca ratios of the pastes surrounding sand and LWFA. In general, the Si/Ca ratio of the paste around LWFA ranges from 0.6 to 1.0, which is higher than that in the paste around sand (0.4–0.9). Additionally, the Al/Ca ratio in the paste around LWFA is also higher than in the paste around the sand. As indicated by the arrow in *Figure 9.12A*, the paste around LWFA contains more Si and Al, which can be ascribed to the extra Si and Al supplied by LWFA (*Figure 9.8*). *Figure 9.12B* shows the Al/Si versus Mg/Si ratios of the pastes around sand and LWFA. There is a positive linear correlation between the Al/Si and Mg/Si ratios, despite some irregular data points. As noted in [193], such a linear correlation between the Mg/Si and Al/Si ratios typically suggests the presence of hydrotalcite-like phases. The positive intercept on the X-axis suggests a degree of Al incorporation into the C-S-H gels

in the slag rim, while the slope of the trendline represents the Mg/Al ratio in hydrotalcite. In both groups (sand and LWFA), the Al/Si ratio of gels in the slag rim and the Mg/Al ratio in hydrotalcite are comparable in the pastes around sand and LWFA, as they are mainly determined by the chemical composition of slag.

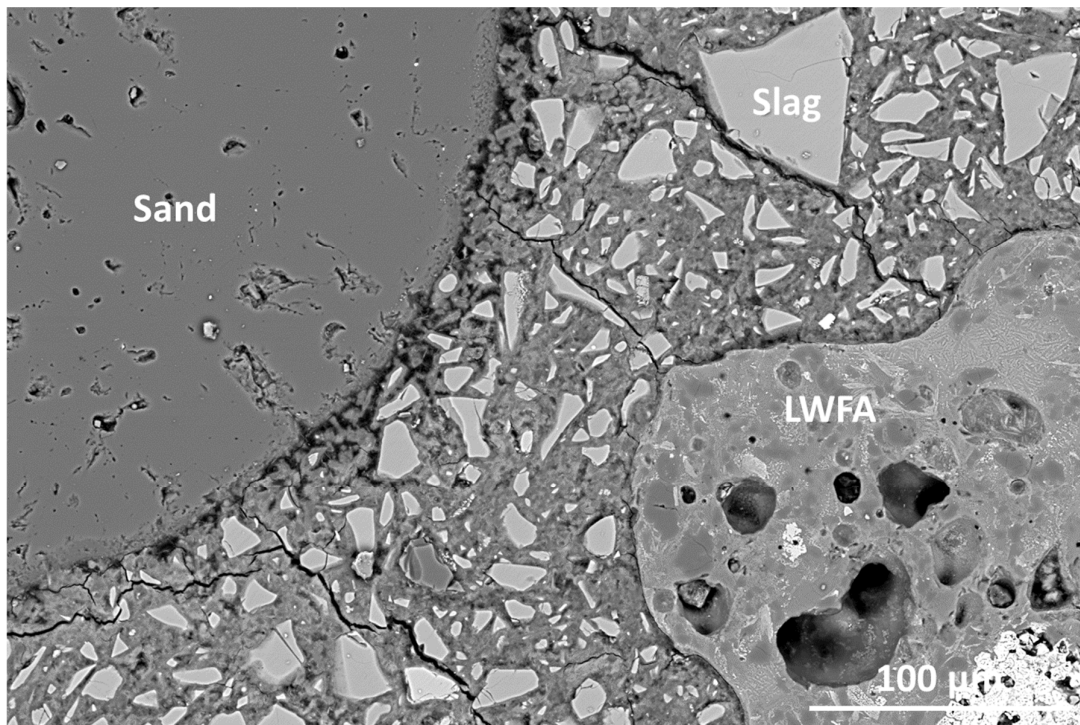


Figure 9.11. Typical morphology of pastes around sand and LWFA.

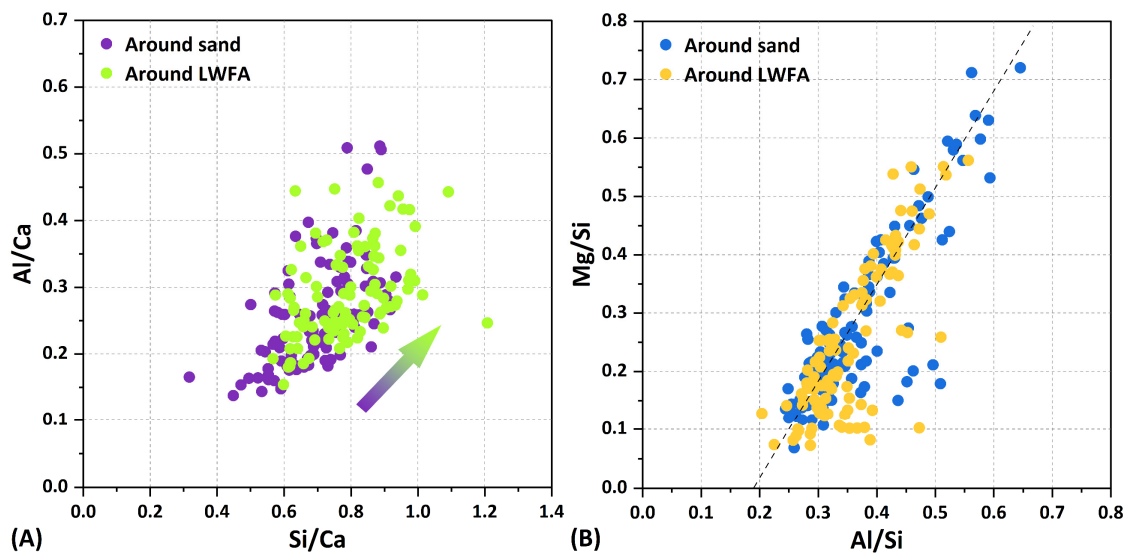


Figure 9.12. (A) Si/Ca versus Al/Ca ratios and (B) Al/Si versus Mg/Si ratios of the pastes around sand and LWFA. The arrow in (A) indicates the variation of the data point of the paste around the aggregate from sand and LWFA.

Figure 9.13 shows the box plot of different elemental ratios in the paste around sand and LWFA. Consistent with the result in Figure 9.12A, the paste around LWFA shows a lower $\text{Ca}/(\text{Si}+\text{Al})$ ratio than that around sand (Figure 9.13A). In contrast, the paste around LWFA shows a higher $\text{Na}/(\text{Si}+\text{Al})$ ratio than that around sand (Figure 9.13B). This indicates a higher uptake of Na in the paste with the incorporation of LWFA, which agrees with the leaching result of powdered mortar (Figure 9.7B). Figure 9.13C shows the Mg/Al ratio of the paste. Mg stems from the hydrotalcite, while Al is derived from both hydrotalcite and gels. Given the similar chemical composition of hydrotalcite, as indicated in Figure 9.12B, the relatively lower Mg/Al ratio in the paste around LWFA is due to a higher Al content in the gels. This finding aligns with the Al/Ca ratio observed in Figure 9.12A.

Figure 9.13D shows the $\text{Fe}/(\text{Si}+\text{Al})$ ratio in the paste around sand and LWFA. It can be seen that Fe can also be incorporated into the paste. In PC systems rich in ferrite, Fe can contribute to the formation of various hydrates such as Fe-containing siliceous hydrogarnet, alumina ferric monosulfate, and Fe-ettringite [278–280]. In addition, Fe(III) is incorporated into C-S-H gels, with a stronger sorption capacity than Al(III). However, due to the lower solubility of $\text{Fe}(\text{OH})_3$ than $\text{Al}(\text{OH})_3$, the uptake of Fe by gels is quite limited. As shown in Figure 9.13D, most data points for paste around sand show negligible Fe content, with an average Fe/Si ratio of about 0.001, which is significantly lower than the ratio in pastes around LWFA (0.006). This difference is due to the higher Fe_2O_3 content in LWFA (9%) compared to slag (0.6%). As stated in [279], Fe(III) is octahedrally coordinated in the interlayers of gels with high Ca/Si ratios (1.2 and 1.5), while in gels with lower Ca/Si ratios (around 0.8), Fe(III) tends to form a separate secondary Ca-Si-rich phase or cluster. Regardless of its state in gels, the presence of additional Fe in gels likely enhances the charge negativity, similar to the role of Al. This increase in charge negativity may promote cation absorption, which could also explain the elevated $\text{Na}/(\text{Si}+\text{Al})$ ratios observed in pastes around LWFA.

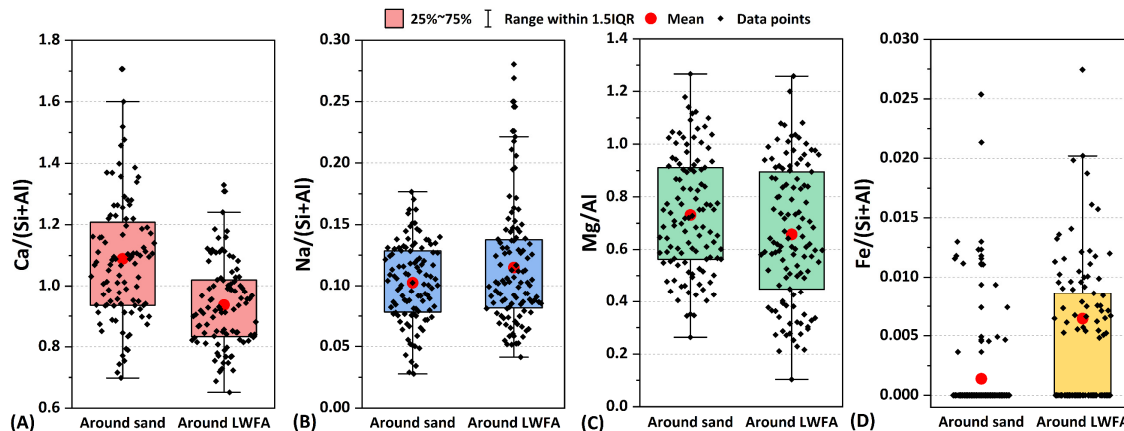


Figure 9.13. Box plot of elemental ratios of the paste around sand and LWFA. In each box, 25%–75% indicates the data points ranging from the 25th to 75th percentiles. The “IQR” indicates the interquartile range (25%–75%), and the whisker is located at 1.5 times of “IQR”. The red circle refers to the mean value of atomic ratios.

9.3.3.4 Pore structure and sorptivity

Figure 9.14A presents the porosity of AAS mortars with different LWFA contents. The porosity of “LWFA_0%”, “LWFA_20%” and “LWFA_50%” in the range of 7 nm to 400 μm is 14%, 19.2% and 24.5%, respectively. This indicates that the addition of LWFA significantly coarsens the microstructure of AAS mortars. The primary reason is the high porosity of LWFA (49.2%) (Figure 9.2), which is much higher than that of the matrix of pastes. As indicated by the pore size distribution (Figure 9.14B), the presence of LWFA increases the pores ranging from 50 nm to 1000 nm. While the pozzolanic effect of LWFA can promote the formation of gels, it is insufficient to compensate for the pores introduced by LWFA within 28 d.

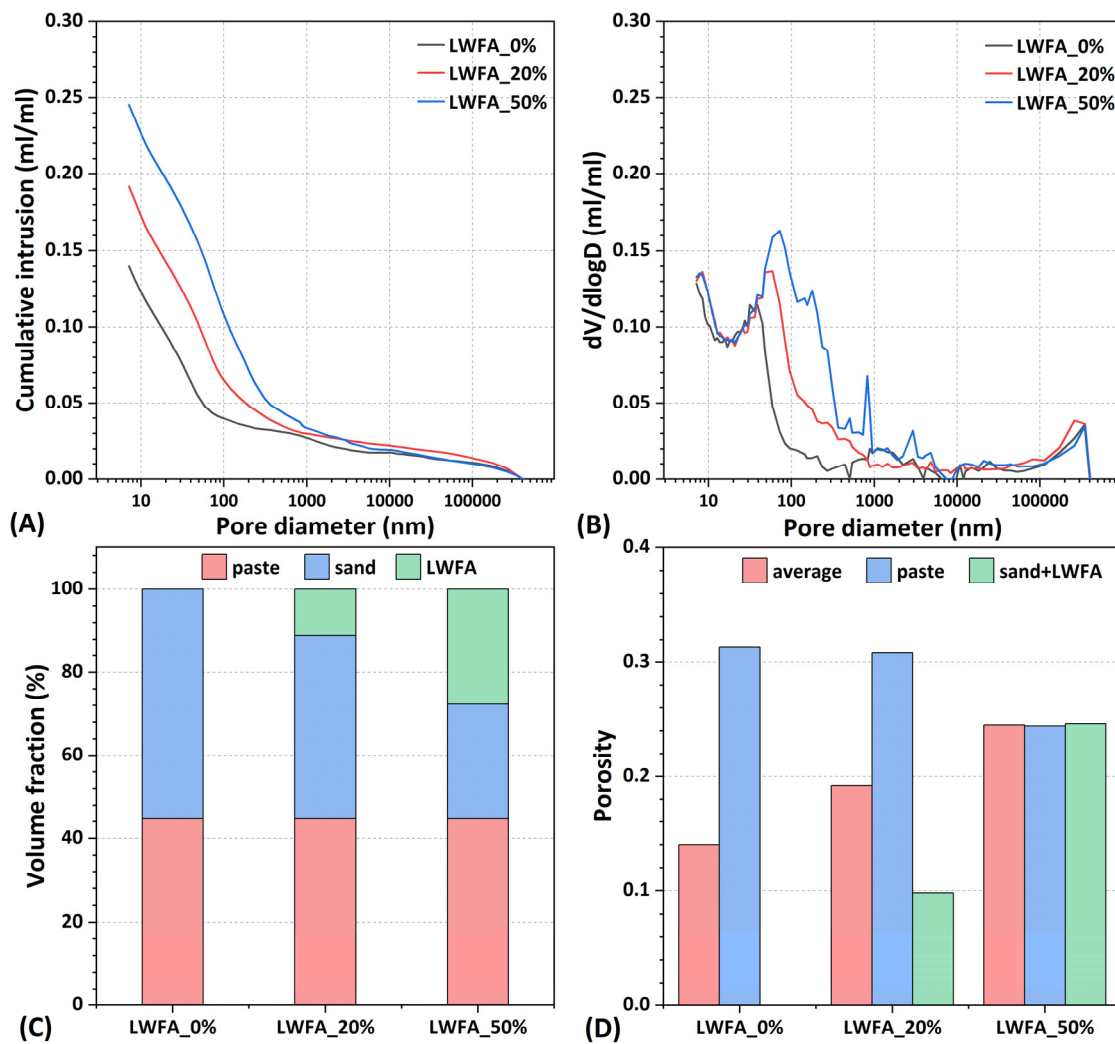


Figure 9.14 (A) Pore volume and (B) Pore size distribution of 28 d sealed AAS mortars; (C) Volume fraction of paste and fine aggregate in AAS mortars; (D) Calculated porosity of paste and aggregate in AAS mortars. The “average” in the label of (D) indicates the mean porosity of pastes and aggregates, equivalent to the total porosity of the mortar. The porosity of sand is considered zero.

According to the mixture design, the volume fractions of paste, sand, and LWFA can be calculated, as shown in *Figure 9.14C*. The total volume of fine aggregate is 55%, consisting of both sand and LWFA. Given the porosities of LWFA (49.2%) and sand (0%), the porosity of the paste in the mortar can be determined, as shown in *Figure 9.14D*. Compared to the total porosity of the mortar, the paste porosity decreases with the addition of LWFA. This observation supports the conclusion that the pozzolanic and internal curing effects of LWFA contribute to the densification of the surrounding paste. It is important to note that the accuracy of the calculated paste porosity is based on the assumption that the reaction of LWFA is limited, and its porosity change is minimal within 28 d.

The sorptivity test was typically performed on dried specimens to evaluate the open porosity and pore connectivity of materials. However, in this chapter, I conducted tests directly on mortars sealed for 28 d, without drying. These mortars were subjected to the same conditions as those used for efflorescence observation. The water sorptivity behaviour of AAS mortars over 7 d is shown in *Figure 9.15*. Water was continuously absorbed through the capillary suction of the unsaturated pores, with the sorptivity rate gradually decreasing over time. During the 7 d of measurement, the water absorption of the mortar with LWFA was significantly lower than that of the mortar without LWFA, which appeared to contradict the MIP results in *Figure 9.14A*. This discrepancy arose because the MIP test was conducted on dried samples, thereby ignoring the presence of water in the pore structure under real conditions. The additional water pre-absorbed by LWFA was likely to maintain higher internal humidity within the mortar, leading to reduced water sorptivity. The lower water absorption in LWFA-based mortars aligned with the finding in *Figure 9.4*, where the cylinder containing LWFA showed a lower efflorescence front.

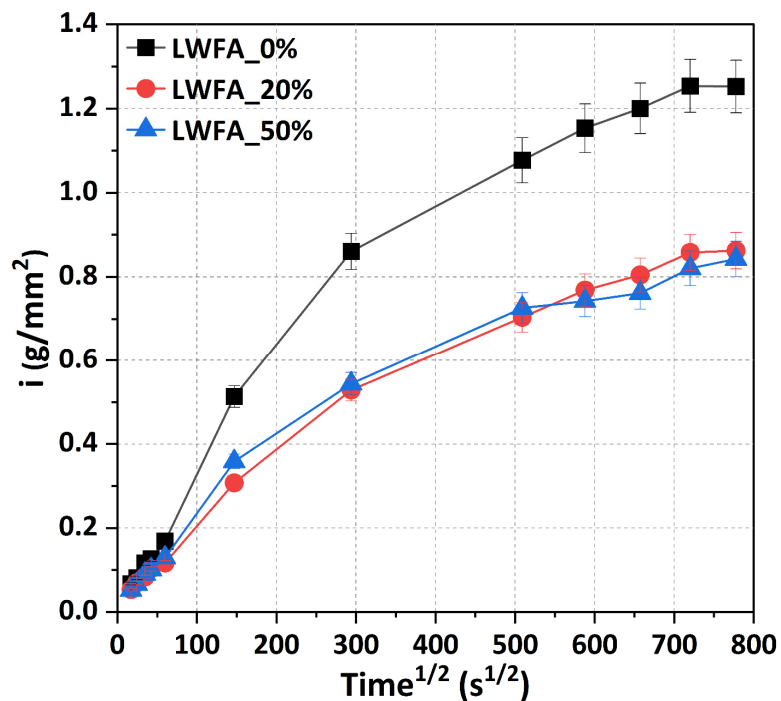


Figure 9.15. Water sorptivity of AAS mortars upon 28 d of sealed curing.

9.3.3.5 Strength

Figure 9.16 shows the flexural strength and compressive strength of AAS mortars at 7 d and 28 d. In general, the compressive strength of specimens increases over time, whereas the flexural strength tends to decrease, which indicates that ambient conditions adversely affect the development of flexural strength. Similar results are also found in [241]. Since the flexural strength is more sensitive to cracks, its reduction can be attributed to cracks induced by dry shrinkage. In contrast, compressive strength is more related to porosity. Since slag progressively reacts and gels constantly form during 28 d, the compressive strength shows positive development.

As shown in Figure 9.16A, the flexural strength of LWFA_0% at 7 d is higher than that of LWFA_20% and LWFA_50%, however, by 28 d, the flexural strength of LWFA_0% is lower than that of the mortars containing LWFA. During the first 7 d, the samples were kept under sealed conditions, which largely prevents cracking, suggesting that cracks are not the main factor influencing flexural strength at this stage. The lower flexural strength of LWFA-blended mortars in the early stage can be attributed to the porous structure and lower stiffness of LWFA compared to sand. After 7 d, the samples are exposed to ambient conditions, where a reduction in environmental humidity leads to water loss and dry shrinkage [281]. Due to the internal curing effect of LWFA, mortars with LWFA maintain higher internal humidity than normal mortars, which suppresses the shrinkage and cracking potential [282]. Additionally, the pozzolanic reaction of LWFA under alkaline conditions contributes to the densification of the paste-aggregate interface. As a result, the flexural strength of LWFA-based mortars improves by 28 d. Unfortunately, as shown in Figure 9.16B, the compressive strength of LWFA blended mortars remains consistently lower than that of the reference mortar, with higher LWFA substitution leading to greater reductions in strength. This is because the addition of LWFA increases the total porosity of AAS mortars, as indicated in Figure 9.14A.

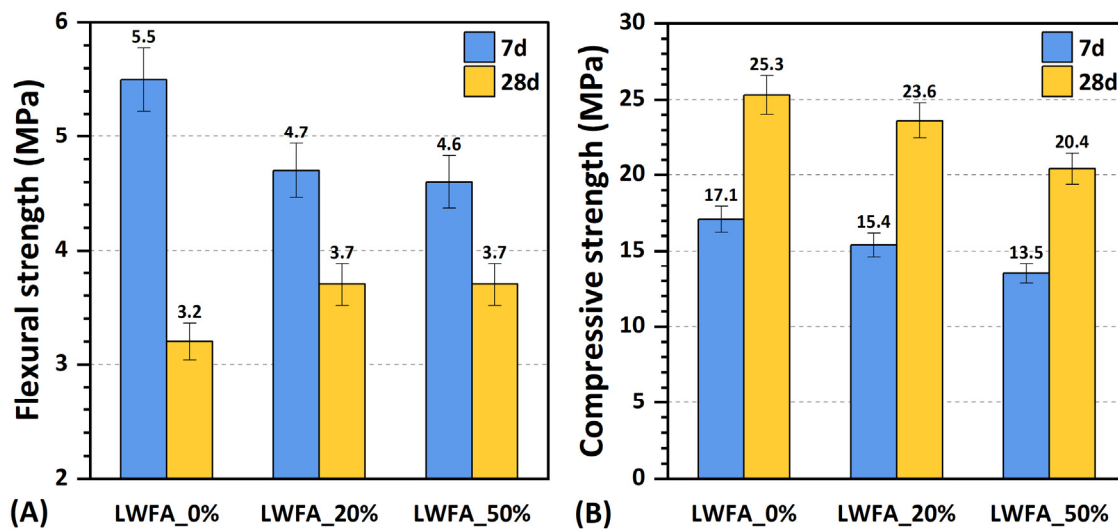


Figure 9.16. Flexural and compressive strengths of AAS mortars at 7 d and 28 d. “7 d” refers to the specimen that was cured under sealed conditions for 7 d, while “28 d” denotes the specimen that was initially cured under sealed conditions for 7 d, followed by ambient curing until 28 d.

9.4 Discussion

9.4.1 Mitigating mechanisms of LWFA on the efflorescence of AAS mortars

It has been shown that the addition of LWFA effectively mitigates the efflorescence of AAS mortars. To better understand the underlying mechanisms, *Figure 9.17* shows a schematic representation of the mitigation mechanisms of LWFA on the efflorescence of AAS mortars. LWFA, being an aluminosilicate material containing amorphous Si and Al, can dissolve under alkali conditions. Experimental results show that the dissolved Si and Al species participate in the formation of gels, which results in the gel surrounding LWFA having a lower Ca/(Si+Al) ratio (*Figure 9.17A*). According to the leaching test and EDX point analyses, the gel in LWFA-based mortars exhibits a higher uptake of Na (*Figure 9.1B*). This is primarily because gels with a lower Ca/(Si+Al) ratio have a higher charge negativity on the surface (as discussed in *Chapter 3*), allowing them to bind more Na from the pore solution. Meanwhile, the continuous pozzolanic reaction of LWFA reduces the pH of the pore solution. As a result, the concentration of both Na⁺ and OH⁻ in the pore solution decreases, limiting the availability of the species needed for efflorescence formation. Furthermore, a denser ITZ is observed around LWFA compared to the ITZ between normal sand and the paste (*Figure 9.1C*). This desification can be ascribed to both the pozzolanic effect and the internal curing effect of LWFA. LWFA provides raw species, and the pre-absorbed water supports ongoing reactions. A densified pore structure (*Figure 9.14D*) inhibits ion migration and water transport, thereby reducing the potential for efflorescence formation.

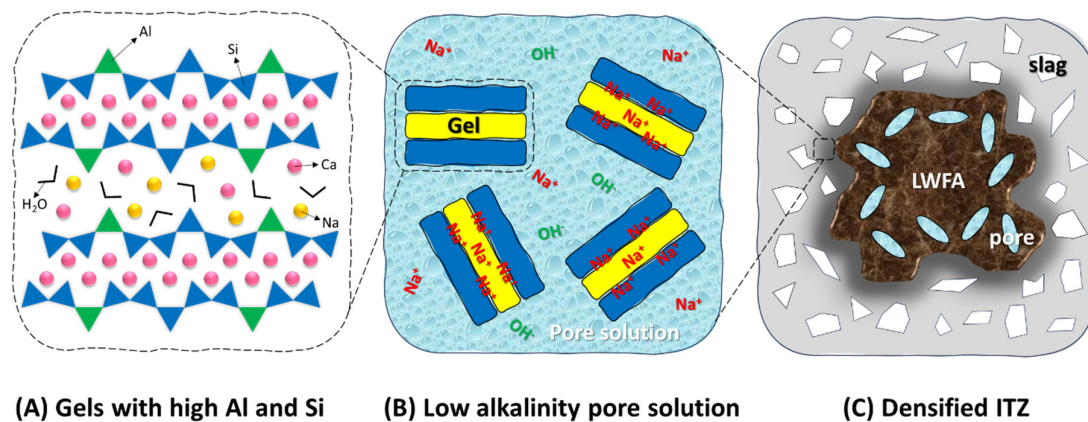


Figure 9.17. Schematic representation of the mitigation mechanisms of LWFA on the efflorescence of AAS mortars.

While the primary focus of this chapter is on NH mortars due to the time efficiency of the efflorescence experiments and the simplified nature of the AAS systems, I also conducted tests on NS-activated AAS mortars with a silicate modulus of 1. *Appendix C Figure C1* shows the NS cylinders sealed for 28 d, followed by 90 d of efflorescence under ambient conditions. It can be observed that efflorescence on NS mortars developed more slowly and was less pronounced than in NH mortars at the same exposure age, likely due to the denser microstructure of NS mortars. However, LWFA appeared to be less effective in NS mortars during the first 28 d, as the extent of efflorescence in the three NS cylinders was similar at this stage (*Appendix C Figures C1 (D–F)*). This may be attributed to the significantly higher porosity of LWFA compared to NS pastes, which leads to noticeable coarsening of the microstructure in NS systems when LWFA is introduced. Fortunately, after 90 d of exposure,

NS mortars containing LWFA exhibit less efflorescence than those without LWFA (*Appendix C Figures C1 (G–I)*), indicating that LWFA becomes more effective in mitigating efflorescence in NS mortars over an extended period.

9.4.2 Advantages and limitations of LWFA in AAS materials

In addition to its effectiveness in mitigating efflorescence, LWFA also shows promise in reducing the cracking potential of AAS mortars, particularly in NS systems. *Appendix C Figure C2* shows the surface appearance of three NS cylinders sealed for 28 d. The surface of the “LWFA_0%” cylinder is covered with microcracks, whereas the surfaces of the “LWFA_20%” and “LWFA_50%” cylinders are smooth and free from visible cracks. This is probably attributed to the release of water from wet LWFA during the early reaction of slag, which is conducive to impeding the shrinkage and cracking potential induced by self-desiccation [282,283]. This is meaningful for the application of AAS concrete, as it typically shows larger shrinkage compared to traditional cementitious materials.

Although LWFA has a porous structure and lower stiffness than sand, the compressive strength of the “LWFA_20%” mortar only decreases by 6.7% compared to the “LWFA_0%” mortar at 28 d (*Figure 9.16A*). Interestingly, the flexural strength of LWFA-based mortars is 15.6% higher than that of mortar without LWFA (*Figure 9.16B*), likely due to the internal curing effect of LWFA, which helps to prevent the formation of microcracks. In cementitious materials, elevated temperatures and chemical agents are commonly employed to enhance the pozzolanic reactivity of LWFA [269,270]. However, in AAM systems, the naturally high alkaline conditions seem to provide a favourable environment for LWFA's reactivity without the need for additional treatments.

9.5 Conclusions

In this chapter, the efflorescence of AAS mortars with and without aluminosilicate-based LWFA under ambient conditions was investigated. The impacts of LWFA on the properties of AAS mortars were comprehensively investigated. The mitigation mechanism of LWFA on the efflorescence of AAS mortars and some prospects were revealed. The key conclusions are shown as follows.

1. LWFA effectively mitigated the efflorescence of AAS mortars. Substituting sand with LWFA by 20% or 50% in volume reduced the efflorescence of AAS mortars by 14.6% or 43%, respectively. LWFA-based mortars exhibited a lower efflorescence front compared to normal mortar. Additionally, the efflorescence product (thermonatrite) remained the same in mortars with and without LWFA.
2. Leaching of Na from fresh AAS mortar pieces decreased as the dosage of LWFA increased, while that from reaction-stopped powdered AAS mortar increased with the LWFA dosage. This indicated that LWFA reduced the Na content in the pore solution and enhanced the Na binding within the gel structure.
3. The dissolution test of LWFA in the NH activator, along with the ion concentration analysis of the pore solution, showed that LWFA consumed OH⁻ and Na⁺ in the solution and promoted the dissolution of Si and Al. These additional Si and Al species contributed to the gel formation, enhancing the microstructure surrounding LWFA.
4. The introduction of LWFA increased the total porosity of AAS mortars at 28 d but reduced the porosity of the pastes. Mortars containing LWFA showed lower water absorption due

to the extra water provided by LWFA, resulting in a lower efflorescence front compared to normal mortars.

5. Despite the porous structure of LWFA, the compressive strength of LWFA_20% mortar was only 6.7% lower than that of the LWFA_0% mortar at 28 d. The internal curing effect of LWFA improved the flexural strength of both LWFA_20% and LWFA_50% mortars by 15.6% compared to normal mortar. This indicated the excellent adaptability of LWFA in AAS materials, supporting its potential application in AAMs.
6. The synergistic effect of internal curing and the pozzolanic reaction of LWFA contributed to densifying the ITZ through additional gel formation. A denser matrix reduced ion and water transport, mitigating efflorescence. Moreover, these extra gels had a lower $\text{Ca}/(\text{Si}+\text{Al})$ ratio, which enhanced the Na binding in the pore solution, reducing the amount of free Na available for efflorescence.

Chapter 10

Retrospection, conclusions, and prospects

10.1 Retrospection

Alkali-activated slag (AAS) materials have gained significant importance as key elements in the present and future landscape of sustainable building materials, attracting extensive interest from both academia and industry. These cement-free materials offer substantial reductions in CO₂ emissions compared to traditional concrete products. Additionally, these environmentally friendly binders can match or even exceed conventional cementitious materials in various areas, including early strength development, chemical resistance, and thermal durability.

However, increasing studies indicate that AAS materials are more susceptible to degradation than cementitious materials when exposed to high-humidity conditions. Leaching is identified as the main reason responsible for this deterioration, yet the underlying mechanisms remain insufficiently understood. Moreover, efflorescence, characterised by white deposits forming on the surface of materials, is regarded as a derivative engineering problem of leaching. The mechanisms behind the efflorescence of AAS materials and their correlation with leaching need further exploration. To address these research gaps, the mechanisms of leaching and efflorescence of AAS materials were revealed at multiple scales (gels, pastes, mortars), and then a mitigation strategy for efflorescence was proposed in this research.

As C-(N-)A-S-H gels were the main reaction products in AAS systems, C-(N-)A-S-H gels with different Ca/Si and Al/Si ratios were first synthesised. In *Chapter 3*, the leaching behaviours of C-(N-)A-S-H gels were investigated and the underlying mechanisms were revealed by molecular dynamics (MD) simulations. More specifically, the dissolution free energy of Ca and Na ions from the gel surface and the diffusion coefficient of Ca and Na in confined gel pores were calculated. In *Chapter 4*, the structural evolution of C-(N-)A-S-H gels due to the leaching of Na was elucidated by solid-state NMR and the potential mechanisms were revealed.

Subsequently, sodium hydroxide (NH) and sodium silicate (NS) based AAS pastes were prepared to investigate their degradations under water immersion. In *Chapter 5*, AAS paste pieces were employed to fully examine the degradation mechanisms, including ion leaching, pore solution, slag reaction, paste chemistry, pore structure and compressive strength. In *Chapter 6*, the degradation of bulk AAS pastes subjected to water immersion was investigated with depth. Additionally, a thermodynamics-based diffusion-dissolution model was developed to predict the pore structure deterioration over a long period. Moreover, as highlighted in the literature survey (*Chapter 2*), reduced flexural strength and cracking occurred on AAS materials subjected to humid conditions. In *Chapter 7*, the cracking mechanisms of AAS pastes induced by water immersion were revealed from both chemical and mechanical points of view.

In *Chapter 8*, the efflorescence of AAS pastes with different alkali activators and alkali dosages was examined under different atmospheres and relative humidities. The impacts of efflorescence on the phase assemblage, pore structure and compressive strength were investigated. Additionally, a quantitative method for assessing efflorescence was proposed.

The relationship between leaching and efflorescence was established, and the efflorescence process of AAS pastes was clarified. Based on the previous chapters, an aluminosilicate-based lightweight fine aggregate (LWFA) was employed to mitigate the efflorescence of AAS mortars in *Chapter 9*. The underlying mechanisms were elucidated from the pore solution, paste chemistry, and pore structure points of view.

10.2 Conclusions

Generally, the C-(N-)A-S-H gel with a higher Ca/Si ratio and lower Al/Si ratio showed a lower Na content but a higher leaching potential for Na. The leaching of Na induced structural change in gels, with more extensive Na leaching leading to more pronounced structural alterations. NH pastes were particularly vulnerable to long-term leaching due to their porous pore structures. In contrast, NS pastes were denser but more susceptible to cracking due to a higher internal tensile stress induced by capillary suction. Efflorescence was effectively assessed using a proposed quantitative method that correlated well with visual observations. Efflorescence was positively related to the leaching of Na. LWFA can effectively mitigate the efflorescence of AAS mortars, attributed to its pozzolanic activity and internal curing effects. The detailed findings from this thesis are summarised as follows:

Leaching behaviour of C-(N-)A-S-H gels

MD simulations revealed that Ca generally showed a higher average dissolution free energy than Na, resulting in a lower leaching potential for Ca than Na in C-(N-)A-S-H gels. An increased Ca/Si ratio and decreased Al/Si ratio reduced the charge negativity of gel surfaces. This weakened the binding and absorption of Ca and Na ions within the matrix and promoted the dissolution of both Ca and Na ions. Furthermore, the gel with a higher Ca/Si ratio featured shorter and more defective aluminosilicate chains, reducing surface restraints on Ca and Na ions and thereby diminishing the inhibition of ion leaching.

Structural change of C-(N-)A-S-H gels subjected to leaching

C-(N-)A-S-H gels showed rapid and substantial Na leaching when subjected to water immersion, resulting in longer aluminosilicate chains. This effect can be attributed to the changes in the charge compensator within the interlayer of the C-(N-)A-S-H gels. As Na ions leached away from the interlayer, Ca progressively took the role of charge compensator, resulting in the decalcification of the intralayer and the formation of longer silicate chains. Additionally, the gel with a higher Ca/Si ratio had a lower content of Na, thus a lower leaching of Na, demonstrating enhanced resistance to water immersion.

Leaching mechanisms of AAS pastes

AAS pastes showed degraded microstructure under tap water immersion, with the underlying mechanisms attributed to lower slag reaction, gel decomposition and underwater carbonation. In the early stages, the leaching of Na^+ and OH^- lowered the pH of the pore solution, which hindered the reaction of slag and the formation of reaction products. In the later stages, continued leaching resulted in gel decomposition, leading to a coarser pore structure and reduced compressive strength of AAS pastes than those under sealed conditions. Additionally, leached Ca ions can react with the dissolved CO_2 in tap water to form calcium carbonate. A calcium carbonate layer was observed surrounding the paste after 90 d of immersion.

Prediction of the microstructural deterioration of AAS pastes

Deterioration of the pore structures was observed in both NH and NS pastes with depth, with NS pastes demonstrating better resistance to leaching. After 90 d of deionised water immersion, the deteriorated pore structure in the NH paste reached 600 μm , approximately 6 times higher than that of the NS paste. The simulation results indicated that ion concentrations of the pore solution in the entire simulated 100 mm were changed after 10 y. The leaching of ions disrupted the equilibrium between reaction products and liquid phases. Significant decomposition of gels was simulated within a depth of 1.5 mm at 10 y, leading to severe degradation of the paste near the exposure front. Additionally, the leaching of Na induced the reorganisation of gel phases throughout the whole simulated 100 mm depth at 10 y, but minimal coarsening of the microstructure was observed across the simulated region.

Cracking mechanisms of AAS pastes induced by water immersion

AAS pastes can crack during water immersion at early ages. It was observed that the paste with a higher silicate modulus exhibited more pronounced cracking. Chemically, the C-(N-)A-S-H gel in the paste with a higher silicate modulus showed a higher Na/Si ratio and experienced more severe leaching of Na and structural change of gels after immersion. This can initiate the propagation of pre-existing cracks. Physically, the paste with a higher silicate modulus (e.g. $m=1$ and $m=1.5$) featured a denser microstructure and lower permeability, resulting in an uneven spatial distribution of water content in the matrix. The wetted part relaxed pore pressure locally, generating compressive stress at the surface and tensile stress at the centre. Once the tensile stress exceeded the inherent tensile strength of the material, cracks initiated at the centre. In severe cases, particularly for $m=1.5$, these central cracks propagated outward, culminating in extensive fractures and corner spalling.

Mechanisms of efflorescence of AAS pastes

A higher alkali dosage, a coarser pore structure and a lower relative humidity accelerated and intensified efflorescence. The paste with a lower porosity showed a lower efflorescence front. Compared to NH pastes, NS pastes subjected to semi-contact water conditions were more vulnerable to cracking problems, which were exacerbated by the formation of efflorescence products. An efflorescence quantification method was developed, corresponding well with both visual observations and leaching experiments. The paste with a higher porosity showed higher permeability, which contributed to the formation of sodium carbonate with a higher content of chemical-bound water. Furthermore, a competitive reaction between Ca and Na in the presence of carbonate ions was identified. CaCO_3 , a representative product of natural carbonation, was rarely found in the regions where efflorescence products formed. Regarding compressive strength, NS pastes were more adversely impacted by efflorescence than NH pastes.

Mitigating the efflorescence of AAS mortars by LWFA

Substituting sand with aluminosilicate-based lightweight fine aggregate (LWFA) at 20% and 50% in volume reduced the efflorescence in AAS mortars by 14.6% or 43%, respectively. The mitigation mechanisms of LWFA involved the paste chemistry, pore solution and pore structure. Specifically, the pozzolanic reaction of LWFA provided gels with additional Si and Al, which contributed to binding Na ions in the pore solution, thereby reducing the availability of Na for efflorescence formation. Additionally, the internal curing effect of LWFA densified the surrounding pastes, hindering the transport of ions and water and further limiting

efflorescence. Furthermore, the incorporation of LWFA improved the flexural strength of mortars without significantly compromising compressive strength.

10.3 Contributions

The scientific and engineering contributions of this thesis are summarised as follows:

Leaching of AAS materials

1. Dissolution free energies: For the first time, the dissolution free energies of Ca and Na in C-(N-)A-S-H gels were calculated by MD simulations. This provides valuable insights into the intrinsic differences in the dissolution behaviour of Ca and Na ions and advances our understanding of how chemical composition influences their dissolution.
2. A deeper understanding of Na in gels: C-(N-)A-S-H gels with controlled Ca/Si and Al/Si ratios were successfully synthesised under high alkaline conditions using the sol-gel method, offering experimental guidance for rapid gel synthesis in AAS systems. The structural evolution of C-(N-)A-S-H gels caused by Na leaching was revealed, shedding light on the role of Na in C-(N-)A-S-H gels.
3. A diffusion-dissolution model: A novel thermodynamics-based diffusion-dissolution model was developed to understand ion concentrations, phase assemblage, and pore structure in AAS pastes subjected to water immersion at various depths. This model is a valuable tool for predicting the degradation depth of AAS materials in aqueous environments.
4. Cracking mechanisms: The cracking mechanisms of AAS pastes during water immersion. This understanding not only explains the structural damage observed in engineering applications but also supports optimising the mixture design of AAS materials.

Efflorescence of AAS materials

1. Quantitative assessment method: A novel quantitative method for evaluating the efflorescence in AAS materials was developed, providing an effective and reliable approach to measuring efflorescence severity. This method offers a new perspective for establishing standardised criteria for efflorescence in AAMs.
2. Mitigation strategy at the mortar level: A strategy for mitigating efflorescence in AAS materials using LWFA was proposed. This approach effectively reduces efflorescence and lowers the cracking potential of AAS materials without significantly compromising mechanical properties, making it a promising solution for AAS-based construction applications, when leaching and efflorescence are concerned.

10.4 Prospect

Perspectives and further work on the leaching and efflorescence of AAMs are shown as follows:

1. **Blended AAS Systems:** In this thesis, the investigation of leaching concentrated exclusively on the plain AAS systems. However, in practical engineering applications in the Netherlands, a small amount of fly ash is commonly introduced to AAM concretes to improve workability and reduce shrinkage. Therefore, it would be essential to elucidate the leaching properties of blended AAS materials, *e.g.* the dissolution behaviour and structural evolution of the characteristic reaction products of N-A-S-H or N-(C)-A-S-H gels formed from the reaction of fly ash.
2. **Refinement of the diffusion-dissolution model:** The diffusion-dissolution model for AAS materials developed in this thesis requires further refinement, incorporating additional factors, including the continued reaction of slag, the presence of external ions in the host solution, and the influence of aggregates.
3. **Efflorescence standards for AAMs:** The testing standards for durability issues in concrete, including carbonation, chloride ion penetration, sulfate attack, and freeze-thaw cycles, are well-established and widely applied in construction and building materials. In spite of the different chemistry between cementitious materials and AAMs, appropriate adjustments and modifications to the criteria for cementitious materials can be made to assess the durability of AAMs. However, there are currently no corresponding standards for the efflorescence of AAMs. To promote the broader application of this low-carbon alternative binder, the formulation of standards on efflorescence (experimental setup and quantification methods) is urgently needed.
4. **Extended work on efflorescence:** According to previous studies, the impact of efflorescence on the mechanical properties of AAMs has been extensively studied, whereas its effect on the durability of these materials remains largely unexplored. This is important because reduced strength is not the direct factor leading to the structural failure of materials in some cases. Moreover, the efflorescence of AAMs under different aqueous environments, such as marine conditions, deserves consideration, as these environments may involve different efflorescence mechanisms compared to those under normal water.

Appendix A

Use of a heat transfer module in ABAQUS to simulate the water transport process

The water transport equation is shown in *Equation A1*. The heat transfer equation is shown in *Equation A2*. By comparing the following two equations and their variables (*Table A1*), it can be seen that the heat transfer equation has only two additional variables: density and specific heat. Setting their product to 1 makes the equations equivalent, with water content (θ) analogous to temperature (T) and the water permeability (K_θ) analogous to thermal conductivity (λ_T). Thus, the heat transfer module in ABAQUS can be used to simulate the water transport in porous materials.

$$\frac{\partial \theta}{\partial t} = \frac{\partial}{\partial x} \left(K_\theta \frac{\partial \theta}{\partial x} \right) + \frac{\partial}{\partial y} \left(K_\theta \frac{\partial \theta}{\partial y} \right) \quad (A1)$$

$$\rho c \frac{\partial T}{\partial t} = \frac{\partial}{\partial x} \left(\lambda_T \frac{\partial T}{\partial x} \right) + \frac{\partial}{\partial y} \left(\lambda_T \frac{\partial T}{\partial y} \right) \quad (A2)$$

Table A1. Comparison of water transport equation and heat transfer equation.

Heat transfer equation	Unit	Water transport equation	Unit
Temperature (T)	°C	Water content (θ)	–
Thermal conductivity (λ_T)	W/(m·°C)	Water permeability (K_θ)	m/s
Coordinates	m	Coordinates	m
Time (t)	s	Time (t)	s
Density (ρ)	kg/m ³	–	–
Specific heat (c)	J/(kg·°C)	–	–

Table A2. Input parameters in the water transport model.

	m = 0	m = 0.5	m = 1	m = 1.5
Open porosity	0.265	0.182	0.111	0.079
Initial water content	0.25069	0.17072	0.10245	0.07126
B	25000	60000	200000	400000

Figure A1 shows the appearance of the paste of $m = 1.5$ immersed in water with time. The crack was identified on the samples after 1 d of water immersion. The cracking problem was more and more severe over time. Additionally, the white flocculent precipitate suspended in the water was calcium carbonate, as mentioned in Chapter 5.

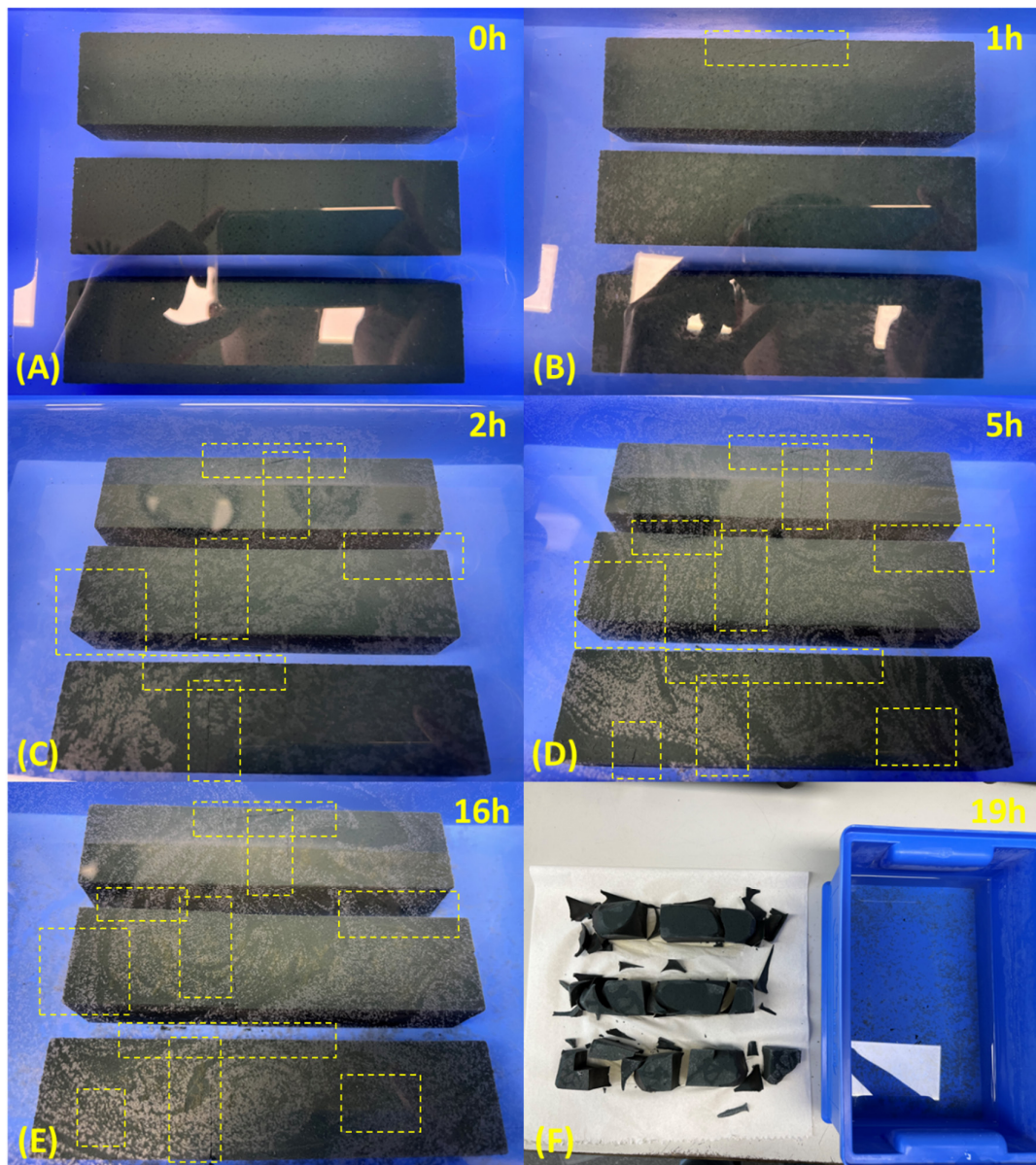


Figure A1. Appearance of the paste with $m = 1.5$ immersed in water with time. The cracks on the sample are indicated by the yellow dashed rectangular frame. The photo of (F) was taken immediately after the samples were removed from water, without undergoing the drying process.

Figure A2 shows the relationship between capillary diffusivity and water content for the four AAS pastes. The paste with a higher silicate modulus showed a lower capillary diffusivity. The capillary diffusivity increased significantly with the increase in water content.

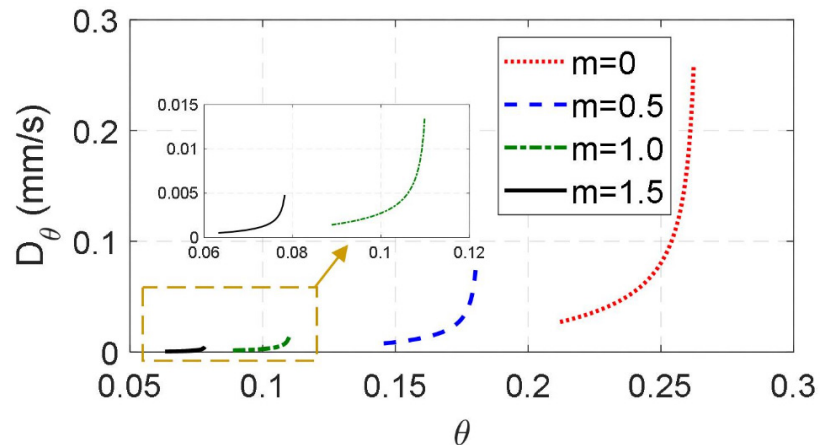


Figure A2. Relationship between capillary diffusivity D_θ and water content θ for AAS pastes with different silicate moduli. The saturation degree (θ/φ) ranges from 0.8 to 0.999. φ is the open porosity of pastes.

The mixture design of AAS mortars is presented in Table A3. Figure A4 shows the flexural and compressive strength of AAS mortars with $m = 0, 0.5, 1$ and 1.5 under sealed (s) and water-immersed (w) conditions, respectively. As shown in Figure A3A, other than the $m = 1.5$ group, the flexural strength of the remaining three mortars under immersed conditions is higher than that under sealed conditions, which is significantly different from the results of pastes. This indicated that the introduction of sand was effective in reducing the cracking induced by water exposure. However, a lower flexural strength of the $m = 1.5$ mortar was identified under water immersion than under sealed conditions. This suggested that cracking problems still happened in the mortar with high silicate moduli. As shown in Figure A3B, the compressive strength of mortars under immersed conditions is slightly lower than that under sealed conditions. This was consistent with the results of pastes.

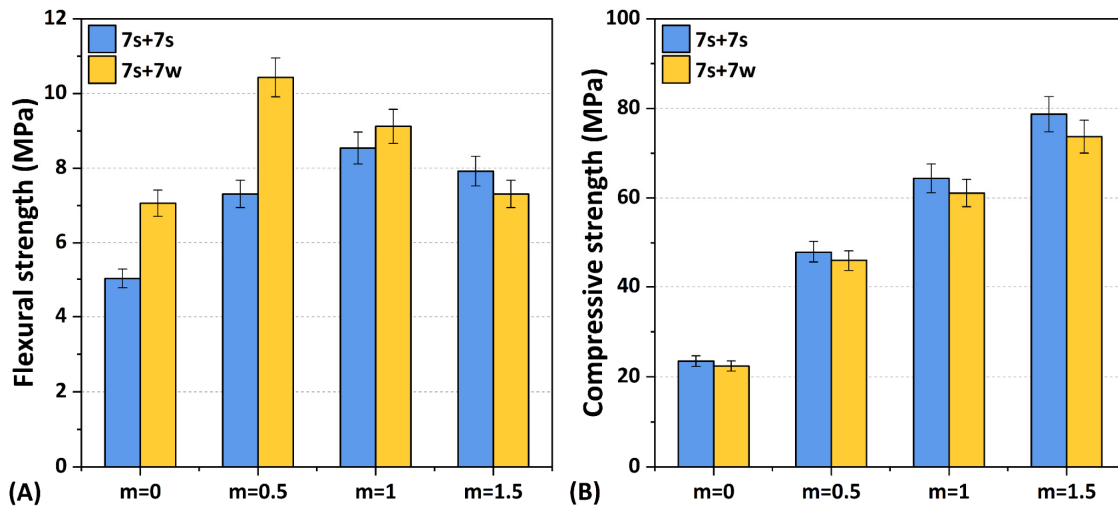


Figure A3. Flexural and compressive strengths of AAS mortars with different silicate moduli under sealed and water-immersed conditions.

Table A3. Mixture proportions of AAS mortars.

	Slag (g)	SiO ₂ (mol)	Na ₂ O (mol)	Water (g)	sand
m = 0	1000	0	0.8	505	2500
m = 0.5	1000	0.4	0.8	505	2500
m = 1	1000	0.8	0.8	505	2500
m = 1.5	1000	1.2	0.8	505	2500

Appendix B

Figure B1 shows the phase assemblage of efflorescence products on NH and NS cylinders under 0.2% CO₂ conditions. In the NH system, the main phase was Trona (Na₃H(CO₃)₂·2H₂O), considered a combination of NaHCO₃ and Na₂CO₃. Conversely, the efflorescence product of the NS system was dominated by Na₂CO₃. Under ambient conditions, the primary phase of the efflorescence product of AAS pastes was Na₂CO₃·xH₂O (Figure 8.14). Under a high concentration of CO₂, a conversion from Na₂CO₃ to NaHCO₃ occurred on NH cylinders due to elevated CO₂ concentration in the environment. However, little NaHCO₃ was identified on the cylinders of NS, possibly due to inadequate water supply from the bottom hindering the conversion to NaHCO₃.

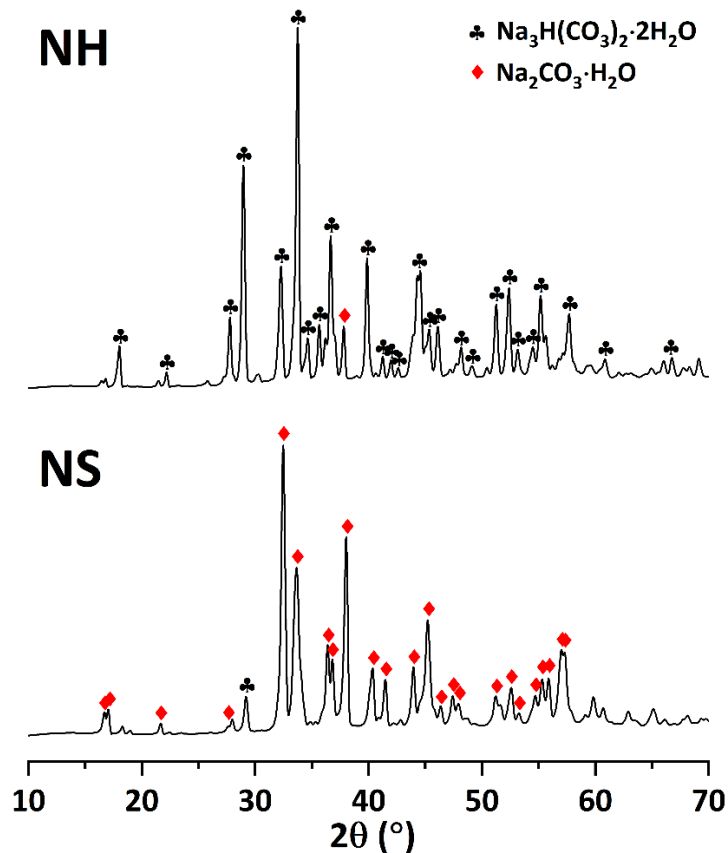


Figure B1. XRD patterns of efflorescence products on NH and NS cylinders under 0.2% CO₂ condition.

Appendix C

Figure C1 shows the efflorescence of NS mortars under ambient conditions with time. It can be seen that the efflorescence of the three NS mortars at 28 d was comparable, while the efflorescence of two LWFA-based NS mortars was lower than that of the normal mortars at 90 d.



Figure C1. Visual observation of efflorescence of NS mortars with time.

Figure C2 shows the surface of NS mortar cylinders sealed for 28 d. The surface of the mortar without LWFA (LWFA_0%) was covered by microcracks while that of the two mortars containing LWFA (LWFA_20% and LWFA_50%) showed no visible cracks on the surface.

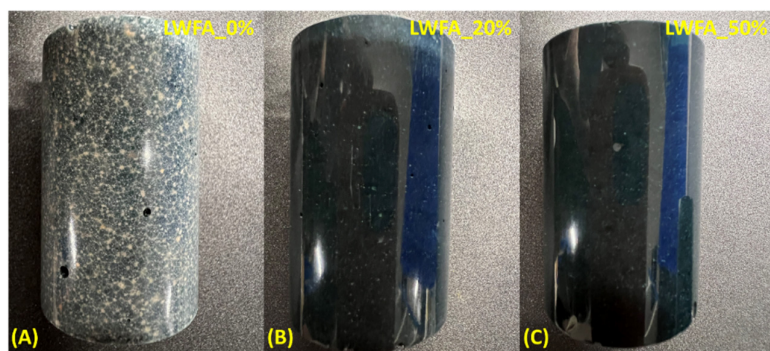


Figure C2. Appearance of NS mortar cylinders after 28 d of sealed curing.



Reference

- [1] P.J.M. Monteiro, S.A. Miller, A. Horvath, Towards sustainable concrete, *Nat. Mater.* 16 (2017) 698–699. <https://doi.org/10.1038/nmat4930>.
- [2] N. Mohamad, K. Muthusamy, R. Embong, A. Kusbiantoro, M.H. Hashim, Environmental impact of cement production and Solutions: A review, *Mater. Today Proc.* 48 (2021) 741–746. <https://doi.org/10.1016/j.matpr.2021.02.212>.
- [3] J.L. Provis, Alkali-activated materials, *Cem. Concr. Res.* 114 (2018) 40–48. <https://doi.org/10.1016/j.cemconres.2017.02.009>.
- [4] F. Pacheco-Torgal, Z. Abdollahnejad, A.F. Camões, M. Jamshidi, Y. Ding, Durability of alkali-activated binders: A clear advantage over Portland cement or an unproven issue?, *Constr. Build. Mater.* 30 (2012) 400–405. <https://doi.org/10.1016/j.conbuildmat.2011.12.017>.
- [5] K. Arbi, M. Nedeljković, Y. Zuo, G. Ye, A Review on the Durability of Alkali-Activated Fly Ash/Slag Systems: Advances, Issues, and Perspectives, *Ind. Eng. Chem. Res.* 55 (2016) 5439–5453. <https://doi.org/10.1021/acs.iecr.6b00559>.
- [6] S.A. Bernal, J.L. Provis, Durability of alkali-activated materials: Progress and perspectives, *J. Am. Ceram. Soc.* 97 (2014) 997–1008. <https://doi.org/10.1111/jace.12831>.
- [7] B. Ozer, M.H. Ozkul, The influence of initial water curing on the strength development of ordinary portland and pozzolanic cement concretes, *Cem. Concr. Res.* 34 (2004) 13–18. [https://doi.org/10.1016/S0008-8846\(03\)00185-6](https://doi.org/10.1016/S0008-8846(03)00185-6).
- [8] P. Termkhajornkit, T. Nawa, K. Kurumisawa, Effect of water curing conditions on the hydration degree and compressive strengths of fly ash-cement paste, *Cem. Concr. Compos.* 28 (2006) 781–789. <https://doi.org/10.1016/j.cemconcomp.2006.05.018>.
- [9] G. Huang, Y. Ji, L. Zhang, J. Li, Z. Hou, The influence of curing methods on the strength of MSWI bottom ash-based alkali-activated mortars: The role of leaching of OH⁻ and free alkali, *Constr. Build. Mater.* 186 (2018) 978–985. <https://doi.org/10.1016/j.conbuildmat.2018.07.224>.
- [10] Y. Zhu, M.A. Longhi, A. Wang, D. Hou, H. Wang, Z. Zhang, Alkali leaching features of 3-year-old alkali activated fly ash-slag-silica fume: For a better understanding of stability, *Compos. Part B Eng.* 230 (2021) 109469. <https://doi.org/10.1016/j.compositesb.2021.109469>.
- [11] X. Yao, T. Yang, Z.Z. Zhang, Y. Wang, X. Liu, W.D. Zhang, Z. Li, Y. Zhang, Y. Li, Y. Ren, K. Sun, X. Peng, S. Wang, L. Zeng, P. Ran, G. Ji, M.A. Longhi, E.D. Rodríguez, B. Walkley, Z.Z. Zhang, A.P. Kirchheim, S.P. Kang, S.J. Kwon, X. Xue, Y.L. Liu, J.G. Dai, C.S. Poon, W.D. Zhang, P. Zhang, Z.Z. Zhang, J.L. Provis, X. Ma, A. Reid, H. Wang, J.L. Provis, A. Reid, X. Yao, T. Yang, Z.Z. Zhang, J.L. Provis, A. Reid, H. Wang, R.R. Lloyd, J.L. Provis, J.S.J. Van Deventer, Compressive strength development and shrinkage of alkali-activated fly ash-slag blends associated with efflorescence, *Mater. Struct.* 49 (2016) 165–177. <https://doi.org/10.1016/j.cemconcomp.2018.06.010>.
- [12] F. Škvára, V. Šmilauer, P. Hlaváček, L. Kopecký, Z. Cílová, A weak alkali bond in (N, K)-A-S-H gels: Evidence from leaching and modeling, *Ceram. - Silikaty.* 56 (2012) 374–382.
- [13] X. Zhu, M. Zhang, Y. Yang, K. Yang, F. Wu, Q. Li, L. Yu, C. Yang, M. Basheer, Understanding the aqueous phases of alkali-activated slag paste under water curing, *Adv. Cem. Res.* 33 (2021) 59–73. <https://doi.org/10.1680/jadcr.18.00202>.
- [14] M.H. Hubler, J.J. Thomas, H.M. Jennings, Influence of nucleation seeding on the hydration kinetics and compressive strength of alkali activated slag paste, *Cem. Concr. Res.* 41 (2011) 842–846. <https://doi.org/10.1016/j.cemconres.2011.04.002>.
- [15] C.L. Hwang, D.H. Vo, V.A. Tran, M.D. Yehualaw, Effect of high MgO content on the performance of alkali-activated fine slag under water and air curing conditions, *Constr. Build. Mater.* 186 (2018) 503–513. <https://doi.org/10.1016/j.conbuildmat.2018.07.129>.
- [16] P. Russell, Efflorescence and the Discoloration of Concrete, CRC Press, 1983.

[17] A. Allahverdi, E. Najafi Kani, K.M.A. Hossain, M. Lachemi, Methods to control efflorescence in alkali-activated cement-based materials, *Handb. Alkali-Activated Cem. Mortars Concr.* (2015) 463–483. <https://doi.org/10.1533/9781782422884.3.463>.

[18] C. Dow, F.P. Glasser, Calcium carbonate efflorescence on Portland cement and building materials, *Cem. Concr. Res.* 33 (2003) 147–154. [https://doi.org/10.1016/S0008-8846\(02\)00937-7](https://doi.org/10.1016/S0008-8846(02)00937-7).

[19] H. Brocken, T.G. Nijland, White efflorescence on brick masonry and concrete masonry blocks, with special emphasis on sulfate efflorescence on concrete blocks, *Constr. Build. Mater.* 18 (2004) 315–323. <https://doi.org/10.1016/j.conbuildmat.2004.02.004>.

[20] C. Liu, Z. Li, S. Nie, S. Skibsted, G. Ye, Structural evolution of calcium sodium aluminosilicate hydrate (C-(N-)A-S-H) gels induced by water exposure: the impact of Na leaching, *Cem. Concr. Res.* 178 (2024). <https://doi.org/10.1016/j.cemconres.2024.107432>.

[21] M.A. Longhi, Z. Zhang, B. Walkley, E.D. Rodríguez, A.P. Kirchheim, Strategies for control and mitigation of efflorescence in metakaolin-based geopolymers, *Cem. Concr. Res.* 144 (2021). <https://doi.org/10.1016/j.cemconres.2021.106431>.

[22] Z. Zhang, J.L. Provis, A. Reid, H. Wang, Fly ash-based geopolymers: The relationship between composition, pore structure and efflorescence, *Cem. Concr. Res.* 64 (2014) 30–41. <https://doi.org/10.1016/j.cemconres.2014.06.004>.

[23] Z. Zhang, J.L. Provis, X. Ma, A. Reid, H. Wang, Efflorescence and subflorescence induced microstructural and mechanical evolution in fly ash-based geopolymers, *Cem. Concr. Compos.* 92 (2018) 165–177. <https://doi.org/10.1016/j.cemconcomp.2018.06.010>.

[24] X. Xue, Y.L. Liu, J.G. Dai, C.S. Poon, W.D. Zhang, P. Zhang, Inhibiting efflorescence formation on fly ash-based geopolymer via silane surface modification, *Cem. Concr. Compos.* 94 (2018) 43–52. <https://doi.org/10.1016/j.cemconcomp.2018.08.013>.

[25] M.A. Longhi, E.D. Rodríguez, B. Walkley, Z. Zhang, A.P. Kirchheim, Metakaolin-based geopolymers: Relation between formulation, physicochemical properties and efflorescence formation, *Compos. Part B Eng.* 182 (2020). <https://doi.org/10.1016/j.compositesb.2019.107671>.

[26] Z. Zhang, H. Wang, J.L. Provis, A. Reid, Efflorescence : A Critical Challenge for Geopolymer Applications ?, *Concr. Inst. Aust. Bienn. Natl. Conf.* (2013).

[27] S.A. Bernal, J.L. Provis, A. Fernández-jiménez, P. V Krivenko, E. Kavalerova, M. Palacios, C. Shi, *Alkali Activated Materials*, 2014. <http://link.springer.com/10.1007/978-94-007-7672-2>.

[28] J.L. Provis, Geopolymers and other alkali activated materials: Why, how, and what?, *Mater. Struct. Constr.* 47 (2014) 11–25. <https://doi.org/10.1617/s11527-013-0211-5>.

[29] J.L. Provis, S.A. Bernal, Geopolymers and related alkali-activated materials, *Annu. Rev. Mater. Res.* 44 (2014) 299–327. <https://doi.org/10.1146/annurev-matsci-070813-113515>.

[30] A. Vollpracht, B. Lothenbach, R. Snellings, J. Haufe, The pore solution of blended cements: a review, *Mater. Struct. Constr.* 49 (2016) 3341–3367. <https://doi.org/10.1617/s11527-015-0724-1>.

[31] K. Natkunarajah, K. Masilamani, S. Maheswaran, B. Lothenbach, D.A.S. Amarasinghe, D. Attygalle, Analysis of the trend of pH changes of concrete pore solution during the hydration by various analytical methods, *Cem. Concr. Res.* 156 (2022) 106780. <https://doi.org/10.1016/j.cemconres.2022.106780>.

[32] P. Faucon, F. Adenot, R. Cabrillac, M. Jorda, Deterioration mechanisms of a cement paste under water attack, *Concr. under Sev. Cond.* 2 (1998) 123–132.

[33] M. Mainguy, C. Tognazzi, J.M. Torrenti, F. Adenot, Modelling of leaching in pure cement paste and mortar, *Cem. Concr. Res.* 30 (2000) 83–90. [https://doi.org/10.1016/S0008-8846\(99\)00208-2](https://doi.org/10.1016/S0008-8846(99)00208-2).

[34] J. Jain, N. Neithalath, Analysis of calcium leaching behavior of plain and modified cement pastes in pure water, *Cem. Concr. Compos.* 31 (2009) 176–185. <https://doi.org/10.1016/j.cemconcomp.2009.01.003>.

[35] C. Carde, R. François, Effect of the leaching of calcium hydroxide from cement paste on mechanical and physical properties, *Cem. Concr. Res.* 27 (1997) 539–550. [https://doi.org/10.1016/S0008-8846\(97\)00042-2](https://doi.org/10.1016/S0008-8846(97)00042-2).

[36] K. Haga, S. Sutou, M. Hironaga, S. Tanaka, S. Nagasaki, Effects of porosity on leaching of Ca from hardened ordinary Portland cement paste, *Cem. Concr. Res.* 35 (2005) 1764–1775. <https://doi.org/10.1016/j.cemconres.2004.06.034>.

[37] D.P. Bentz, K. a Snyder, P.E. Stutzman, Hydration of Portland cement: The effects of curing conditions, 10th Int. Congr. Chem. Cem. Vol 2. (1997) 2ii078.

[38] M. LUO, Q. ZENG, X. PANG, K. LI, Effect of curing conditions on pore structure of cement based materials, *J. Chinese Ceram. Soc.* 41 (2013) 597–604.

[39] N. Shafiq, J.G. Cabrera, Effects of initial curing condition on the fluid transport properties in OPC and fly ash blended cement concrete, *Cem. Concr. Compos.* 26 (2004) 381–387. [https://doi.org/10.1016/S0958-9465\(03\)00033-7](https://doi.org/10.1016/S0958-9465(03)00033-7).

[40] A. Bhalodia, Effect of Curing Methods on Strength and Elastic Properties of Concrete, *Int. J. Res. Appl. Sci. Eng. Technol.* 6 (2018) 1358–1363. <https://doi.org/10.22214/ijraset.2018.5223>.

[41] S. Han, Y. Cui, H. Huang, M. An, Z. Yu, Effect of Curing Conditions on the Shrinkage of Ultra High-Performance Fiber-Reinforced Concrete, *Adv. Civ. Eng.* 2018 (2018). <https://doi.org/10.1155/2018/5238278>.

[42] O.M. Jensen, P.F. Hansen, Autogenous deformation and RH-change in perspective, *Cem. Concr. Res.* 31 (2001) 1859–1865. [https://doi.org/10.1016/S0008-8846\(01\)00501-4](https://doi.org/10.1016/S0008-8846(01)00501-4).

[43] Z. Abdollahnejad, T. Luukkonen, M. Mastali, C. Giosue, O. Favoni, M.L. Ruello, P. Kinnunen, M. Illikainen, Microstructural Analysis and Strength Development of One-Part Alkali-Activated Slag/Ceramic Binders Under Different Curing Regimes, *Waste and Biomass Valorization.* 11 (2020) 3081–3096. <https://doi.org/10.1007/s12649-019-00626-9>.

[44] M. Nedeljković, Y. Zuo, K. Arbi, G. Ye, Carbonation Resistance of Alkali-Activated Slag Under Natural and Accelerated Conditions, *J. Sustain. Metall.* 4 (2018) 33–49. <https://doi.org/10.1007/s40831-018-0166-4>.

[45] Z. Zhang, C. Xie, Z. Sang, D. Li, Optimizing the Mechanical Performance and Microstructure of Alkali-Activated Soda Residue-Slag Composite Cementing Materials by Various Curing Methods, *Sustain.* 14 (2022). <https://doi.org/10.3390/su142013661>.

[46] A.H. Sevinç, Investigating the Properties of GGBFS Hazelnut Ash-Based Cement-Free Mortars Produced at Ambient Temperature under Different Curing Conditions, *J. Mater. Civ. Eng.* 34 (2022). [https://doi.org/10.1061/\(asce\)mt.1943-5533.0004425](https://doi.org/10.1061/(asce)mt.1943-5533.0004425).

[47] C.H.W.Z.L.H.S.G.Y. Liu, Effect of curing condition on mechanical properties and durability of alkali-activated slag mortar, (2020) 1934472.

[48] M. Nedeljković, B. Ghiassi, S. van der Laan, Z. Li, G. Ye, Effect of curing conditions on the pore solution and carbonation resistance of alkali-activated fly ash and slag pastes, *Cem. Concr. Res.* 116 (2019) 146–158. <https://doi.org/10.1016/j.cemconres.2018.11.011>.

[49] T. Wei, H. Zhao, C. Ma, A comparison of water curing and standard curing on one-part alkali-activated fly ash sinking beads and slag: Properties, microstructure and mechanisms, *Constr. Build. Mater.* 273 (2021) 121715. <https://doi.org/10.1016/j.conbuildmat.2020.121715>.

[50] H. Maghsoodloorad, A. Allahverdi, Efflorescence formation and control in alkali-activated phosphorus slag cement, *Int. J. Civ. Eng.* 14 (2016) 425–438. <https://doi.org/10.1007/s40999-016-0027-0>.

[51] A.S. Pawar, M.N. Patil, S.K. Dubey, The Influences of curing condition on properties of concrete, 6 (2019) 804–806.

[52] L. Srinivasamurthy, V.S. Chevali, Z. Zhang, H. Wang, Effect of fly ash to slag ratio and Na₂O content on leaching behaviour of fly Ash/Slag based alkali activated materials, *Constr. Build. Mater.* 383 (2023) 131234. <https://doi.org/10.1016/j.conbuildmat.2023.131234>.

[53] J.L. Provis, A. Palomo, C. Shi, Advances in understanding alkali-activated materials, *Cem. Concr. Res.* 78 (2015) 110–125. <https://doi.org/10.1016/j.cemconres.2015.04.013>.

[54] E. Duque-Redondo, P.A. Bonnaud, H. Manzano, A comprehensive review of C-S-H empirical and computational models, their applications, and practical aspects, *Cem. Concr. Res.* 156 (2022) 106784.

[https://doi.org/10.1016/j.cemconres.2022.106784.](https://doi.org/10.1016/j.cemconres.2022.106784)

[55] R.J. Myers, E. L'Hôpital, J.L. Provis, B. Lothenbach, Effect of temperature and aluminium on calcium (alumino)silicate hydrate chemistry under equilibrium conditions, *Cem. Concr. Res.* 68 (2015) 83–93. <https://doi.org/10.1016/j.cemconres.2014.10.015>.

[56] R.J. Myers, S.A. Bernal, R. San Nicolas, J.L. Provis, Generalized structural description of calcium-sodium aluminosilicate hydrate gels: The cross-linked substituted tobermorite model, *Langmuir*. 29 (2013) 5294–5306. <https://doi.org/10.1021/la4000473>.

[57] R.J. Myers, E. L'Hôpital, J.L. Provis, B. Lothenbach, Composition-solubility-structure relationships in calcium (alkali) aluminosilicate hydrate (C-(N,K)-A-S-H), *Dalt. Trans.* 44 (2015) 13530–13544. <https://doi.org/10.1039/c5dt01124h>.

[58] I. Garcia-Lodeiro, A. Palomo, A. Fernández-Jiménez, D.E. MacPhee, Compatibility studies between N-A-S-H and C-A-S-H gels. Study in the ternary diagram Na₂O-CaO-Al₂O₃-SiO₂-H₂O, *Cem. Concr. Res.* 41 (2011) 923–931. <https://doi.org/10.1016/j.cemconres.2011.05.006>.

[59] Y. Wang, Y. Cao, Z. Zhang, J. Huang, P. Zhang, Y. Ma, H. Wang, Study of acidic degradation of alkali-activated materials using synthetic C-(N)-A-S-H and N-A-S-H gels, *Compos. Part B Eng.* 230 (2021) 109510. <https://doi.org/10.1016/j.compositesb.2021.109510>.

[60] I.G. Richardson, A.R. Brough, G.W. Groves, C.M. Dobson, The characterization of hardened alkali-activated blast-furnace slag pastes and the nature of the calcium silicate hydrate (C-S-H) phase, *Cem. Concr. Res.* 24 (1994) 813–829. [https://doi.org/10.1016/0008-8846\(94\)90002-7](https://doi.org/10.1016/0008-8846(94)90002-7).

[61] S.-D. Wang, K.L. Scrivener, Hydration products of alkali activated slag cement, *Cem. Concr. Res.* 25 (1995) 561–571. [https://doi.org/https://doi.org/10.1016/0008-8846\(95\)00045-E](https://doi.org/https://doi.org/10.1016/0008-8846(95)00045-E).

[62] R.J. Myers, S.A. Bernal, J.D. Gehman, J.S.J. Van Deventer, J.L. Provis, The role of al in cross-linking of alkali-activated slag cements, *J. Am. Ceram. Soc.* 98 (2015) 996–1004. <https://doi.org/10.1111/jace.13360>.

[63] M. Jin, Y. Ma, W. Li, J. Huang, Y. Yan, H. Zeng, C. Lu, J. Liu, Multi-scale investigation on composition-structure of C-(A)-S-H with different Al/Si ratios under attack of decalcification action, *Cem. Concr. Res.* 172 (2023). <https://doi.org/10.1016/j.cemconres.2023.107251>.

[64] A.G. Kalinichev, R.J. Kirkpatrick, Molecular dynamics modeling of chloride binding to the surfaces of calcium hydroxide, hydrated calcium aluminate, and calcium silicate phases, *Chem. Mater.* 14 (2002) 3539–3549. <https://doi.org/10.1021/cm0107070>.

[65] E. Duque-Redondo, P.A. Bonnaud, H. Manzano, A comprehensive review of C-S-H empirical and computational models, their applications, and practical aspects, *Cem. Concr. Res.* 156 (2022) 106784. <https://doi.org/10.1016/j.cemconres.2022.106784>.

[66] T. Pan, K. Xia, L. Wang, Chloride binding to calcium silicate hydrates (C-S-H) in cement paste: a molecular dynamics analysis, *Int. J. Pavement Eng.* 11 (2010) 367–379. <https://doi.org/10.1080/10298436.2010.488732>.

[67] J. Jiang, P. Wang, D. Hou, The mechanism of cesium ions immobilization in the nanometer channel of calcium silicate hydrate: A molecular dynamics study, *Phys. Chem. Chem. Phys.* 19 (2017) 27974–27986. <https://doi.org/10.1039/c7cp05437h>.

[68] K. Zehnder, A. Arnold, CRYSTAL GROWTH IN SALT EFFLORESCENCE Konrad ZEHNDER and Andreas ARNOLD, *J. Cryst. Growth.* 97 (1989) 513–521.

[69] Y. Zuo, M. Nedeljković, G. Ye, Pore solution composition of alkali-activated slag/fly ash pastes, *Cem. Concr. Res.* 115 (2019) 230–250. <https://doi.org/10.1016/j.cemconres.2018.10.010>.

[70] A. Allahverdi, E. Najafi Kani, B. Shaverdi, Carbonation Versus Efflorescence in Alkali-Activated Blast-Furnace Slag in Relation with Chemical Composition of Activator, *Int. J. Civ. Eng.* 15 (2017) 565–573. <https://doi.org/10.1007/s40999-017-0225-4>.

[71] L. Srinivasamurthy, V.S. Chevali, Z. Zhang, A. Longhi, T.W. Loh, H. Wang, Mechanical property and microstructure development in alkali activated fly ash slag blends due to efflorescence, *Constr. Build.*

Mater. 332 (2022). <https://doi.org/10.1016/j.conbuildmat.2022.127273>.

[72] R. Jia, Q. Wang, T. Luo, Deterioration and mitigation of efflorescence of alkali-activated phosphorus slag, Constr. Build. Mater. 407 (2023) 133500. <https://doi.org/10.1016/j.conbuildmat.2023.133500>.

[73] X. Liu, E. Liu, Y. Fu, Reduction in Drying Shrinkage and Efflorescence of Recycled Brick and Concrete Fine Powder-Slag-Based Geopolymer, Appl. Sci. 13 (2023). <https://doi.org/10.3390/app13052997>.

[74] X. Yao, T. Yang, Z. Zhang, Fly ash-based geopolymers: Effect of slag addition on efflorescence, J. Wuhan Univ. Technol. Mater. Sci. Ed. 31 (2016) 689–694. <https://doi.org/10.1007/s11595-016-1430-8>.

[75] I. Ismail, S.A. Bernal, J.L. Provis, R. San Nicolas, S. Hamdan, J.S.J. Van Deventer, Modification of phase evolution in alkali-activated blast furnace slag by the incorporation of fly ash, Cem. Concr. Compos. 45 (2014) 125–135. <https://doi.org/10.1016/j.cemconcomp.2013.09.006>.

[76] L. Srinivasamurthy, V.S. Chevali, Z. Zhang, H. Wang, Phase changes under efflorescence in alkali activated materials with mixed activators, Constr. Build. Mater. 283 (2021) 122678. <https://doi.org/10.1016/j.conbuildmat.2021.122678>.

[77] H.A. Ali, K. Sun, D. Xuan, J.X. Lu, M. Cyr, C.S. Poon, Recycling of high-volume waste glass powder in alkali-activated materials: An efflorescence mitigation strategy, J. Build. Eng. 65 (2023) 105756. <https://doi.org/10.1016/j.jobe.2022.105756>.

[78] X. Lu, Y. Tian, I.M. Jiskani, W. Zhou, B. Zhao, X. Ding, Z. Ao, Innovate geopolymer synthesis for green mine road construction: Analysis of efflorescence behavior and strength analysis, Constr. Build. Mater. 401 (2023) 132963. <https://doi.org/10.1016/j.conbuildmat.2023.132963>.

[79] K. Hyeok-Jung, S.P. Kang, G.C. Choe, Effect of Red Mud Content on Strength and Efflorescence in Pavement using Alkali-Activated Slag Cement, Int. J. Concr. Struct. Mater. 12 (2018). <https://doi.org/10.1186/s40069-018-0258-3>.

[80] M. Zhang, M. He, J. Zhang, Mitigation of efflorescence for multi-componential geopolymer: Influence of steel slag, flue gas desulfurization gypsum and pre-curing periods, J. Clean. Prod. 403 (2023) 136835. <https://doi.org/10.1016/j.jclepro.2023.136835>.

[81] E. Najafi Kani, A. Allahverdi, J.L. Provis, Efflorescence control in geopolymer binders based on natural pozzolan, Cem. Concr. Compos. 34 (2012) 25–33. <https://doi.org/10.1016/j.cemconcomp.2011.07.007>.

[82] M.T. Marvila, A.R. Garcez de Azevedo, J.A. Tostes Linhares Júnior, C.M. Fontes Vieira, Activated alkali cement based on blast furnace slag: effect of curing type and concentration of Na₂O, J. Mater. Res. Technol. 23 (2023) 4551–4565. <https://doi.org/10.1016/j.jmrt.2023.02.088>.

[83] R. Zhang, Y. Zhang, T. Liu, Q. Wan, D. Zheng, Effect of high alumina-based solid waste on efflorescence behavior of alkali-activated steel slag, Constr. Build. Mater. 349 (2022) 128804. <https://doi.org/10.1016/j.conbuildmat.2022.128804>.

[84] J.B. Wang, F.S. Li, Z.H. Zhou, P. Du, D. Xu, N. Xie, X. Cheng, Y. Liu, Effect of zeolite on waste based alkali-activated inorganic binder efflorescence, Constr. Build. Mater. 158 (2018) 683–690. <https://doi.org/10.1016/j.conbuildmat.2017.10.065>.

[85] X. Huang, S. Hu, F. Wang, Y. Liu, Y. Mu, Properties of alkali-activated slag with addition of cation exchange material, Constr. Build. Mater. 146 (2017) 321–328. <https://doi.org/10.1016/j.conbuildmat.2017.03.127>.

[86] J. Wang, T. Zhou, D. Xu, Z. Zhou, P. Du, N. Xie, X. Cheng, Y. Liu, Effect of nano-silica on the efflorescence of waste based alkali-activated inorganic binder, Constr. Build. Mater. 167 (2018) 381–390. <https://doi.org/10.1016/j.conbuildmat.2018.02.006>.

[87] P. Du, T. Zhou, P. Zhao, Z. Zhou, Y. Liu, X. Cheng, Efflorescence inhibition of alkali-activated steel slag-slag material by nano SiO₂, Ceram. - Silikaty. 62 (2018) 285–292. <https://doi.org/10.13168/cs.2018.0023>.

[88] S. Aydin, B. Baradan, Mechanical and microstructural properties of heat cured alkali-activated slag mortars, Mater. Des. 35 (2012) 374–383. <https://doi.org/10.1016/j.matdes.2011.10.005>.

[89] H. El-Hassan, E. Shehab, A. Al-Sallamin, Influence of different curing regimes on the performance and

microstructure of alkali-activated slag concrete, *J. Mater. Civ. Eng.* 30 (2018) 4018230. [https://doi.org/https://doi.org/10.1061/\(ASCE\)MT.1943-5533.0002436](https://doi.org/https://doi.org/10.1061/(ASCE)MT.1943-5533.0002436).

[90] F. Matalkah, A. Ababneh, R. Aqel, Efflorescence Control in Calcined Kaolin-Based Geopolymer Using Silica Fume and OPC, *J. Mater. Civ. Eng.* 33 (2021) 2–9. [https://doi.org/10.1061/\(asce\)mt.1943-5533.0003764](https://doi.org/10.1061/(asce)mt.1943-5533.0003764).

[91] A. Saludung, T. Azeyanagi, Y. Ogawa, K. Kawai, Effect of silica fume on efflorescence formation and alkali leaching of alkali-activated slag, *J. Clean. Prod.* 315 (2021) 128210. <https://doi.org/10.1016/j.jclepro.2021.128210>.

[92] X. Sen Lv, Y. Qin, Z.X. Lin, Z.K. Tian, X.M. Cui, Inhibition of Efflorescence in Na-Based Geopolymer Inorganic Coating, *ACS Omega.* 5 (2020) 14822–14830. <https://doi.org/10.1021/acsomega.0c01919>.

[93] B. Wu, X. Ma, H. Deng, Y. Li, Y. Xiang, Y. Zhu, An efficient approach for mitigation of efflorescence in fly ash-based geopolymer mortars under high-low humidity cycles, *Constr. Build. Mater.* 317 (2022). <https://doi.org/10.1016/j.conbuildmat.2021.126159>.

[94] K. Pasupathy, S. Ramakrishnan, J. Sanjayan, Effect of hydrophobic surface-modified fine aggregates on efflorescence control in geopolymer, *Cem. Concr. Compos.* 126 (2022) 104337. <https://doi.org/10.1016/j.cemconcomp.2021.104337>.

[95] D. Tang, C. Yang, X. Li, X. Zhu, K. Yang, L. Yu, Mitigation of efflorescence of alkali-activated slag mortars by incorporating calcium hydroxide, *Constr. Build. Mater.* 298 (2021) 123873. <https://doi.org/10.1016/j.conbuildmat.2021.123873>.

[96] Y. Zhao, B. Chen, H. Duan, Effect of rice husk ash on properties of slag based geopolymer pastes, *J. Build. Eng.* 76 (2023) 107035. <https://doi.org/10.1016/j.jobe.2023.107035>.

[97] M.J. Abdolhosseini Qomi, F.J. Ulm, R.J.M. Pelléenq, Evidence on the dual nature of aluminum in the calcium-silicate-hydrates based on atomistic simulations, *J. Am. Ceram. Soc.* 95 (2012) 1128–1137. <https://doi.org/10.1111/j.1551-2916.2011.05058.x>.

[98] S. V. Churakov, C. Labbez, Thermodynamics and Molecular Mechanism of Al Incorporation in Calcium Silicate Hydrates, *J. Phys. Chem. C.* 121 (2017) 4412–4419. <https://doi.org/10.1021/acs.jpcc.6b12850>.

[99] J. Yang, D. Hou, Q. Ding, Structure, Dynamics, and Mechanical Properties of Cross-Linked Calcium Aluminosilicate Hydrate: A Molecular Dynamics Study, *ACS Sustain. Chem. Eng.* 6 (2018) 9403–9417. <https://doi.org/10.1021/acssuschemeng.8b01749>.

[100] D. Hou, T. Li, Influence of aluminates on the structure and dynamics of water and ions in the nanometer channel of calcium silicate hydrate (C-S-H) gel, *Phys. Chem. Chem. Phys.* 20 (2018) 2373–2387. <https://doi.org/10.1039/c7cp06985e>.

[101] D. Hou, T. Li, P. Wang, Molecular Dynamics Study on the Structure and Dynamics of NaCl Solution Transport in the Nanometer Channel of CASH Gel, *ACS Sustain. Chem. Eng.* 6 (2018) 9498–9509. <https://doi.org/10.1021/acssuschemeng.8b02126>.

[102] P. Anil, K. Nair, W. Luiz, K. Paine, A review on applications of sol-gel science in cement, *Constr. Build. Mater.* 291 (2021) 123065. <https://doi.org/10.1016/j.conbuildmat.2021.123065>.

[103] M. Ben Haha, B. Lothenbach, G. Le Saout, F. Winnefeld, Influence of slag chemistry on the hydration of alkali-activated blast-furnace slag - Part I: Effect of MgO, *Cem. Concr. Res.* 41 (2011) 955–963. <https://doi.org/10.1016/j.cemconres.2011.05.002>.

[104] M. Ben Haha, G. Le Saout, F. Winnefeld, B. Lothenbach, Influence of activator type on hydration kinetics, hydrate assemblage and microstructural development of alkali activated blast-furnace slags, *Cem. Concr. Res.* 41 (2011) 301–310. <https://doi.org/10.1016/j.cemconres.2010.11.016>.

[105] A. Gruskovnjak, B. Lothenbach, L. Holzer, R. Figi, F. Winnefeld, Hydration of alkali-activated slag: Comparison with ordinary Portland cement, *Adv. Cem. Res.* 18 (2006) 119–128.

[106] E. L'Hôpital, B. Lothenbach, G. Le Saout, D. Kulik, K. Scrivener, Incorporation of aluminium in calcium-silicate-hydrates, *Cem. Concr. Res.* 75 (2015) 91–103. <https://doi.org/10.1016/j.cemconres.2015.04.007>.

[107] Y. Yan, S.Y. Yang, G.D. Miron, I.E. Collings, E. L'Hôpital, J. Skibsted, F. Winnefeld, K. Scrivener, B.

Lothenbach, Effect of alkali hydroxide on calcium silicate hydrate (C-S-H), *Cem. Concr. Res.* 151 (2022). <https://doi.org/10.1016/j.cemconres.2021.106636>.

[108] D. Hou, Molecular Simulation on Cement-Based Materials, n.d.

[109] E. Bonaccorsi, S. Merlino, A.R. Kampf, The crystal structure of tobermorite 14 Å (plumbierite), a C-S-H phase, *J. Am. Ceram. Soc.* 88 (2005) 505–512.

[110] M.J. Abdolhosseini Qomi, K.J. Krakowiak, M. Bauchy, K.L. Stewart, R. Shahsavari, D. Jagannathan, D.B. Brommer, A. Baronnet, M.J. Buehler, S. Yip, F.J. Ulm, K.J. Van Vliet, R.J.M. Pellenq, Combinatorial molecular optimization of cement hydrates, *Nat. Commun.* 5 (2014) 1–10. <https://doi.org/10.1038/ncomms5960>.

[111] Y. Tao, S. Zare, F. Wang, M.J.A. Qomi, Atomistic thermodynamics and kinetics of dicalcium silicate dissolution, *Cem. Concr. Res.* 157 (2022) 106833. <https://doi.org/10.1016/j.cemconres.2022.106833>.

[112] Y. Tao, Y. Gao, Y. Sun, R.J.M. Pellenq, C.S. Poon, C-S-H decalcification in seawater: The view from the nanoscale, *Cem. Concr. Res.* 175 (2024) 107385. <https://doi.org/10.1016/j.cemconres.2023.107385>.

[113] A.J. Allen, J.J. Thomas, H.M. Jennings, Composition and density of nanoscale calcium-silicate-hydrate in cement, *Nat. Mater.* 6 (2007) 311–316. <https://doi.org/10.1038/nmat1871>.

[114] S. Plimpton, P. Crozier, A. Thompson, LAMMPS-large-scale atomic/molecular massively parallel simulator, *Sandia Natl. Lab.* 18 (2007) 43.

[115] D.L. Beveridge, F.M. DiCapua, Free energy via molecular simulation: applications to chemical and biomolecular systems., *Annu. Rev. Biophys. Biophys. Chem.* 18 (1989) 431–492. <https://doi.org/10.1146/annurev.bb.18.060189.002243>.

[116] A. Barducci, M. Bonomi, M. Parrinello, Metadynamics, *Wiley Interdiscip. Rev. Comput. Mol. Sci.* 1 (2011) 826–843. <https://doi.org/10.1002/wcms.31>.

[117] J. Kastner, Umbrella sampling, *Wiley Interdiscip. Rev. Comput. Mol. Sci.* 1 (2011) 932–942. <https://doi.org/10.1002/wcms.66>.

[118] S. Park, K. Schulten, Calculating potentials of mean force from steered molecular dynamics simulations, *J. Chem. Phys.* 120 (2004) 5946–5961. <https://doi.org/10.1063/1.1651473>.

[119] A. Barducci, G. Bussi, M. Parrinello, Well-tempered metadynamics: a smoothly converging and tunable free-energy method, *Phys. Rev. Lett.* 100 (2008) 20603.

[120] A. Laio, M. Parrinello, Escaping free-energy minima, *Proc. Natl. Acad. Sci.* 99 (2002) 12562–12566.

[121] M. Bonomi, D. Branduardi, G. Bussi, C. Camilloni, D. Provasi, P. Raiteri, D. Donadio, F. Marinelli, F. Pietrucci, R.A. Broglia, PLUMED: A portable plugin for free-energy calculations with molecular dynamics, *Comput. Phys. Commun.* 180 (2009) 1961–1972.

[122] Y. Tao, S. Zare, F. Wang, M.J.A. Qomi, Atomistic thermodynamics and kinetics of dicalcium silicate dissolution, *Cem. Concr. Res.* 157 (2022) 106833.

[123] I.N. Stranski, Zur theorie des kristallwachstums, *Zeitschrift Für Phys. Chemie.* 136 (1928) 259–278.

[124] W. Kossel, Extending the law of Bravais, *Nachr. Ges. Wiss. Göttingen.* 143 (1927) 135–143.

[125] R.T. Cygan, J.-J. Liang, A.G. Kalinichev, Molecular models of hydroxide, oxyhydroxide, and clay phases and the development of a general force field, *J. Phys. Chem. B.* 108 (2004) 1255–1266.

[126] C. Liu, X. Liang, Y. Chen, Z. Li, G. Ye, Degradation of alkali-activated slag subject to water immersion, *Cem. Concr. Compos.* 142 (2022). <https://doi.org/10.1016/j.cemconcomp.2023.105157>.

[127] S. Grangeon, F. Claret, Y. Linard, C. Chiaberge, X-ray diffraction: a powerful tool to probe and understand the structure of nanocrystalline calcium silicate hydrates, *Acta Crystallogr. Sect. B Struct. Sci. Cryst. Eng. Mater.* 69 (2013) 465–473.

[128] L. Liu, C. Sun, G. Geng, P. Feng, J. Li, R. Dähn, Influence of decalcification on structural and mechanical properties of synthetic calcium silicate hydrate (C-S-H), *Cem. Concr. Res.* 123 (2019). <https://doi.org/10.1016/j.cemconres.2019.105793>.

[129] Y. Tao, S. Zare, F. Wang, M. Javad, A. Qomi, Atomistic thermodynamics and kinetics of dicalcium silicate dissolution, *Cem. Concr. Res.* 157 (2022) 106833. <https://doi.org/10.1016/j.cemconres.2022.106833>.

[130] G. Henkelman, B.P. Uberuaga, H. Jónsson, Climbing image nudged elastic band method for finding saddle points and minimum energy paths, *J. Chem. Phys.* 113 (2000) 9901–9904. <https://doi.org/10.1063/1.1329672>.

[131] S. Diamond, W.L. Dolch, J.L. White, Studies on tobermorite-like calcium silicate hydrates, *Highw. Res. Rec.* (1964).

[132] R.J. Pellenq, J.M. Caillol, A. Delville, Electrostatic Attraction between Two Charged Surfaces : A (N , V , T) Monte Carlo Simulation, 5647 (1997) 8584–8594.

[133] R. Mills, V.M.M. Lobo, Self-diffusion in electrolyte solutions: a critical examination of data compiled from the literature, Elsevier, 2013.

[134] Z. Li, K.M. Merz, Systematic Evaluation of Ion Diffusion and Water Exchange, *J. Chem. Theory Comput.* (2021). <https://doi.org/10.1021/acs.jctc.1c01189>.

[135] P. Li, K.M. Merz, Metal Ion Modeling Using Classical Mechanics, *Chem. Rev.* 117 (2017) 1564–1686. <https://doi.org/10.1021/acs.chemrev.6b00440>.

[136] G. Sposito, *The chemistry of soils*, Oxford university press, 2008.

[137] P. Atkins, P.W. Atkins, J. de Paula, *Atkins' physical chemistry*, Oxford university press, 2014.

[138] J. Polte, Fundamental growth principles of colloidal metal nanoparticles—a new perspective, *CrystEngComm.* 17 (2015) 6809–6830.

[139] H. Helmholtz, Ueber einige Gesetze der Vertheilung elektrischer Ströme in körperlichen Leitern mit Anwendung auf die thierisch-elektrischen Versuche, *Ann. Phys.* 165 (1853) 211–233. <https://doi.org/https://doi.org/10.1002/andp.18531650603>.

[140] P.W. Atkins, J. De Paula, J. Keeler, *Physical Chemistry*, Oxford university press, 1998.

[141] H.A.M. Snelders, *De geschiedenis van de scheikunde in Nederland. Deel*, (2008).

[142] J.H.M. Visser, Fundamentals of alkali-silica gel formation and swelling: Condensation under influence of dissolved salts, *Cem. Concr. Res.* 105 (2018) 18–30. <https://doi.org/10.1016/j.cemconres.2017.11.006>.

[143] J. Skibsted, J. Hjorth, H.J. Jakobsen, Correlation between ^{29}Si NMR chemical shifts and mean SiO bond lengths for calcium silicates, *Chem. Phys. Lett.* 172 (1990) 279–283. [https://doi.org/10.1016/0009-2614\(90\)85403-Y](https://doi.org/10.1016/0009-2614(90)85403-Y).

[144] S. Nie, R.M. Thomsen, J. Skibsted, Impact of Mg substitution on the structure and pozzolanic reactivity of calcium aluminosilicate (CaO-Al₂O₃-SiO₂) glasses, *Cem. Concr. Res.* 138 (2020) 106231. <https://doi.org/10.1016/j.cemconres.2020.106231>.

[145] S.Y. Yang, Y. Yan, B. Lothenbach, J. Skibsted, Incorporation of Sodium and Aluminum in Cementitious Calcium-Alumino-Silicate-Hydrate C-(A)-S-H Phases Studied by ^{23}Na , ^{27}Al , and ^{29}Si MAS NMR Spectroscopy, *J. Phys. Chem. C.* 125 (2021) 27975–27995. <https://doi.org/10.1021/acs.jpcc.1c08419>.

[146] E. Kapeluszna, Ł. Kotwica, A. Różycka, Ł. Gołek, Incorporation of Al in C-A-S-H gels with various Ca/Si and Al/Si ratio: Microstructural and structural characteristics with DTA/TG, XRD, FTIR and TEM analysis, *Constr. Build. Mater.* 155 (2017) 643–653. <https://doi.org/10.1016/j.conbuildmat.2017.08.091>.

[147] N. V Chukanov, IR spectra of minerals and reference samples data, in: *Infrared Spectra Miner. Species*, Springer, 2014: pp. 21–1701.

[148] A. Vidmer, G. Sclauzero, A. Pasquarello, Infrared spectra of jennite and tobermorite from first-principles, *Cem. Concr. Res.* 60 (2014) 11–23. <https://doi.org/10.1016/j.cemconres.2014.03.004>.

[149] M. Król, P. Rożek, D. Chlebda, W. Mozgawa, Influence of alkali metal cations/type of activator on the structure of alkali-activated fly ash – ATR-FTIR studies, *Spectrochim. Acta - Part A Mol. Biomol. Spectrosc.* 198 (2018) 33–37. <https://doi.org/10.1016/j.saa.2018.02.067>.

[150] P. Yu, R.J. Kirkpatrick, B. Poe, P.F. McMillan, X. Cong, Structure of calcium silicate hydrate (C-S-H): Near-

, Mid-, and Far-infrared spectroscopy, *J. Am. Ceram. Soc.* 82 (1999) 742–748.

[151] Z. Zhang, H. Wang, J.L. Provis, F. Bullen, A. Reid, Y. Zhu, Quantitative kinetic and structural analysis of geopolymers. Part 1. the activation of metakaolin with sodium hydroxide, *Thermochim. Acta.* 539 (2012) 23–33. <https://doi.org/10.1016/j.tca.2012.03.021>.

[152] A. Kunhi Mohamed, P. Moutzouri, P. Berruyer, B.J. Walder, J. Siramanont, J. Siramanont, M. Harris, M. Negroni, S.C. Galmarini, S.C. Parker, S.C. Parker, K.L. Scrivener, L. Emsley, P. Bowen, The Atomic-Level Structure of Cementitious Calcium Aluminate Silicate Hydrate, *J. Am. Chem. Soc.* 142 (2020) 11060–11071. <https://doi.org/10.1021/jacs.0c02988>.

[153] M. Sakiyama, Synthesis and Crystal Chemistry of Al - Substituted 11 A Tobermorite MAESHIMA and Takeshi MITSUDA, 419 (2000) 413–419.

[154] T. Maeshima, H. Noma, M. Sakiyama, T. Mitsuda, Natural 1.1 and 1.4 nm tobermorites from Fuka, Okayama, Japan: Chemical analysis, cell dimensions, ²⁹Si NMR and thermal behavior, *Cem. Concr. Res.* 33 (2003) 1515–1523. [https://doi.org/10.1016/S0008-8846\(03\)00099-1](https://doi.org/10.1016/S0008-8846(03)00099-1).

[155] G.K. Sun, J.F. Young, R.J. Kirkpatrick, The role of Al in C-S-H: NMR, XRD, and compositional results for precipitated samples, *Cem. Concr. Res.* 36 (2006) 18–29. <https://doi.org/10.1016/j.cemconres.2005.03.002>.

[156] T.F. Sevelsted, J. Skibsted, Carbonation of C-S-H and C-A-S-H samples studied by ¹³C, ²⁷Al and ²⁹Si MAS NMR spectroscopy, *Cem. Concr. Res.* 71 (2015) 56–65. <https://doi.org/10.1016/j.cemconres.2015.01.019>.

[157] J.J. Chen, J.J. Thomas, H.F.W. Taylor, H.M. Jennings, Solubility and structure of calcium silicate hydrate, *Cem. Concr. Res.* 34 (2004) 1499–1519. <https://doi.org/10.1016/j.cemconres.2004.04.034>.

[158] F. Puertas, M. Palacios, H. Manzano, J.S. Dolado, A. Rico, J. Rodríguez, A model for the C-A-S-H gel formed in alkali-activated slag cements, *J. Eur. Ceram. Soc.* 31 (2011) 2043–2056. <https://doi.org/10.1016/j.jeurceramsoc.2011.04.036>.

[159] Y. Zhang, L. Guo, J. Shi, Q. Luo, J. Jiang, D. Hou, Full process of calcium silicate hydrate decalcification: Molecular structure, dynamics, and mechanical properties, *Cem. Concr. Res.* 161 (2022) 106964. <https://doi.org/10.1016/j.cemconres.2022.106964>.

[160] R.S. Barneyback Jr, S. Diamond, Expression and analysis of pore fluids from hardened cement pastes and mortars, *Cem. Concr. Res.* 11 (1981) 279–285.

[161] V. Kocabă, E. Gallucci, K.L. Scrivener, Methods for determination of degree of reaction of slag in blended cement pastes, *Cem. Concr. Res.* 42 (2012) 511–525. <https://doi.org/10.1016/j.cemconres.2011.11.010>.

[162] E. Demoulian, C. Vernet, F. Hawthorn, P. Gourdin, Slag content determination in cements by selective dissolution, in: Proc. 7th Int. Congr. Chem. Cem. Paris, Fr., 1980: pp. 151–156.

[163] J.S. Lumley, R.S. Gollop, G.K. Moir, H.F.W. Taylor, Degrees of reaction of the slag in some blends with Portland cements, *Cem. Concr. Res.* 26 (1996) 139–151.

[164] J.I. Escalante, L.Y. Gomez, K.K. Johal, G. Mendoza, H. Mancha, J. Mendez, Reactivity of blast-furnace slag in Portland cement blends hydrated under different conditions, *Cem. Concr. Res.* 31 (2001) 1403–1409.

[165] P.E. Stutzman, Guide for X-ray powder diffraction analysis of Portland cement and clinker, US Department of Commerce, Technology Administration, National Institute of ..., 1996.

[166] R. Snellings, J. Chwast, Ö. Cizer, N. De Belie, Y. Dhandapani, P. Durdzinski, J. Elsen, J. Haufe, D. Hooton, C. Patapy, M. Santhanam, K. Scrivener, D. Snoeck, L. Steger, S. Tongbo, A. Vollpracht, F. Winnefeld, B. Lothenbach, Report of TC 238-SCM: hydration stoppage methods for phase assemblage studies of blended cements—results of a round robin test, *Mater. Struct.* 51 (2018) 111. <https://doi.org/10.1617/s11527-018-1237-5>.

[167] B.S.I. NEN-EN, 196-1. Methods of Testing Cement—Part 1: Determination of Strength, BSI London, UK. (2016).

[168] C. Shi, R.L. Day, A calorimetric study of early hydration of alkali-slag cements, *Cem. Concr. Res.* 25 (1995) 1333–1346.

[169] Z. Huanhai, W. Xuequan, X. Zhongzi, T. Mingshu, Kinetic study on hydration of alkali-activated slag, *Cem. Concr. Res.* 23 (1993) 1253–1258. [https://doi.org/10.1016/0008-8846\(93\)90062-E](https://doi.org/10.1016/0008-8846(93)90062-E).

[170] B.S. Gebregiabiher, R. Thomas, S. Peethamparaman, Very early-age reaction kinetics and microstructural development in alkali-activated slag, *Cem. Concr. Compos.* 55 (2015) 91–102. <https://doi.org/10.1016/j.cemconcomp.2014.09.001>.

[171] K.C. Newlands, M. Foss, T. Matchei, J. Skibsted, D.E. Macphee, Early stage dissolution characteristics of aluminosilicate glasses with blast furnace slag-and fly-ash-like compositions, *J. Am. Ceram. Soc.* 100 (2017) 1941–1955.

[172] P. Raiteri, R. Demichelis, J.D. Gale, Thermodynamically Consistent Force Field for Molecular Dynamics Simulations of Alkaline-Earth Carbonates and Their Aqueous Speciation, *J. Phys. Chem. C.* 119 (2015) 24447–24458. <https://doi.org/10.1021/acs.jpcc.5b07532>.

[173] C. Liu, Y. Liu, Z. Liu, C. Hu, X. Huang, L. Yang, F. Wang, Heat-cured concrete: Improving the early strength and pore structure by activating aluminosilicate internal curing agent with triisopropanolamine, *J. Am. Ceram. Soc.* 102 (2019) 6227–6238.

[174] D.M. Kern, The hydration of carbon dioxide, *J. Chem. Educ.* 37 (1960) 14.

[175] W. Stumm, J.J. Morgan, *Aquatic chemistry: chemical equilibria and rates in natural waters*, John Wiley & Sons, 2012.

[176] C. Liu, L. Yang, Z. Li, S. Nie, C. Hu, F. Wang, Improve the long-term property of heat-cured mortars blended with fly ash by internal curing, *J. Build. Eng.* 54 (2022) 104624. <https://doi.org/10.1016/j.jobe.2022.104624>.

[177] B. Lagerblad, Carbon dioxide uptake during concrete life cycle: State of the art, Swedish Cement and Concrete Research Institute Stockholm, 2005.

[178] S. von Greve-Dierfeld, B. Lothenbach, A. Vollpracht, B. Wu, B. Huet, C. Andrade, C. Medina, C. Thiel, E. Gruyaert, H. Vanoutrive, I.F. Saéz del Bosque, I. Ignjatovic, J. Elsen, J.L. Provis, K. Scrivener, K.C. Thienel, K. Sideris, M. Zajac, N. Alderete, Ö. Cizer, P. Van den Heede, R.D. Hooton, S. Kamali-Bernard, S.A. Bernal, Z. Zhao, Z. Shi, N. De Belie, Understanding the carbonation of concrete with supplementary cementitious materials: a critical review by RILEM TC 281-CCC, 2020. <https://doi.org/10.1617/s11527-020-01558-w>.

[179] M. Nedeljković, Carbonation mechanism of alkali-activated fly ash and slag materials In view of long-term performance predictions, 2019. <https://doi.org/10.4233/uuid>.

[180] X. Ke, S.A. Bernal, J.L. Provis, B. Lothenbach, Thermodynamic modelling of phase evolution in alkali-activated slag cements exposed to carbon dioxide, *Cem. Concr. Res.* 136 (2020) 106158. <https://doi.org/10.1016/j.cemconres.2020.106158>.

[181] E. Kanezaki, Thermal behavior of the hydrotalcite-like layered structure of Mg and Al-layered double hydroxides with interlayer carbonate by means of in situ powder HTXRD and DTA/TG, *Solid State Ionics.* 106 (1998) 279–284.

[182] K. Rozov, U. Berner, C. Taviot-Gueho, F. Leroux, G. Renaudin, D. Kulik, L.W. Diamond, Synthesis and characterization of the LDH hydrotalcite–pyroaurite solid-solution series, *Cem. Concr. Res.* 40 (2010) 1248–1254.

[183] G. Villain, M. Thiery, G. Platret, Measurement methods of carbonation profiles in concrete: Thermogravimetry, chemical analysis and gammadensimetry, *Cem. Concr. Res.* 37 (2007) 1182–1192. <https://doi.org/10.1016/j.cemconres.2007.04.015>.

[184] J.I. Escalante-García, A.F. Fuentes, A. Gorokhovsky, P.E. Fraire-Luna, G. Mendoza-Suarez, Hydration products and reactivity of blast-furnace slag activated by various alkalis, *J. Am. Ceram. Soc.* 86 (2003) 2148–2153.

[185] R. Chambers, B.W. Zweifach, Intercellular cement and capillary permeability, *Physiol. Rev.* 27 (1947) 436–463.

[186] W.K.W. Lee, J.S.J. Van Deventer, Use of infrared spectroscopy to study geopolymers of heterogeneous amorphous aluminosilicates, *Langmuir.* 19 (2003) 8726–8734.

[187] C.A. Rees, J.L. Provis, G.C. Lukey, J.S.J. Van Deventer, The mechanism of geopolymer gel formation investigated through seeded nucleation, *Colloids Surfaces A Physicochem. Eng. Asp.* 318 (2008) 97–105.

[188] Y. Yan, B. Ma, G.D. Miron, D.A. Kulik, K. Scrivener, B. Lothenbach, tetrahedron Dreierketten chain Basal spacing Interlayer, 162 (2022). <https://doi.org/10.1016/j.cemconres.2022.106957>.

[189] E. Bernard, Y. Yan, B. Lothenbach, Effective cation exchange capacity of calcium silicate hydrates (C-S-H), *Cem. Concr. Res.* 143 (2021) 106393. <https://doi.org/10.1016/j.cemconres.2021.106393>.

[190] O. Burciaga-Díaz, J.I. Escalante-García, Structure, mechanisms of reaction, and strength of an alkali-activated blast-furnace slag, *J. Am. Ceram. Soc.* 96 (2013) 3939–3948. <https://doi.org/10.1111/jace.12620>.

[191] M. Palacios, F. Puertas, Effect of carbonation on alkali-activated slag paste, *J. Am. Ceram. Soc.* 89 (2006) 3211–3221.

[192] B. Walkley, R. San Nicolas, M.A. Sani, G.J. Rees, J. V. Hanna, J.S.J. van Deventer, J.L. Provis, Phase evolution of C-(N)-A-S-H/N-A-S-H gel blends investigated via alkali-activation of synthetic calcium aluminosilicate precursors, *Cem. Concr. Res.* 89 (2016) 120–135. <https://doi.org/10.1016/j.cemconres.2016.08.010>.

[193] H.F.W. Taylor, *Cement chemistry*, Thomas Telford London, 1997.

[194] M. Ben Haha, B. Lothenbach, G. Le Saout, F. Winnefeld, Influence of slag chemistry on the hydration of alkali-activated blast-furnace slag - Part II: Effect of Al₂O₃, *Cem. Concr. Res.* 42 (2012) 74–83. <https://doi.org/10.1016/j.cemconres.2011.08.005>.

[195] I.G. Richardson, Tobermorite/jennite-and tobermorite/calcium hydroxide-based models for the structure of CSH: applicability to hardened pastes of tricalcium silicate, β -dicalcium silicate, Portland cement, and blends of Portland cement with blast-furnace slag, metakaolin, *Cem. Concr. Res.* 34 (2004) 1733–1777.

[196] S.-D. Wang, K.L. Scrivener, ²⁹Si and ²⁷Al NMR study of alkali-activated slag, *Cem. Concr. Res.* 33 (2003) 769–774.

[197] A.C.A. Muller, Characterization of porosity & CSH in cement pastes by ¹H NMR, EPFL, 2014.

[198] Z. Li, T. Lu, Y. Chen, B. Wu, G. Ye, Prediction of the autogenous shrinkage and microcracking of alkali-activated slag and fly ash concrete, *Cem. Concr. Compos.* 117 (2021) 103913. <https://doi.org/10.1016/j.cemconcomp.2020.103913>.

[199] H. Ye, C. Cartwright, F. Rajabipour, A. Radlińska, Understanding the drying shrinkage performance of alkali-activated slag mortars, *Cem. Concr. Compos.* 76 (2017) 13–24.

[200] Z. Li, T. Lu, X. Liang, H. Dong, G. Ye, Mechanisms of autogenous shrinkage of alkali-activated slag and fly ash pastes, *Cem. Concr. Res.* 135 (2020) 106107. <https://doi.org/10.1016/j.cemconres.2020.106107>.

[201] Z. Li, M. Wyrzykowski, H. Dong, J. Granja, M. Azenha, P. Lura, Internal curing by superabsorbent polymers in alkali-activated slag, *Cem. Concr. Res.* 135 (2020) 106123. <https://doi.org/10.1016/j.cemconres.2020.106123>.

[202] J. Osio-Norgaard, J.P. Gevau dan, W. V. Srubar, A review of chloride transport in alkali-activated cement paste, mortar, and concrete, *Constr. Build. Mater.* 186 (2018) 191–206. <https://doi.org/10.1016/j.conbuildmat.2018.07.119>.

[203] X. Hu, C. Shi, Z. Shi, L. Zhang, Compressive strength, pore structure and chloride transport properties of alkali-activated slag/fly ash mortars, *Cem. Concr. Compos.* 104 (2019) 103392. <https://doi.org/10.1016/j.cemconcomp.2019.103392>.

[204] R.J. Thomas, E. Ariyachandra, D. Lezama, S. Peethamparan, Comparison of chloride permeability methods for Alkali-Activated concrete, *Constr. Build. Mater.* 165 (2018) 104–111. <https://doi.org/10.1016/j.conbuildmat.2018.01.016>.

[205] J. Zhang, C. Shi, Z. Zhang, Chloride binding of alkali-activated slag/fly ash cements, *Constr. Build. Mater.* 226 (2019) 21–31. <https://doi.org/10.1016/j.conbuildmat.2019.07.281>.

[206] J. Zhang, C. Shi, Z. Zhang, X. Hu, Reaction mechanism of sulfate attack on alkali-activated slag/fly ash cements, *Constr. Build. Mater.* 318 (2022) 126052. <https://doi.org/10.1016/j.conbuildmat.2021.126052>.

[207] I. Ismail, S.A. Bernal, J.L. Provis, S. Hamdan, J.S.J. Van Deventer, Microstructural changes in alkali activated fly ash/slag geopolymers with sulfate exposure, *Mater. Struct.* 46 (2013) 361–373. <https://doi.org/10.1617/s11527-012-9906-2>.

[208] H. Ye, Z. Chen, L. Huang, Mechanism of sulfate attack on alkali-activated slag: The role of activator composition, *Cem. Concr. Res.* 125 (2019) 105868. <https://doi.org/10.1016/j.cemconres.2019.105868>.

[209] A. Koenig, A. Herrmann, S. Overmann, F. Dehn, Resistance of alkali-activated binders to organic acid attack: Assessment of evaluation criteria and damage mechanisms, *Constr. Build. Mater.* 151 (2017) 405–413. <https://doi.org/10.1016/j.conbuildmat.2017.06.117>.

[210] W. Zhang, X. Yao, T. Yang, Z. Zhang, The degradation mechanisms of alkali-activated fly ash/slag blend cements exposed to sulphuric acid, *Constr. Build. Mater.* 186 (2018) 1177–1187. <https://doi.org/10.1016/j.conbuildmat.2018.08.050>.

[211] T.A. Aiken, L. Gu, J. Kwasny, G.F. Huseien, D. McPolin, W. Sha, Acid resistance of alkali-activated binders: A review of performance, mechanisms of deterioration and testing procedures, *Constr. Build. Mater.* 342 (2022) 128057. <https://doi.org/10.1016/j.conbuildmat.2022.128057>.

[212] S. Preibisch, S. Saalfeld, P. Tomancak, Globally optimal stitching of tiled 3D microscopic image acquisitions, *Bioinformatics* 25 (2009) 1463–1465. <https://doi.org/10.1093/bioinformatics/btp184>.

[213] Y. Zuo, G. Ye, GeoMicro3D: A novel numerical model for simulating the reaction process and microstructure formation of alkali-activated slag, *Cem. Concr. Res.* 141 (2021) 106328. <https://doi.org/10.1016/j.cemconres.2020.106328>.

[214] R.J. Myers, S.A. Bernal, J.L. Provis, A thermodynamic model for C-(N)-A-S-H gel: CNASH-ss. Derivation and validation, *Cem. Concr. Res.* 66 (2014) 27–47. <https://doi.org/10.1016/j.cemconres.2014.07.005>.

[215] R.J. Myers, B. Lothenbach, S.A. Bernal, J.L. Provis, Thermodynamic modelling of alkali-activated slag cements, *Appl. Geochemistry* 61 (2015) 233–247. <https://doi.org/10.1016/j.apgeochem.2015.06.006>.

[216] J.J. Thomas, H.M. Jennings, A.J. Allen, Relationships between composition and density of tobermorite, jennite, and nanoscale CaO-SiO₂-H₂O, *J. Phys. Chem. C* 114 (2010) 7594–7601. <https://doi.org/10.1021/jp910733x>.

[217] Z. Xu, G. Ye, Understanding Chloride Diffusion Coefficient in Cementitious Materials, *Materials* (Basel). 16 (2023). <https://doi.org/10.3390/ma16093464>.

[218] P.F. Worthington, The uses and abuses of the Archie equations, 1: The formation factor-porosity relationship, *J. Appl. Geophys.* 30 (1993) 215–228.

[219] B. Lothenbach, D.A. Kulik, T. Matschei, M. Balonis, L. Baquerizo, B. Dilnesa, G.D. Miron, R.J. Myers, Cemdata18: A chemical thermodynamic database for hydrated Portland cements and alkali-activated materials, *Cem. Concr. Res.* 115 (2019) 472–506. <https://doi.org/10.1016/j.cemconres.2018.04.018>.

[220] T. Wagner, D.A. Kulik, F.F. Hingerl, S. V Dmytrieva, GEM-Selektor geochemical modeling package: TSolMod library and data interface for multicomponent phase models, *Can. Mineral.* 50 (2012) 1173–1195.

[221] D.A. Kulik, T. Wagner, S. V. Dmytrieva, G. Kosakowski, F.F. Hingerl, K. V. Chudnenko, U.R. Berner, GEM-Selektor geochemical modeling package: Revised algorithm and GEMS3K numerical kernel for coupled simulation codes, *Comput. Geosci.* 17 (2013) 1–24. <https://doi.org/10.1007/s10596-012-9310-6>.

[222] Y. Zhang, S. Zhang, C. Liu, O. Çopuroğlu, Characterizing two types of zonation within slag rims of aged alkali-activated slag pastes through SEM and TEM, *Cem. Concr. Res.* 176 (2024) 107409. <https://doi.org/10.1016/j.cemconres.2023.107409>.

[223] W. Gardner, Note on the dynamics of capillary flow, *Phys. Rev.* 18 (1921) 206–209. <https://doi.org/10.1103/PhysRev.18.206>.

[224] L.A. Richards, Capillary conduction of liquids through porous mediums, *J. Appl. Phys.* 1 (1931) 318–333. <https://doi.org/10.1063/1.1745010>.

[225] M.W. Farthing, F.L. Ogden, Numerical Solution of Richards' Equation: A Review of Advances and Challenges, *Soil Sci. Soc. Am. J.* 81 (2017) 1257–1269. <https://doi.org/10.2136/sssaj2017.02.0058>.

[226] A. Caggiano, D. Said Schicchi, C. Mankel, N. Ukrainczyk, E.A.B. Koenders, A mesoscale approach for modeling capillary water absorption and transport phenomena in cementitious materials, *Comput. Struct.* 200 (2018) 1–10. <https://doi.org/10.1016/j.comstruc.2018.01.013>.

[227] B. Zheng, T. Li, H. Qi, L. Gao, X. Liu, L. Yuan, 3D meso-scale simulation of chloride ion transportation in cracked concrete considering aggregate morphology, *Constr. Build. Mater.* 326 (2022) 126632. <https://doi.org/10.1016/j.conbuildmat.2022.126632>.

[228] Y. Li, X. Chen, L. Jin, R. Zhang, Experimental and numerical study on chloride transmission in cracked concrete, *Constr. Build. Mater.* 127 (2016) 425–435. <https://doi.org/10.1016/j.conbuildmat.2016.10.044>.

[229] W. Chen, B. Li, J. Wang, N. Thom, Effects of alkali dosage and silicate modulus on autogenous shrinkage of alkali-activated slag cement paste, *Cem. Concr. Res.* 141 (2021). <https://doi.org/10.1016/j.cemconres.2020.106322>.

[230] Z. Li, Y. Chen, J.L. Provis, G. Ye, Autogenous shrinkage of alkali-activated slag : A critical review, 172 (2023). <https://doi.org/10.1016/j.cemconres.2023.107244>.

[231] D. Coefficent, Simple Model for Alkali Leaching from Geopolymers : Effects of Raw Materials and Acetic Acid Concentration on Apparent, Materials (Basel). (2021).

[232] Z. Jia, C. Chen, H. Zhou, Y. Zhang, The characteristics and formation mechanism of the dark rim in alkali-activated slag, *Cem. Concr. Compos.* 112 (2020) 103682. <https://doi.org/10.1016/j.cemconcomp.2020.103682>.

[233] I.G. Richardson, G.W. Groves, Microstructure and microanalysis of hardened cement pastes involving ground granulated blast-furnace slag, *J. Mater. Sci.* 27 (1992) 6204–6212. <https://doi.org/10.1007/BF01133772>.

[234] J. Li, W. Zhang, P.J.M. Monteiro, Structure and Intrinsic Mechanical Properties of Nanocrystalline Calcium Silicate Hydrate, *ACS Sustain. Chem. Eng.* 8 (2020) 12453–12461. <https://doi.org/10.1021/acssuschemeng.0c03230>.

[235] F. Spectroscopy, Structure of Calcium Silicate Hydrate (C-S-H): Near-, Mid-, and Far-Infrared Spectroscopy, 48 (1999) 742–748.

[236] T.C. Powers, L.E. Copeland, H.M. Mann, Capillary continuity or discontinuity in cement pastes, 1959.

[237] L. Cui, J.H. Cahyadi, Permeability and pore structure of OPC paste, *Cem. Concr. Res.* 31 (2001) 277–282. [https://doi.org/10.1016/S0008-8846\(00\)00474-9](https://doi.org/10.1016/S0008-8846(00)00474-9).

[238] J.M. Whitney, M. Knight, The relationship between tensile strength and flexure strength in fiber-reinforced composites: Flexure-and tensile-coupon data on unidirectional graphite-epoxy composites are compared to a weibull two-parameter statistical-strength model, *Exp. Mech.* 20 (1980) 211–216.

[239] M.R. Wisnom, The relationship between tensile and flexural strength of unidirectional composites, *J. Compos. Mater.* 26 (1992) 1173–1180.

[240] N. Fischer, R. Haerdtl, P.J. McDonald, Observation of the redistribution of nanoscale water filled porosity in cement based materials during wetting, *Cem. Concr. Res.* 68 (2015) 148–155. <https://doi.org/10.1016/j.cemconres.2014.10.013>.

[241] C. Liu, W. Haoming, L. Zhenming, S. Hu, Y. Guang, Effect of curing condition on mechanical properties and durability of alkali-activated slag mortar, *Constr. Build. Mater.* 439 (2024) 137376. <https://doi.org/10.1016/j.conbuildmat.2024.137376>.

[242] European committee for standardization. NEN-EN 196-1. Methods of testing cement - Part 1: Determination of strength. 2016., (n.d.).

[243] M. Chaouche, X.X. Gao, M. Cyr, M. Cotte, L. Frouin, On the origin of the blue/green color of blast-furnace slag-based materials: Sulfur K-edge XANES investigation, *J. Am. Ceram. Soc.* 100 (2017) 1707–1716. <https://doi.org/10.1111/jace.14670>.

[244] H. Ye, A. Radlińska, Shrinkage mechanisms of alkali-activated slag, *Cem. Concr. Res.* 88 (2016) 126–135. <https://doi.org/10.1016/j.cemconres.2016.07.001>.

[245] C. Duran Atış, C. Bilim, Ö. Çelik, O. Karahan, Influence of activator on the strength and drying shrinkage of alkali-activated slag mortar, *Constr. Build. Mater.* 23 (2009) 548–555. <https://doi.org/10.1016/j.conbuildmat.2007.10.011>.

[246] K. Sun, X. Peng, S. Wang, L. Zeng, P. Ran, G. Ji, Effect of nano-SiO₂ on the efflorescence of an alkali-activated metakaolin mortar, *Constr. Build. Mater.* 253 (2020) 118952. <https://doi.org/10.1016/j.conbuildmat.2020.118952>.

[247] H. Haynes, R. O'Neill, M. Neff, P. Kumar Mehta, Salt weathering of concrete by sodium carbonate and sodium chloride, *ACI Mater. J.* 107 (2010) 258–266. <https://doi.org/10.14359/51663754>.

[248] S.D. Wang, X.C. Pu, K.L. Scrivener, P.L. Pratt, Alkali-activated slag cement and concrete: A review of properties and problems, *Adv. Cem. Res.* 7 (1995) 93–102. <https://doi.org/10.1680/adcr.1995.7.27.93>.

[249] T. Bakharev, J.G. Sanjayan, Y.B. Cheng, Resistance of alkali-activated slag concrete to carbonation, *Cem. Concr. Res.* 31 (2001) 1277–1283. [https://doi.org/10.1016/S0008-8846\(01\)00574-9](https://doi.org/10.1016/S0008-8846(01)00574-9).

[250] F. Puertas, M. Palacios, T. Vázquez, Carbonation process of alkali-activated slag mortars, *J. Mater. Sci.* 41 (2006) 3071–3082. <https://doi.org/10.1007/s10853-005-1821-2>.

[251] S.A. Bernal, R. San Nicolas, R.J. Myers, R. Mejía De Gutiérrez, F. Puertas, J.S.J. Van Deventer, J.L. Provis, MgO content of slag controls phase evolution and structural changes induced by accelerated carbonation in alkali-activated binders, *Cem. Concr. Res.* 57 (2014) 33–43. <https://doi.org/10.1016/j.cemconres.2013.12.003>.

[252] E. Bernard, W.J. Zucha, B. Lothenbach, U. Mäder, Stability of hydrotalcite (Mg-Al layered double hydroxide) in presence of different anions, *Cem. Concr. Res.* 152 (2022). <https://doi.org/10.1016/j.cemconres.2021.106674>.

[253] N. Li, N. Farzadnia, C. Shi, Microstructural changes in alkali-activated slag mortars induced by accelerated carbonation, *Cem. Concr. Res.* 100 (2017) 214–226. <https://doi.org/10.1016/j.cemconres.2017.07.008>.

[254] Z. Shi, C. Shi, S. Wan, N. Li, Z. Zhang, Effect of alkali dosage and silicate modulus on carbonation of alkali-activated slag mortars, *Cem. Concr. Res.* 113 (2018) 55–64. <https://doi.org/10.1016/j.cemconres.2018.07.005>.

[255] L. Alarcon-Ruiz, G. Platret, E. Massieu, A. Ehrlacher, The use of thermal analysis in assessing the effect of temperature on a cement paste, *Cem. Concr. Res.* 35 (2005) 609–613. <https://doi.org/10.1016/j.cemconres.2004.06.015>.

[256] H. Ye, R. Cai, Z. Tian, Natural carbonation-induced phase and molecular evolution of alkali-activated slag: Effect of activator composition and curing temperature, *Constr. Build. Mater.* 248 (2020) 118726. <https://doi.org/10.1016/j.conbuildmat.2020.118726>.

[257] J.D. Rodriguez-Blanco, S. Shaw, L.G. Benning, The kinetics and mechanisms of amorphous calcium carbonate (ACC) crystallization to calcite, via vaterite., *Nanoscale.* 3 (2011) 265–271. <https://doi.org/10.1039/c0nr00589d>.

[258] J.J. Chen, J.J. Thomas, H.M. Jennings, Decalcification shrinkage of cement paste, *Cem. Concr. Res.* 36 (2006) 801–809. <https://doi.org/10.1016/j.cemconres.2005.11.003>.

[259] K. Adamczyk, M. Prémont-Schwarz, D. Pines, E. Pines, E.T.J. Nibbering, Real-time observation of carbonic acid formation in aqueous solution, *Science* (80-). 326 (2009) 1690–1694.

[260] S.A. Bernal, J.L. Provis, D.G. Brice, A. Kilcullen, P. Duxson, J.S.J. Van Deventer, Accelerated carbonation testing of alkali-activated binders significantly underestimates service life: The role of pore solution chemistry, *Cem. Concr. Res.* 42 (2012) 1317–1326. <https://doi.org/10.1016/j.cemconres.2012.07.002>.

[261] S. Hasdemir, A. Tuğrul, M. Yılmaz, The effect of natural sand composition on concrete strength, *Constr. Build. Mater.* 112 (2016) 940–948.

[262] Y. Zhao, X. Hu, C. Shi, Z. Zhang, D. Zhu, A review on seawater sea-sand concrete: Mixture proportion, hydration, microstructure and properties, *Constr. Build. Mater.* 295 (2021) 123602.

[https://doi.org/10.1016/j.conbuildmat.2021.123602.](https://doi.org/10.1016/j.conbuildmat.2021.123602)

[263] M. Selva Ganesh, P. Jagadeesh, Assessment of usage of manufactured sand and recycled aggregate as sustainable concrete: A review, *Mater. Today Proc.* 64 (2022) 1029–1034. <https://doi.org/10.1016/j.matpr.2022.05.094>.

[264] A. Bentur, S.I. Igarashi, K. Kovler, Prevention of autogenous shrinkage in high-strength concrete by internal curing using wet lightweight aggregates, *Cem. Concr. Res.* 31 (2001) 1587–1591. [https://doi.org/10.1016/S0008-8846\(01\)00608-1](https://doi.org/10.1016/S0008-8846(01)00608-1).

[265] D. Cusson, T. Hoogeveen, Internal curing of high-performance concrete with pre-soaked fine lightweight aggregate for prevention of autogenous shrinkage cracking, *Cem. Concr. Res.* 38 (2008) 757–765. <https://doi.org/10.1016/j.cemconres.2008.02.001>.

[266] Minhong zhang; Odd E. Ojørv, Pozzolanic reactivity of lightweight aggregates, *Cem. Concr. Res.* 20 (1990) 884–890.

[267] L. Kong, L. Hou, Y. Du, Chemical reactivity of lightweight aggregate in cement paste, *Constr. Build. Mater.* 64 (2014) 22–27. <https://doi.org/10.1016/j.conbuildmat.2014.04.024>.

[268] S. Nie, S. Hu, F. Wang, C. Hu, X. Li, Y. Zhu, Pozzolanic reaction of lightweight fine aggregate and its influence on the hydration of cement, *Constr. Build. Mater.* 153 (2017) 165–173.

[269] C. Liu, L. Yang, F. Wang, S. Hu, Enhance the durability of heat-cured mortars by internal curing and pozzolanic activity of lightweight fine aggregates, *Constr. Build. Mater.* 270 (2021) 121439. <https://doi.org/10.1016/j.conbuildmat.2020.121439>.

[270] C. Liu, Y. Liu, Z. Liu, C. Hu, X. Huang, L. Yang, F. Wang, Heat-cured concrete: Improving the early strength and pore structure by activating aluminosilicate internal curing agent with triisopropanolamine, *J. Am. Ceram. Soc.* 102 (2019) 6227–6238. <https://doi.org/10.1111/jace.16458>.

[271] ASTM C1585-13, Standard Test Method for Measurement of Rate of Absorption of Water by Hydraulic Cement Concretes, *ASTM Int.* 41 (2013) 1–6.

[272] C. Thomas, V. Loodts, L. Rongy, A. De Wit, Convective dissolution of CO₂ in reactive alkaline solutions: Active role of spectator ions, *Int. J. Greenh. Gas Control.* 53 (2016) 230–242. <https://doi.org/10.1016/j.ijggc.2016.07.034>.

[273] R. Snellings, J. Chwast, Ö. Cizer, N. De Belie, Y. Dhandapani, P. Durdzinski, J. Elsen, J. Haufe, D. Hooton, C. Patapy, M. Santhanam, K. Scrivener, D. Snoeck, L. Steger, S. Tongbo, A. Vollpracht, F. Winnefeld, B. Lothenbach, RILEM TC-238 SCM recommendation on hydration stoppage by solvent exchange for the study of hydrate assemblages, *Mater. Struct. Constr.* 51 (2018). <https://doi.org/10.1617/s11527-018-1298-5>.

[274] N. Meftah, M.S. Mahboub, Spectroscopic Characterizations of Sand Dunes Minerals of El-Oued (Northeast Algerian Sahara) by FTIR, XRF and XRD Analyses, *Silicon.* 12 (2020) 147–153. <https://doi.org/10.1007/s12633-019-00109-5>.

[275] Y. Chen, Y. Mao, L. Yang, W. Wei, Q. Meng, J. Cai, A Comprehensive Review of Factors Affecting Dynamic Capillary Effect in Two-Phase Flow, *Transp. Porous Media.* 144 (2022) 33–54. <https://doi.org/10.1007/s11242-021-01723-x>.

[276] Y. Gao, G. De Schutter, G. Ye, Z. Tan, K. Wu, The ITZ microstructure, thickness and porosity in blended cementitious composite: Effects of curing age, water to binder ratio and aggregate content, *Compos. Part B Eng.* 60 (2014) 1–13. <https://doi.org/10.1016/j.compositesb.2013.12.021>.

[277] A. Elsharief, M.D. Cohen, J. Olek, Influence of lightweight aggregate on the microstructure and durability of mortar, *Cem. Concr. Res.* 35 (2005) 1368–1376.

[278] B.Z. Dilnesa, B. Lothenbach, G. Renaudin, A. Wichser, D. Kulik, Synthesis and characterization of hydrogarnet Ca₃(Al_xFe_{1-x})₂(SiO₄)_y(OH)₄(3-y), *Cem. Concr. Res.* 59 (2014) 96–111. <https://doi.org/10.1016/j.cemconres.2014.02.001>.

[279] A. Mancini, E. Wieland, G. Geng, R. Dähn, J. Skibsted, B. Wehrli, B. Lothenbach, Fe(III) uptake by calcium silicate hydrates, *Appl. Geochemistry.* 113 (2020). <https://doi.org/10.1016/j.apgeochem.2019.104460>.

[280] B.Z. Dilnesa, E. Wieland, B. Lothenbach, R. Dähn, K.L. Scrivener, Fe-containing phases in hydrated cements, *Cem. Concr. Res.* 58 (2014) 45–55. <https://doi.org/10.1016/j.cemconres.2013.12.012>.

[281] F. Collins, J.G. Sanjayan, Microcracking and strength development of alkali activated slag concrete, *Cem. Concr. Compos.* 23 (2001) 345–352. [https://doi.org/10.1016/S0958-9465\(01\)00003-8](https://doi.org/10.1016/S0958-9465(01)00003-8).

[282] X. Zheng, H. Liu, S. You, S. Easa, K. Cheng, Z. Chen, T. Ji, Cracking resistance and sustainability assessment of alkali-activated slag concrete incorporating lightweight aggregate, *Cem. Concr. Compos.* 131 (2022) 104556. <https://doi.org/10.1016/j.cemconcomp.2022.104556>.

[283] M.S. Tale Masoule, N. Bahrami, M. Karimzadeh, B. Mohasanati, P. Shoaei, F. Ameri, T. Ozbakaloglu, Lightweight geopolymers concrete: A critical review on the feasibility, mixture design, durability properties, and microstructure, *Ceram. Int.* 48 (2022) 10347–10371. <https://doi.org/10.1016/j.ceramint.2022.01.298>.

List of publications

Related to this thesis:

1. **C Liu**, Y Tao, S Nie, Y Chen, Z Li, C S Poon, G Ye. (2025) Dissolution of cations in C-(N,K-)A-S-H gels at the nanoscale. *Composites Part B: Engineering*.
2. **C Liu**, Z Li, G Ye. (2025) Mitigating the efflorescence of alkali-activated slag mortars by aluminosilicate-based lightweight fine aggregate. *Cement and Concrete Research*.
3. **C Liu**, J Xie, Z Li, G Ye. (2025) An experimental and numerical study on the cracking of alkali-activated slag pastes induced by water immersion. *Cement and Concrete Research*.
4. **C Liu**, Z Li, S Nie, J Skibsted, G Ye. (2024) Structural evolution of calcium sodium aluminosilicate hydrate (C-(N-)A-S-H) gels induced by water exposure: The impact of Na leaching. *Cement and Concrete Research*.
5. **C Liu**, Z Li, G Ye. (2025) Mechanisms of efflorescence of alkali-activated slag. *Cement and Concrete Composites*.
6. **C Liu**, X Liang, Y Chen, Z Li, G Ye. (2023) Degradation of alkali-activated slag subjected to water immersion. *Cement and Concrete Composites*.
7. **C Liu**, Z Xu, S He, G Ye. (2025) A reactive transport model to predict microstructural deterioration of alkali-activated slag induced by leaching. *Cement and Concrete Research* (under review).

Out of this thesis:

1. **C Liu**, Y Zhang, M Liang, Z Li, G Ye. (2024) Underwater carbonation of alkali-activated slag pastes. *Construction and Building Materials*.
2. **C Liu**, H Wu, Z Li, H Shi, G Ye. (2024) Effect of curing condition on mechanical properties and durability of alkali-activated slag mortar. *Construction and Building Materials*.
3. **C Liu**, L Yang, Z Li, S Nie, C Hu, F Wang. (2022) Improve the long-term property of heat-cured mortars blended with fly ash by internal curing. *Journal of Building Engineering*.
4. **C Liu**, L Yang, F Wang, S Hu. (2021) Enhance the durability of heat-cured mortars by internal curing and pozzolanic activity of lightweight fine aggregates. *Construction and Building Materials*.
5. **C Liu**, Y Liu, Z Liu, C Hu, X Huang, L Yang, F Wang. (2019) Heat-cured concrete: Improving the early strength and pore structure by activating aluminosilicate internal curing agent with triisopropanolamine. *Journal of the American Ceramic Society*.
6. X Yang, S Wu, S Xu, **C Liu**, B Chen, D Chen, C Yang. (2025) Synthesis, characterization, and environmental impact analysis of one-part alkali-activated materials based on alkali-fused basic oxygen furnace slag. *Construction and Building Materials*.

7. X Liang, H Dong, Z Li, **C Liu**, S Zhang, G Ye. (2025) Characterization, pretreatment, and valorization of wood biomass fly ash in a binary cement-free binder. *Developments in the Built Environment*.
8. Y Zhang, S Nie, **C Liu**. (2025) Phosphorus slags: Structural insights, dissolution behavior, and potential as sustainable supplementary cementitious materials. *Chemical Engineering Journal*.
9. Y Zuo, Y Chen, **C Liu**, Y Gan, L Goebel, G Ye, JL Provis. (2025) Modeling and simulation of alkali-activated materials (AAMs): A critical review. *Cement and Concrete Research*.
10. Z Guo, J Qiu, D Huang, K Liu, A Kirichek, **C Liu**, B Chen, Y Zhao, Z Qu. (2025) Rheology of flexible fiber-reinforced cement pastes: Maximum packing fraction determination and structural build-up analysis. *Composite Structures*.
11. S Hu, J Qiu, Q Zhang, Z Guo, **C Liu**. (2025) Quantitative Analysis of Yield Stress and Its Evolution in Fiber-Reinforced Cemented Paste Backfill. *Minerals*.
12. Y Chen, B Ma, J Chen, Z Li, X Liang, LM de Lima, **C Liu**, S Yin, Q Yu, B Lothenbach, G Ye. (2024) Thermodynamic modeling of alkali-activated fly ash paste. *Cement and Concrete Research*.
13. Y Zhang, S Zhang, **C Liu**, O Çopuroğlu. (2024) Characterizing two types of zonation within slag rims of aged alkali-activated slag pastes through SEM and TEM. *Cement and Concrete Research*.
14. L Feng, S Yi, S Zhao, Q Zhong, F Ren, **C Liu**, Y Zhang, W Wang, N Xie, Z Li, N Cui. (2024) Recycling of aluminosilicate-based solid wastes through alkali-activation: preparation, characterization, and challenges. *Buildings*.
15. Z Guo, J Qiu, A Kirichek, H Zhou, **C Liu**, L Yang. (2024) Recycling waste tyre polymer for production of fibre reinforced cemented tailings backfill in green mining. *Science of the Total Environment*.
16. M Liang, **C Liu**, X Liang, Z Chang, E Schlangen, B Šavija. (2024) Effects of temperature on autogenous deformation and early-age stress evolution in cement pastes with low water to cement ratio. *Construction and Building Materials*.
17. B Tu, X Yang, S Xu, X Liang, **C Liu**, J Jiang, L Fan, L Tu. (2023) Exploring the utilization of PHC pile waste concrete as filler in asphalt mastics. *Materials*.
18. T Lu, X Liang, **C Liu**, Y Chen, Z Li. (2023) Experimental and numerical study on the mitigation of autogenous shrinkage of cementitious material. *Cement and Concrete Composites*.
19. Z Li, X Liang, **C Liu**, M Liang, K van Breugel, G Ye. (2022) Thermal deformation and stress of alkali-activated slag concrete under semi-adiabatic condition: Experiments and simulations. *Cement and Concrete Research*.
20. S Zhao, Z Liu, F Wang, S Hu, **C Liu**. (2021) Effect of Extended Carbonation Curing on the Properties of γ -C2S Compacts and Its Implications on the Multi-Step Reaction Mechanism. *ACS Sustainable Chemistry & Engineering*.

Acknowledgments

Time has flown by, and in what feels like the blink of an eye, more than four years have passed. Yet, the memories of this journey remain as vivid as ever. During my doctoral studies, I have been fortunate to receive the help and support of many people, to whom I wish to express my deepest gratitude.

First and foremost, I am profoundly grateful to my motherland, China. I sincerely thank the China Scholarship Council and Wuhan University of Technology for their generous financial support.

My heartfelt thanks go to my promoter, Prof. Guang Ye, for placing your trust in me and accepting me as your student. Your insightful guidance throughout my PhD has continuously sharpened my research skills and enabled me to complete my studies smoothly. I am equally indebted to my co-promoter, Prof. Erik Schlangen, for providing excellent experimental facilities in the Microlab and for your valuable guidance, particularly in the mechanics-related part of my dissertation. I also extend my gratitude to my master's promoter, Prof. Fazhou Wang, whose recommendation was pivotal in allowing me to pursue my studies in the Netherlands.

I would like to thank all the members of my doctoral defence committee: Prof. Anya Vollpracht, Prof. Maria J. Santofimia Navarro, Prof. Zhichao Liu, Prof. Zhenming Li and Dr. Branko Šavija. Thank you for your valuable comments and positive evaluation, which allowed me to defend my dissertation successfully.

I am grateful to everyone who contributed to my dissertation. Thank you, Zhenming Li, for your meticulous revisions of my papers as a daily supervisor, which taught me how to write with logic and clarity. My thanks also go to the “modelling guys,” including Zhiyuan Xu, Yong Tao, and Jinbao Xie. Your contributions significantly deepened the quality of my thesis. I am also grateful to my former master's colleague, Shuai Nie, for teaching me everything about solid-state NMR.

My sincere appreciation goes to the technicians, without whose dedication I could not have achieved so many experimental results. Thank you, John—not only for performing countless ICP experiments for me, but also for being my best English pronunciation coach. Thank you, Arjan—you are both a gentleman and a marvellous SEM photographer. Thank you, Ton—you helped me conduct numerous pore solution experiments patiently, which I know were a nightmare

for you. Thank you, Maiko, my “nutritionist,” for your eggs, which were an essential source of protein for a gymmer. Thank you, Ruud—your expertise in XRD and XRF is as remarkable as your height. Finally, my thanks to all the secretaries, Jaap, Jacqueline, Iris, Sandra, and Claire, whose assistance made both my academic work and daily life much easier.

My thanks also go to my colleagues in the Microlab: Xuhui Liang, Yun Chen, and Hu Shi. Your companionship made my PhD journey far less lonely. Thanks to my office mates, Luiz Miranda de Lima, Ali Ghaderiaram, and Irving Flores Beltran, for the joyful moments we shared in our daily conversations. I am also grateful to my workout and badminton partners, Junkai Lan, Rui Wu, and many others, whose presence kept my passion for sports alive.

I would also like to thank my other colleagues, listed here in alphabetical order: Ameya Kamat, Bei Wu, Boyu Chen, Burcu Aytekin Turkoglu, Eyuphan Kucukkalfa, Farnaz Aghabeyk, Gabriel Mohallem Ferreira, Gozde Ozerkan, Guilherme da Silva Munhoz, Hao Cheng, Hao Huang, Haoming Wu, Henk Jonkers, Hua Dong, Jiandong Lu, Jiayi Chen, Marija Nedeljković, Mayank Gupta, Minfei Liang, Mohammad Fotouhi, Oguzhan Copuroglu, Patrick Holthuizen, Rauf Hassan, Rowin Bol, Shan He, Shi Xu, Shisong Ren, Shizhe Zhang, Stefan Chaves Figueiredo, Tianshi Lu, Wen Zhou, Xinrui Zhang, Xuliang Hou, Yading Xu, Yi Zheng, Yibing Zuo, Yidong Gan, Yitao Huang, Yu Chen, Yu Zeng, Yu Zhang, Yubao Zhou, Yuguang Yang, Ze Chang, Zhaozheng Meng, Zhenxu Qian, Mladena Luković, Zhi Wan, Zhipei Chen, Zhiwei Qian. Although I may not have mentioned every name here, each of you holds a special place in my heart. My gratitude for your help and friendship is beyond words, and I look forward to keeping in touch in the years to come.

Finally, I owe my deepest gratitude to my parents for raising me with unconditional love and fully supporting my studies in the Netherlands. Your son will never let you down. Last but certainly not least, I wish to thank my fiancée, Sixue Zhao. During our more than four years of long-distance relationship, you have given me unwavering understanding, patience, and companionship. I believe we will share a wonderful future.

Chen Liu

Aug, 2025, Delft

Curriculum Vitae

Name: Chen LIU (刘晨)

Date of Birth: 11 Sep, 1993

Mobile phone: +86 13971159158

E-mail: lc@whut.edu.cn



10/2020 - 10/2025	Doctor of Philosophy Faculty of Civil Engineering and Geosciences Delft University of Technology Delft, the Netherlands
09/2016 - 06/2019	Master of Science School of Materials Science and Engineering Wuhan University of Technology Wuhan, P.R.China “University Outstanding Master Thesis”
09/2012 - 06/2016	Bachelor of Science School of Materials Science and Engineering Wuhan University of Technology Wuhan, P.R.China



9 789465 181004